Calculated final state probability distributions for T_2 β-decay measurements

A Thesis submitted for the Degree

of

Doctor of Philosophy of the University of London

by

Natasha Doss

Department of Physics & Astronomy

University College London

August 2007

The question of a possible finite neutrino mass is one of the most investigated and controversial topics in particle physics and cosmology. The most promising direct experiments for determining the neutrino mass are based on the study of the β-decay of molecular tritium. The mass of the neutrino is deduced by analysing the shape of the continuous energy spectrum of the electrons emitted in the β-decay.

In this thesis, the molecular physics issues facing these experiments are investigated. Theoretical final state probability distributions of the daughter molecule are calculated to satisfy the higher resolution requirements and increased sensitivity of the future experiments.

Transition probabilities to the six lowest electronically bound states of $^3HeT^+$ are calculated. Rotational excitation of the daughter molecule is considered and probabilities obtained for the β-decay of T_2 in the first four rotational states. Isotope contamination from DT and HT molecules is also investigated, and the probability distributions for $^3HeD^+$ and $^3HeH^+$ are calculated. The sensitivity of the initial temperature, ortho:para ratio and isotopic composition of the source is considered. Estimates of the error in the value of the neutrino mass deduced from fitting theoretical spectra, due to uncertainties in temperature, ortho:para ratio of T_2 and percentage of DT molecules, are obtained.

The R-matrix method is used to treat the electronic continuum of $^3HeT^+$. Resonances converging to the first eight excited target states are obtained, and the transition probabilities to these resonances and background continuum are calculated.

Endpoint effects due to the decay of other possible species in the source – T^-, T, T^+, T_2^+, T_3^+ and T_5^+ – are also investigated.

It is hoped that this data will be used as part of the forthcoming KATRIN experiment.

Contents

List of Figures

List of Tables

Acknowledgements

I would like to thank Professor Jonathan Tennyson for his dedicated guidance and encouragement over the last few years.

I thank Svante Jonsell, Alejandro Saenz and Klaus Eitel for many useful discussions and comments.

I also thank my many friends I have made in the TAMPA group which have made my time here a valuable and enjoyable experience.

Finally I would like to thank my family and friends for their love and support, and dedicate this work to them.

Chapter 1

Introduction

1.1 Neutrinos - A brief history

In the Standard Model of particle physics, there are 12 fundamental particles that make up the basis of matter, 6 quarks and 6 leptons (see figure 1.1). Neutrinos form part of the fundamental group of leptons, and according to the Standard Model they have zero charge, zero mass and spin $\frac{1}{2}$ (i.e. they are fermions). Neutrinos do not interact with the strong or electromagnetic forces, they are only affected by the weak force. This means that they can pass through great distances of matter without being affected by it, making them extremely difficult to detect. There are three known types/flavours of neutrinos; the electron neutrino, the muon neutrino and the tau neutrino. Each neutrino is related to one of the charged leptons (the electron, the muon and the tau) after which it is named.

The first indirect evidence for the existence of the neutrino came in 1914 when James Chadwick reported that the energy spectrum of electrons emitted in the β-decay of a nucleus was *continuous*. This was very surprising at the time since, as the neutrino was not yet known to exist, the final state was believed to consist of just two bodies, the daughter ion and the electron, therefore giving a discrete spectrum for the electron energy. In order to retain the conservation of energy and momentum in β-decay, Wolfgang Pauli in 1930 postulated the existence of a third neutral, and as yet undetected, particle that is 'created' in the decay which carries away the remaining energy and momentum. In 1934 Enrico Fermi developed his theory of weak interaction decay, including Pauli's hypothetical particle, which explained many experimentally observed results [2]. As the neutrino was very difficult to detect, it was not until two decades later that it was first

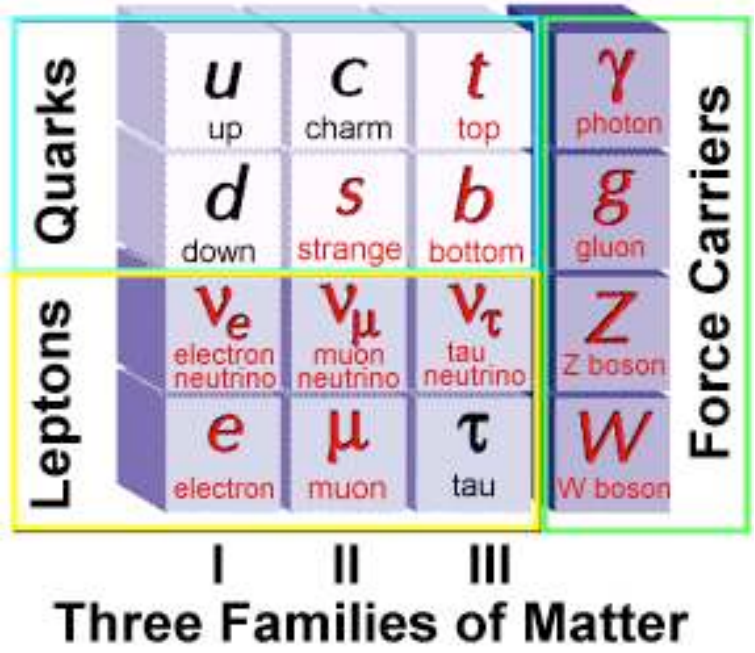

Figure 1.1: The fundamental matter particles of the Standard Model. Also shown are the force carrier particles. Image taken from the web-pages of the Stanford Linear Accelerator Center at Stanford University [1]

detected. In 1956 Clyde Cowan and Frederick Reines performed an experiment to detect neutrinos by placing a detector consisting of 400 l of water nearby a nuclear power plant [3]. They detected the neutrons produced from the interaction of the incoming neutrinos from the reactor with the protons in the water. It was later determined that the neutrino detected was an electron anti-neutrino. This was the first direct detection of neutrinos, a result which led them to receive the Nobel prize in 1995. In 1962 Leon Lederman, Melvin Schwartz and Jack Steinberger discovered that neutrinos produced in association with muons behaved differently to those produced in association with electrons, showing that there exists more than one type of neutrino [4]. The possible existence of a third type of neutrino was not suggested until 1978, when the tau particle was discovered. In 2000, the first observation of tau neutrino interactions was reported by the DONUT collaboration at Fermilab [5].

There are still many unknown properties of the neutrino which form some of the experimental goals in particle physics today: how many types of neutrino are there?, is the neutrino identical to its anti-particle? and as recent evidence has shown, do neutrinos have mass? and if so, what is it?

1.2 The neutrino mass problem - Implications of a non-zero neutrino rest mass

The determination of the rest masses of neutrinos is one of the most intriguing tasks in particle physics today. The existence of a non-zero neutrino mass has some fundamental implications in particle physics, cosmology and astrophysics.

According to the Standard Model (SM) of particle physics neutrinos are massless. Fermion masses in general are one of the major mysteries of the SM. There exist several theories beyond the SM in which neutrinos naturally acquire mass. Measurements of neutrino mass could be used to exclude some of these theories and determine the scale of new physics. They may also help to answer questions on what the mass scale hierarchy for neutrinos is and whether neutrinos are Majorana (identical to their anti-particles) or Dirac particles.

In cosmology and astrophysics, neutrinos play an important role in many scenarios including the formation of light nuclei during the Big Bang nucleosynthesis and the end of a heavy star (supernovae explosions). Massive neutrinos have been suggested as a possible contributor to the non-visible (dark) matter in the Universe. Many cosmological models depend on the relative contributions of the cold dark matter (CDM) and neutrino hot dark matter (νHDM) to the total content. The amount of νHDM could help us understand the role of neutrinos in the formation of large scale structures.

1.3 Neutrino mixing

The following discussion on neutrino mixing is based on the review by Kayser [6].

Experimental investigations of neutrino oscillations have provided compelling evidence for non-zero neutrino masses. These experiments are summarised in the next section and references given. Observations show that while travelling from the source to the detector, a neutrino flavour eigenstate, e.g. a muon neutrino, can transform into another flavour eigenstate, e.g. an electron neutrino. The existence of these neutrino oscillations requires a non-trivial mixing between the neutrino flavour eigenstates (ν_e, ν_μ, ν_τ) and the corresponding mass eigenstates (ν_1, ν_2, ν_3) via a unitary mixing matrix U. They also require that the mass eigenvalues (m_1, m_2, m_3) differ from each other and hence must be non-zero.

The flavour states $|\nu_\alpha\rangle$ are expressed as linear combinations of the three neutrino

mass eigenstates $|\nu_i\rangle$:

$$|\nu_\alpha\rangle = \sum_{i=1}^{3} U^*_{\alpha i}|\nu_i\rangle. \tag{1.1}$$

The $U_{\alpha i}$ are the elements of the unitary mixing matrix, which is referred to as the Pontecorvo-Maki-Nakagawa-Sakata (PMNS) matrix. For Dirac neutrinos the matrix is given by:

$$U = \begin{pmatrix} c_{12}c_{13} & s_{12}c_{13} & s_{13}e^{-i\delta} \\ -s_{12}c_{23} - c_{12}s_{23}s_{13}e^{+i\delta} & c_{12}c_{23} - s_{12}s_{23}s_{13}e^{+i\delta} & s_{23}c_{13} \\ s_{12}s_{23} - c_{12}c_{23}s_{13}e^{+i\delta} & -c_{12}s_{23} - s_{12}c_{23}s_{13}e^{+i\delta} & c_{23}c_{13} \end{pmatrix}, \tag{1.2}$$

where $\mathrm{c}_{ij} = \cos\theta_{ij}$ and $\mathrm{s}_{ij} = \sin\theta_{ij}$. θ_{ij} are the mixing angles and δ is a CP violating phase. For Majorana neutrinos two more phases enter the mixing matrix as:

$$U \rightarrow U \times \begin{pmatrix} e^{i\alpha_1/2} & 0 & 0 \\ 0 & e^{i\alpha_2/2} & 0 \\ 0 & 0 & 1 \end{pmatrix}. \tag{1.3}$$

The matrix therefore has six (four) parameters, three angles and three (one) phases for Majorana (Dirac) neutrinos. In addition there are the three neutrino masses. Equations (1.1)-(1.3) assume the existence of only three neutrinos. If more neutrinos exist, the matrix U would contain more elements and parameters.

1.4 Neutrino oscillation experiments - Evidence for massive neutrinos

Neutrino oscillations do not depend on the absolute masses of the neutrinos but on the differences of the masses. Results from the experiments have constrained some of the parameters of the mixing matrix. The data from these experiments has been used to obtain values for the three mixing angles θ_{12}, θ_{23} and θ_{13} and also for two mass squared differences, Δm^2_{21} and Δm^2_{31}, but they do not give any information on the phases, see the recent review by Fogli *et al.* [7]. In this section several neutrino oscillation experiments are discussed. The experiments are divided into four categories depending on the origin of the neutrinos; atmospheric, solar, reactor and accelerator. For more detail on the phenomenology of neutrino oscillations and recent experimental results, the reader is referred to the review article by Gonzalez-Garcia and Maltoni [8].

1.4.1 Atmospheric neutrinos

Atmospheric neutrinos are produced isotropically by the interaction of cosmic ray protons with atoms in the upper atmosphere ($\sim$ 15 km above the surface of the Earth), generating pions and kaons that then decay giving electron and muon neutrinos:

$$\pi^+ \rightarrow \mu^+ \nu_\mu, \tag{1.4a}$$

$$\mu^+ \rightarrow e^+ \nu_\mu \nu_e. \tag{1.4b}$$

The expected ratio of muon to electron neutrinos is 2:1. Neutrino oscillations can be investigated by detecting variations of this ratio as a function of the neutrino energy and distance travelled. Atmospheric neutrinos have been observed in several underground experiments using different techniques.

In 1998 the Super-Kamiokande experiment reported the first model independent evidence of ν_μ oscillations [9] at the Neutrino '98 conference. Super-Kamiokande is a water Cerenkov detector, which detects the Cerenkov light emitted by the charged leptons that are produced when a neutrino interacts inside the detector. The light is detected by an array of photomultipliers on the detector wall. The detector can distinguish between muon neutrinos and electron neutrinos as they produce different shape rings of light, muon neutrinos produce sharp rings while electron neutrinos produce blurred rings. Super-Kamiokande detected a smaller ratio of ν_μ events to ν_e events than expected. They also observed that the deficit of ν_μ depended on the zenith angle, the deficit being larger for neutrinos coming from the bottom of the detector than those from above. This suggested the deficit increased with the distance travelled by the neutrinos as the neutrinos from below would have had to travel through the Earth (an extra $\sim$ 13000 km) to reach the detector. This was not seen for the ν_e. The evidence suggested that the deficit was due to $\nu_\mu \rightarrow \nu_\tau$ oscillations.

The results from Super-Kamiokande have also been confirmed by two other experiments Soudan-2 [10] and MACRO [11] which use iron calorimeter detectors.

1.4.2 Solar neutrinos

Electron neutrinos are produced in the thermonuclear reactions in the Sun. The number of neutrinos that are produced are obtained from detailed knowledge of the nuclear physics in the Sun and its evolution. Over the last few decades, the solar models have been steadily refined. The most updated version of the Standard Solar Model (SSM) is

the one developed by Bahcall and Serenelli [12].

In 1968, Ray Davis Jr announced the first detection of solar (electron) neutrinos [13]. The Homestake experiment used a detector consisting of ~ 615 tons of liquid chlorine, which detects the neutrinos by counting the ^{37}Ar atoms created in the reaction:

$$\nu_e + {}^{37}\mathrm{Cl} \rightarrow e^- + {}^{37}\mathrm{Ar}. \tag{1.5}$$

The experiment reported observing less than half the expected amount of neutrinos [14], giving rise to the 'solar neutrino problem'.

In the early 1990's two more radiochemical experiments SAGE [15] and GALLEX [16] (which was later succeeded by GNO [17]) reported detecting neutrino fluxes less than the expected value. Both experiments used gallium as a target to detect the neutrinos via:

$$\nu_e + {}^{71}\mathrm{Ga} \rightarrow e^- + {}^{71}\mathrm{Ge}. \tag{1.6}$$

As the radiochemical experiments are only sensitive to electron neutrinos, they cannot explain the transitions of the ν_e's into other neutrinos. The Sudbury Neutrino Observatory (SNO) was designed to give model independent evidence for the deficit. The SNO is a water Cerenkov detector that is sensitive to all neutrino flavours, not just ν_e. SNO reported evidence for the presence of ν_μ and ν_τ in the solar neutrino flux on Earth [18–20], suggesting the flavour transition of ν_e into ν_μ and/or ν_τ.

1.4.3 Reactor neutrinos

Neutrino oscillations are also investigated using the electron anti-neutrino beams from nuclear reactors. These experiments search for the disappearance of $\bar{\nu}_e$, which have energies of about 3 MeV.

The short baseline experiment CHOOZ [21], which is located about 1 km from a French power station, found no deficit in the flux of the electron neutrinos. The experiment Palo Verde [22] also did not detect any disappearance of $\bar{\nu}_e$. Both experiments detect electron anti-neutrinos by observing the inverse β-decay process:

$$\bar{\nu}_e + p \rightarrow n + e^+. \tag{1.7}$$

KamLAND is a long baseline experiment (~ 180 km) situated in Japan, that works on the same detection principle as CHOOZ and Palo Verde. In 2003, they published their first results and reported a deficit in the number of $\bar{\nu}_e$ events observed compared to those expected [23], supporting the solar neutrino data.

Several new reactor experiments have been proposed, including Double CHOOZ [24] which will commence running in 2009.

1.4.4 Accelerator neutrinos

In accelerators proton beams are generated which are accelerated and scattered off a fixed target. The interaction produces charged pions in hadronic showers, which then decay into muons and muon neutrinos. The muons also decay giving electron neutrinos and muon neutrinos. These neutrino beams, which are similar to the atmospheric neutrinos, can be used to test the atmospheric oscillation signal.

The first of these experiments is the K2K which shoots a neutrino beam 250 km from the KEK proton synchrotron to the Super-Kamiokande detector. MINOS is a new experiment that is currently running. It has a baseline of 730 km from Fermilab to the Soudan mine. Both of these long-baseline experiments show clear evidence of ν_μ disappearance [25–27].

Two future experiments will investigate $\nu_\mu \rightarrow \nu_e$ oscillations. T2K (Tokai-to Kamioka) [28] will direct a ν_μ beam to Super-Kamiokande with a baseline of $\sim$ 295 km. NOνA [29] will use the MINOS neutrino beam and a far 30 kT liquid scintillator detector with a baseline of $\sim$ 800 km.

1.5 Mixing parameters and neutrino mass hierarchy

Fogli *et al.* [30] performed a global analysis of all the available oscillation data and gives best-fit values for the oscillation parameters, which are listed in table 1.1. The parameters Δm^2_{21} and θ_{12} are determined from the combination of data from the solar and KamLAND reactor experiments. The parameters $|\Delta m^2_{31}|$ and θ_{23} are obtained from atmospheric, accelerator and CHOOZ data.

The data from the experiments allows for three possible mass schemes: normal hierarchy, inverted hierarchy and quasi-degenerate neutrinos. The **normal hierarchy** has $m_1 \ll m_2 \ll m_3$. In this case Δm^2_{31} is positive. The **inverted hierarchy** has $m_1 \simeq m_2 \gg m_3$, and $\Delta m^2_{31} \simeq \Delta m^2_{32}$. In this case Δm^2_{31} is negative. Both of these schemes are shown in figure 1.2. In the **degenerate scheme** $m_1 \simeq m_2 \simeq m_3 \gg \sqrt{\Delta m^2_{31}}$.

Table 1.1: Best fit (at 2σ) for the oscillation parameters obtained in the global analysis of Fogli *et al.* [30].

Parameter	Best fit
Δm^2_{21}	$7.92(1\pm0.09)\text{x}10^{-5}$
$\sin^2\theta_{12}$	$0.314(1^{+0.18}_{-0.15})$
$\lvert\Delta m^2_{31}\rvert$	$2.6(1^{+0.14}_{-0.15})\text{x}10^{-3}$
$\sin^2\theta_{23}$	$0.45(1^{+0.35}_{-0.20})$
$\sin^2\theta_{13}$	$0.8^{+2.3}_{-0.8}\text{x}10^{-2}$

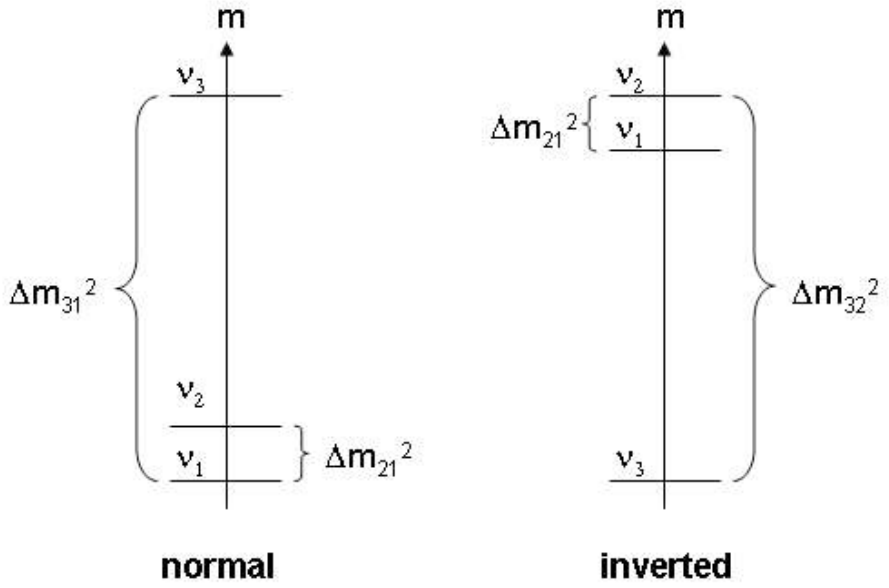

Figure 1.2: The normal and inverted hierarchy mass schemes for the neutrino masses.

1.5.1 Sterile neutrinos

Unlike the K2K and MINOS experiments, the short-baseline ($\sim$ 30 m) experiment LSND investigated $\bar{\nu}_\mu \rightarrow \bar{\nu}_e$ transitions by searching for the *appearance* of $\bar{\nu}_e$. They reported an excess in $\bar{\nu}_e$ suggesting $\Delta m^2 = 0.2 - 10$ eV^2/c^4 and a neutrino mass > 0.4 eV/c^2 [31]. In the three neutrino model, this result is incompatible with the solar, atmospheric and accelerator results, indicating the existence of at least one sterile neutrino. However this result still requires confirmation. The KARMEN experiment, which is very similar to LSND, did not find any oscillation [32] thus not confirming the LSND result. The MiniBooNE experiment was designed specifically to test the LSND result and is currently running at Fermilab [33].

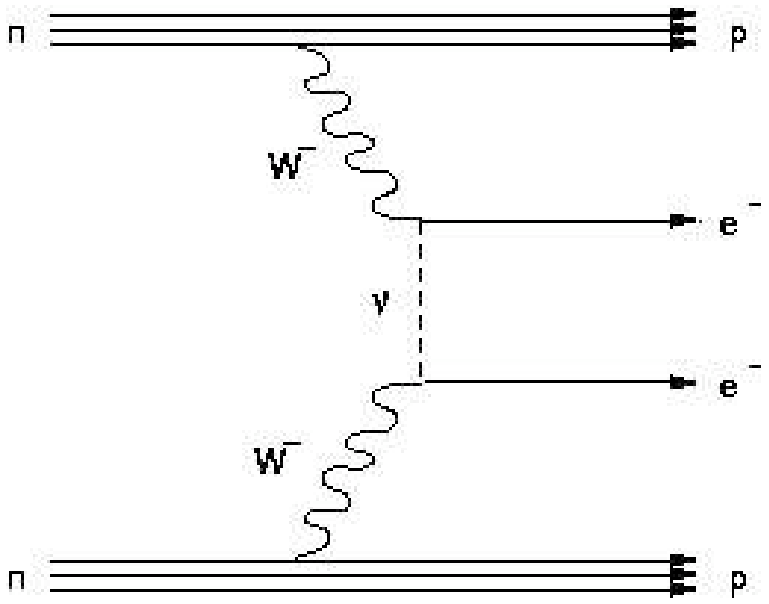

Figure 1.3: Feynmann diagram for the neutrinoless double beta decay process. Image taken from the web-pages of the NEMO experiment [34]

1.6 Absolute mass searches

Neutrino oscillation experiments have shown us that neutrinos are massive and have provided us with very important information on the differences in the masses squared. However they are insensitive to the absolute masses of the neutrinos. In this section I discuss three of the main methods used to give upper limits for the neutrino mass.

1.6.1 Neutrinoless double beta decay

Neutrinoless double beta decay ($0\nu\beta\beta$) is a very sensitive means of obtaining an absolute value of a neutrino mass. The process, which is forbidden by the Standard Model due to the non-conservation of the total lepton number ($\Delta L = 2$), is of the type [34]:

$$(A, Z) \rightarrow (A, Z + 2) + e^- + e^- \tag{1.8}$$

Two neutrons in the nucleus are simultaneously converted into protons, emitting two electrons but not emitting any anti-neutrinos. The decay can progress via the exchange of a massive Majorana neutrino between the two W^- bosons, as shown in figure 1.3. The neutrino must be Majorana as the anti-neutrino $\bar{\nu}_e$ emitted at the first vertex must be absorbed immediately as a neutrino ν_e at the second vertex, implying that the neutrino is identical to its anti-neutrino, hence Majorana.

The exchange of a neutrino is not the only possible mechanism that can induce $0\nu\beta\beta$. In models beyond the Standard Model, there can be other interactions/particles that also violate the lepton number conservation and can cause $0\nu\beta\beta$ [35]. Therefore a positive $0\nu\beta\beta$ signal does not necessarily mean that a direct measurement of a Majorana neutrino mass has been made. If neutrino exchange is the inducing mechanism then the $0\nu\beta\beta$ decay rate is proportional to the effective Majorana mass [36]:

$$m_{ee} = \left| \sum_i |U_{ei}|^2 e^{i\alpha_i} m_i \right|, \tag{1.9}$$

which depends on the CP violating phases as well as the masses and mixing parameters.

There are several experiments that have studied/are currently studying $0\nu\beta\beta$, using different $\beta\beta$ unstable nuclei such as ^{76}Ge, ^{100}Mo, ^{82}Se, ^{130}Te, ^{136}Xe, ^{116}Cd etc (a detailed discussion of the experiments to date can be found in [35] and the references therein). The detection of a signal requires the observation of a single significant peak in the energy spectrum as the total energy of the two emitted electrons is well defined.

The Heidelberg-Moscow experiment in Gran Sasso searched for $0\nu\beta\beta$ of ^{76}Ge. They first reported no evidence of a $0\nu\beta\beta$ signal leading to an upper limit of $m_{ee} < 0.35$ eV/c^2 [37]. A sub-group of Heidelberg-Moscow later claimed evidence of a signal at a 2.2σ or 3.1σ level, resulting in $m_{ee} = 0.11 - 0.56$ eV/c^2 with a best fit value of $m_{ee} = 0.39$ eV/c^2 [38]. After further analysis they claimed detection at 4σ, resulting in $m_{ee} = 0.2 - 0.6$ eV/c^2 [39].

The result from Heidelberg-Moscow attracted criticism [40, 41]. A similar experiment IGEX, also using ^{76}Ge, did not detect any signal giving an upper limit of $m_{ee} < 0.33 - 1.35$ eV/c^2 [42]. Apart from Heidelberg-Moscow no other experiments have reported positive signals.

Two currently running experiments are NEMO3 and Cuoricino. NEMO3 uses two different nuclei ^{100}Mo and ^{82}Se. In 2005 they published their first results where no signal was observed giving upper limits of $m_{ee} < 0.7 - 2.8$ eV/c^2 (^{100}Mo) and $m_{ee} < 1.7 - 4.9$ eV/c^2 (^{82}Se) [43]. Cuoricino looks for the double beta decay of ^{130}Te. The latest results give an upper bound of $m_{ee} < 0.2 - 1.1$ eV/c^2 [44]. A new experiment, Cuore, is also planned [44].

To determine m_{ee} from the data requires the theoretical calculation of the nuclear matrix elements (NME's) of the $0\nu\beta\beta$. The NME's are model-dependent and difficult to calculate. Different approaches give different results, which result in large systematic uncertainty in the value of m_{ee} deduced from the data [35].

1.6.2 Cosmological constraints

Neutrinos contribute to the total energy density of the Universe and therefore play a large role in large scale structure formation, leaving key signatures in several cosmological observables. Cosmological data can give (model-dependent) information on the *sum* of the neutrino masses $\sum_i m_i$, but not on individual masses or mixing, independently of whether neutrinos are Majorana or Dirac. The most relevant data comes from the studies of:

- **Cosmic Microwave Background (CMB).** Data consists of measurements of density fluctuations in the CMB. The most precise determination of these anisotropies, at present, come from the WMAP experiment [45–47].

- **Large Scale Structures (LSS).** The effect of neutrino masses on LSS can be studied by observing the distribution of galaxies, which traces the matter density of the Universe. At present there is data from two large projects: the Sloan Digital Sky Survey (SDSS) [48, 49] which will reach completion soon with data from 1 million galaxies, and the 2 degree Field Galaxy Redshift Survey (2dFGRS) [50, 51] that obtained results from 220,000 galaxies.

- **Lyman-α forests.** Corresponds to the Lyman-α absorption lines in the spectra of distant quasars due to intergalactic hydrogen clouds that lie in the line of sight. The distribution of these clouds is used to obtain important clues about structure formation.

For more detail see the review articles by Hannestad [52] and Lesgourgues and Pastor [53].

Data from the recent WMAP 3-year analysis alone places an upper bound on the sum of the neutrino masses at 1.8 eV/c^2 [45]. By the addition of other data such as LSS surveys and supernova measurements, the bounds can be improved [52, 53]. Including the Lyman-α data strengthens the bounds significantly, however due to the systematic uncertainties in the Lyman-α data, its robustness is still a subject of discussion [53]. Due to the different sets of data available, authors have used different combinations of the data and obtained different upper bounds. The lowest upper bound at present is that obtained by Seljak, Slosar and McDonald [54]. Combining data from CMB measurements (including the new WMAP 3-year analysis), LSS analysis, Lyman-α constraints and supernovae data they obtain the upper bound:

$$\sum m_\nu < 0.17 \text{ eV/c}^2 \text{ (95\% C.L.)}.$$

For recent limits obtained from different combinations of data the reader is referred to the following sources [30, 45, 52, 53, 55] and the references therein.

1.6.3 Kinematical/direct measurements

Investigations that are based solely on kinematic arguments provide the most direct measurements of the neutrino mass. They make use of the principle of conservation of energy and momentum and the relativistic energy momentum relation $E^2 = p^2c^2 + m^2c^4$. They are also independent of the nature, Majorana or Dirac, of the neutrino. Kinematic experiments are based on the detection of the energies and/or momenta of the charged decay products that are produced in weak decays.

The ALEPH experiment at the Large Electron Positron (LEP) collider at CERN investigated the mass of the tau neutrino by analysis of the processes:

$$\tau^- \rightarrow 2\pi^- + \pi^+ + \nu_\tau \tag{1.10a}$$

$$\tau^- \rightarrow 3\pi^- + 2\pi^+ + \nu_\tau \tag{1.10b}$$

$$\tau^- \rightarrow 3\pi^- + 2\pi^+ + \pi^0 + \nu_\tau. \tag{1.10c}$$

They reported an upper limit for the mass of [56]:

$$m_{\nu_\tau} < 18.2 \text{ MeV/c}^2 \text{ (95\% C.L.)}.$$

The mass of the muon neutrino was measured by Assamagan *et al.* [57] by analysis of the process:

$$\pi^+ \rightarrow \mu^+ + \nu_\mu \tag{1.11}$$

where they obtained an upper limit of:

$$m_{\nu_\mu} < 0.17 \text{ MeV/c}^2 \text{ (90\% C.L.)}.$$

Several experiments have investigated the mass of the electron neutrino, the most sensitive of which are from the analysis of the β-decay of tritium. These experiments and upper limits for the mass are discussed in the next section.

1.7 Tritium β-decay experiments

These experiments are based on the study of the energy spectrum of the electrons produced in the β-decay of tritium:

$$^3\text{H} \rightarrow {}^3\text{He}^+ + e^- + \bar{\nu}_e \tag{1.12}$$

with the energy released in the decay being shared between the daughter ion, the electron and the neutrino. The idea is to detect the energies of the electrons created in the decay, and deduce the mass of the electron anti-neutrino, $m_{\overline{\nu}_e}$, by analysing the electron energy (beta) spectrum. As the intensity of β electrons near the endpoint is very weak and their detection is hampered by background noise, an exact value for the experimental endpoint energy, the maximum β electron energy, is difficult to obtain. Instead $m_{\overline{\nu}_e}$ must be obtained by analysing the *shape* of the β spectrum close to the endpoint.

The electron energy spectrum is given by [58, 59]:

$$\frac{dN}{dE} = C{\times}F(Z,E)p(E{+}m_ec^2)(W_0{-}E)\sqrt{(W_0-E)^2 - m^2_{\overline{\nu}_e}c^4}H(W_0{-}E{-}m_{\overline{\nu}_e}c^2), \quad (1.13)$$

where E is the electron energy, N is the number of electrons with energies between E and $E + dE$ emitted per unit time, W_0 is the maximum kinetic energy of the electron if the neutrino mass were zero, m_e is the electron rest mass, p is the electron momentum, $F(Z,E)$ is the Fermi function describing the Coulombic interaction of the final particles and H is the Heavyside step function. $m_{\overline{\nu}_e}$ is the effective electron anti-neutrino mass given by:

$$m^2_{\overline{\nu}_e} = \sum_i |U_{ei}|^2 m_i^2. \quad (1.14)$$

For more theoretical detail see chapter 3.

A non-zero neutrino mass causes a distortion in the spectrum that is only statistically significant in the region close to the endpoint (see figure 1.4), hence only a narrow region close to the endpoint is analysed by the experiments. For this reason it is preferable to use a β-emitter with a low endpoint energy. The fraction of β-decays falling in the last 1 eV is $\sim 2{\times}10^{-13}$ therefore experiments with high sensitivity require high luminosity and high energy resolution.

The neutrino mass (and endpoint energy) is determined by a fit procedure where the deviation of a theoretical spectrum from the experimental one is minimised by varying the fit parameters $m_{\overline{\nu}_e}$ and W_0, as well as experimental free parameters (e.g. background).

Tritium is the most suitable atom because:

- it has the second lowest endpoint ($\sim$ 18.6 keV) of all the β unstable isotopes,
- it has relatively short life-time ($t_{\frac{1}{2}}$ = 12.3 y),

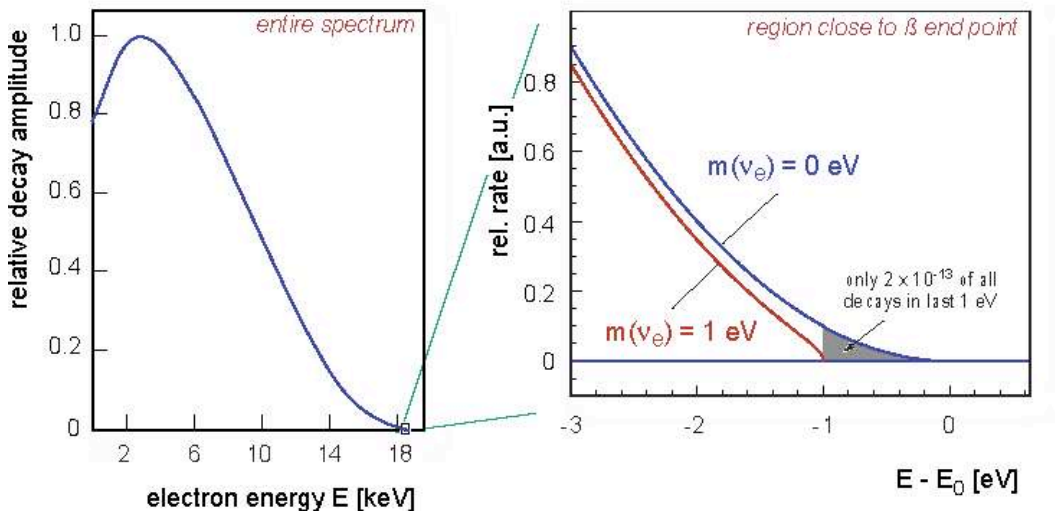

Figure 1.4: The electron energy spectrum of tritium β-decay. E_0 is the maximum kinetic energy of the electron if the neutrino mass were zero (i.e. W_0 in equation 1.13). Image taken from the KATRIN homepage [60]

- T and $^3He^+$ have simple electronic shell configurations therefore corrections due to atomic/molecular excitations and scattering can be calculated in a straight forward way.

Different experiments have used tritium atoms embedded in various molecules/ environments. However it later became evident that as the daughter ion can be left in an excited state, it is crucial to include the final state distribution in the analysis. Therefore recent experiments have used molecular tritium, T_2, as the final state distribution can be calculated with reasonable accuracy.

1.7.1 Summary of early experiments

In this section I shall give a summary of the early tritium β-decay experiments. For a more complete description of the experimental techniques, the reader is referred to the reviews by Holzschuh [59], and Robertson and Knapp [58].

The first measurements of the β spectrum of tritium were performed by Curran *et al.* in 1948 [61–63] and Hanna and Pontecorvo in 1949 [64] using proportional counters. Both observed upper limits of the neutrino mass of 1 keV/c^2. The use of high resolution spectrometers was introduced in the 1950's in the experiments by Langer and Moffat [65] and Hamilton *et al.* [66]. Both groups reported upper limits of 250 eV/c^2, although their calculated endpoints differed significantly (by $\sim$ 1.5 keV). After a quiet period in

this field, two experiments performed in 1969 by Salgo and Staub [67] and Daris and St. Pierre [68] reduced the upper limit further to 200 eV/c^2 and 75 eV/c^2 respectively. In 1972 Bergkvist placed the upper limit for the neutrino mass at 55 eV/c^2 [69, 70] .

The work by Bergkvist is considered a landmark in the field of tritium β-decay experiments, not only because of the experimental improvements, but he recognised that the final decay product He^+ can be left in an excited state, and the effect of this final state distribution must be taken into account in order to make further improvements on the neutrino mass.

In 1976 the ITEP group in Moscow reported the result of their first measurement, $m_{\overline{\nu}_e} < 35$ eV/c^2 [71]. Four years later they announced that they had found evidence for a finite neutrino mass of 34.3 eV/c^2 [72]. This surprising result was soon met with criticism. Simpson [73] and Bergkvist [74, 75] found that the resolution function of the spectrometer had not been well understood by the ITEP group, resulting in an overestimation of the measured neutrino mass. The ITEP group made several improvements, however in 1985 and 1987 they reported similar results [76, 77]. The finite results from ITEP and the surrounding controversy provided a strong motivation for new experiments and in the following years much interest was stimulated. The Zurich group reported upper limits of $m_{\overline{\nu}_e} < 18$ eV/c^2 (1986) [78] and $m_{\overline{\nu}_e} < 11$ eV/c^2 (1992) [79] . From 1987-1991 the group at INS in Tokyo published results of $m_{\overline{\nu}_e} < 32$ eV/c^2 [80], $m_{\overline{\nu}_e} < 29$ eV/c^2 [81] and $m_{\overline{\nu}_e} < 13$ eV/c^2 [82]. The group at the Los Alamos National Laboratory was the first group to attempt using gaseous molecular tritium as a source. In 1987 and 1991 they reported upper limits for the neutrino mass of < 27 eV/c^2 [83] and < 9.3 eV/c^2 [84] respectively. In 1995 the group at Lawrence Livermore reduced this limit further to < 3.9 eV/c^2 [85]. The results of these experiments are summarised in table 1.2.

In the early 1990's two groups at Mainz and Troitsk also began running β-decay experiments, using molecular tritium. The results from these two experiments are shown in table 1.3. These two experiments are discussed below in more detail.

1.7.2 Unphysical results

In the 50 years since the first measurement was made by Curran *et al.* the tritium β-decay experiments became more sophisticated. However, as the upper limit for the electron anti-neutrino mass decreased, a more disturbing trend in the experimental data became apparent. The analysis of the β spectra returned negative (unphysical) values for

Table 1.2: Summary of tritium β-decay experiments. The masses are in units of eV/c^2. Uncertainties are statistical and systematical respectively.

Authors/Group	Year	$m^2_{\overline{\nu}_e}$	$m_{\overline{\nu}_e}$	Ref.
Curran *et al.*	1948		<1000	[61–63]
Hanna and Pontecorvo	1949		<1000	[64]
Langer and Moffat	1952		<250	[65]
Hamilton *et al.*	1953		<250	[66]
Salgo and Staub	1969		<200	[67]
Daris and St. Pierre	1969		<75	[68]
Bergkvist	1972		<55	[69, 70]
ITEP	1976		<35	[71]
ITEP	1980		=34.3±4	[72]
ITEP	1985	1215±130	=34.8±1.9	[76]
Zurich	1986	-11±63±204	<18	[78]
ITEP	1987	970±50±160	=30.3±	[77]
Los Alamos	1987	-57±453±118	<27	[83]
INS Tokyo	1987		<32	[80]
INS Tokyo	1988		<29	[81]
INS Tokyo	1991	-65±85±65	<13	[82]
Los Alamos	1991	-147±68±41	<9.3	[84]
Zurich	1992	-24±48±61	<11	[79]
Lawrence Livermore	1995	-130±20±15	<3.9	[85]

the fit parameter $m^2_{\overline{\nu}_e}$, see column 3 in tables 1.2 and 1.3. When extracting a quantity that is very close to zero from experimental data using a fit procedure, experimental uncertainties can lead to negative values being obtained, with error bars extending into the positive region. In the earlier experiments the negative values could be explained by the large uncertainties. However, as the resolution of the experiments improved, and the error bars reduced, these statistical uncertainties could no longer explain the negative values. It became evident that this negative mass squared problem must be due to some systematic error in the experiments or in the theory. Several possibilities were suggested:

1. The fit had to be extended into the negative $m^2_{\overline{\nu}_e}$ region. As this extension is arbitrary, due to the region being unphysical, different groups used different forms.

Table 1.3: Summary of the results from the Mainz and Troitsk experiments. The masses are in units of eV/c^2. Uncertainties are statistical and systematical respectively.

Group	Year	$m^2_{\overline{\nu}_e}$	$m_{\overline{\nu}_e}$	Ref.
Mainz	1993	-39±34±15	<7.2	[86]
Mainz	1994	-22±17±14	<5.6	[87]
Troitsk	1994	-22±4.8	<4.35	[88]
Troitsk	1994-1998	-1.9±3.4±2.2	<2.5	[89]
Mainz	1998	-3.7±5.3±2.1	<2.8	[90]
Troitsk	Comb.(1994-1999)	-1.0±3.0±2.1	<2.5	[91]
Mainz	Comb.(1998-1999)	-1.6±2.5±2.1	<2.2	[92]

Jonsell and Monkhorst [93] investigated the effect of various extensions on the value of the obtained neutrino mass.

2. The size of the energy interval below the endpoint used in the fit. It was found that as the data range extended further below the endpoint, the fit became worse and $m^2_{\overline{\nu}_e}$ became more negative [86].

3. Experimental errors. Possible sources are: source inhomogeneities, energy losses from inelastic scattering of the electrons, backscattering etc.

4. Inaccuracy in the theoretical final state distribution.

1.7.3 The Mainz and Troitsk experiments

The two most recent neutrino mass experiments to be performed were the Mainz experiment [90] that ran from 1991 to 2001 and the Troitsk experiment [89] that ran from 1994 to 2001. Both experiments used similar integrating MAC-E-Filter (Magnetic Adiabatic Collimation combined with an Electrostatic Filter) type spectrometers to perform the energy analysis of the β electrons. This new type of spectrometer was first proposed by Beamson *et al.* [94] in 1980, and redeveloped independently by Lobashev *et al.* [95, 96] and Picard *et al.* [97] specifically for the search of the electron neutrino mass in the Troitsk and Mainz experiments respectively. The advantage of using this type of spectrometer is the combination of high luminosity with high energy resolution, both of which are essential for providing the high sensitivity required to measure the neutrino mass from the β spectrum endpoint region.

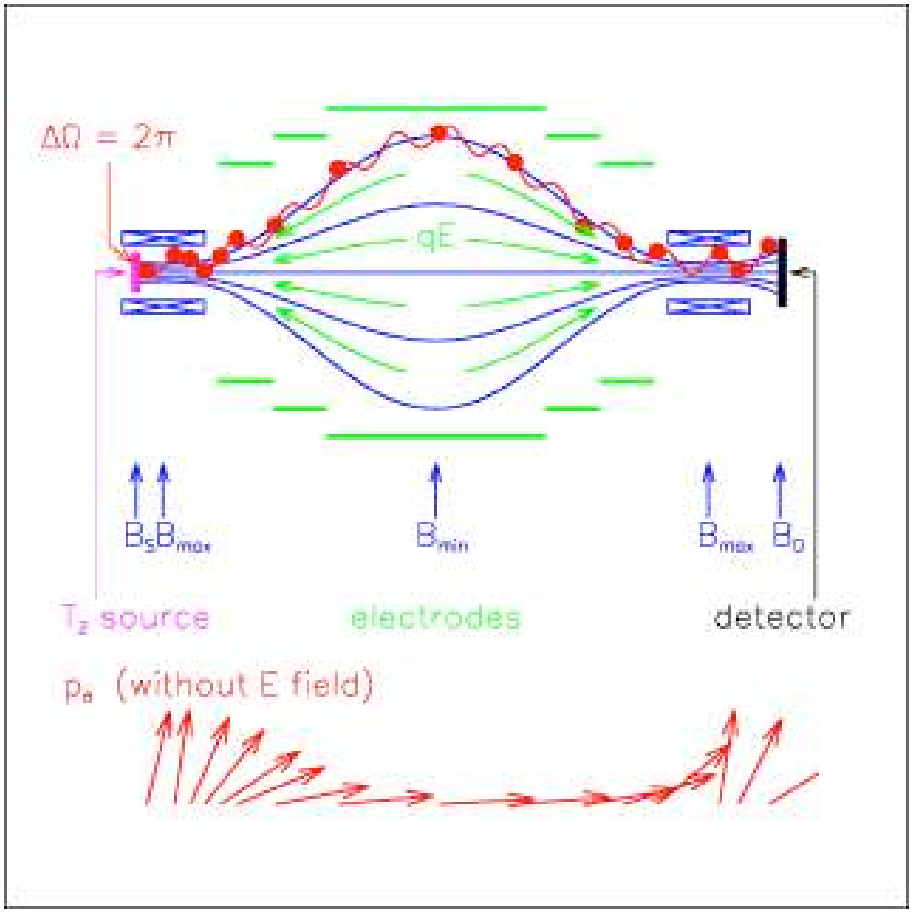

Figure 1.5: Principle of the MAC-E-Filter. Image taken from the KATRIN homepage [60]

Figure 1.5 shows the principle of the MAC-E-Filter. Two superconducting solenoids produce a magnetic field that guides the β electrons, coming from the tritium source, into the spectrometer in a cyclotronic motion around the magnetic field lines. On the way to the centre of the spectrometer the magnetic field drops several orders of magnitude, transforming the cyclotron energy of the electrons into longitudinal motion. The β electrons are thus transformed into a beam of electrons moving through the spectrometer parallel to the magnetic field lines. Cylindrical electrodes produce an electrostatic potential against the beam of electrons. Electrons with enough energy to pass the electrostatic barrier are re-accelerated and collimated onto the detector. Those that do not have enough energy are reflected. The spectrometer therefore acts as an integrating high-energy pass filter. The recorded spectrum obtained by the experiments is therefore an *integral* β-decay spectrum.

The main difference between the two experiments is the nature of their tritium sources. The Mainz experiment used a thin film of molecular tritium frozen onto a

cold graphite substrate, while the Troitsk experiment used a windowless gaseous molecular tritium source (WGTS). The WGTS approach was first pioneered in the Los Alamos experiment [84]. It is based on the principle of the adiabatic transport of electrons in a strong longitudinal magnetic field and the circulation of the tritium gas at low pressure by means of a differential pumping system. The use of the WGTS over the frozen source has several advantages including guaranteed homogeneity over the cross section of the source and almost total suppression of backscattering [98]. It also means that theoretical calculations of the final state distribution of free T_2 molecules can be used in the analysis of the β spectrum.

Both the Mainz and Troitsk experiments initially reported negative $m^2_{\overline{\nu}_e}$ from the analysis of their early runs. Each group analysed the systematic effects and made improvements to their experimental set-ups and $m^2_{\overline{\nu}_e}$ fitting procedures.

Mainz results

The Mainz data of 1991 and 1994 observed a trend towards negative values of $m^2_{\overline{\nu}_e}$ for larger fit intervals [86, 87]. An upgrade of the Mainz experiment between 1995 and 1997 improved the set-up considerably [87]. The signal to background ratio was improved by a factor of ten and the statistical quality of the data by long term measurements was much improved [90]. Figure 1.6 shows the endpoint region of the Mainz 1994, 1998 and 1999 data. The main systematic uncertainties were connected to the physics and properties of the quench-condensed tritium source. They originated from the dewetting of the tritium film, inelastic scatterings of electrons within the film, and the self-charging of the film. These uncertainties were investigated in detail [87, 99, 100] and significantly reduced.

By reducing these uncertainties and the lowering and stabilisation of the background rate, the Mainz runs of 1998-2001 reported values of $m^2_{\overline{\nu}_e}$ compatible with zero [102].

Combining the data from 1998, 1999 and 2001 (in an analysis where only the last 70 eV of the β spectrum below the endpoint is used) gives [102]:

$$m^2_{\overline{\nu}_e} = -0.6 \pm 2.2 \pm 2.1 \text{ eV}^2/\text{c}^4$$

corresponding to an upper limit for the neutrino mass of:

$$m_{\overline{\nu}_e} < 2.3 \text{ eV}/\text{c}^2 \text{ (95\% C.L.)}.$$

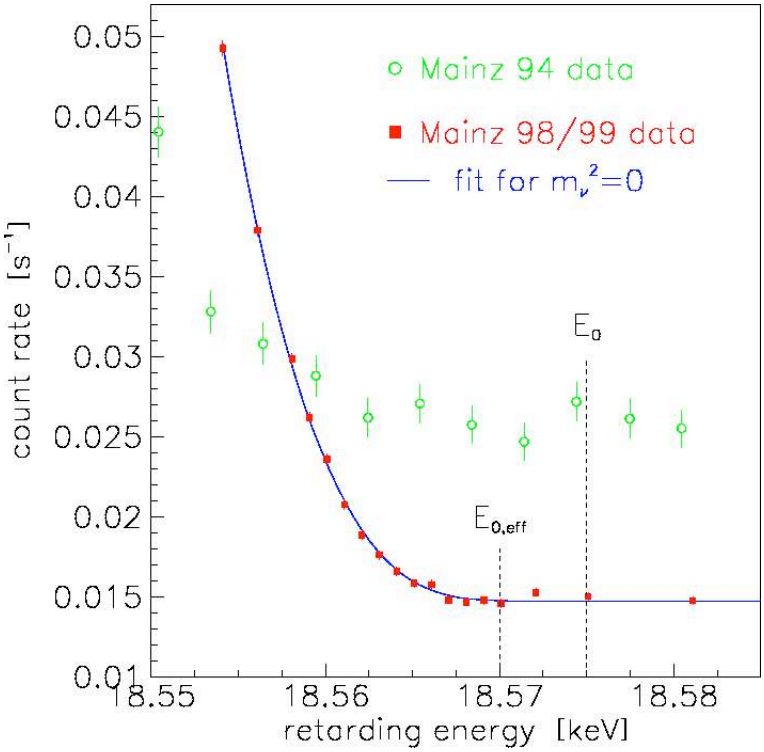

Figure 1.6: Mainz fit results. Image from the Mainz web-page [101]

Troitsk results

From its first measurements in 1994, the Troitsk group observed the existence of excess count rate in the experimental energy spectrum located a few eV below the endpoint [88]. As the MAC-E-Filter is used as an integrating spectrometer, this excess in the count rate corresponds to a narrow line in the differential β spectrum, carrying a fraction of about 10^{-10} of the total intensity. From 1998, the Troitsk group reported that the position of the line oscillates between 5 eV and 15 eV below the endpoint with a frequency of half a year [89]. Only one data set at Mainz showed evidence of a similar bump, but this was before the background was stabilised and reduced [90]. The origin of the anomaly is still unknown, however parallel measurements at Troitsk and Mainz indicate that the 'Troitsk anomaly' is an experimental artifact [103]. The size of the anomaly was reduced when experimental upgrades to lower the background rate were performed at Troitsk.

Fitting a standard β spectrum to the data resulted in large negative values of $m^2_{\overline{\nu}_e}$ in the range -10 to -20 eV^2/c^4 being obtained. However by taking the bump into account with the addition of a mono-energetic line, with variable amplitude and position, to the theoretical spectrum (and after correcting for the trapping of electrons in the tritium source) resulted in values of $m^2_{\overline{\nu}_e}$ compatible with zero, thus eliminating the negative-

value problem [103].

Combining the results of 1994-1999 and 2001 gives [103]:

$$m^2_{\overline{\nu}_e} = \text{-2.3} \pm 2.5 \pm 2.0 \text{ eV}^2/\text{c}^4$$

corresponding to an upper limit for the neutrino mass of:

$$m_{\overline{\nu}_e} < 2.05 \text{ eV/c}^2 \text{ (95\% C.L.)}.$$

Due to design limitations, both experiments have reached their sensitivity limits, therefore new data from the experiments will not improve the upper limit on $m_{\overline{\nu}_e}$ significantly. To measure an electron neutrino mass in the sub-eV region requires a new next generation experiment with much higher sensitivity. The main requirements for a new experiment are [98, 104]:

- High energy resolution. To reach a sensitivity in the sub-eV range, an energy resolution of ΔE $\sim$ 1 eV is necessary.

- High signal rate in the endpoint region. The energy interval of the region of interest below the endpoint is proportional to the mass of the neutrino. Also the count rate decreases significantly as you get closer to the endpoint. Therefore a higher signal rate is required for smaller neutrino masses.

- Low background rate in the endpoint region. To probe the sub-eV mass range a low background count rate of the order of 10^{-2} counts/sec or less is required.

1.7.4 KATRIN

The Karlsruhe Tritium Neutrino (KATRIN) experiment is a next generation tritium β-decay experiment currently under construction at the Forschungszentrum Karlsuhe (FZK) in Germany. The KATRIN collaboration includes nearly the complete world-wide expertise on tritium β-decay experiments. The main requirements for a sub-eV experiment mentioned in the previous section form the basis of the design of the experiment which combines the best features of the Mainz and Troitsk experiment, namely the WGTS and MAC-E-Filter, but on a much larger scale. The FZK was chosen as the location for the experiment due to its ability to meet the extensive experimental demands, in particular its close proximity to the Tritium Labor Karlsruhe (TLK), which is the only European scientific laboratory certified to handle and process the total tritium inventory of the experiment.

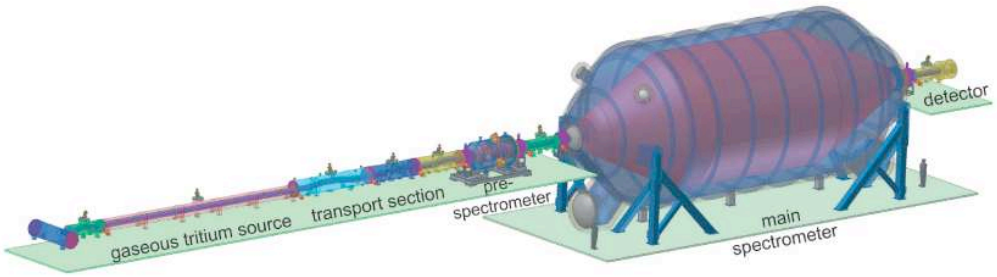

Figure 1.7: Design of the KATRIN experiment, showing the five major components of the design. Image taken from the KATRIN homepage [60]

The KATRIN experiment [104, 105] anticipates a sensitivity on the neutrino mass of $m_{\overline{\nu}_e} < 0.2$ eV/c^2 (90% C.L.), a factor of ten higher sensitivity compared to the Mainz and Troitsk experiments. This number corresonds to the upper limit of the neutrino mass if no signal is observed. In the case of a positive signal, a neutrino mass of $m_{\overline{\nu}_e} < 0.35$ eV/c^2 could be detected with 5σ significance. This will allow KATRIN to probe the quasi-degenerate scenario for neutrino mass. The combination of the result obtained by KATRIN with other laboratory (neutrino oscillation and $0\nu\beta\beta$ decay) and cosmological data will improve our estimate of the neutrino mass and answer many open problems in this field.

The KATRIN experiment aims to deduce the mass of the neutrino by analysing the last 30 eV of the β spectrum below the endpoint. However other parameters such as the background noise will be obtained, and tests performed, by considering a much larger energy interval.

The design of the KATRIN experiment is shown in figure 1.7. It consists of a linear configuration approximately 70 m long with about 40 superconducting solenoids that will guide the β electrons from the source to the detector. The experiment can be divided into five sections which are briefly described below. For more technical information the reader is referred to the KATRIN Letter of Intent [104] and the KATRIN Design Report [98].

- **Windowless gaseous tritium source (WGTS).** The WGTS consists of a cylindrical tube that is 10 m long and 90 mm in diameter. This is much larger than the Troitsk design as the total β-luminosity is proportional to the cross sectional area of the source tube. The tritium gas will be injected at the centre of the tube

and diffuse over the length of the tube. The column density of the source will be fixed at a value of 5x10^{17} molecules/cm^2. The decay probability of a single tritium molecule in the source is about 10^{-9}. The WGTS will deliver a total of about 10^{11} β-decays per second. With these values the count rate is increased by two orders of magnitude with respect to the Troitsk experiment. The tritium gas will have an isotopic purity of $> 95\%$ (atomic composition), with the main contamination coming from deuterium atoms, and an isotopic stability of better than 1%. The source will be at a working temperature of around 30 K, which must be stabilised to a precision of 1% to avoid tritium density changes in the source. Laser Raman spectroscopy will be used to provide a real-time quantitative analysis of the composition of the gas mixture, in particular to monitor the contribution from the hydrogen isotopomers DT and HT.

- **Transport section.** The electron transport system guides the β electrons adiabatically from the source to the spectrometer, while also eliminating any tritium flow. The spectrometer must be kept free of tritium for background and safety reasons. This section consists of two parts: a differential pumping section (DPS) that reduces the tritium flow at the front and rear ends of the WGTS tube, and a cryogenic pumping section (CPS) that eliminates any remaining tritium flow by trapping the tritium onto a liquid helium cold surface.

- **Pre-spectrometer.** A MAC-E-Filter type pre-spectrometer is located between the tritium source and the main spectrometer, acting as an energy pre-filter in order to reduce the background in the main spectrometer. The smaller pre-spectrometer will work at a fixed retarding potential approximately a few hundred eV below the β spectrum endpoint, filtering out all the lower energy electrons that carry no information on the neutrino mass. Only electrons with energies close to the endpoint will be allowed through to the main spectrometer. The pre-spectrometer will have a diameter of 1.2 m and a length of 3.5 m, comparable to the spectrometers used at Mainz and Troitsk.

- **Main spectrometer.** The main spectrometer is much larger than those used at Mainz and Troitsk, having a diameter of 10 m and a length of approximately 22 m. It will mainly work in the standard integrating MAC-E-Filter mode of operation as described above. It will scan the tritium energy spectrum close to the endpoint

with an energy resolution of about 1 eV, a factor of four better than the Mainz and Troitsk designs. The spectrometer will also perform short term measurements in the differential time-of-flight (MAC-E-TOF) mode, to investigate systematic uncertainties, such as inelastic scattering of the β electrons in the source, with a higher precision than can be achieved in the integral mode. In this mode it will also be able to search for non-SM physics and investigate the 'Troitsk anomaly' more clearly.

- **Detector.** The detector is a multi-pixel silicon semi-conducting detector with ultra-high energy resolution and a very thin entrance window. This design is significantly advanced in energy and spatial resolution over the rather simple detectors used at Mainz and Troitsk. It requires simultaneously a high efficiency for electron detection and a low sensitivity to the environmental gamma- and X-ray background. It also requires a good energy resolution in order to suppress background events, a good position resolution to map the source profile, and a good time resolution (for the MAC-E-TOF mode).

1.8 Objectives of this work

The aim of this work is to investigate the molecular physics issues facing the KATRIN experiment and perform a new calculation of the molecular final state distribution (FSD) to accommodate the higher resolution requirements and increased sensitivity of the experiment. The main objectives are:

- To calculate the FSD of the six lowest-lying electronic states of $^3HeT^+$ resulting from the β-decay of T_2. This is the part of the FSD which is required for an analysis of only the last 30 eV of the β spectrum.

- To account for isotopic contamination of the source by explicitly calculating the FSD's of the six lowest-lying electronic states of $^3HeD^+$ and $^3HeH^+$ resulting from the β-decays of DT and HT respectively.

- To consider the effect of rotational excitation of the parent molecule on the FSD, due to the source in the KATRIN experiment being at a temperature of 30 K, by explicitly calculating separate FSD's of the six lowest-lying electronic states of the daughter molecule resulting from the β-decay of rotationally excited T_2.

- To consider the sensitivity of the initial temperature, ortho:para ratio of T_2 and isotopic contamination of the source by obtaining estimates of the error in the value of the neutrino mass deduced from fitting theoretical spectra, due to uncertainties in the temperature, ortho:para ratio and amount of DT molecules in the source.

- To treat the electronic continuum of $^3HeT^+$ by using the R-matrix method to consider e^- - $^3HeT^{2+}$ scattering and perform a geometry dependent calculation of the resonance states of $^3HeT^+$.

- To calculate the FSD of the electronic continuum of $^3HeT^+$, accounting for the nuclear motion effects of the resonance states, and search for the missing probability of the previous FSD [106], which has been associated to this region.

- To investigate endpoint effects due to the decay of other possible tritium containing species in the source.

Chapter 2

Theoretical background I - Molecular excitations in the β-decay process

2.1 The physics of β-decay

By 1934, Fermi had developed a successful theory of β-decay [2] that included the existence of the neutrino proposed by Pauli. As the decay of a neutron into a proton requires the creation of the two particles, the β electron and neutrino, Fermi treated the decay using a similar method to that describing the process of electromagnetic radiation, where a photon is emitted. According to Fermi's theory, by treating the decay-causing interaction as a weak perturbation, the transition rate is given by:

$$\lambda = \frac{2\pi}{\hbar}|V_{fi}|^2\rho(E_f), \tag{2.1}$$

where $\rho(E_f)$ is the density of final states. The matrix element V_{fi} is given by:

$$V_{fi} = \int \Phi_f^* V \Phi_i \, dv, \tag{2.2}$$

where Φ_f and Φ_i are the final and initial quantum states, and V is the weak interaction operator causing the decay.

At the time, the exact nature of the weak interaction was unknown. It was not until 25 years later, with the help of experimental results, that the mathematical form was established.

Equation (2.1) is the familiar expression known as Fermi's Golden Rule, and is a general result for the transition rate from one energy eigenstate of a quantum system into a continuum of energy eigenstates, due to a perturbation.

2.2 The β spectrum and the effect of a non-zero neutrino mass on the endpoint

When a nucleus in an atom undergoes β-decay, it is possible that the daughter atom will be left in an electronically excited or ionised state. The different possible energy sharings between the emitted electron and the daughter ion result in a distortion of the β spectrum compared with that for the decay of a bare nucleus. The situation becomes more complicated when the decaying nucleus is part of a molecule as the molecule can also be vibrationally and rotationally excited. This rovibrational excitation can occur as a result of the recoil momentum given to the decaying nucleus, which depends on the momentum of both the emitted neutrino and β electron.

Several papers have investigated the theoretical treatment of the problem of molecular excitation in β-decay using time dependent perturbation theory (i.e. using Fermi's Golden Rule), and have derived expressions for the β spectrum and probability of molecular excitation.

In 1956, Cantwell considered the general case of a polyatomic molecule [107]. He also treated the special case of a diatomic molecule in more detail by using the Born-Oppenheimer approximation (see section 3.2) to give simple vibrational and rotational wavefunctions. Szalewicz *et al.* [108] also give a detailed derivation of the β spectrum for the decay of an isolated T_2 molecule. Both Cantwell and Szalewicz *et al.* perform a zeroth order (sudden approximation) treatment of the matrix elements, neglecting the Coulombic interactions between the β electron and the remaining molecular system. However as the interaction between the β electron and the decaying nucleus can be taken into account in a comparatively simple manner [109], they include this in the zeroth order treatment. Williams and Koonin show that the error in the transition probabilities introduced by the sudden approximation for *atomic* tritium is 0.17% for transitions to the $1s$ and $2s$ states of He^+ and $\leq 0.01\%$ for transitions to the higher excited states [110]. Kolos *et al.* [111] claim that the error should be of the same order for T_2. Saenz and Froelich give a detailed derivation of the β spectrum in a beyond sudden approximation treatment of the β-decay [109]. They derive explicit formulas for the matrix elements occurring in the perturbational treatment up to the pure first order correction term.

The intensity of β electrons $I(E_\beta^{kin})$, with kinetic energy E_β^{kin} and momentum p_β,

within the sudden approximation, is given by [108], [102]:

$$\begin{aligned} I(E_\beta^{kin}) = AF(Z,p_\beta)p_\beta(E_\beta^{kin}+m_ec^2) \\ \times\sum_{fj}[P_f(W_0-E_f^{^3\mathrm{HeT}^+}-E_\beta^{kin})H(W_0-E_f^{^3\mathrm{HeT}^+}-E_\beta^{kin}-m_{\nu_j}c^2) \\ \times|U_{ej}|^2[(W_0-E_f^{^3\mathrm{HeT}^+}-E_\beta^{kin})^2-m_{\nu_j}^2c^4]^{1/2}], \end{aligned} \tag{2.3}$$

where

$$W_0 = m_{\mathrm{T}_2}+E_0^{\mathrm{T}_2}-m_{^3\mathrm{HeT}^+}-E_0^{^3\mathrm{HeT}^+}-m_ec^2-E_{\mathrm{rec}} \tag{2.4}$$

is the maximum kinetic energy of the β electron if the neutrino mass were zero. m_{T_2}, $m_{^3\mathrm{HeT}^+}$ and m_e are the masses of the parent molecule, daughter molecule and electron respectively, $E_0^{\mathrm{T}_2}$ and $E_0^{^3\mathrm{HeT}^+}$ are the ground state energies of the molecules and E_{rec} is the recoil energy transferred to the centre of mass motion of the molecular system. $E_f^{^3\mathrm{HeT}^+}$ is the energy of the final molecular state f of $^3\mathrm{HeT}^+$ relative to its ground state energy $E_0^{^3\mathrm{HeT}^+}$ and P_f is the probability that the $^3\mathrm{HeT}^+$ ion will be left in final state f after the β-decay and is given by [109]:

$$P_f = \left|\int \Psi_f^{^3\mathrm{HeT}^+*} e^{i\mathbf{K}.\mathbf{R}}\Psi_i^{\mathrm{T}_2}\,d\tau\right|^2. \tag{2.5}$$

$\Psi_f^{^3\mathrm{HeT}^+}$ and $\Psi_i^{\mathrm{T}_2}$ are the wavefunctions describing the quantum states of the daughter and parent molecule respectively and are functions of relative coordinates only. The exponential $e^{i\mathbf{K}.\mathbf{R}}$ arises from the recoil from the β electron on the decaying nucleus, where

$$\mathbf{K} = -\frac{\mathbf{p}_\beta m_{\mathrm{T}}}{(m_{\mathrm{T}}+m_{\mathrm{He}}+2m_e)\hbar}, \tag{2.6}$$

and $\mathbf{R}$ is the internuclear vector. It was stated previously that the recoil momentum given to the decaying nucleus depends on the momentum of the β electron and neutrino. However, close to the endpoint the momentum of the neutrino is several orders of magnitude smaller than that of the electron and so can be neglected. Also, it has been found [112] that P_f is quite insensitive to changes of E_β of the order of 100 eV. The derivation of $\mathbf{K}$ is given by Szalewicz *et al* [108]. An estimate of the effect of the approximation when using $\mathbf{R}$ is given by Saenz *et al* [109].

In equation (2.3) $F(Z,p_\beta)$ is the Fermi function for an electron moving with the momentum p_β in the field of a nucleus with the charge Z. This term accounts for the Coulombic interaction between the β electron and the decaying nucleus. H is the Heaviside step function ensuring the intensity is real. The constant A is given by:

$$A = \frac{1}{2\pi^3\hbar^4c^5}|T^{weak}|^2, \tag{2.7}$$

where $|T^{weak}|^2$ is the squared weak transition matrix element for the β-decay summed over the final nucleonic states of the ^{3}He nucleus and integrated over the directions of the β electron. If the transition probability is integrated over all directions of the neutrino then, in the case of allowed decays, the term $|T^{weak}|^2$ is constant.

We note here that for comparison with the β spectrum obtained by the experiment, one must perform a sum/integration over any observables that are not resolved by the experiment. Therefore to obtain equations (2.3) and (2.5), integration over the directions and energies of the neutrino and integration over the directions of the β electron has been performed.

As described in chapter 1, the existence of neutrino oscillations requires a non-trivial mixing between the neutrino flavour eigenstates (ν_e, ν_μ, ν_τ) produced in weak interactions and the corresponding mass eigenstates (ν_1, ν_2, ν_3) via a unitary mixing matrix U. It also requires that the mass eigenvalues (m_1, m_2, m_3) differ from each other and hence must be non-zero. For a quasi-degenerate model of the neutrino masses ($m_1 \approx m_2 \approx m_3$) we can parameterise the analysis of the β spectrum by [102]:

$$m^2_{\overline{\nu}_e} = \sum_{j=1}^{3} |U_{ej}|^2 m^2_{\nu_j}, \tag{2.8}$$

where $m_{\overline{\nu}_e}$ is the effective electron anti-neutrino mass. However, for a hierarchical ordering of the neutrino masses ($m_1 \ll m_2 \ll m_3$), the three mass eigenstates and also the mixing angles and CP phases that characterise the mixings must be taking into account, resulting in several more independent fit parameters [102].

The effects of mixing result in the following modifications of the β spectrum [98]:

- the β spectrum will have an experimental endpoint energy $E = W_0 - m_1c^2$ (where m_1 is the lightest mass eigenstate),
- the appearance of kinks at energies $E^i \approx W_0 - m_ic^2$ (where the magnitude of the kinks are determined by $|U_{ei}|^2$).

The mass of the neutrino is obtained by fitting the experimental data to theoretical spectra given by equation (2.3). P_f and $E_f^{^3\mathrm{HeT}^+}$ are obtained from theory while A, W_0 and $m^2_{\overline{\nu}_e}$ (as well as the background rate) are free parameters.

2.3 The final state probability distribution

Different final quantum states of the $^3HeT^+$ ion give rise to separate branches of the β spectrum, each with a different endpoint energy. For the measured β spectrum, a sum over all final states is performed (with appropriate probabilities) as in equation (2.3). A very accurate knowledge of the final state probability distribution (FSPD), including nuclear motion effects, is crucial in the determination of the neutrino mass from the β spectrum, as the accuracy of the neutrino mass is limited by the accuracy of the FSPD. The effect of different levels of accuracy of the FSPD on the β spectrum is shown by Fackler *et al* [113]. This is one of the reasons why T_2 is the source of choice. It is one of the simplest tritium containing compounds and for both T_2 and $^3HeT^+$ high accuracy quantum chemical computations can be performed and reliable energies and probabilities calculated.

The calculation of the FSPD can be split into two parts:

1. The FSPD of the bound electronic states of $^3HeT^+$ and,
2. The FSPD of the electronic continuum of $^3HeT^+$.

Part 1 can be split further to consider separately:

1. The FSPD of the bound rovibrational states and,
2. The FSPD of the rovibrational continuum.

In this section the equations needed to calculate the final state probability distribution are derived. As seen from equation (2.5), the final state probability distribution depends on the initial state of the T_2 molecule. Separate expressions are derived for the decay of a T_2 molecule in the first four rotational states of the vibrational and electronic ground state. As the temperature of the KATRIN experiment is expected to be around 30 K this is sufficient.

2.3.1 Bound rovibrational states

If the sudden approximation is assumed, the probability of finding the daughter ion in a final state f following the β-decay of the parent molecule in an initial state i, is given by equation (2.5). Invoking the Born-Oppenheimer approximation for Ψ_i and Ψ_f:

$$\Psi_i = \psi^i_{n_i}(r_1, r_2; R) R^{-1} f^i_{n_i v_i J_i}(R) Y_{J_i M_i}(\theta, \phi), \tag{2.9a}$$

$$\Psi_f = \psi^f_{n}(r_1, r_2; R) R^{-1} f^f_{nvJ}(R) Y_{JM}(\theta, \phi). \tag{2.9b}$$

where ψ_n are the clamped-nuclei electronic wavefunctions, f_{nvJ} are the radial vibrational wavefunctions, Y_{JM} are the spherical harmonics, r_1 and r_2 denote the spatial positions of the electrons, (R, θ, ϕ) are the spherical coordinates of $\mathbf{R}$, and n, v, J and M are the electronic, vibrational, rotational and azimuthal quantum numbers, equation (2.5) then becomes:

$$P_{nvJM} = \left| \int S_n(R) R^{-2} {f^f_{nvJ}}^*(R) {Y_{JM}}^*(\theta,\phi) e^{i\mathbf{K}.\mathbf{R}} f^i_{n_i v_i J_i}(R) Y_{J_i M_i}(\theta,\phi)\, d\mathbf{R} \right|^2. \quad (2.10)$$

$S_n(R)$ is the overlap integral providing the R dependent probability amplitude of transition to the n^{th} electronic state of the daughter system, and is given by:

$$S_n(R) = \int \psi^{f*}_n(r_1, r_2; R) \psi^i_{n_i}(r_1, r_2; R)\, dr_1\, dr_2. \quad (2.11)$$

It is noted that the square of the overlap integral, $S^2_n(R)$, gives the R dependent probability of finding the daughter molecule in the electronic state ψ^f_n, following the β-decay of the parent molecule in the state $\psi^i_{n_i}$.

Using the standard partial wave expansion for $e^{i\mathbf{K}.\mathbf{R}}$ [114]:

$$e^{i\mathbf{K}.\mathbf{R}} = 4\pi \sum_{l=0}^{\infty} \sum_{m=-l}^{+l} i^l j_l(KR) Y^*_{lm}(\theta_K, \phi_K) Y_{lm}(\theta, \phi), \quad (2.12)$$

where $j_l(KR)$ is the spherical Bessel function and (K, θ_K, ϕ_K) are the spherical components of $\mathbf{K}$, and

$$d\mathbf{R} = R^2\, d\Omega_R\, dR, \quad (2.13)$$

the integration is reduced to:

$$P_{nvJM}(K) = (4\pi)^2 \left| \sum_{lm} Y^*_{lm}(\theta_K, \phi_K) \int S_n(R) {f^f_{nvJ}}^*(R) f^i_{n_i v_i J_i}(R) j_l(KR)\, dR \right. \\ \left. \times \int Y^*_{JM}(\theta,\phi) Y_{lm}(\theta,\phi) Y_{J_i M_i}(\theta,\phi)\, d\Omega_R \right|^2, \quad (2.14)$$

Averaging over initial M_i, summing over final M and averaging over final directions K gives:

$$P_{nvJ}(K) = \frac{4\pi}{(2J_i+1)} \sum_{MM_i} \int \sum_{lml'm'} Y^*_{lm}(\theta_K, \phi_K) Y_{l'm'}(\theta_K, \phi_K)\, d\Omega_K \\ \times \left| \int S_n(R) {f^f_{nvJ}}^*(R) f^i_{n_i v_i J_i}(R) j_l(KR)\, dR \right|^2 \\ \times \left| \int {Y_{JM}}^*(\theta,\phi) Y_{lm}(\theta,\phi) Y_{J_i M_i}(\theta,\phi)\, d\Omega_R \right|^2. \quad (2.15)$$

Since,

$$\int Y^*_{lm}(\theta_K,\phi_K)Y_{l'm'}(\theta_K,\phi_K)d\Omega_K = \delta_{ll'}\delta_{mm'}, \tag{2.16}$$

one has:

$$P_{nvJ}(K) = \frac{4\pi}{(2J_i+1)}\sum_{MmM_i}\left|\int {Y_{JM}}^*(\theta,\phi)Y_{lm}(\theta,\phi)Y_{J_iM_i}(\theta,\phi)d\Omega_R\right|^2 \times \sum_l \left|\int S_n(R){f^f_{nvJ}}^*(R)f^i_{n_iv_iJ_i}(R)j_l(KR)dR\right|^2. \tag{2.17}$$

The integration over three spherical harmonics can be represented in terms of matrix elements:

$$\int {Y_{JM}}^*(\theta,\phi)Y_{lm}(\theta,\phi)Y_{J_iM_i}(\theta,\phi)d\Omega_R = \langle JM \mid Y_{lm} \mid J_iM_i\rangle. \tag{2.18}$$

The Wigner-Eckart Theorem for the factorisation of the matrix elements of tensor operators is:

$$\langle j'm' \mid \mathbf{T}(kq) \mid jm\rangle = (-1)^{j'-m'}\begin{pmatrix} j' & k & j \\ -m' & q & m\end{pmatrix}\langle j'\|\mathbf{T}_k\|j\rangle \tag{2.19}$$

where $\mathbf{T}(kq)$ is a tensor operator of rank k and $q = -k, -k+1, ..., k-1, k$. The theorem states that the dependence of the matrix element $\langle j'm' \mid \mathbf{T}(kq) \mid jm\rangle$ on the projection quantum numbers is entirely contained in the Wigner 3j-symbol. $\langle j'\|\mathbf{T}_k\|j\rangle$ are the reduced matrix elements and are independent of the magnetic quantum numbers m, m' and q. The total transition probability (summed over magnetic quantum numbers) is therefore:

$$\sum_{m'qm}\left|\langle j'm' \mid \mathbf{T}(kq) \mid jm\rangle\right|^2 = \left|\langle j'\|\mathbf{T}_k\|j\rangle\right|^2\sum_{m'qm}\begin{pmatrix} j' & k & j \\ -m' & q & m\end{pmatrix}^2 = \left|\langle j'\|\mathbf{T}_k\|j\rangle\right|^2. \tag{2.20}$$

The orthogonality property of 3j-symbols has been used, and is given by:

$$\sum_{\alpha\beta}\begin{pmatrix} a & b & c \\ \alpha & \beta & \gamma\end{pmatrix}\begin{pmatrix} a & b & c' \\ \alpha & \beta & \gamma'\end{pmatrix} = \frac{1}{(2c+1)}\delta_{cc'}\delta_{\gamma\gamma'}\delta(abc), \tag{2.21}$$

where $\delta(abc) = 1$ if a, b, c satisfy the triangular condition:

$$|a-b| \le c \le |a+b| \tag{2.22}$$

and is zero otherwise.

Therefore one gets:

$$\sum_{MmM_i} \left| \int {Y_{JM}}^*(\theta,\phi) Y_{lm}(\theta,\phi) Y_{J_iM_i}(\theta,\phi) d\Omega_R \right|^2 = |\langle J \| Y_l \| J_i \rangle|^2 . \tag{2.23}$$

The reduced matrix elements of spherical harmonics are given by:

$$\langle j' \| Y_k \| j \rangle = (-1)^{j'} \left[\frac{(2j'+1)(2k+1)(2j+1)}{4\pi} \right]^{\frac{1}{2}} \begin{pmatrix} j' & k & j \\ 0 & 0 & 0 \end{pmatrix}, \tag{2.24}$$

hence:

$$|\langle J \| Y_l \| J_i \rangle|^2 = \frac{(2J+1)(2l+1)(2J_i+1)}{4\pi} \begin{pmatrix} J & l & J_i \\ 0 & 0 & 0 \end{pmatrix}^2 . \tag{2.25}$$

A 3j-symbol with $m_1 = m_2 = m_3 = 0$ can be computed using the general formula:

$$\begin{pmatrix} j_1 & j_2 & j_3 \\ 0 & 0 & 0 \end{pmatrix} = \left[\frac{(J-2j_1)!(J-2j_2)!(J-2j_3)!}{(J+1)!} \right]^{\frac{1}{2}} \frac{\frac{J}{2}!}{(\frac{J}{2}-j_1)!(\frac{J}{2}-j_2)!(\frac{J}{2}-j_3)!}, \tag{2.26}$$

where

$$J = j_1 + j_2 + j_3. \tag{2.27}$$

J must be even otherwise the 3j-symbol = 0.

The angular momentum algebra (equations (2.18)-(2.26)) has been obtained from [115, 116].

To obtain a final equation for the probability, one needs to evaluate equation (2.17) by first evaluating the equations (2.25) and (2.26) for different values of J_i. The final equations for $J_i = 0$ and 1, have been given previously in reference [117]. Below, the equations for $J_i = 0$ and 1 are given, and the equations for $J_i = 2$ and 3 are also derived.

For $\mathbf{J_i = 0}$

From the triangular condition and the fact that $a+b+c$ must be even, $l = J$. Therefore:

$$\begin{aligned} |\langle J \| Y_l \| J_i \rangle|^2 = |\langle J \| Y_J \| 0 \rangle|^2 \delta_{l,J} &= \frac{(2J+1)(2J+1)}{4\pi} \begin{pmatrix} J & J & 0 \\ 0 & 0 & 0 \end{pmatrix}^2 \delta_{l,J}, \\ &= \frac{2J+1}{4\pi} \delta_{l,J}. \end{aligned} \tag{2.28}$$

Substituting this back into equation (2.17) gives (as given in [117]):

$$P_{nvJ}(K) = (2J+1) \left| \int S_n(R) {f^f_{nvJ}}^*(R) f^i_{n_i v_i 0}(R) j_J(KR) dR \right|^2 . \tag{2.29}$$

For $J_i = 1$

Here $l = J \pm 1$.

$$\begin{aligned}|\langle J\|Y_l\|J_i\rangle|^2 &= |\langle J\|Y_{J+1}\|1\rangle|^2 \delta_{l,J+1} + |\langle J\|Y_{J-1}\|1\rangle|^2 \delta_{l,J-1}, \\ &= \frac{3}{4\pi}\left[(J+1)\delta_{l,J+1} + J\delta_{l,J-1}\right]. \end{aligned} \tag{2.30}$$

Therefore (as stated in [117]):

$$\begin{aligned}P_{nvJ}(K) = (J+1)&\left|\int S_n(R) {f^f_{nvJ}}^*(R) f^i_{n_i v_i 1}(R) j_{J+1}(KR) dR\right|^2 \\ &+ J\left|\int S_n(R) {f^f_{nvJ}}^*(R) f^i_{n_i v_i 1}(R) j_{J-1}(KR) dR\right|^2. \end{aligned} \tag{2.31}$$

For $J_i = 2$

We have $l = J \pm 2$ and $l = J$.

$$\begin{aligned}|\langle J\|Y_l\|J_i\rangle|^2 &= |\langle J\|Y_{J+2}\|2\rangle|^2 \delta_{l,J+2} + |\langle J\|Y_J\|2\rangle|^2 \delta_{l,J} + |\langle J\|Y_{J-2}\|2\rangle|^2 \delta_{l,J-2}, \\ &= \frac{5}{4\pi}\left[\frac{3}{2}\frac{(J+2)(J+1)}{(2J+3)}\delta_{l,J+2} + \frac{(J+1)J(2J+1)}{(2J+3)(2J-1)}\delta_{l,J} + \frac{3}{2}\frac{J(J-1)}{(2J-1)}\delta_{l,J-2}\right]. \end{aligned} \tag{2.32}$$

Therefore:

$$\begin{aligned}P_{nvJ}(K) = \frac{3}{2}&\frac{(J+2)(J+1)}{(2J+3)}\left|\int S_n(R) {f^f_{nvJ}}^*(R) f^i_{n_i v_i 2}(R) j_{J+2}(KR) dR\right|^2 \\ &+ \frac{(J+1)J(2J+1)}{(2J+3)(2J-1)}\left|\int S_n(R) {f^f_{nvJ}}^*(R) f^i_{n_i v_i 2}(R) j_J(KR) dR\right|^2 \\ &+ \frac{3}{2}\frac{J(J-1)}{(2J-1)}\left|\int S_n(R) {f^f_{nvJ}}^*(R) f^i_{n_i v_i 2}(R) j_{J-2}(KR) dR\right|^2. \end{aligned} \tag{2.33}$$

For $J_i = 3$

$l = J \pm 3$ and $l = J \pm 1$.

$$\begin{aligned}|\langle J\|Y_l\|J_i\rangle|^2 &= |\langle J\|Y_{J+3}\|3\rangle|^2 \delta_{l,J+3} + |\langle J\|Y_{J+1}\|3\rangle|^2 \delta_{l,J+1} \\ &\quad + |\langle J\|Y_{J-1}\|3\rangle|^2 \delta_{l,J-1} + |\langle J\|Y_{J-3}\|3\rangle|^2 \delta_{l,J-3}, \\ &= \frac{7}{4\pi}\left[\frac{5}{2}\frac{(J+3)(J+2)(J+1)}{(2J+5)(2J+3)}\delta_{l,J+3} + \frac{3}{2}\frac{(J+2)(J+1)J}{(2J+5)(2J-1)}\delta_{l,J-1}\right. \\ &\quad \left. + \frac{3}{2}\frac{(J+1)J(J-1)}{(2J+3)(2J-3)}\delta_{l,J-1} + \frac{5}{2}\frac{J(J-1)(J-2)}{(2J-1)(2J-3)}\delta_{l,J-3}\right]. \end{aligned} \tag{2.34}$$

Therefore:

$$P_{nvJ}(K) = \frac{5}{2}\frac{(J+3)(J+2)(J+1)}{(2J+5)(2J+3)}\left|\int S_n(R) {f^f_{nvJ}}^*(R) f^i_{n_i v_i 3}(R) j_{J+3}(KR) dR\right|^2 + \frac{3}{2}\frac{(J+2)(J+1)J}{(2J+5)(2J-1)}\left|\int S_n(R) {f^f_{nvJ}}^*(R) f^i_{n_i v_i 3}(R) j_{J+1}(KR) dR\right|^2 + \frac{3}{2}\frac{(J+1)J(J-1)}{(2J+3)(2J-3)}\left|\int S_n(R) {f^f_{nvJ}}^*(R) f^i_{n_i v_i 3}(R) j_{J-1}(KR) dR\right|^2 + \frac{5}{2}\frac{(J(J-1)(J-2)}{(2J-1)(2J-3)}\left|\int S_n(R) {f^f_{nvJ}}^*(R) f^i_{n_i v_i 3}(R) j_{J-3}(KR) dR\right|^2. \quad (2.35)$$

2.3.2 The rovibrational (nuclear motion) continuum and predissociative resonance states

Jeziorski *et al.* [112] showed that for transitions to the nuclear motion continuum, equation (2.5) is valid if the left hand side is interpreted as the probability per unit energy, E_f, and if the final states are normalized such that:

$$\int \Psi^*_f \Psi_{f'} \, d\mathbf{R} = \delta(E_f - E_{f'}). \quad (2.36)$$

The bound radial functions, $f^f_{nvJ}(R)$ in equations (2.9b, 2.10, 2.29, 2.31, 2.33, 2.35) are replaced by energy normalised radial functions of the continuous spectrum, $f^f_{nJ}(R|E)$. For the β-decay of a T_2 molecule in the $J_i = 0$ state the analog of equation (2.29) is therefore given by [112]:

$$P_{nJ}(E) = (2J+1)\left|\int_0^\infty S_n(R) j_J(KR) f^f_{nJ}(R|E) f^i_{100}(R)\, dR\right|^2, \quad (2.37)$$

where $P_{nJ}(E)$ is the probability per unit energy that the $^3HeT^+$ molecule dissociates via the n^{th} electronic state and that the dissociation products are in a state with energy E and angular momentum J.

2.3.3 Sum rules

Wolniewicz [118] gives a useful sum rule for the total probability to all rovibrational states of a given electronic state n, P_n. By summing equation (2.5) over all rovibrational states belonging to electronic state n gives [118]:

$$P_n = \sum_{v,J,m_J}\left|\int \Psi_f^{^3HeT^+ *} e^{i\mathbf{K}.\mathbf{R}} \Psi_i^{T_2}\, d\tau\right|^2 = \int_0^\infty S_n^2(R)[f^i_{100}(R)]^2\, dR. \quad (2.38)$$

A derivation of equation (2.38) is given in reference [109].

Jeziorski *et al.* [112] give an analogous equation for the (energy-unresolved) probability that the daughter system ends up in its n^{th} electronic state rotationally excited to an angular momentum J, P_{nJ}:

$$P_{nJ} = (2J+1)\int_0^\infty S_n^2(R) j_J^2(KR)[f_{100}^i(R)]^2\, dR. \tag{2.39}$$

These sum rules provide a useful check of results as they are computed without solving the radial Schrödinger equation of the daughter molecule.

Chapter 3

Theoretical background II - Approximations and programs

3.1 Sudden approximation

Suppose that there is a sudden perturbation at time $t = 0$ that causes the Hamiltonian H describing a system to instantaneously change from H_0 to H_1, where H_0 and H_1 are both independent of time. Up until $t = 0$, the time-independent Schrödinger equation is:

$$H_0\psi_k = E_k^{(0)}\psi_k, \tag{3.1}$$

where $E_k^{(0)}$ and ψ_k are the eigenvalues and eigenfunctions of H_0 respectively. The eigenfunctions ψ_k are assumed to be orthonormal and form a complete set. The general solution of the time-dependent Schrödinger equation:

$$i\hbar\frac{\partial\Psi}{\partial t} = H\Psi, \tag{3.2}$$

is then given by:

$$\Psi(t) = \sum_k a_k\psi_k \mathrm{e}^{\frac{-iE_k^{(0)}t}{\hbar}}, \tag{3.3}$$

where the summation is over the complete set of eigenfunctions $\{\psi_k\}$ and a_k are time-independent coefficients. Assuming that Ψ is normalised to unity, the coefficients a_k are the probability amplitudes of finding the system in the state ψ_k.

After $t = 0$ the time-independent Schrödinger equation is:

$$H_1\phi_n = E_n^{(1)}\phi_n. \tag{3.4}$$

where $E_n^{(1)}$ and ϕ_n are the eigenvalues and eigenfunctions of H_1 respectively. The general solution of the time-dependent Schrödinger equation is now:

$$\Psi(t) = \sum_n c_n \phi_n \mathrm{e}^{\frac{-iE_n^{(1)}t}{\hbar}}, \tag{3.5}$$

where the summation is over the complete set of eigenfunctions $\{\phi_n\}$ and c_n are the time-independent coefficients.

As equation (3.2) is of first order in time, $\Psi(t)$ must be a continuous function of t and must remain continuous when the Hamiltonian suddenly changes. Therefore at $t = 0$ we have:

$$\sum_k a_k \psi_k = \sum_n c_n \phi_n, \tag{3.6}$$

and the coefficients c_n are thus given by:

$$c_n = \sum_k a_k \langle \phi_n \mid \psi_k \rangle. \tag{3.7}$$

Equation (3.7) is exact for cases where the Hamiltonian changes instantaneously, however in practise this change happens over a finite time interval.

Suppose now that the Hamiltonian H describing the system changes during an interval of time τ. For $t < 0$ we assume $H = H_0$ and the general solution for the wavefunction is given by equation (3.3). For $t > \tau$ we assume $H = H_1$ and the general solution for the wavefunction is given by equation (3.5). During the intermediate period $0 < t < \tau$ it is assumed that the Hamiltonian is H_i, which is also time-independent, and thus the time-independent Schrödinger equation is:

$$H_i \chi_l = E_l^{(i)} \chi_l, \tag{3.8}$$

and the general solution of the time-dependent Schrödinger equation is:

$$\Psi(t) = \sum_l b_l \chi_l \mathrm{e}^{\frac{-iE_l^{(i)}t}{\hbar}}. \tag{3.9}$$

From the continuity of the wavefunction at $t = 0$ we have:

$$\sum_k a_k \psi_k = \sum_l b_l \chi_l \tag{3.10}$$

and thus:

$$b_l = \sum_k a_k \langle \chi_l \mid \psi_k \rangle. \tag{3.11}$$

Similarly at $t = \tau$ we have:

$$\sum_l b_l \chi_l \mathrm{e}^{\frac{-iE_l^{(i)}\tau}{\hbar}} = \sum_n c_n \phi_n \mathrm{e}^{\frac{-iE_n^{(1)}\tau}{\hbar}} \tag{3.12}$$

and thus:

$$c_n = \sum_k \sum_l a_k \langle \phi_n \mid \chi_l \rangle \langle \chi_l \mid \psi_k \rangle \mathrm{e}^{\frac{i(E_n^{(1)} - E_l^{(i)})\tau}{\hbar}}, \tag{3.13}$$

where equation (3.11) has been used for b_l.

If the change of the Hamiltonian were instantaneous (i.e. $\tau = 0$) then by using the closure relation for χ_l, equation (3.13) reduces to the form (3.7) as expected. When $\tau \neq 0$, by comparing equations (3.13) and (3.7) we see that the difference between them lies in the fact that the exponential term differs from unity.

If τ is small in comparison to the quantities $\hbar/|E_n^{(1)} - E_l^{(i)}|$, i.e. if:

$$\frac{(E_n^{(1)} - E_l^{(i)})\tau}{\hbar} \ll 1, \tag{3.14}$$

then the change of the wavefunction during the time τ is small and one may in first approximation set $\tau = 0$ and equation (3.7) can be used. This is the *sudden approximation*. The sudden approximation is used to treat cases where a perturbation (or disturbance) of a system occurs very rapidly compared to the natural period of the system. The non-trivial part in the application of this approximation is deciding whether the change of the Hamiltonian is rapid enough by estimating the time it takes for the change and the periods of motion associated with the system.

As discussed in chapter 2, this approximation has been applied in the study of molecular excitations in β-decay [107, 108] and its validity investigated [109, 110]. Close to the endpoint, the β electrons are emitted from the nucleus with high energy and therefore with high speeds. The time it takes for the β electron to leave the atom/molecule is much shorter than the periods of the remaining electrons. Therefore the β electron can hardly influence the motion of the remaining slow molecular ion.

3.2 Born-Oppenheimer approximation

Consider a molecular system composed of N electrons of mass m and charge $-e$, and L nuclei of mass M_A and charge $Z_A e$ $(A = 1, ..., L)$. In the LAB frame, which has a spaced fixed z-axis, the electrons have vector positions $\mathbf{r}_i$ $(i = 1, ..., N)$ and the nuclei have vector positions $\mathbf{R}_A$. The non-relativistic time independent Schrödinger equation

for the system is written:

$$H\Psi(\{\mathbf{R}_A\},\{\mathbf{r}_i\}) = E\Psi(\{\mathbf{R}_A\},\{\mathbf{r}_i\}), \tag{3.15}$$

where H is the Hamiltonian operator given by:

$$H = -\sum_{i=1}^{N}\frac{\hbar^2}{2m}\nabla_i^2 - \sum_{A=1}^{L}\frac{\hbar^2}{2M_A}\nabla_A^2 + V(\{\mathbf{R}_A\},\{\mathbf{r}_i\}), \tag{3.16}$$

$\Psi(\{\mathbf{R}_A\},\{\mathbf{r}_i\})$ is the molecular wavefunction describing the system and E is the total energy of the system. The first and second terms in equation (3.16) are the operators for the kinetic energy of the electrons and nuclei respectively. The potential $V(\{\mathbf{R}_A\},\{\mathbf{r}_i\})$ contains all the Coulombic terms:

$$V(\{\mathbf{R}_A\},\{\mathbf{r}_i\}) = \sum_{i=1}^{N}\sum_{j>i}^{N}\frac{e^2}{|\mathbf{r}_j-\mathbf{r}_i|} + \sum_{A=1}^{L}\sum_{B>A}^{L}\frac{Z_A Z_B e^2}{|\mathbf{R}_B-\mathbf{R}_A|} - \sum_{i=1}^{N}\sum_{A=1}^{L}\frac{Z_A e^2}{|\mathbf{R}_A-\mathbf{r}_i|}, \tag{3.17}$$

where the first term is the electron-electron repulsion, the second term is the nuclear-nuclear repulsion and the third term is the electron-nuclear attraction.

This Hamiltonian is not analytically soluble even for the most simplest molecular system, H_2^+ ($N = 1, L = 2$). However it is possible to simplify the problem by taking into account the fact that the electrons are much lighter than the nuclei, i.e. $m \ll M$, and therefore move much faster. To a good approximation the electrons are assumed to relax instantaneously to a change in the nuclear geometry and can be considered as moving in the field of fixed nuclei. The two sets of particles can then be studied separately. This is known as the Born-Oppenheimer approximation [119].

In this approximation the total wavefunction is separable:

$$\Psi(\{\mathbf{R}_A\}) = \Psi_{\text{elec}}(\{\mathbf{r}_i\};\{\mathbf{R}_A\})\Psi_{\text{nucl}}(\{\mathbf{R}_A\}), \tag{3.18}$$

where $\Psi_{\text{elec}}(\{\mathbf{r}_i\};\{\mathbf{R}_A\})$ is the electronic wavefunction which describes the motion of the electrons and $\Psi_{\text{nucl}}(\{\mathbf{R}_A\})$ is the nuclear wavefunction.

The electronic wavefunctions, Ψ_{elec}, which depends explicitly on the electron coordinates but only *parametrically* on the nuclear coordinates, are solutions of the electronic Schrödinger equation:

$$H_{\text{elec}}\Psi_{\text{elec}} = E_{\text{elec}}\Psi_{\text{elec}}, \tag{3.19}$$

where H_{elec} is the electronic Hamiltonian:

$$H_{\text{elec}} = -\sum_{i=1}^{N}\frac{\hbar^2}{2m}\nabla_i^2 + V(\{\mathbf{R}_A\},\{\mathbf{r}_i\}). \tag{3.20}$$

The energies E_{elec} also depend parametrically on the nuclear coordinates. If the electronic problem is solved, it is then possible to solve for the motion of the nuclei. The energies $E_{\text{elec}}(\{\mathbf{R}_A\})$ provide a potential for nuclear motion. These potentials only have meaning within the Born-Oppenheimer approximation. Within the approximation, the nuclei move on the potential energy surface, and the nuclear motion includes the vibrational, rotational and translational motion of the molecule. The nuclear wavefunctions are solutions of the nuclear Schrödinger equation:

$$H_{\text{nucl}}\Psi_{\text{nucl}} = E_{\text{total}}\Psi_{\text{nucl}}, \tag{3.21}$$

where the Hamiltonian is given by:

$$H_{\text{nucl}} = -\sum_{A=1}^{L} \frac{\hbar^2}{2M_A}\nabla_A^2 + E_{\text{elec}}(\{\mathbf{R}_A\}), \tag{3.22}$$

and E_{total} is the Born-Oppenheimer approximation to the total energy E of equation (3.15). Thus, E_{total} includes electronic, vibrational, rotational and translational energy.

3.3 The Hartree-Fock approximation and configuration interaction

The Coulombic electron-electron repulsion term makes the electronic Hamiltonian for many-electron systems very difficult to solve. The Hartree-Fock approximation replaces the many-electron problem by a one-electron problem with averaged electron-electron repulsions. The electron is assumed to move in the field of the nuclei and the averaged field of the remaining (N-1) electrons.

An electron is not only described by its vector position $\mathbf{r}$, but also by its spin coordinate w. The wavefunction of an electron that describes both its spatial distribution and its spin is called a *spin orbital* and is written as:

$$\Phi(\mathbf{x}) = \psi(\mathbf{r})\chi(w) \tag{3.23}$$

where $\psi(\mathbf{r})$ is a *spatial orbital* and $\chi(w)$ is a spin function.

The simplest antisymmetric wavefunction that can be used to describe the ground state of an N-electron system is expressed as the Slater determinant (where electron-

electron interactions are neglected):

$$\Psi_0(\mathbf{x}_1, \mathbf{x}_2, ..., \mathbf{x}_N) = (N!)^{-1/2} \begin{vmatrix} \Phi_i(\mathbf{x}_1) & \Phi_j(\mathbf{x}_1) & \cdots & \Phi_k(\mathbf{x}_1) \\ \Phi_i(\mathbf{x}_2) & \Phi_j(\mathbf{x}_2) & \cdots & \Phi_k(\mathbf{x}_2) \\ \vdots & \vdots & & \vdots \\ \Phi_i(\mathbf{x}_N) & \Phi_j(\mathbf{x}_N) & \cdots & \Phi_k(\mathbf{x}_N) \end{vmatrix}, \tag{3.24}$$

where the N electrons occupy N spin orbitals without specifying which electron is in which orbital. According to the variational principle, for a time independent Hamiltonian, any trial wavefunction will have an energy expectation value that is greater than or equal to the true energy. Therefore the best wavefunction of the form of equation (3.24) is found by minimising the energy expectation value:

$$E_0 = < \Psi_0 | H | \Psi_0 >, \tag{3.25}$$

where H is the full electronic Hamiltonian, subject to the condition that the spin orbitals are orthonormal.

By minimising E_0 with respect to the choice of spin orbitals, one can derive the Hartree-Fock equation:

$$f(i)\Phi(\mathbf{x}_i) = \epsilon\Phi(\mathbf{x}_i), \tag{3.26}$$

to determine the optimal spin orbitals, where the Fock operator, $f(i)$, is an effective one-electron operator given by:

$$f(i) = h(i) + G^{\mathrm{HF}}(i). \tag{3.27}$$

$h(i)$ is the core Hamiltonian for electron i which represents the kinetic energy of the electron and its Coulombic attraction with the nuclei, and $G^{\mathrm{HF}}(i)$ is the Hartree-Fock potential which is the averaged potential experienced by electron i due to the other (N-1) electrons.

As $G^{\mathrm{HF}}(i)$ depends on the spin orbitals of the other electrons, the non-linear equation (3.26) must be solved iteratively until the solutions are self-consistent, hence this iterative procedure is called the self-consistent field (SCF) method. This is performed by using an initial guess of the spin orbital set to determine the Fock operator, then solving the Hartree-Fock equation to obtain a new set of spin orbitals, and repeating the procedure until convergence is reached.

The Slater determinant describing the ground state of the system is therefore made up of the N optimal spin orbitals with the lowest energies ϵ. These are the *occupied*

orbitals. The remaining orbitals are *unoccupied*. For Slater determinants describing excited states of the system, electrons are promoted from the ground state occupied orbitals to unoccupied orbitals. However, this single determinant description does not give an accurate representation of the excited states. Therefore for a better description, one must use the method of *configuration interaction* (CI).

The difference between the exact non-relativistic energy and the Hartree-Fock energy is known as the *correlation energy*:

$$E_{\text{corr}} = E_{\text{exact}} - E_{\text{HF}}, \tag{3.28}$$

since in the Hartree-Fock approximation, the correlation of the motion of the electrons with opposite spins is neglected. The correlation effects are accounted for in the CI method where the exact wavefunction is expanded in terms of Slater determinants or *configuration state functions*:

$$\Psi = c_0\Psi_0 + \sum_{ra} c_a^r \Psi_a^r + \sum_{\substack{a<b \\ r<s}} c_{ab}^{rs}\Psi_{ab}^{rs} + \ldots, \tag{3.29}$$

where Ψ_a^r are determinants describing singly excited states where one electron which is in an occupied state Φ_a in the ground state has been promoted to the virtual state Φ_r. Similarly Ψ_{ab}^{rs} are doubly excited determinants etc. If the expansion in equation (3.29) included the complete infinite set of N-electron determinants then eigenvalues of the Hamiltonian would give the exact energies of the system, however this cannot be implemented in practise and so finite sets of spin orbitals are used. If all the N-tuply excited configurations of the finite set are included in the expansion then the solutions of the finite Hamiltonian are exact within the N-electron subspace spanned by the determinants. This is called a *full* CI calculation. This is however only feasible for small systems and basis sets as the size of the Hamiltonian, and hence the calculation, gets extremely large otherwise.

3.4 Solving the radial Schrödinger equation of diatomic molecules - The LEVEL and BCONT programs

The need to determine the number, energies and properties of vibrational-rotational levels of an electronic potential arises in many problems in chemical physics. In this section two programs by Robert J. Le Roy, LEVEL [120] and BCONT [121], that tackle

this problem for one-dimensional potentials, are described. These codes have been used to calculate the energies and radial wavefunctions of the rovibrational states and nuclear motion continuum discussed in chapter 2.

The core of both programs is concerned with solving the radial or (effective) one-dimensional Schrödinger equation:

$$-\frac{\hbar^2}{2\mu}\frac{d^2 f_{nvJ}(R)}{dR^2} + U_{nJ}^{\text{eff}}(R) f_{nvJ}(R) = E_{nvJ} f_{nvJ}(R), \tag{3.30}$$

where $f_{nvJ}(R)$ are the radial wavefunctions, μ is the effective or reduced mass of the system and n, v and J are the electronic, vibrational and rotational quantum numbers. The effective one-dimensional potential, $U_{nJ}^{\text{eff}}(R)$ is written:

$$\begin{aligned} U_{nJ}^{\text{eff}}(R) = \frac{J(J+1)\hbar^2}{2\mu R^2} + U_{\text{BO}}(R) + U_{\text{ad}}(R) \\ + U_{\text{rel}}(R) + U_{\text{rad}}(R), \end{aligned} \tag{3.31}$$

and is a sum of a centrifugal term $\frac{J(J+1)\hbar^2}{2\mu R^2}$ and the rotationless potential, which consists of the electronic potential in the non-relativistic Born-Oppenheimer approximation $U_{\text{BO}}(R)$, and if known, the mass-dependent adiabatic $U_{\text{ad}}(R)$, relativistic $U_{\text{rel}}(R)$ and radiative $U_{\text{rad}}(R)$ corrections, see figure 3.1. The adiabatic correction, which is an electronically diagonal correction, can be considered as a first order correction to the BO electronic energy due to the coupling between the electronic and nuclear motion, and is given by:

$$\langle \Psi_{\text{elec}} \mid \hat{T}_n \mid \Psi_{\text{elec}} \rangle, \tag{3.32}$$

where Ψ_{elec} is the electronic wavefunction which describes the motion of the electrons and $\hat{T}_n$ is the kinetic energy operator of the nuclei (see section 3.2). The relativistic correction is, in principle, the difference in energy between the full relativistic treatment (Dirac equation) and the Schrödinger equation. In practise, it is often put in by perturbation theory in terms if the fine structure constant. The radiative correction is the difference in energy between the full quantum electrodynamic (QED) equation and the Dirac equation. It is equivalent to the Lamb shift in hydrogen atoms.

The LEVEL program determines the discrete eigenvalues E_{nvJ} and eigenfunctions $f_{nvJ}(R)$ for a specified one-dimensional potential. If requested the program also calculates matrix elements, transition intensities, Franck-Condon factors and other off-diagonal matrix elements, coupling levels of a single potential or levels of two separate potentials. The BCONT program, which is designed to calculate bound to continuum

transition intensities associated with photodissociation, spontaneous emission and predissociation, determines the discrete eigenvalues and eigenfunctions for an initial state potential and calculates continuum state wavefunctions at a given energy in the continuum above the asymptote of the final state potential.

The solution of equation (3.30) is performed in subroutine SCHRQ, which is based on the Cooley-Cashion-Zare routines SCHR [122–126]. The numerical integration of equation (3.30) is performed for a range of internuclear separations using the Numerov algorithm [122, 127]. The accuracy of the eigenvalues and eigenfunctions obtained for a given potential is largely determined by the size of the fixed radial mesh used in the numerical integration. In the Cooley procedure for obtaining the eigenvalues [122, 123], for a given trial energy the numerical integration proceeds outwards from a minimum separation RMIN and inwards from maximum separation RMAX until the two solutions meet at a point R. The discontinuity in the slopes at R is used to estimate the energy correction required to converge on the eigenvalue closest to the trial energy [128]. This is repeated until the chosen convergence criterion is reached. RMIN and RMAX must lie far enough into the classically forbidden regions that the amplitude of the wavefunction has decayed by several orders of magnitude relative to its amplitude in the classically allowed region.

The LEVEL and BCONT programs also contain a special feature in subroutine SCHRQ that allows 'quasibound' levels (also known as tunnelling predissociative resonances) to be automatically located and their widths calculated. These are metastable states that lie above the dissociation limit, but whose dissociation is inhibited by the potential energy barrier that results from the centrifugal term in the potential, as shown in figure 3.1. The height of this barrier varies for each value of the rotation quantum number J. The energies of these levels are determined using a bound state type method where an Airy function boundary condition is applied to the third outermost turning point [129, 130]. This method is virtually exact for narrow, long-lived states, but becomes less reliable for broader levels that lie just below the barrier maxima. The widths are calculated using a uniform semiclassical procedure in which the predissociation rate is thought of as being the product of the probability of tunnelling past the barrier at the specified energy times the vibrational frequency for the state trapped in the well behind the barrier. Again this procedure becomes less exact as the resonance becomes broader.

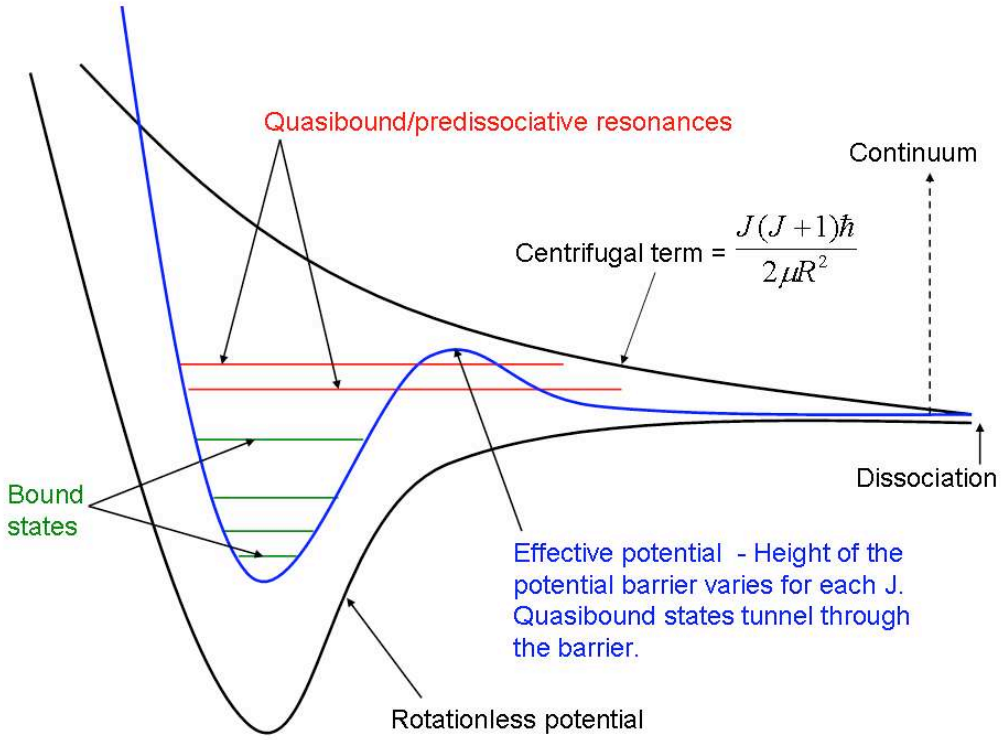

Figure 3.1: Graphic representation of the effective potential energy curve and predissociative resonances

3.5 Molecular R-matrix theory and implementation

In this section the process of electron scattering by a diatomic molecule as modelled using the R-matrix method is described. The UK Molecular R-matrix codes that have been used in this work for the study of the resonance states of $^3HeT^+$ that arise in electron - $^3HeT^{2+}$ collisions and also the background electronic continuum of $^3HeT^+$ are discussed. For a more detailed discussion, the development of the R-matrix approach to electron-atom and electron-molecule scattering is well documented in reference [131].

The time independent Schrödinger equation for a scattering system formed by an N-electron target and colliding electron is:

$$H^{N+1}\Psi_E = E\Psi_E. \tag{3.33}$$

where Ψ_E is the wavefunction describing the system and E is the total energy of the system. H^{N+1} is the non-relativistic fixed-nuclei Hamiltonian given by:

$$H^{N+1} = \sum_{i=1}^{N+1}(-\frac{1}{2}\nabla_i^2 - \frac{Z_A}{r_{Ai}} - \frac{Z_B}{r_{Bi}}) + \frac{Z_A Z_B}{R} + \sum_{i>j=1}^{N+1}\frac{1}{r_{ij}} \tag{3.34}$$

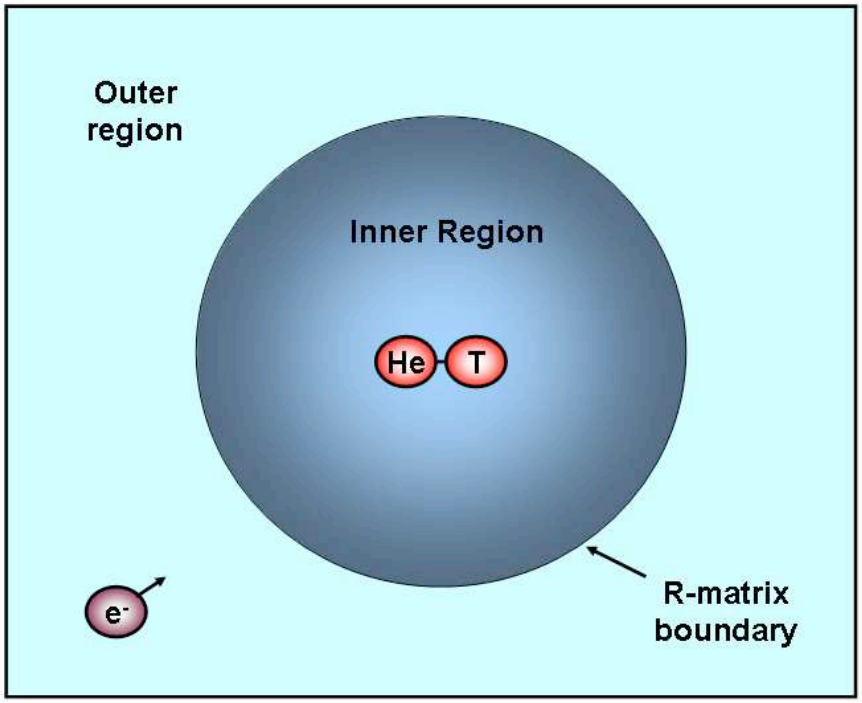

Figure 3.2: Splitting of configuration space in the R-matrix model.

where Z_A and Z_B are the nuclear charges, $r_{Ai} = |r_A - r_i|$, $r_{Bi} = |r_B - r_i|$ and $r_{ij} = |r_i - r_j|$ where r_A, r_B are the coordinates of the two nuclei, r_i and r_j are the coordinates of electrons i and j and R is the internuclear separation.

The R-matrix method is based on the division of configuration space into two regions by a spherical boundary of radius a centred on the centre of mass of the target molecule (figure 3.2). a is chosen such that the entire electronic charge distribution of the molecule is contained within the sphere, hence the contributions that dominate the Hamiltonian differ in the two regions.

In the inner region, $r < a$ (where r is the radial coordinate of the scattered electron), the scattered electron lies within the molecular charge cloud and therefore short range interactions such as electron exchange and correlation must be taken into account. The target molecule and scattering electron complex behaves similarly to a bound state, and so rigorous quantum chemistry methods can be used to obtain the wavefunctions.

In the outer region, $r > a$, exchange and correlation become negligible, and the electron moves in the long range multi-pole potential of the target and a single-centre expansion of the wavefunction can be used.

3.5.1 The inner region

The target molecular orbitals (MO's) are constructed from a basis set of Slater-type atomic orbitals (STO's), which can be expressed using basis functions centred on the nuclei. STO's are based on solutions of the hydrogenic atom problem and give a correct representation of the cusp of the wavefunction on the nucleus and the exponential fall-off of the wavefunction at long range. Normalised STO's are of the form [132]:

$$\rho_{ik}(n,l,m,\zeta_i) = \sqrt{\frac{(2\zeta_i)^{2n+1}}{(2n)!}} r_k^{n-1} e^{-\zeta_i r_k} Y_{lm}(\theta,\phi), \tag{3.35}$$

where i is the orbital index, k is the nuclear centre index, n, l, m have their usual hydrogenic meanings, and $Y_{lm}(\theta,\phi)$ are spherical harmonics. ζ_i is the orbital exponent which can be varied to provide optimum representation. The target molecular orbitals are linear combinations of these atomic orbitals (LCAO), with the coefficients found through a self-consistent field (SCF) or Hartree-Fock calculation (see, for example, [133]).

The electrons are placed in certain combinations of the target molecular orbitals multiplied by spin functions to produce configuration state functions (CSF's), ϕ_i^N, of different total symmetries. For a few-electron molecule (as in our case where the target molecule, HeT^{2+}, has only one electron) all possible combinations can be used. The target molecular wavefunctions, ψ_I^N, are linear combinations of all the CSF's of the wavefunctions symmetry in a configuration interaction (CI) expansion

$$\psi_I^N = \sum_i c_{iI} \phi_i^N. \tag{3.36}$$

The coefficients c_{iI} are found by diagonalising the N-electron target Hamiltonian matrix given by:

$$< \phi_i^N | H_N | \phi_{i'}^N >, \tag{3.37}$$

using the configuration state functions as a basis.

The target molecular orbitals are supplemented with a set of continuum orbitals, ξ_j, centred on the centre of mass of the molecule, which describe the scattering electron in a partial wave expansion.

In some cases linear dependence between the target and continuum molecular orbitals can arise. To eliminate this linear dependence the continuum orbitals may be Lagrange orthogonalised to several of the target molecular orbitals [134]. Each time a Lagrange orthogonalisation is performed the linear combinations of continuum orbitals

most linearly dependent on a target orbital are removed. The continuum and target orbitals are then orthogonalised using the Schmidt orthogonalisation procedure [134].

The inner region scattering energy-independent eigenfunctions of the target molecule plus scattering electron system are represented by a close-coupling expansion:

$$\psi_k^{N+1} = \mathcal{A} \sum_I \psi_I^N(\mathbf{X}_1, ..., \mathbf{X}_N) \sum_j \bar{\xi}_j(\mathbf{X}_{N+1}) a_{Ijk} + \sum_m \chi_m(\mathbf{X}_1, ..., \mathbf{X}_N, \mathbf{X}_{N+1}) b_{mk}, \tag{3.38}$$

where $\mathcal{A}$ is the anti-symmetrisation operator, $\mathbf{X}_n = (\mathbf{r}_n, \sigma_n)$ where $\mathbf{r}_n$ is the spatial coordinate and σ_n is the spin state of the n^{th} electron, $\bar{\xi}_j$ is a continuum molecular orbital spin-coupled with the scattering electron and a_{Ijk} and b_{mk} are variational coefficients.

The first term summation runs over CI target states. It accounts for one electron in a continuum state with the remaining electrons in a target state, known as a 'target+continuum' configuration. The second term summation runs over configurations χ_m in which all the electrons are placed in target molecular orbitals and are known as L^2 functions. These functions account for polarisation and correlation effects. The coefficients a_{Ijk} and b_{mk} are found through diagonalisation of the H^{N+1} Hamiltonian matrix in the inner region. In principle an extra term, the Bloch term, needs to be added to make the Hamiltonian Hermitian in the inner region. However due to the choice of continuum functions in the diatomic code, the boundary conditions make the Bloch term zero.

Once the energy independent eigenfunctions have been found, the final inner region wavefunction can be determined as a linear combination of these eigenfunctions with the coefficients found by matching with the computed outer region functions at the boundary using the R-matrix. The R-matrix on the boundary is determined from the solutions of the Hamiltonian matrix. The R-matrix contains a complete description of the collision problem in the inner region for the energy range defined by the choice of target states and continuum orbitals, and provides the boundary conditions necessary to match the inner and outer region wavefunctions, and solve the problem in the outer region.

3.5.2 The outer region

In the outer region, the wavefunction is expanded in a single-centre close-coupling expansion over target states [135]:

$$\Psi = \sum_I \bar{\psi}_I^N(\mathbf{x}_1 ... \mathbf{x}_N, \sigma_{N+1}) r_{N+1}^{-1} F_I(r_{N+1}) Y_{l_I m_I}(\hat{\mathbf{r}}_{N+1}), \tag{3.39}$$

where $\mathbf{x}_j = (\hat{\mathbf{r}}_j, \sigma_j)$ is the position and spin of the j^{th} target electron, $\bar{\psi}_I^N$ are the functions formed by coupling the scattering electron spin σ_{N+1} with the target state ψ_I^N, and F_I are reduced radial wavefunctions evaluated on the R-matrix sphere. The reduced radial functions can be solved by propagating the R-matrix from the boundary to the asymptotic region where the interaction between the scattering electron and the target molecule may be assumed to be zero [136, 137]. The outer region functions are then solved using Gailitis [138] asymptotic expansion techniques [139]. The asymptotic form of the solutions for F_I in the limit $r \to \infty$ defines the K-matrix, which contains all the scattering information.

The T-matrix is formed from a transformation of the K-matrix:

$$\mathbf{T} = \frac{\mathbf{1} + i\mathbf{K}}{\mathbf{1} - i\mathbf{K}} - \mathbf{1}, \tag{3.40}$$

and is used to derive physical observables such as cross sections and also multichannel quantum defects.

3.5.3 Resonances

Under certain conditions, it is possible for an electron which collides with an atom/molecule to be temporarily captured in a quasistationary orbit in the field of the target molecule. These metastable states which occur at very specific energies are called resonances, and are parameterised by an energy position and width. According to the uncertainty principle, the narrower the width, the longer the lifetime of the resonance and hence the more stable it is. These resonances can be classified into the following types.

- **Ground state shape resonances.** These resonances are associated with the ground state of a molecule and are a one-electron phenomenon. The electron is temporarily trapped by a barrier in the effective potential caused by the combination of the attractive polarisation potential and centrifugal repulsive potential. A molecule plus electron resonance is formed, until the electron can tunnel through the barrier. These resonances are normally broad (short lifetimes) as they can easily decay into the ground state. They do not occur for s-waves ($l = 0$).

Resonances that are associated with excited states are known as core-excited resonances. These are doubly excited states where two electrons occupy excited orbitals, i.e. the target is in an electronically excited state with the other electron in an orbit of the field produced by the excited target. There are two types.

- **Feshbach resonances.** These resonances [140, 141] (which are also called closed-channel or Type I) are associated with a parent singly excited state with positive electron affinity. They lie *below* their parent and their energy curve tracks that of the parent state. Due to energy restrictions, they are prevented from decaying into their parent and must decay into lower target states. They are normally narrow (long-lived) and can occur for all partial waves. In the case of scattering by positively charged molecular ions there will be a positive electron affinity and so this type of resonance is expected.

- **Core-excited shape resonances.** Also called Type II, these resonances are associated with parent states with negative electron affinity, and lie above their parent. They have some similarities to the ground state shape resonances and can decay into all lower target states, although normally decay preferentially into their parent state.

There are several methods that are used to fit resonances. In this work, the eigenphase method has been used, which is the most common way of finding resonances. The eigenphase sum, δ, is a sum of the eigenphases, δ_i, of the open channels i, which are found by diagonalising the K-matrix, and is written as:

$$\delta = \sum_i \tan^{-1}(K_{ii}^D). \tag{3.41}$$

A resonance will produce a characteristic form in the eigenphase sum as a function of energy. Near an isolated resonance, the eigenphase sum can be fitted to a Breit-Wigner profile given by [142]:

$$\delta(E) = \delta_{\rm bg}(E) + \tan^{-1}\left(\frac{\Gamma}{2(E_r - E)}\right), \tag{3.42}$$

where E_r and Γ are the position and width of the resonance respectively, and $\delta_{\rm bg}(E)$ is the background eigenphase sum. As E passes through the resonance region the eigenphase sum will increase approximately by π. The position of the resonance lies at the point of inflection of the curve. Therefore using this method for fitting it is possible to obtain the resonance parameters.

If two or more resonances overlap, or if a resonance is near to or on top of a threshold, the resonance becomes very difficult to fit. Hence eigenphase fitting programs work well for single, narrow resonances which are away from a threshold, but the results become very unreliable close to thresholds or in regions of resonance crossings.

3.5.4 The UK Molecular R-matrix package (diatomic code)

The UK Molecular R-matrix scattering package has been developed over many years by a variety of people. The inner region code was originally based on the quantum chemistry package ALCHEMY [143] developed by IBM in the 1970's with many modifications to make it suitable for the scattering problem [144]. The outer region codes have been developed by Morgan, unless otherwise stated. The program comprises the following modules:

Inner region

- **INTS** generates 1-electron, 2-electron and property integrals. For the target calculation it provides the necessary integrals to be used by the **SCF** module in setting up the target. It is later used again to provide the integrals for the $(N+1)$ calculation. This module was modified by Noble [144] to restrict the range of the radial coordinate to within the R-matrix boundary.

- **SCF** performs a self-consistent field (Hartree-Fock) calculation to produce the target orbitals from linear combinations of atomic orbitals.

- **NUMBAS** generates the continuum orbitals.

- **MOS** computes molecular orbitals. Initially it takes as input the target orbitals from **SCF** to output the molecular orbitals to be used in the target CI calculation. In the $(N+1)$ calculation it takes both the target orbitals and the continuum orbitals from **NUMBAS** and outputs orthogonalised molecular orbitals. It has the option to Lagrange orthogonalise the continuum orbitals to a specified number of target orbitals in order to eliminate linear dependence between the continuum and the target orbitals, and then to Schmidt orthogonalise all the orbitals [134]. Each time a Lagrange orthogonalisation is performed, the linear combination of continuum orbitals most linearly dependent on a target orbital are removed. This module also computes the amplitudes of the continuum orbitals on the R-matrix boundary.

- **TRANS** takes the atomic integrals produced by **INTS** and multiplies them by combinations of molecular orbital coefficients generated by **MOS** to transform them into molecular integrals which are required for the construction of the Hamiltonian.

- **CONGEN** generates the configuration state functions (CSF's) with appropriate spin and symmetry couplings first for the target and then for the $(N+1)$ system. The molecular orbitals are hand picked by the user. It also computes phase factors to keep the phases between the target and $(N+1)$ system consistent [145]. The module had been adapted for scattering calculations to allow explicit coupling of the continuum electron to individual target states [144].

- **SCATCI** [146] performs the configuration interaction calculation for the target and $(N+1)$ system. It takes the molecular integrals from **TRANS** and the configurations from **CONGEN** to build the Hamiltonian matrix. The matrix is then diagonalised to find all the eigenvectors and eigenvalues. For the $(N+1)$ calculation the matrix is first contracted using the target eigenstate vectors before diagonalisation.

- **DENPROP** calculates the dipole and quadrupole moments of the target from the target CI vectors and the property integrals produced by **INTS**. The target properties are used in the outer region calculation.

The flow diagram for the inner region calculation of the target is shown in figure 3.3 and for the $(N+1)$ calculation in figure 3.4.

Outer region

- **INTERF** provides the interface between the inner and outer regions. It constructs the surface amplitudes using the boundary amplitudes and CI vectors generated in the inner region. It also passes on target and channel data.

- **RSOLVE** takes the output of **INTERF** and propagates the R-matrix to the asymptotic region [136, 137], solves the wavefunctions in this region and calculates the K-matrices [139] .

- **EIGENP** takes the K-matrices produced by **RSOLVE** and produces eigenphase sums.

- **RESON** [147] searches the eigenphase for resonances. It automatically detects and parameterises resonances by fitting a standard Breit-Wigner form [142] to the eigenphase sum.

- **TMATRX** transforms K-matrices into T-matrices.

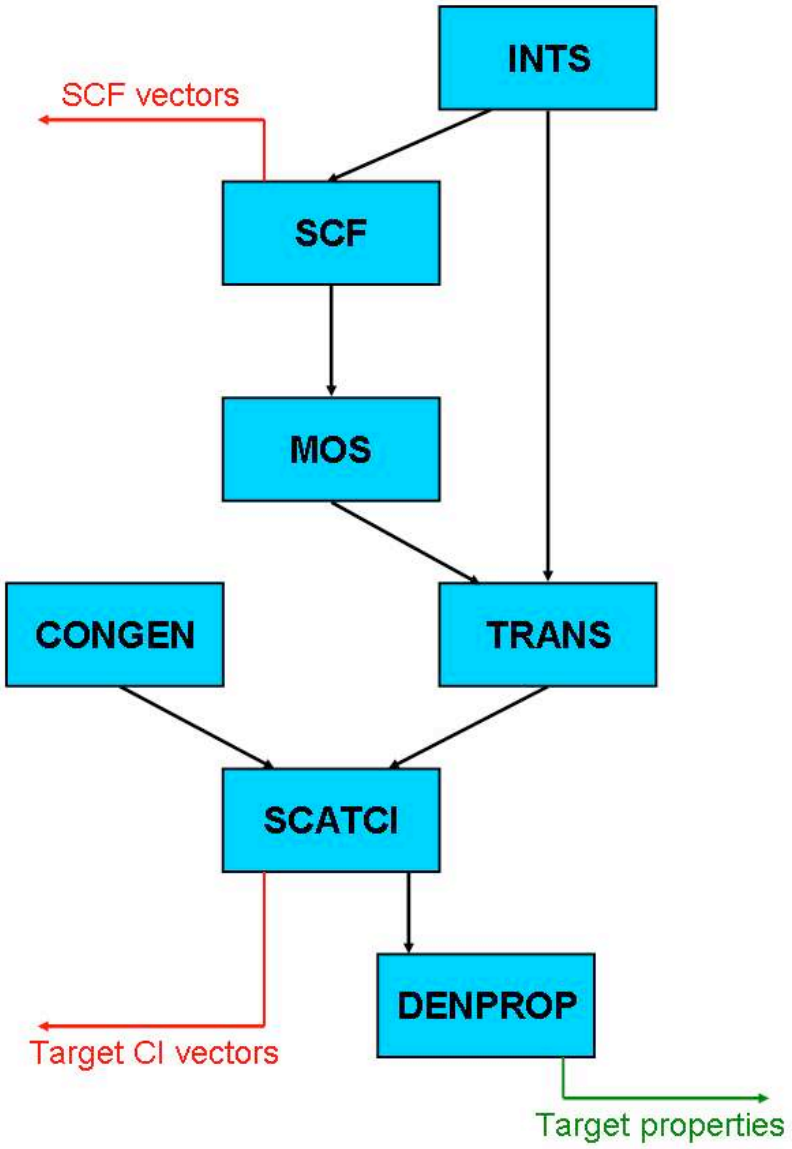

Figure 3.3: Flow diagram of the inner region target state calculation. Red arrows indicate input required by the scattering calculation, green arrows indicate input required by the outer region codes.

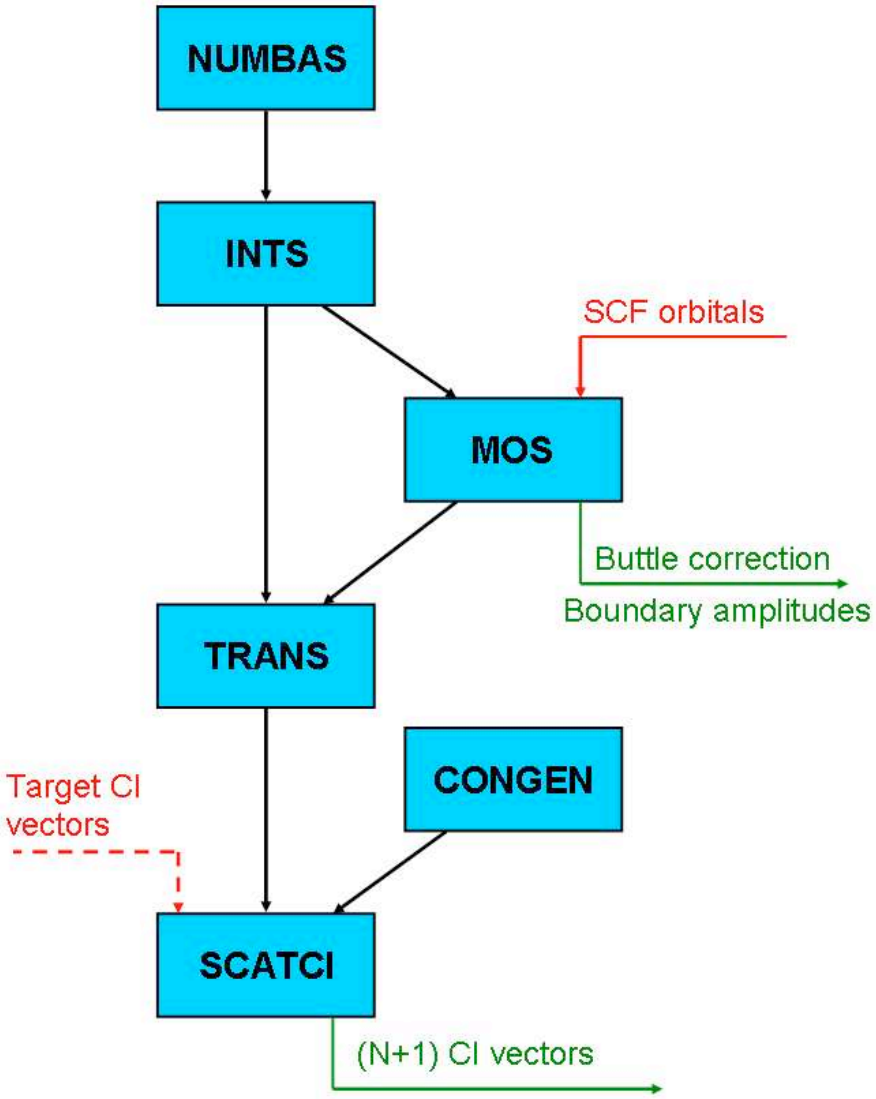

Figure 3.4: Flow diagram of the inner region (N+1) scattering calculation. Green arrows indicate input required by the outer region codes.

- **MCQD** calculates multichannel quantum defects for a given set of input T-matrices.

Other modules such as **IXSECS** and **DCS**, which calculate integral and differential cross sections respectively, and **RATES**, which gives the integration of collision strengths over a Maxwellian temperature distribution, are also available, however these modules have not been used in this work.

A flow diagram for the outer region codes used in this work is shown in figure 3.5.

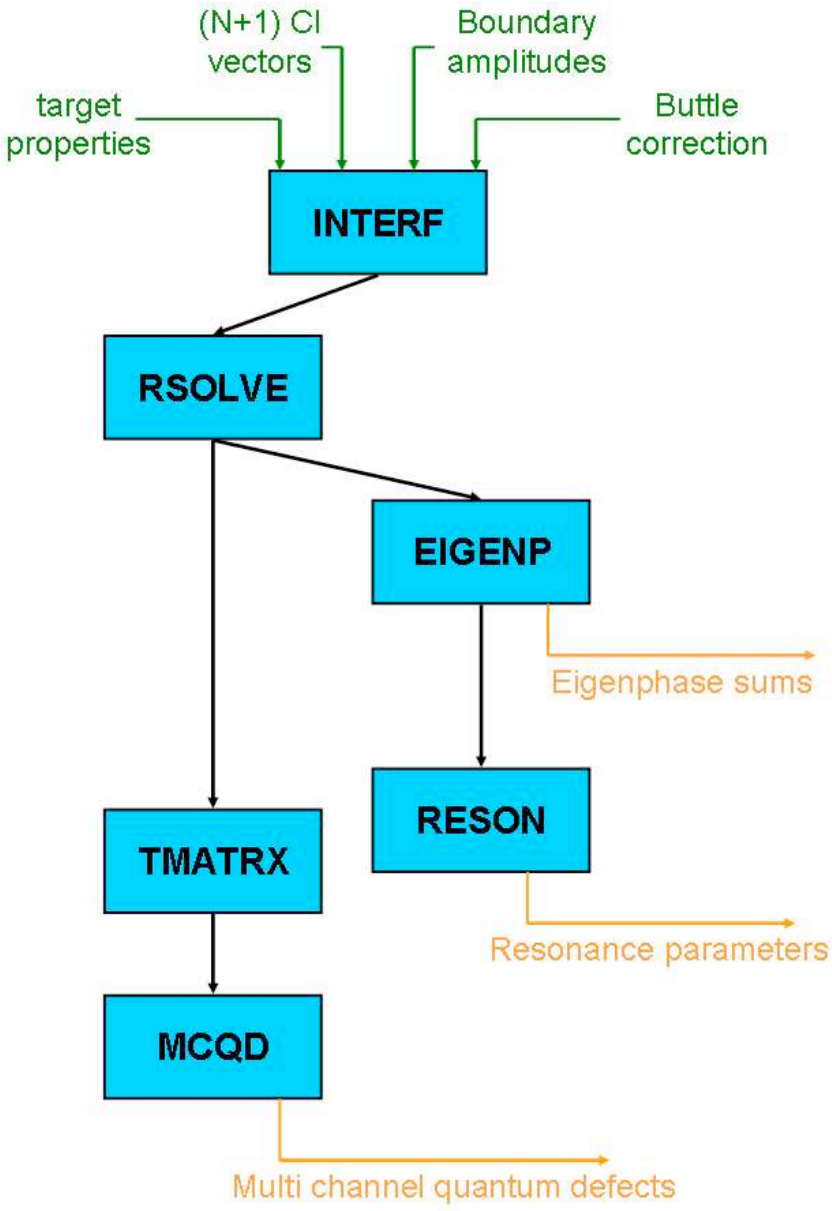

Figure 3.5: Flow diagram of the outer region scattering calculation. Other modules are also available (see text for details).

Chapter 4

Previous studies

In the 1980's an elaborate molecular final state distribution (FSD) for the β-decay of T_2 was constructed and presented by Fackler *et al.* [113] using the results of the detailed studies reported in [108, 111, 112, 148]. The aim of this investigation was to aid the interpretation of the neutrino mass experiment at the Lawrence Livermore National Laboratory. However the contemporaneous experiments were reporting negative values for the neutrino mass squared, obtained from fitting the experimental results to theoretical spectra, which lay outside the error bars extending into the negative region. This indicated a possible systematic error in the experimental results or adopted theory, and initiated a reinvestigation of the FSD being performed [109, 117, 149–152] leading to the distribution reported by Saenz *et al.* [106]. The main aim of this new calculation was to investigate the validity of the underlying approximations used in the previous work. A further motivation for this new calculation was the increased sensitivity of the experimental setups at Mainz and Troitsk.

In this chapter, the studies which lead to the two final state distributions [113] and [106] are described and their main results given. For more detail and full results, the reader is referred to the individual articles.

4.1 The final state distribution of Fackler *et al.*

In 1985, Kołos *et al.* [111] considered transitions to the discrete ($^1\Sigma^+$ symmetry) electronic states of the daughter molecule. The electronic wavefunctions, ψ_n, for HeT^+ were

assumed to be in the form of an expansion in elliptical coordinates:

$$\psi = \sum_i c_i[\Phi_i(1,2) + \Phi_i(2,1)], \tag{4.1}$$

where c_i are variational parameters and Φ_i are the basis functions defined by:

$$\Phi_i(1,2) = \exp(-\alpha\xi_1 - \bar{\alpha}\xi_2 - \beta\eta_1 - \bar{\beta}\eta_2)\xi_1^{r_i}\xi_2^{\bar{r}_i}\eta_1^{s_i}\eta_2^{\bar{s}_i}\rho^{\mu_i}. \tag{4.2}$$

ξ_1,η_1 and ξ_2,η_2 denote the elliptical coordinates of electrons 1 and 2 respectively and are given by:

$$\xi_j = \frac{r_{Aj} + r_{Bj}}{R} \tag{4.3a}$$

$$\eta_j = \frac{r_{Aj} - r_{Bj}}{R} \tag{4.3b}$$

where r_{Aj} is the distance from nucleus A to electron j, r_{Bj} is the distance from nucleus B to electron j and R is the internuclear distance. α, $\bar{\alpha}$, β and $\bar{\beta}$ are variational parameters, r_i, $\bar{r}_i$, s_i, $\bar{s}_i$ and μ_i are integers, $\rho = 2r_{12}/R$ and r_{12} is interelectronic distance. The wavefunctions for the first five excited states of HeT^+ were computed by performing a stepwise optimisation of the exponents in equation (4.2) for several values of R, resulting in 77, 76, 85, 85 and 86 term expansions for the second through sixth electronic state. The ground state wavefunction for HeT^+ was taken from [153]. For T_2 the 72 term expansion from [154] was used for $R > 2.2\ a_0$ and a 69 term expansion obtained from the 80 term expansion from [155] was used for $R \leq 2.2\ a_0$. Using these basis sets, the energies and wavefunctions for the six lowest electronic states of HeT^+ were computed for $0.6 \leq R \leq 4.0\ a_0$. The wavefunctions were then used to compute the overlap integrals, $S_n(R)$, between each electronic state and the ground state of T_2, to an accuracy of 0.0001 in $S_n^2(R)$. Using the equation (c.f. equation (2.38)):

$$P_n = \int_0^\infty S_n^2(R)[f_{100}^i(R)]^2\, dR. \tag{4.4}$$

the total transition probability, P_n, to all rovibrational and scattering states associated with electronic state n of HeT^+, averaged over the zero-point vibration of the parent molecule, was obtained for $n = 1 - 6$. The total probability to the six states is given as 84.22%. By considering 'vertical' transitions at $R = 1.4\ a_0$, they also report that the contribution to higher electronic states is only about 1%, meaning the remaining probability, 14.8%, is connected to the electronic continuum.

Following on from [111], Jeziorski *et al.* [112] took into account the nuclear motion effects by considering the transitions from the ground electronic, vibrational and rotational state of T_2, to the various bound rovibrational and scattering states connected

to the first six electronic states of HeT^+. Within the sudden approximation, and by invoking the Born-Oppenheimer approximation, Jeziorski *et al.* derive expressions for the probability that the HeT^+ molecule will be left in a bound rovibrational state (v, J) of electronic state n (c.f. equation 2.29) and the probability per unit energy that the HeT^+ molecule dissociates via the n^{th} electronic state and that the dissociation products are in a state with energy E and angular momentum J (c.f. equation 2.37). Using equation (2.29) and the overlap integrals calculated by Kołos *et al.* [111], they calculate probabilities for all bound rovibrational states of the electronic ground state of HeT^+. The radial functions were obtained by using Cooley's method and the Numerov integration routine [122] (as used by the Le Roy codes discussed in chapter 3). The most accurate ground state adiabatic potentials for T_2 [154, 155] and HeT^+ [153, 156, 157] were used. For the T_2 potential, relativistic corrections from [155] were also included. A total of 300 bound states were found, with a total probability of 40.826%. For the nuclear motion continuum and rotationally predissociative resonance states, they obtain the probability density using equation (2.37). However for very narrow resonances the total probability of the resonance was obtained from their bound state program. The total probability associated with the scattering states is given as 16.586%, therefore giving a total probability for the electronic ground state of HeT^+ of 57.412%. As the excited electronic states of HeT^+ are purely repulsive, no bound states are supported and the probability density distribution for the continuous spectrum of each state were obtained using equation (2.37). The total probability of the excited states was given as 26.809%. Using the sum rule for P_n given in reference [118], and the sum rule for P_{nJ} given by them (see chapter 2), they checked their calculations for missing probability. For all n and J the sum rule for P_{nJ} was satisfied with errors smaller than 0.01%. The authors estimate that the errors in the probability calculated is determined by the error in the overlap integral. An analogous calculation of the FSD of the ground state of HeH^+ resulting from the β-decay of TH was also calculated. A total of 150 bound states with a probability of 55.72% were found. The probability of the scattering states was 1.36% giving a total probability for the ground state of 57.08%.

The FSD of the electronic continuum of HeT^+ was investigated by Kołos *et al.* [148] and the calculation extended by Szalewicz *et al.* [108]. The resonance states were studied by using the stabilisation method to determine potential energy curves for these states for a range of internuclear distances. The resonances are detected by the presence

of the stable values of their energies, as the wavefunction describing the continuum is changed by either increasing the number of terms in the expansion, or by scaling the nonlinear parameters. This method is based on the observation that at an energy close to the position of a resonance the inner part of the continuum state wavefunctions should resemble the wavefunction of a bound state, with the amplitude of the wavefunction in the asymptotic region being much smaller than in the inner part. The wavefunction can then be represented approximately by exponentially decaying trial functions, and expanded in a square integrable basis, and the hamiltonian matrix diagonalised. Some of the roots obtained will refer to the resonance states and others to the background continuum. If the wavefunction is changed as described above, then a different set of eigenvalues will be obtained. As long as the wavefunction expansion remains reasonably accurate, then the energies of the resonance states should not vary much. However the roots corresponding to the background continuum may change considerably. The resonance states can then be determined by plotting the eigenvalues against the number of terms in the expansion or the scaling parameter applied to the exponents. It is crucial, however, that the starting approximation of the wavefunction is reasonably accurate. (The above description of the stabilisation method is based on the discussion in [148]). In [148] and [108] a 200 term expansion was used and the nonlinear parameters varied. Using this method the energies of the lowest five resonances were obtained for a range of R. Problems were encountered for the higher resonances as a state that appeared with one set of parameters would disappear for other sets. Some results are also given for the sixth and seventh resonance states. At each internuclear distance, the overlap integrals of the wavefunctions with the T_2 electronic ground state wavefunction was determined. Using equation (2.38), and therefore not taking into account the nuclear motion, the total probabilities connected with the resonance states and with the discretized background continuum were obtained. For the background continuum, only the vertical transition probability at $R = 1.4\ a_0$. was considered. The majority (two-thirds) of the probability in the electronic continuum was found to be associated with the two lowest resonance states. The accuracy of the FSD in the electronic continuum was considered to be lower than the FSD obtained below the ionisation threshold, due to possible errors in the positions of the resonance states.

Fackler *et al.* [113] combined the results from the studies discussed above [108, 111, 112, 148] to give the overall FSD. They also compared the Kurie plots (which is a form

of describing the β spectrum) for different levels of accuracy of the FSD. By considering a neutrino mass of 30 eV/c^2, Kurie plots were obtained for pure nuclear, atomic and molecular processes. For the molecular processes, three versions of construction of the FSD were considered; (i) fixed value of the internuclear distance $R = 1.4\ a_0$, (ii) various R averaged over the ground rovibrational state of the T_2 molecule, and (iii) the same as (ii) but with the nuclear motion effects of the lowest six electronic states of $^3HeT^+$ taken into account. They found that the molecular effects are important and that the nuclear motion effect must be considered in all regions of the spectrum. By considering several neutrino masses in the range of 0 - 50 eV/c^2, they also found that the nuclear motion effect is significant at all values of the neutrino mass. The accuracy of the FSD was considered, and they reported that the main source of error arises from the sudden approximation, i.e. the neglect of the interaction of the β electron with the remaining molecular electrons.

The FSD given in [113] is for gaseous T_2, however the experiment at Livermore used a frozen T_2 source. The solid state effects were considered by Kołos *et al.* [158], by computing the excitation probabilities of the T_2 molecules in the crystal surrounding the β-decaying tritium and studying the influence of this effect on the neutrino mass determination. It was found that for a neutrino mass of the order of a few eV/c^2, the solid state effects are very important.

4.2 The final state distribution of Saenz *et al.*

As the experiments were still reporting negative values for the neutrino mass squared, a reinvestigation of the FSD was performed in the 1990's, with the aim of investigating the validity of the underlying approximations used and to meet the new requirements of the Mainz and Troitsk experiments, resulting from their increased sensitivity.

Froelich *et al.* [149] performed a reinvestigation of the FSD of the electronic continuum, as it was felt that in the previous probability distribution the resonant part of the spectrum had not been sufficiently described. They used a novel technique whereby the probability density distribution, including the contribution from both the resonances and background scattering, was obtained by avoiding the explicit calculation of the wavefunctions describing the continuum states of $^3HeT^+$. Their method was based on the observation that the probability density, $P(E)$, can be given by the imaginary part of the expectation value of the $^3HeT^+$ resolvent operator with respect to the ground state

of T_2, $G(E)$, provided that a meaningful approximation to the resolvent operator can be found. Hence:

$$P(E) = \pi^{-1} Im\{G(E)\}. \tag{4.5}$$

In this way, the probability density at a given energy is obtained, without explicitly calculating the transition probability to a specific final state. This is not a problem, since for the analysis by the neutrino mass experiments, it is not necessary to resolve the molecular final states that are energetically degenerate. The probability density of the electronic continuum was evaluated by applying the complex scaling method [159]. The clamped-nuclei approximation was assumed and the probability density obtained for the T_2 equilibrium separation, $R = 1.4\ a_0$. Unlike the discretized FSD given in [108, 113], the probability density distribution calculated within the complex scaling method exhibits a smooth background and broadened resonances. It was also found [151] that the FSD obtained with the complex scaling method, is to a good approximation, basis set independent. Using this approach the probability distribution for the electronic continuum was improved but the fits of the neutrino mass were found to remain nearly unchanged [151].

Fackler *et al.* [113] reported that the main source of error in the FSD was due to the neglect of the interaction of the β electron with the remaining molecular electrons, therefore Saenz and Froelich investigated the validity of the use of the sudden approximation [109, 150, 151]. In reference [109] a detailed derivation of the β spectrum in a beyond sudden approximation treatment of the β-decay of a nucleus embedded in an atom/molecule was performed. Explicit expressions for the zeroth and first order transition amplitudes are derived and final expressions for the molecular higher order transition probabilities were given. Calculations for the specific case of T_2 were given in [150, 151]. For the first time, the probability distribution, including electronically bound and continuous states, were calculated in a beyond sudden approximation [151]. They found that if the interaction of the β electron with the decaying nucleus is already included in the zeroth order treatment (see equation (2.3) and the discussion given in chapter 2) then the largest corrections arise from the interference term between the zeroth order and first order amplitudes. These corrections were calculated explicitly in [151] and found to be negligible.

In [151] Saenz and Froelich also examined the reliability of the β spectrum within the sudden approximation. The investigation concentrated on considering the effect of

nuclear motion in the electronic continuum and extending the previous distributions, which go up to an energy of 165 eV, to larger energies, up to 800 eV. The effect of nuclear motion in the electronic continuum was taken into account by use of the reflection approximation which assumes that the transition from the initial T_2 state to the final HeT^+ state occurs without a change of the internuclear geometry and that the nuclear wavefunction of the final dissociative state is given by a delta function at the classical turning point of the potential curve. The FSD was calculated at different values of internuclear separation and the final distribution obtained from the R-dependent distributions weighted with the vibrational wavefunction of the rovibronic ground state of T_2. It was found that the main effect of the nuclear recoil, was a considerable broadening of the resonance contributions due to the strong dependence of the resonance positions on the internuclear separation. The FSD of the Rydberg states (high lying electronically bound states) was also calculated using the same basis functions used for the electronic continuum.

Jonsell *et al.* [117] performed a reinvestigation of the FSD for the electronically bound states of $^3HeT^+$ and $^3HeH^+$, since recent experimental results had indicated that the source of the negative neutrino mass squared problem lay close to the endpoint of the β spectrum [88, 89]. The refinements added to this new calculation included a relativistic correction to the molecular recoil caused by the emitted electron, improved potential energy curves and improved overlaps for the excited electronic states. The validity of the Born-Oppenheimer approximation was investigated by considering the non-adiabatic corrections. Also the decay from rotationally excited T_2 ($J_i = 1$) was considered (previously only $J_i = 0$ had been considered). In reference [112] the relation $p_\beta = \sqrt{2m_e E_\beta}$ was used for the momentum of the β electron. Jonsell *et al.* found that by using the relativistic relation for p_β, which increased the recoil momentum by 1%, the probability of transitions to certain v, J states changed by as much as 40%. However they stated that as the sum rule is unaffected by a change in the recoil momentum, changes in the probability for one state must be compensated by changes in other states. They found that this correction moved probability from lower to higher vibrational levels, and that the relative change to individual bins compared to [112] was up to 10%. For the ground state of $^3HeT^+$, the same data as in reference [112] was used for the potential and electronic overlap. The Born-Oppenheimer energies and overlaps of the excited states were recalculated using the same method as in [111], 400 basis functions, three sets of

nonlinear exponents and the T_2 ground state wavefunction from [160]. The electronic energies were obtained from [161]. A separate FSD was calculated for the β-decay of T_2 in its $J_i = 1$ state. It was found that this not only changed the probability of the rovibrational states, but also transfered probability between different electronic states. The FSD due to the β-decay of HT was also calculated for the first six electronic states (previously it had only been calculated for the ground state [112]). The first order correction to the transition probability to a given rovibrational state resulting from non-adiabatic couplings was derived by Jonsell *et al.* [152] where the largest change in probability was found to occur in the coupling between the ground state and first excited state. In [117] the corrections were calculated for rovibrational states of the ground electronic state. They found these corrections to be very small, therefore validating the Born-Oppenheimer approximation.

Using the results from [109, 117, 149–152] an improved FSD for $^3HeT^+$ and $^3HeH^+$ was presented in reference [106]. The total probability to all states was given as 99.83% for T_2. It was reported that the missing 0.17%, was distributed uniformly over the electronic continuum, and so the FSD above 40 eV was multiplied by the factor 1.0106. They obtained an estimate of the improvement of the new FSD over the one presented in [113], by creating synthetic experimental spectra using typical parameters from the Mainz experiment and the new FSD assuming a zero neutrino mass, and then extracting the neutrino mass squared using the previous FSD. The fitted value of the neutrino mass squared was found to be as large as 1 eV/c^2 depending on the energy range included in the fit.

Chapter 5

The final state probability distribution for the electronically bound states

In chapter 4 the previous studies that have been performed on the molecular final state distributions were discussed. Each of these works were performed based on the requirements of the neutrino mass experiments at that time. The increased sensitivity and changes in requirements for the future KATRIN experiment has therefore led us to perform a reinvestigation of the molecular final state distribution.

As described in chapter 1, the KATRIN experiment aims to obtain an upper limit for the value of the neutrino mass by analysing the β spectrum in an energy interval with a lower limit of 30 eV below the endpoint energy [98]. In this energy interval the effect from only the six lowest electronic states of $^3HeT^+$ need to be considered. The Rydberg states (high-lying electronic states) and electronic continuum of $^3HeT^+$ begin to have an effect from 40 eV below the endpoint.

In this chapter the calculation of the final state distribution of the first six electronic states of $^3HeT^+$, $^3HeD^+$ and $^3HeH^+$ performed by us is discussed. The emphasis of this new calculation is to investigate the effect of uncertainties in the temperature of the T_2 source and amount of isotope contamination from HT and DT molecules on the deduced value of the neutrino mass obtained from fitting. This error budget will be discussed in the following chapter.

5.1 The electronic ground state of $^3HeT^+$

The calculation of the probability distribution of the electronic ground state of $^3HeT^+$ can be split into two parts.

1. the discrete probability distribution of the bound and 'quasibound' rovibrational states,

2. the continuous probability density distribution of the nuclear motion continuum.

These two areas must be treated differently, and are discussed below.

5.1.1 Probability distribution of bound and quasibound states

In chapter 2 an expression for the probability that the $^3HeT^+$ molecule will be left in a bound rovibrational state (v, J) of electronic state n was given. For now, the T_2 molecules are assumed to be in their lowest energy state (rotational excitation, $J > 0$, of the T_2 molecules is discussed in section 5.2). For the case where the initial T_2 molecule is in its ground electronic and rovibrational state and $^3HeT^+$ in its ground electronic state, this expression becomes:

$$P_{1vJ}(K) = (2J+1)\left|\int S_1(R) j_J(KR) f^f_{1vJ}(R) f^i_{100}(R) dR\right|^2 . \tag{5.1}$$

In order to calculate the probabilities, the radial parts of the rovibrational wavefunctions of $^3HeT^+$ and T_2, $f^f_{1vJ}(R)$ and $f^i_{100}(R)$ respectively, need to be determined. To do this, Le Roy's program LEVEL [120], discussed in section 3.4, was used.

To calculate the wavefunctions and energies the LEVEL program must be supplied with:

1. the rotationless electronic potentials for T_2 and $^3HeT^+$ and,

2. the nuclear masses of T and He in order to obtain the reduced mass.

For the ground state rotationless electronic potential of $^3HeT^+$ the same procedure as in reference [117] was used. The Born-Oppenheimer potential was taken from references [153, 156, 157] and the adiabatic correction from reference [157]. Kolos and Peek [153] give the Born-Oppenheimer potential of HeH^+ for 28 values of internuclear separation R between 0.9 and 4.5 a.u. Kolos [156] gives the Born-Oppenheimer potential for 8 values of R between 5.0 and 9.0 a.u. and also at $R = \infty$. Bishop and Cheung [157] report an improved calculation of the Born-Oppenheimer potential giving corrections, $\Delta E(R)$, to

the values given in references [153, 156] for seven internuclear separations, $R = 0.9$, 1.46, 1.8, 3.0, 4.5, 6.0 and ∞. They also report adiabatic corrections for $^4He^1H^+$ by using the Born method to take into account the coupling between electronic and nuclear motion.

To obtain the required energy corrections for the other separations, the $\Delta E(R)$ for the six finite R from [157] were fitted to the polynomial (also given in [157]):

$$\Delta E(R) = \sum_{k=-3}^{k=2} a_k R^k, \tag{5.2}$$

and values of $\Delta E(R)$ were interpolated for the 31 separations R (between 0.9 and 6.0 a_0) considered in [153, 156]. For separations between R = 6.0 a_0 and ∞, a linear interpolation of $\Delta E(R)$ was performed. These energy corrections were then subtracted from the Born-Oppenheimer energies in [153, 156].

The Born-Oppenheimer curve, $E(R)$, is corrected for adiabaticity in the following way:

$$U(R) = E(R) - \frac{\langle(\nabla_1 + \nabla_2)^2\rangle}{8\mu} - \frac{\langle\nabla_R^2\rangle}{2\mu} - \frac{\langle\nabla_R \cdot (\nabla_1 + \nabla_2)\rangle}{2\mu_a}, \tag{5.3}$$

where $U(R)$ is the corrected curve, ∇_R^2 is the Laplacian operator for one nucleus relative to the other, μ is the reduced nuclear mass $\frac{m_H m_{He}}{(m_{He}+m_H)}$ and μ_a is the mass ratio $\frac{m_H m_{He}}{(m_{He}-m_H)}$. m_H and m_{He} are the masses of the hydrogen nucleus and helium nucleus respectively. In reference [157] values are given for each of the three terms separately for the same separations R for which the Born-Oppenheimer energy corrections were given (see above) and for $R = 1.2$ and 2.4 a_0 also, using $\mu = 1466.898$ and $\mu_a = 2453.844$ in atomic units, for $^4He^1H^+$. However as the adiabatic corrections are mass dependent, to obtain the corrections for $^3HeT^+$ a mass scaling of the values given in [157] must be performed. Using values of $\mu = 2748.201$ and μ_a = -29132525.73 (where $m_{^3He} = 5495.883$ and $m_T = 5496.920$ taken from the NIST Physical Reference Data website [162] have been used), the total adiabatic correction for $^3HeT^+$ for the 9 separations R were determined. These values were then fitted to the polynomial (given in [157]):

$$\sum_{k=-5}^{k=2} b_k R^k, \tag{5.4}$$

and the total adiabatic correction for $^3HeT^+$ was interpolated for all the other separations. The adiabatic corrections were then subtracted from the Born Oppenheimer values to give the final potential.

The ground state rotationless electronic potential for $^3HeT^+$ is given in the second column of table 5.1 and shown in figure 5.1. The potential is given in units of E_h, which

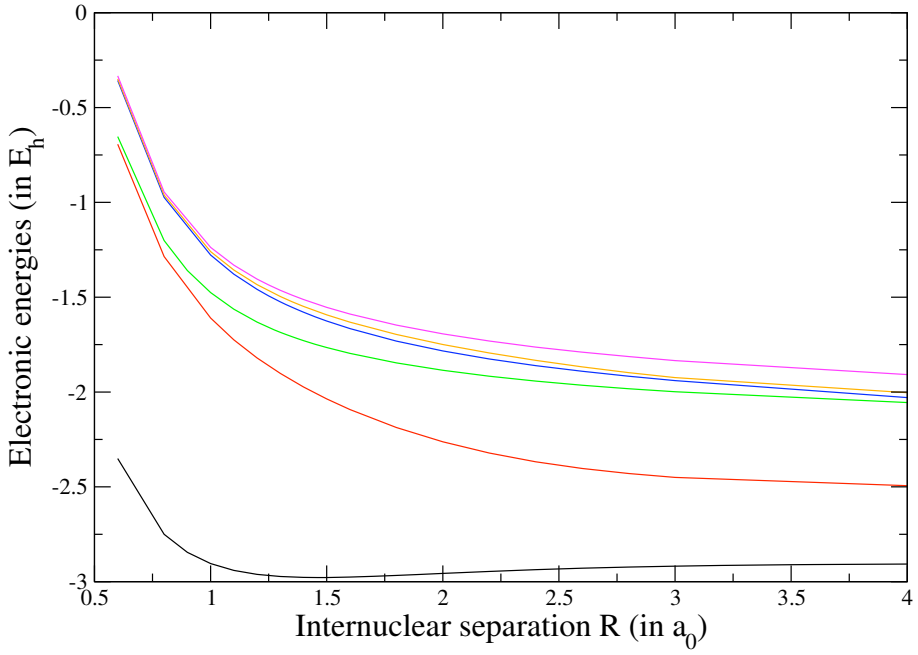

Figure 5.1: Electronic energy curves for the first six electronic states of $^3HeT^+$ as a function of the internuclear separation R. E_h is the Hartree unit of energy.

represents the Hartree unit of energy. The two extra points at $R = 0.6$ and 0.8 a_0 were obtained by using Born-Oppenheimer values from [111] and extrapolating the adiabatic correction.

The ground state rotationless electronic potential of T_2 was obtained by combining the Born-Oppenheimer potential, and the radiative, relativistic and adiabatic corrections of Wolniewicz [163]. The adiabatic corrections given in [163] are for H_2, therefore they were mass scaled to give the corrections for T_2 using the values $\mu_{H_2} = 918.076$ and $\mu_{T_2} = 2748.46$. The radiative and relativistic corrections are mass independent. The electronic potential is given in the third column of table 5.1.

The reduced mass which enters in the radial one-dimensional Schrödinger equation (3.30) solved by the LEVEL program is defined in the program as the atomic reduced mass. In the previous calculation of the final state distribution by Jonsell *et al.* [117], the atomic reduced masses were replaced by nuclear reduced masses when solving the radial Schrödinger equation. Coxon and Hajigeorgiou [164] investigated the effect of using different reduced masses for the isotopes of HeH^+. In this work, the use of the following different reduced masses, as in reference [164], have been tested;

1. the nuclear reduced mass $\mu_{\rm nuc} = \frac{m_1^{\rm nuc} m_2^{\rm nuc}}{m_1^{\rm nuc}+m_2^{\rm nuc}}$.
2. the charge adjusted reduced mass $\mu_{\rm C} = \frac{m_1^{\rm at} m_2^{\rm at}}{m_1^{\rm at}+m_2^{\rm at}+Qm_e}$ (which corrects for net charge

Table 5.1: Electronic energies, in E_h, for the ground states of $^3HeT^+$, T_2, $^3HeD^+$, DT, $^3HeH^+$ and HT as a function of the internuclear separation R, in a_0

R	$^3HeT^+$	T_2	$^3HeD^+$	DT	$^3HeH^+$	HT
0.4		-0.119996959		-0.119931191		-0.119733451
0.5		-0.526410515		-0.526347715		-0.526158897
0.6	-2.35089595	-0.769414400	-2.35078689	-0.769354600	-2.35049017	-0.769174801
0.8	-2.75006498	-1.019851823	-2.75003244	-1.019797531	-2.74993554	-1.019634295
0.9	-2.84507728	-1.083446222	-2.84505095	-1.083394331	-2.84497177	-1.083238312
1.0	-2.90424718	-1.124350006	-2.90422462	-1.124300266	-2.90415670	-1.124150713
1.1	-2.94038588	-1.149874337	-2.94036629	-1.149826507	-2.94030735	-1.149682699
1.2	-2.96150035	-1.164758239	-2.96148330	-1.164712093	-2.96143200	-1.164573347
1.3	-2.97273529	-1.172175518	-2.97272042	-1.172130845	-2.97267573	-1.171996531
1.35		-1.173794540		-1.173750531		-1.173618211
1.4	-2.97747176	-1.174308820	-2.97745878	-1.174265428	-2.97741976	-1.174134964
1.45		-1.173892312		-1.173849492		-1.173720748
1.46	-2.97816767		-2.97815569		-2.97811970	
1.5	-2.97796828	-1.172692313	-2.97795693	-1.172650023	-2.97792281	-1.172522873
1.6	-2.97575292	-1.168424160	-2.97574297	-1.168382807	-2.97571308	-1.168258474
1.7	-2.97186771	-1.162302522	-2.97185898	-1.162261954	-2.97183275	-1.162139980
1.8	-2.96702601	-1.154915030	-2.96701834	-1.154875105	-2.96699529	-1.154755067
1.9	-2.96171761		-2.96171087		-2.96169060	
2.0	-2.95627357	-1.137982819	-2.95626764	-1.137943795	-2.95624981	-1.137826465
2.2	-2.94579234	-1.119983828	-2.94578776	-1.119945246	-2.94577398	-1.119829241
2.4	-2.93656323	-1.102274661	-2.93655971	-1.102236119	-2.93654911	-1.102120239
2.6	-2.92890147	-1.085642352	-2.92889878	-1.085603513	-2.92889070	-1.085486740
2.8	-2.92278531	-1.070532389	-2.92278328	-1.070492987	-2.92277719	-1.070374519
3.0	-2.91803748	-1.057172763	-2.91803598	-1.057132612	-2.91803147	-1.057011894
3.2	-2.91442574	-1.045643141	-2.91442465	-1.045602149	-2.91442137	-1.045478901
3.4	-2.91171328	-1.035915840	-2.91171250	-1.035874002	-2.91171017	-1.035748211
3.5	-2.91062798		-2.91062734		-2.91062539	
3.6	-2.90969236	-1.027883989	-2.90969183	-1.027841375	-2.90969021	-1.027713250
3.8	-2.90819161	-1.021385152	-2.90819125	-1.021341878	-2.90819016	-1.021211769
4.0	-2.90707650	-1.016223786	-2.90707627	-1.016179985	-2.90707556	-1.016048290
4.2		-1.012192137		-1.012147936		-1.012015039
4.4		-1.009087721		-1.009043227		-1.008909449
4.5	-2.90536593		-2.90536584		-2.90536559	
4.6		-1.006725754		-1.006681049		-1.006546639
4.8		-1.004946067		-1.004901213		-1.004766354
5.0	-2.90450147	-1.003615400	-2.90450140	-1.003570439	-2.90450124	-1.003435258
5.2		-1.002626331		-1.002581293		-1.002445881
5.4		-1.001894412		-1.001849319		-1.001713739
5.5	-2.90403198		-2.90403192		-2.90403176	
5.6		-1.001354493		-1.001309359		-1.001173657
5.8		-1.000957040		-1.000911875		-1.000776082
6.0	-2.90375371	-1.000664800	-2.90375370	-1.000619614	-2.90375368	-1.000483753
6.2		-1.000450010		-1.000404807		-1.000268895
6.4		-1.000292018		-1.000246802		-1.000110851
6.5	-2.90358413		-2.90358412		-2.90358410	
6.6		-1.000175863		-1.000130637		-0.999994657
6.8		-1.000090174		-1.000044940		-0.999908937
7.0	-2.90347259	-1.000026857	-2.90347258	-0.999981618	-2.90347256	-0.999845598
7.2		-0.999979922		-0.999934678		-0.999798644
7.4		-0.999945007		-0.999899759		-0.999763716
7.5	-2.90339636		-2.90339636		-2.90334268	
7.6		-0.999918911		-0.999873660		-0.999737608
7.8		-0.999899311		-0.999854059		-0.999718000
8.0	-2.90334270	-0.999884502	-2.90334270	-0.999839248		-0.999703185
8.5		-0.999861058		-0.999815801		-0.999679730
9.0	-2.90327529	-0.999848662	-2.90327528	-0.999803403	-2.90327526	-0.999667326
9.5		-0.999841732		-0.999796472		-0.999660392
10.0		-0.999837631		-0.999792371		-0.999656289
11.0		-0.999833380		-0.999788119		-0.999652035
12.0		-0.999831431		-0.999786169		-0.999650084

Table 5.2: Reduced masses for $^3HeH^+$ and $^3HeD^+$

	$^3HeH^+$	$^3HeD^+$
μ_{nuc}	0.755025526	1.207267369
μ_{dis}	0.75509432	1.207443253
μ_C	0.755505552	1.207772213
μ_{eff}	0.755231243	1.207497908

on the molecule (ion)). The masses here are atomic masses.

3. the dissociation reduced mass μ_{dis}, where the atomic masses of the particles at dissociation are used. (ie. He and H^+).

4. the effective mass μ_{eff}, which assumes that one of the two electrons is essentially tied to the He^{2+} nucleus, with the second electron being distributed between the H^+ and He^+ centres (ie. $He^{\frac{1}{2}+}$ and $H^{\frac{1}{2}+}$).

For each of the reduced masses, the LEVEL program was used to calculate the energies of the rovibrational states. The resulting theoretical transition frequencies were compared to experimental transition frequencies given in references [165–167]. As there are no experimental values available for $^3HeT^+$ the comparison was performed for $^3HeH^+$ and $^3HeD^+$. The values of the reduced masses used are given in table 5.2, based on (atomic) masses $m_H = 1.007825035$, $m_D = 2.014101779$, $m_{^3He} = 3.01602931$ and $m_e = 0.00054858$ u from reference [164]. The differences between the theoretical and experimental frequencies are summarised in table 5.3.

As in [164], μ_{eff} was found to be the best compromise and so was used for the daughter molecular ion in our calculations. However, at the level of a few tenths of an eV, the energy resolution of KATRIN, the choice of reduced mass has negligible effect on the final state distribution. Similar calculations have recently been used to determine the partition function and opacity of various HeH^+ isotopologues for stellar modelling [168], these used μ_{dis}.

For the T_2 potential the nuclear reduced mass was used. As it is only the lowest rovibrational state which is of interest, the choice of reduced mass has negligible effect. The accuracy of the T_2 potential was tested by comparing the theoretical transition frequencies obtained using the energies computed by LEVEL, with experimental transition frequencies from reference [169]. The results are shown in table 5.4.

Table 5.3: Differences between experimental rotation-vibration transition frequencies (cm^{-1}) [165–167] and theoretical frequencies calculated using different reduced masses for $^3HeH^+$ and $^3HeD^+$

			$\nu_{calc} - \nu_{obs}$			
(v',J')	(v'',J'')	ν_{obs}	μ_{nuc}	μ_C	μ_{dis}	μ_{eff}
			$^3HeH^+$			
(0,1)	(0,0)	71.367	0.004	-0.042	-0.005	-0.016
(0,2)	(0,1)	142.293	0.005	-0.084	-0.008	-0.033
(1,0)	(0,1)	2923.680	0.395	-0.408	0.279	0.050
(1,1)	(0,2)	2846.775	0.389	-0.365	0.281	0.066
(1,2)	(0,3)	2764.768	0.388	-0.311	0.288	0.088
(1,3)	(0,4)	2678.113	0.383	-0.258	0.291	0.108
(1,4)	(0,5)	2587.243	0.380	-0.200	0.297	0.131
(1,5)	(0,6)	2492.591	0.372	-0.143	0.298	0.151
(1,1)	(0,0)	3060.433	0.399	-0.488	0.270	0.018
(1,2)	(0,1)	3119.405	0.400	-0.519	0.268	0.006
(1,3)	(0,2)	3171.549	0.402	-0.542	0.266	-0.003
(1,4)	(0,3)	3216.468	0.403	-0.559	0.265	-0.009
(1,5)	(0,4)	3253.785	0.406	-0.567	0.267	-0.011
(1,6)	(0,5)	3283.156	0.404	-0.572	0.264	-0.014
(1,7)	(0,6)	3304.247	0.395	-0.575	0.256	-0.021
(1,8)	(0,7)	3316.761	0.395	-0.560	0.258	-0.014
(6,12)	(5,11)	981.322	0.014	1.380	0.210	0.600
			$^3HeD^+$			
(0,2)	(0,1)	89.932	0.006	-0.031	-0.007	-0.011
(0,3)	(0,2)	134.467	0.009	-0.046	-0.011	-0.016
(1,0)	(0,1)	2378.374	0.374	-0.071	0.219	0.171
(1,2)	(0,3)	2280.081	0.378	-0.025	0.238	0.194
(1,2)	(0,1)	2504.487	0.386	-0.109	0.213	0.160
(1,3)	(0,2)	2540.161	0.391	-0.116	0.214	0.159
(1,4)	(0,3)	2572.388	0.392	-0.126	0.212	0.155
(1,5)	(0,4)	2601.007	0.396	-0.129	0.213	0.156
(6,19)	(5,18)	1034.144	0.048	0.738	0.289	0.363
(7,17)	(5,19)	995.415	0.061	1.215	0.464	0.589

Table 5.4: Differences between experimental rotation-vibration transition frequencies (cm^{-1}) [169, 170] and theoretical frequencies for T_2, DT and HT

		T_2		DT		HT	
(v',J')	(v'',J'')	ν_{obs}	$\nu_{calc}-\nu_{obs}$	ν_{obs}	$\nu_{calc}-\nu_{obs}$	ν_{obs}	$\nu_{calc}-\nu_{obs}$
(0,2)	(0,0)	120.021	0.039				
(0,3)	(0,1)	199.681	0.012				
(0,4)	(0,2)	278.9	-0.2				
(0,5)	(0,3)	357.0	-0.1				
(0,6)	(0,4)	434.1	-0.1				
(0,7)	(0,5)	510.0	-0.2				
(0,8)	(0,6)	584.3	-0.1				
(0,9)	(0,7)	657.0	-0.1				
(0,10)	(0,8)	727.8	-0.1				
(0,11)	(0,9)	796.7	-0.2				
(0,12)	(0,10)	863.2	0.0				
(0,13)	(0,11)	927.8	-0.1				
(1,0)	(0,0)					3434.9	0.7
(1,1)	(0,1)					3431.6	0.8
(1,2)	(0,2)	2461.0	0.7	2738.4	0.8	3425.1	0.8
(1,3)	(0,3)	2457.5	0.7	2733.7	0.7	3415.6	0.7
(1,4)	(0,4)	2453.0	0.6	2727.2	0.8	3402.8	0.7
(1,5)	(0,5)	2447.3	0.6	2719.2	0.8		
(1,6)	(0,6)	2440.5	0.5	2709.8	0.7		
(1,7)	(0,7)	2432.5	0.5	2698.5	0.9		
(1,8)	(0,8)	2423.5	0.4	2686.3	0.6		
(1,9)	(0,9)	2413.2	0.6				
(1,10)	(0,10)	2402.2	0.4				
(1,1)	(0,2)					3273.140	0.801
(1,0)	(0,1)					3355.355	0.788
(1,1)	(0,0)					3511.020	0.812
(1,2)	(0,1)					3583.530	0.830
(1,3)	(0,2)					3651.870	0.863
(1,4)	(0,3)					3715.630	0.898
(1,5)	(0,4)					3774.450	0.918

Modifications were made to the matrix element calculation part of the code by Jonsell (see reference [117]) to include the electronic overlap $S_n(R)$ and calculation of the Bessel function $j_J(KR)$ and therefore to calculate probabilities $P_{nvJ}(K)$. In this work, as in [117], the electronic overlap of reference [111] was used. To calculate K, equation (2.6), and hence the Bessel function, the maximum (endpoint) energy of the β electron, 18.6 keV, was used. As higher states of $^3HeT^+$ become accessible, the endpoint energy and hence K will decrease. However, it has been noted by Jeziorski *et al.* [112] that the effect is small for changes to E_β of the order of 100 eV.

Using the input described above in the LEVEL program, the energies and radial wavefunctions of all the rovibrational and quasibound states of $^3HeT^+$ and the ground ($v = 0$, $J = 0$) state of T_2, and the discrete probabilities that the $^3HeT^+$ molecules will be left in any of its bound or quasibound states were obtained. A total of 300 bound states and 47 quasibound states were found, their energies and probabilities are given in tables 5.5 and 5.6. For the quasibound states, widths and lifetimes calculated by the LEVEL program, are given.

5.1.2 Continuous probability density distribution of the nuclear motion continuum

In chapter 2 an expression was given for the probability per unit energy that the $^3HeT^+$ molecule dissociates via the n^{th} electronic state and that the dissociation products are in a state with energy E and angular momentum J. For the case where the initial T_2 molecule is in its ground electronic and rovibrational state and $^3HeT^+$ in the electronic ground state n=1, this equation becomes:

$$P_{1J}(E) = (2J+1)\left|\int S_1(R) j_J(KR) f^f_{1J}(R|E) f^i_{100}(R) dR\right|^2 . \qquad (5.5)$$

The radial wavefunctions of the continuum states of $^3HeT^+$, $f^f_{1J}(R|E)$, were calculated at chosen energy steps using the BCONT program by Le Roy [121] discussed in chapter 3. Modifications similar to those applied to the LEVEL program were made to the BCONT program by Jonsell, to include the electronic overlap and Bessel function and therefore to determine the probability densities, $P_{1J}(E)$.

Using the same electronic potentials for $^3HeT^+$ and T_2, electronic overlap $S_n(R)$, and β electron energy $E_\beta = 18.6$ keV, as before, the probability density distributions for each value of angular momentum J in the nuclear motion continuum at chosen energy steps was produced.

Table 5.5: Energies and widths, in E_h, of the quasibound bound states of the $^3HeT^+$ ground electronic state. Also given are probabilities, in %, that $^3HeT^+$ will be left in each state after the β-decay of T_2 in the $J_i = 0$ state. The last column gives the program used to give the probability distribution for a particular resonance.

(v, J)	Energy	Probability	Width	Program
(0,33)	1.910063	0.016733	0.10625E-47	LEVEL
(0,34)	1.991289	0.006559	0.59294E-20	LEVEL
(0,35)	2.070840	0.002311	0.45308E-12	LEVEL
(0,36)	2.148150	0.000722	0.13529E-07	LEVEL
(0,37)	2.222360	0.000193	0.11941E-04	BCONT
(0,38)	2.291661	0.000039	0.93654E-03	BCONT
(1,32)	1.960592	0.046456	0.41081E-21	LEVEL
(1,33)	2.032846	0.019701	0.99710E-12	LEVEL
(1,34)	2.102709	0.007504	0.60423E-07	LEVEL
(1,35)	2.168987	0.002453	0.55421E-04	BCONT
(1,36)	2.229113	0.000613	0.29042E-02	BCONT
(2,30)	1.937138	0.138729	0.61557E-23	LEVEL
(2,31)	2.002122	0.068542	0.15943E-11	LEVEL
(2,32)	2.064622	0.030793	0.18971E-06	BCONT
(2,33)	2.123112	0.011830	0.16293E-03	BCONT
(2,34)	2.174620	0.003825	0.54583E-02	BCONT
(3,28)	1.920229	0.251671	0.20831E-25	LEVEL
(3,29)	1.977962	0.139369	0.30187E-11	LEVEL
(3,30)	2.033146	0.070835	0.60819E-06	BCONT
(3,31)	2.083900	0.030363	0.41172E-03	BCONT
(4,26)	1.909065	0.341603	0.14553E-28	LEVEL
(4,27)	1.959569	0.204295	0.94597E-11	LEVEL
(4,28)	2.007459	0.111889	0.23444E-05	BCONT
(4,29)	2.050486	0.050318	0.97402E-03	BCONT
(5,24)	1.902731	0.395636	0.49712E-32	LEVEL
(5,25)	1.946045	0.252255	0.65155E-10	LEVEL
(5,26)	1.986653	0.142652	0.11593E-04	BCONT
(5,27)	2.022052	0.064879	0.21980E-02	BCONT
(6,22)	1.900194	0.393093	0.45300E-33	LEVEL
(6,23)	1.936394	0.279279	0.11571E-08	LEVEL
(6,24)	1.969707	0.160845	0.69944E-04	BCONT
(7,20)	1.900299	0.271892	0.42725E-27	LEVEL
(7,21)	1.929506	0.246894	0.47528E-07	LEVEL
(7,22)	1.955481	0.149744	0.40979E-03	BCONT
(8,18)	1.901783	0.063935	0.21495E-18	LEVEL
(8,19)	1.924178	0.115713	0.27925E-05	BCONT
(8,20)	1.943067	0.094998	0.17872E-02	BCONT
(9,16)	1.903355	0.007309	0.17044E-11	LEVEL
(9,17)	1.919190	0.004426	0.99182E-04	BCONT
(10,14)	1.903914	0.038416	0.71743E-07	LEVEL
(10,15)	1.913835	0.013867	0.93500E-03	BCONT
(11,12)	1.902947	0.000085	0.29773E-04	BCONT
(12,9)	1.897460	0.001896	0.49574E-21	LEVEL
(12,10)	1.901038	0.004332	0.35672E-03	BCONT
(13,7)	1.897727	0.002419	0.37565E-07	LEVEL
(14,5)	1.897593	0.000249	0.60370E-05	BCONT
(15,3)	1.897472	0.000004	0.27283E-04	BCONT

Table 5.6: Energies, in E_h, of the bound states of the $^3HeT^+$ ground electronic state. Also given are the probabilities, in %, that $^3HeT^+$ will be left in each state after the β-decay of T_2 in the $J_i = 0$ state.

(v, J)	Energy	Probability	(v, J)	Energy	Probability	(v, J)	Energy	Probability
(0,0)	0.000000	0.000256	(0,1)	0.004489	0.000000	(0,2)	0.013453	0.001326
(0,3)	0.026865	0.000087	(0,4)	0.044684	0.002252	(0,5)	0.066855	0.001101
(0,6)	0.093311	0.001837	(0,7)	0.123973	0.004631	(0,8)	0.158748	0.000022
(0,9)	0.197532	0.007612	(0,10)	0.240212	0.005119	(0,11)	0.286661	0.001356
(0,12)	0.336745	0.015904	(0,13)	0.390317	0.009826	(0,14)	0.447226	0.001042
(0,15)	0.507310	0.026504	(0,16)	0.570399	0.034441	(0,17)	0.636319	0.005214
(0,18)	0.704886	0.013269	(0,19)	0.775912	0.073863	(0,20)	0.849203	0.098013
(0,21)	0.924561	0.045417	(0,22)	1.001781	0.000024	(0,23)	1.080654	0.060167
(0,24)	1.160967	0.221084	(0,25)	1.242501	0.389116	(0,26)	1.325032	0.475027
(0,27)	1.408329	0.454863	(0,28)	1.492154	0.362316	(0,29)	1.576260	0.248244
(0,30)	1.660389	0.149402	(0,31)	1.744267	0.080063	(0,32)	1.827600	0.038533
(1,0)	0.271315	0.000305	(1,1)	0.275541	0.002453	(1,2)	0.283980	0.002325
(1,3)	0.296605	0.004134	(1,4)	0.313375	0.008060	(1,5)	0.334238	0.001847
(1,6)	0.359127	0.018553	(1,7)	0.387963	0.001140	(1,8)	0.420656	0.019791
(1,9)	0.457104	0.024175	(1,10)	0.497194	0.000740	(1,11)	0.540801	0.044918
(1,12)	0.587793	0.038631	(1,13)	0.638025	0.000480	(1,14)	0.691347	0.067317
(1,15)	0.747598	0.101468	(1,16)	0.806608	0.020223	(1,17)	0.868204	0.026854
(1,18)	0.932201	0.177696	(1,19)	0.998411	0.242630	(1,20)	1.066637	0.115750
(1,21)	1.136677	0.000527	(1,22)	1.208323	0.124628	(1,23)	1.281358	0.470442
(1,24)	1.355560	0.829035	(1,25)	1.430698	1.012787	(1,26)	1.506531	0.975994
(1,27)	1.582806	0.789144	(1,28)	1.659256	0.554576	(1,29)	1.735594	0.346287
(1,30)	1.811508	0.194853	(1,31)	1.886644	0.099637			
(2,0)	0.522315	0.000325	(2,1)	0.526278	0.007503	(2,2)	0.534190	0.000629
(2,3)	0.546026	0.019956	(2,4)	0.561744	0.000324	(2,5)	0.581294	0.030119
(2,6)	0.604608	0.014231	(2,7)	0.631611	0.017617	(2,8)	0.662211	0.058135
(2,9)	0.696309	0.001999	(2,10)	0.733791	0.058018	(2,11)	0.774535	0.087718
(2,12)	0.818409	0.002221	(2,13)	0.865268	0.081593	(2,14)	0.914962	0.173526
(2,15)	0.967329	0.055143	(2,16)	1.022201	0.019801	(2,17)	1.079401	0.229519
(2,18)	1.138741	0.354031	(2,19)	1.200029	0.190183	(2,20)	1.263064	0.005511
(2,21)	1.327635	0.129044	(2,22)	1.393523	0.549686	(2,23)	1.460500	0.994701
(2,24)	1.528323	1.224599	(2,25)	1.596739	1.185690	(2,26)	1.665474	0.966708
(2,27)	1.734234	0.690200	(2,28)	1.802691	0.442277	(2,29)	1.870473	0.258348
(3,0)	0.753000	0.003755	(3,1)	0.756698	0.002746	(3,2)	0.764079	0.016428
(3,3)	0.775118	0.013743	(3,4)	0.789776	0.016862	(3,5)	0.808000	0.044765
(3,6)	0.829725	0.001479	(3,7)	0.854874	0.077886	(3,8)	0.883358	0.027882
(3,9)	0.915075	0.033025	(3,10)	0.949915	0.132166	(3,11)	0.987754	0.028322
(3,12)	1.028458	0.049934	(3,13)	1.071883	0.210858	(3,14)	1.117876	0.116520
(3,15)	1.166275	0.002036	(3,16)	1.216906	0.197843	(3,17)	1.269588	0.393460
(3,18)	1.324127	0.259747	(3,19)	1.380324	0.025182	(3,20)	1.437964	0.080150
(3,21)	1.496825	0.461139	(3,22)	1.556667	0.895092	(3,23)	1.617237	1.128436
(3,24)	1.678260	1.101656	(3,25)	1.739436	0.902088	(3,26)	1.800428	0.648464
(3,27)	1.860849	0.421202						
(4,0)	0.963265	0.005409	(4,1)	0.966692	0.001044	(4,2)	0.973534	0.029317
(4,3)	0.983764	0.000000	(4,4)	0.997343	0.053655	(4,5)	1.014218	0.012829
(4,6)	1.034324	0.046509	(4,7)	1.057585	0.079078	(4,8)	1.083909	0.001039
(4,9)	1.113197	0.122568	(4,10)	1.145334	0.090165	(4,11)	1.180197	0.005885
(4,12)	1.217648	0.177587	(4,13)	1.257543	0.186294	(4,14)	1.299724	0.010465
(4,15)	1.344022	0.107989	(4,16)	1.390257	0.351008	(4,17)	1.438238	0.311186
(4,18)	1.487763	0.069261	(4,19)	1.538613	0.023411	(4,20)	1.590557	0.296677
(4,21)	1.643343	0.668787	(4,22)	1.696699	0.890681	(4,23)	1.750323	0.887972
(4,24)	1.803873	0.731471	(4,25)	1.856950	0.525943			

Table 5.6 – Continued from previous page

(v, J)	Energy	Probability	(v, J)	Energy	Probability	(v, J)	Energy	Probability
(5,0)	1.152880	0.002411	(5,1)	1.156031	0.011669	(5,2)	1.162321	0.017177
(5,3)	1.171722	0.015965	(5,4)	1.184195	0.051472	(5,5)	1.199686	0.002093
(5,6)	1.218131	0.090782	(5,7)	1.239450	0.024336	(5,8)	1.263553	0.049600
(5,9)	1.290336	0.139790	(5,10)	1.319684	0.013816	(5,11)	1.351468	0.082383
(5,12)	1.385546	0.212355	(5,13)	1.421770	0.068536	(5,14)	1.459973	0.022003
(5,15)	1.499977	0.237806	(5,16)	1.541590	0.319498	(5,17)	1.584606	0.133870
(5,18)	1.628800	0.000020	(5,19)	1.673928	0.137180	(5,20)	1.719720	0.423160
(5,21)	1.765875	0.630024	(5,22)	1.812050	0.658737	(5,23)	1.857838	0.551628
(6,0)	1.321503	0.000066	(6,1)	1.324368	0.019384	(6,2)	1.330087	0.002120
(6,3)	1.338631	0.039383	(6,4)	1.349959	0.020362	(6,5)	1.364018	0.030798
(6,6)	1.380741	0.077396	(6,7)	1.400045	0.000045	(6,8)	1.421839	0.103634
(6,9)	1.446013	0.080130	(6,10)	1.472448	0.005302	(6,11)	1.501009	0.149868
(6,12)	1.531549	0.141683	(6,13)	1.563904	0.003840	(6,14)	1.597899	0.098390
(6,15)	1.633337	0.260062	(6,16)	1.670005	0.191504	(6,17)	1.707668	0.026488
(6,18)	1.746064	0.031452	(6,19)	1.784896	0.212998	(6,20)	1.823820	0.394325
(6,21)	1.862426	0.452876						
(7,0)	1.468683	0.000786	(7,1)	1.471252	0.016355	(7,2)	1.476374	0.001322
(7,3)	1.484023	0.042400	(7,4)	1.494156	0.001394	(7,5)	1.506717	0.056038
(7,6)	1.521634	0.036811	(7,7)	1.538825	0.018054	(7,8)	1.558189	0.106648
(7,9)	1.579613	0.022852	(7,10)	1.602967	0.040958	(7,11)	1.628108	0.148401
(7,12)	1.654875	0.059632	(7,13)	1.683088	0.008385	(7,14)	1.712548	0.141511
(7,15)	1.743030	0.197807	(7,16)	1.774282	0.083780	(7,17)	1.806016	0.000168
(7,18)	1.837893	0.067784	(7,19)	1.869499	0.199966			
(8,0)	1.593876	0.002444	(8,1)	1.596130	0.008862	(8,2)	1.600625	0.008171
(8,3)	1.607329	0.029430	(8,4)	1.616199	0.002215	(8,5)	1.627174	0.056251
(8,6)	1.640180	0.008994	(8,7)	1.655125	0.040593	(8,8)	1.671902	0.075102
(8,9)	1.690388	0.001246	(8,10)	1.710439	0.066475	(8,11)	1.731897	0.105631
(8,12)	1.754577	0.015135	(8,13)	1.778270	0.030378	(8,14)	1.802738	0.130415
(8,15)	1.827702	0.119287	(8,16)	1.852830	0.028160	(8,17)	1.877708	0.004168
(9,0)	1.696515	0.003162	(9,1)	1.698436	0.003278	(9,2)	1.702262	0.012706
(9,3)	1.707962	0.015162	(9,4)	1.715487	0.009128	(9,5)	1.724770	0.041179
(9,6)	1.735731	0.000361	(9,7)	1.748269	0.046430	(9,8)	1.762263	0.041426
(9,9)	1.777573	0.001576	(9,10)	1.794038	0.065305	(9,11)	1.811465	0.060815
(9,12)	1.829634	0.001585	(9,13)	1.848280	0.036991	(9,14)	1.867082	0.089043
(9,15)	1.885631	0.058375						
(10,0)	1.776205	0.002803	(10,1)	1.777771	0.000791	(10,2)	1.780885	0.012359
(10,3)	1.785511	0.006256	(10,4)	1.791596	0.012305	(10,5)	1.799066	0.024711
(10,6)	1.807828	0.000647	(10,7)	1.817767	0.037808	(10,8)	1.828743	0.019318
(10,9)	1.840591	0.005174	(10,10)	1.853112	0.046910	(10,11)	1.866063	0.029486
(10,12)	1.879143	0.000003	(10,13)	1.891958	0.024898			
(11,0)	1.833071	0.001951	(11,1)	1.834261	0.000100	(11,2)	1.836623	0.009059
(11,3)	1.840115	0.002202	(11,4)	1.844677	0.010478	(11,5)	1.850225	0.012786
(11,6)	1.856650	0.001698	(11,7)	1.863819	0.023634	(11,8)	1.871563	0.007856
(11,9)	1.879675	0.004838	(11,10)	1.887891	0.023808	(11,11)	1.895853	0.010576
(12,0)	1.868641	0.001098	(12,1)	1.869457	0.000002	(12,2)	1.871066	0.005202
(12,3)	1.873426	0.000708	(12,4)	1.876468	0.006305	(12,5)	1.880099	0.005631
(12,6)	1.884199	0.001347	(12,7)	1.888611	0.010731	(12,8)	1.893130	0.002555
(13,0)	1.887112	0.000498	(13,1)	1.887601	0.000001	(13,2)	1.888557	0.002329
(13,3)	1.889935	0.000218	(13,4)	1.891664	0.002681	(13,5)	1.893644	0.001927
(13,6)	1.895737	0.000506						
(14,0)	1.894747	0.000175	(14,1)	1.894994	0.000001	(14,2)	1.895466	0.000767
(14,3)	1.896118	0.000057	(14,4)	1.896874	0.000675			
(15,0)	1.897070	0.000038	(15,1)	1.897159	0.000000	(15,2)	1.897313	0.000120
(16,0)	1.897422	0.000002						

As the nuclear motion continuum begins at the asymptote of the electronic potential, the predissociative resonances found by the LEVEL program can also appear in the probability density distribution produced by BCONT, therefore giving us two possible ways in which to account for them. These predissociative resonances, which lie in the energy region 0 - 0.5 eV above the dissociation limit result in volatile behaviour of the probability density distribution. There are usually $1-3$ sharp peaks and several broader peaks associated with each J [112]. The method chosen for describing the probability of a particular resonance depended on its position and shape. For resonances with very narrow widths (where the entire resonance falls within a single 0.01 eV bin) and that can be easily isolated from the background continuum, the discrete result from the LEVEL program was used. For resonances with larger widths (therefore spanning across several 0.01 eV bins) and that could not be isolated from the background continuum, the BCONT program was used instead, using very small energy steps, as small as 10^{-9} eV, to obtain a probability density profile of the resonance. In general, the narrow (long-lived) resonances lie close to the dissociation limit while the broader (short-lived) ones lie marginally below the barrier maxima. Below is an example for each case.

Figure 5.2 shows the probability density distribution of the isolated resonance (v, J) = (2,32) with a width of 0.2×10^{-6} eV. The black curve is the probability density distribution of the resonance obtained using the BCONT program. The green line shows the energy position of the resonance given by the LEVEL program. The red curve is a Lorentzian profile of the resonance obtained by using the discrete result from LEVEL and the equation:

$$P_{1J}(E) = \frac{\Gamma^2/4}{(E - E^{res}_{1vJ})^2 + \Gamma^2/4} \times P_{1J}(E^{res}_{1vJ}), \tag{5.6}$$

where

$$\Gamma = \frac{2}{\pi} \frac{P^{res}_{1vJ}}{P_{1J}(E^{res}_{1vJ})}, \tag{5.7}$$

is the resonance width, E^{res}_{1vJ} is the energy at which $P_{1J}(E)$ reaches the maximum, $P_{1J}(E^{res}_{1vJ})$ is the probability density at E^{res}_{1vJ}, $P_{1J}(E)$ is the probability density at energy E and P^{res}_{1vJ} is the total probability of the resonance. Γ, E^{res}_{1vJ} and P^{res}_{1vJ} are given by the LEVEL program. Equation (5.6) has been obtained from the Breit-Wigner formula for resonant cross-sections, adjusted to calculate the probability density distribution of the resonance. By comparing the Lorentzian profile of the LEVEL result with the BCONT result it can be seen that the results are in very close agreement. The entire resonance

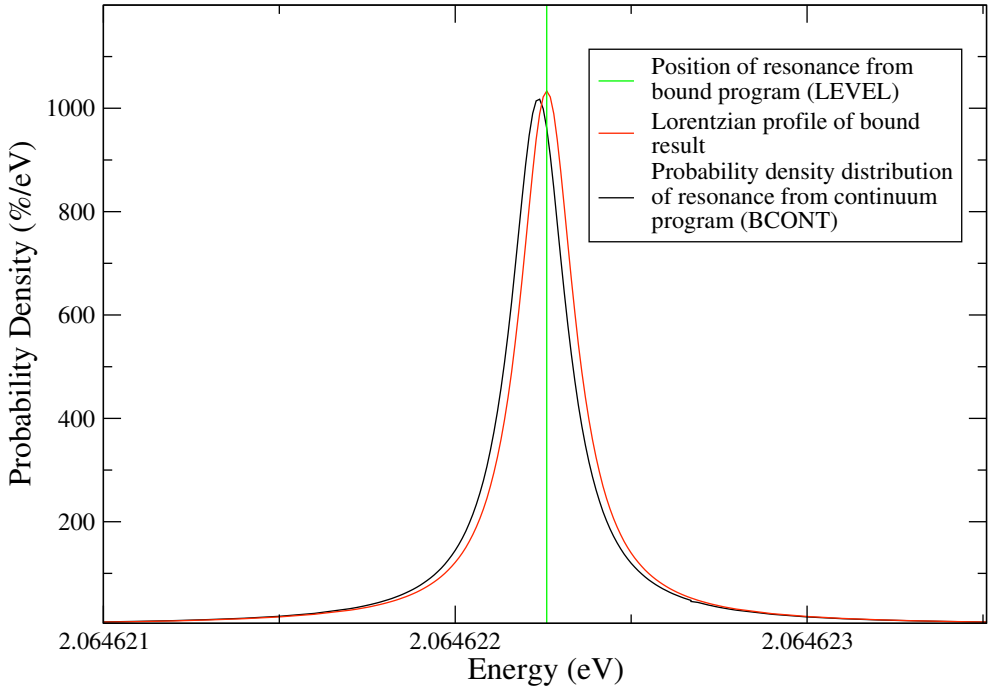

Figure 5.2: Example of a narrow, isolated resonance.

is contained within one of the 0.01 eV bins, therefore the resonance can be treated as a 'bound' state and the LEVEL result used.

Figure 5.3 shows the probability density distribution of the non-isolated resonance $(v, J) = (2,34)$ with a width of 0.5×10^{-2} eV. The black curve is the probability density distribution from BCONT and the red line is the energy position of the resonance from the LEVEL program. This resonance is not easily separable from the background continuum, witness the asymmetric profile. It also spans across several energy bins. It is not accurate enough in this case to use the result from the LEVEL program.

The discrete results from the LEVEL program were used for 24 resonances and the density distribution from the BCONT program for the remaining 23 resonances.

For the region beyond 0.5 eV above the dissociation limit, where no predissociative resonances are present, an energy step of 0.001 eV is sufficient for the determination of the radial functions using BCONT.

5.1.3 Total ground state distribution

The previous final state probability distribution [106] was presented as a finite number of discrete transition probabilities by dividing the spectrum into small energy bins varying in size from 0.1 eV, for the ground state of $^3HeT^+$, to 1.0 eV, for the electronically

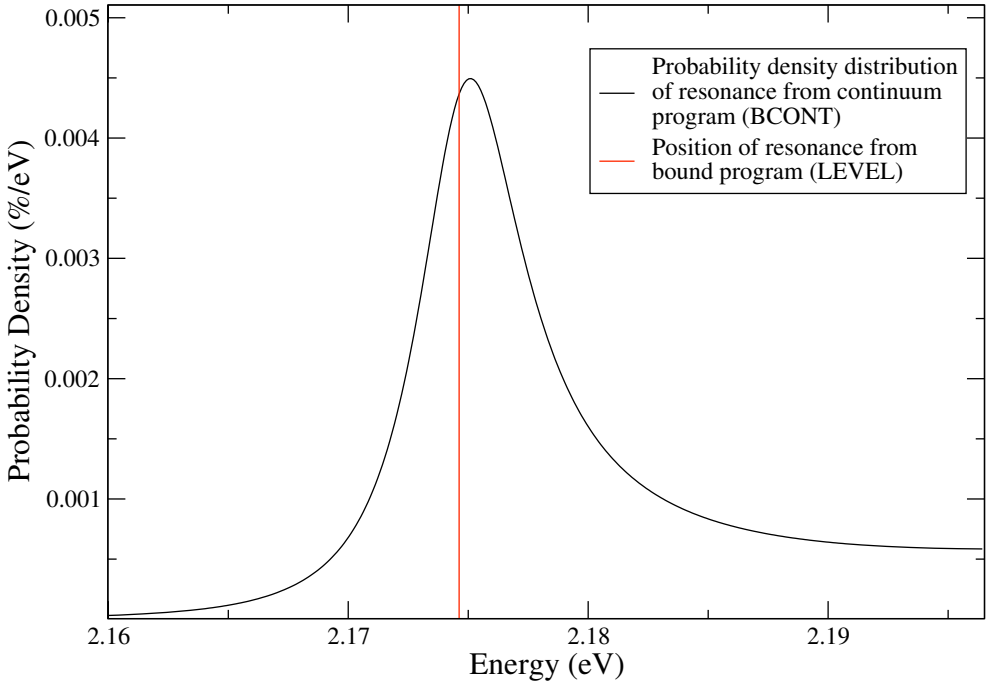

Figure 5.3: Example of a wide non-isolated resonance.

excited states of $^3HeT^+$. This approach is the best for analysis of the experiments and was also used here. However due to the improved sensitivity of the experiment, 0.1 eV bins were no longer sufficient and so bins of 0.01 eV were used throughout. The energy of the ground rovibrational state of $^3HeT^+$ was set as the energy zero, thus giving a dissociation energy for the ground electronic state of 1.89742698 eV. For convenience, the 0.01 eV bins were relative to the dissociation limit, therefore the first energy bin is from 0.0 - 0.00742698 eV.

As probabilities are obtained for the bound part and probability densities for the nuclear motion continuum, the energy binning was performed separately for the two regions. For the bound levels the energy binning was straightforward. The probabilities within a bin were summed and a mean excitation energy calculated. For the nuclear motion continuum, energy binning was performed separately for each J by using the trapezoidal rule, and then combined. For the energies bins where the two regions overlap (1.89742698 - 2.29742698 eV) the probabilities of the two regions were summed together and new mean excitation energies calculated.

The discretized final state probability distribution for the electronic ground state (black lines, left-hand y-axis) is shown in Figure 5.4 (top left). The probability distribution of the ground state covers the energy range up to 6 eV and is the only open channel

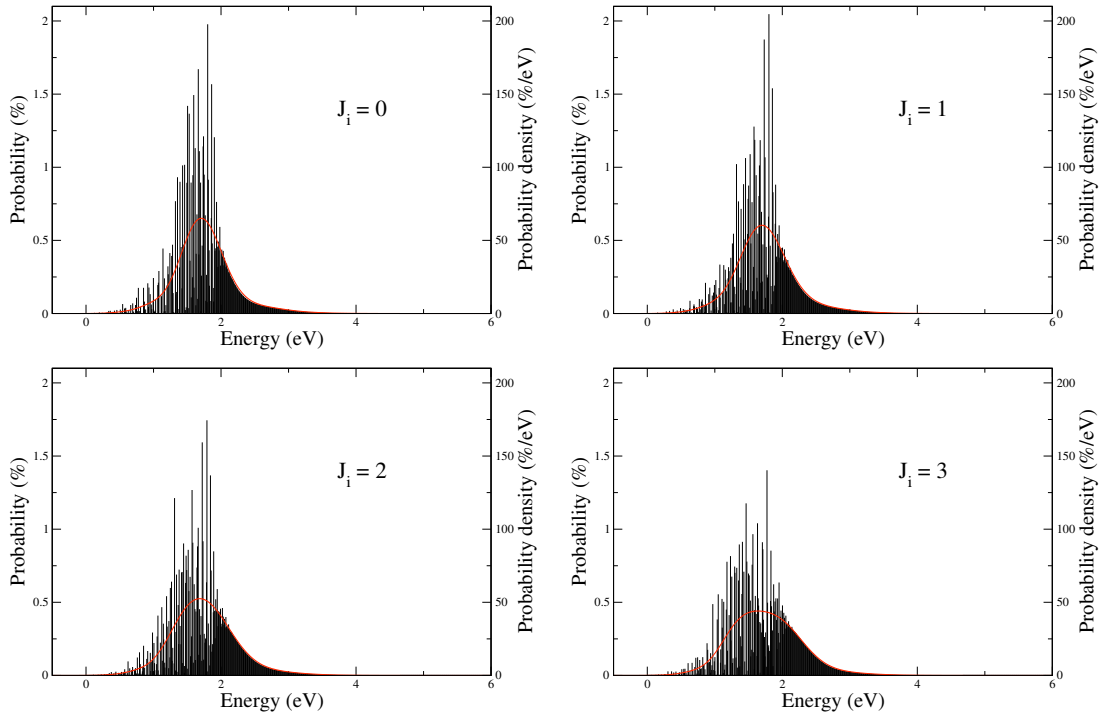

Figure 5.4: The final state probability distribution of the electronic ground state of $^3HeT^+$ for different initial rotational states, $J_i = 0$, 1, 2 and 3, of T_2. The black lines, which correspond with the left-hand y-axis, is the binned (0.01 eV bins) final state probability distribution. The red curve, which corresponds with the right-hand y-axis, is the Gaussian convolution of the binned results in terms of probability density.

up to $\approx$ 20 eV. It accounts for 57.41% of the total probability. To illustrate the shape of the distribution for easier comparison with other results presented in this chapter, a Gaussian convolution of the binned results was performed using a standard deviation of 0.1 eV. The Gaussian convolution is given by the red curve and the right-hand y-axis.

5.2 Rotational excitation of T_2

The KATRIN experiment will be performed with the gaseous T_2 source at a temperature of about 30 K, therefore the majority of the T_2 molecules will be thermally excited. A Boltzmann distribution was used to estimate the rotational state populations of T_2 at this temperature for a thermal source. The T_2 molecules will be mainly distributed in the first four rotational states of the electronic and vibrational ground state, see table 5.7. In fact at 30 K more T_2 molecules will be in the $J_i = 1$ state than $J_i = 0$. Past calculations of the final state distribution focused mainly on $J_i = 0$ [112, 113, 117].

Table 5.7: Rotational state populations for T_2 at a thermal temperature of 30 K. The energies of each state are given where the energy zero is at the asymptote of the potential

J_i	Energy (eV)	Population (%)
0	-4.59093879	42.856
1	-4.58597113	56.458
2	-4.57605227	0.676
3	-4.56121125	0.010

Calculations of transitions with $J_i = 1$ were performed [117], but only for the ground state of $^3HeT^+$. In this work separate probability distributions for the ground state and the first five electronically excited states of $^3HeT^+$, due to the β-decay of T_2 in initial states of $J_i = 1$, 2 and 3 have been calculated. In this section we focus on the ground state of $^3HeT^+$, excited electronic states are discussed in the next section.

In chapter 2, equations for the probability that the $^3HeT^+$ molecule will be left in a bound rovibrational state (v, J) of electronic state n were derived for the case when the T_2 molecule is in the state $J_i = 1$, 2 and 3. Similar equations are obtained for the probability density of the nuclear motion continuum. Using these equations, the probabilities of the bound states and probability densities of the nuclear motion continuum of the $^3HeT^+$ ground state were calculated for each J_i using the same method described in the previous section.

For each initial excited J_i state of T_2, the LEVEL and BCONT programs were run separately for each integral term, i.e. twice for $J = 1$, three times for $J = 2$, etc., see equations (2.31, 2.33, 2.35), and the probabilities/probability densities summed.

As the T_2 molecules are rotationally excited they have more energy than the T_2 molecules in the $J_i = 0$ state. This extra energy is then available to the β electron and therefore the β-decay endpoint energy increases with the rotational excitation of the T_2 molecules. For analysis by the experiment it was necessary to make the endpoint energy consistent. For each final state distribution, before the energy binning was performed, the excitation energies E_f were shifted by the respective rotational excitation energy of the T_2 molecule, in order to make the endpoint energies equal.

The discrete final state probability distribution (black lines) and corresponding Gaussian distributions (red curve) for the electronic ground state of $^3HeT^+$ due to the β-decay of T_2 in initial states of $J_i = 1$, 2 and 3 are shown in figure 5.4. For comparison, figure

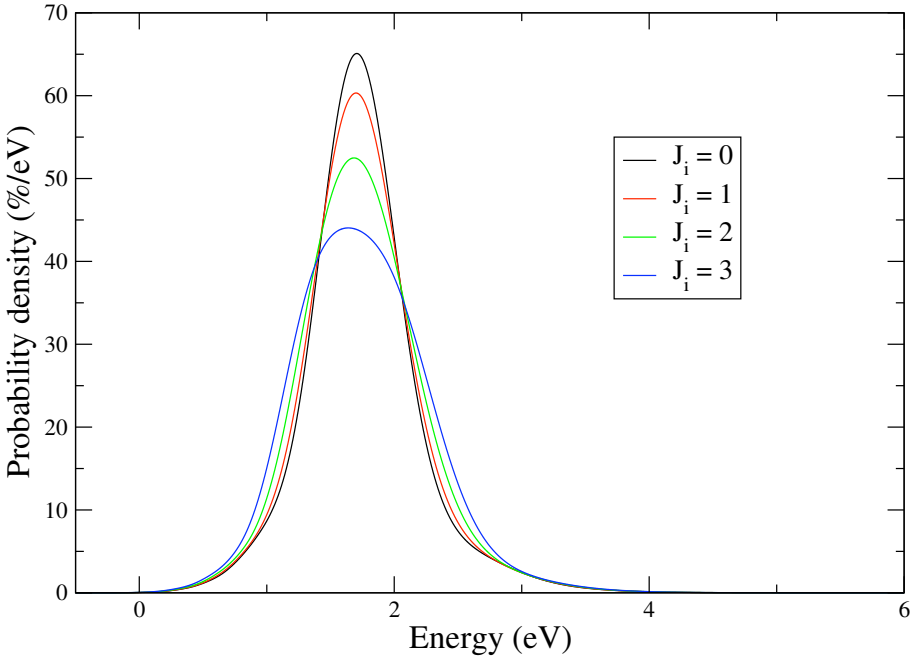

Figure 5.5: The Gaussian distributions for the electronic ground state of $^3HeT^+$ for initial J_i = 0, 1, 2 and 3. The black, red, green and blue curves are for J_i = 0, 1, 2 and 3 respectively.

5.5 shows the Gaussian distributions for the different initial states of T_2.

5.3 Excited electronic states of $^3HeT^+$

The first five electronically excited states of $^3HeT^+$ are purely dissociative. Therefore there are no bound states and only the BCONT program is required to calculate the probability density distribution for each electronic state. The same procedure was used as for the ground state. The Born-Oppenheimer energies of the excited states of $^3HeT^+$ and the electronic overlaps $S_n(R)$ (n = 2 - 6) were taken from [117]. No adiabatic corrections were included for the potentials. The n = 2, 4 and 5 states dissociate to He^+ + T, and the n = 3 and 6 states dissociate to He + T^+ [117]. The relevant dissociation reduced mass was used instead of the effective reduced mass.

The probability density distribution was obtained for each electronic state. The combined probability density distribution for the n = 2 - 6 states is shown in figure 5.6 for each of the initial states of T_2 considered.

The probability was obtained and binned as before in energy bins of 0.01 eV. Table 5.8 shows the total probabilities and the energy range covered by each electronic state of $^3HeT^+$ resulting from the β-decay of T_2 in rotational states J_i = 0, 1, 2 and 3.

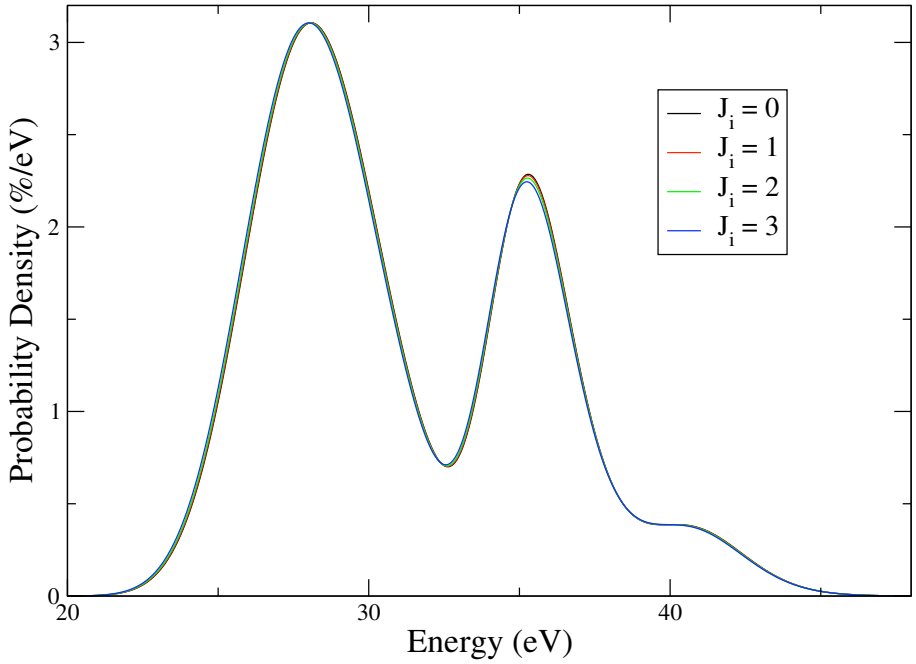

Figure 5.6: The final state probability density distribution for the first five electronically excited states of $^3HeT^+$ for different initial rotational states, $J_i = 0$, 1, 2 and 3, of T_2.

Table 5.8: Total probabilities and energy range for the first six electronic states of $^3HeT^+$ resulting from the β-decay of T_2 in rotational states $J_i = 0$, 1, 2 and 3.

n	P_n ($J_i = 0$)	P_n ($J_i = 1$)	P_n ($J_i = 2$)	P_n ($J_i = 3$)	Energy range
1	57.412	57.394	57.356	57.299	0.00 – 6.07
2	17.359	17.373	17.401	17.443	19.65 – 40.84
3	7.761	7.758	7.752	7.743	30.41 – 44.38
4	0.782	0.781	0.781	0.779	33.88 – 48.06
5	0.011	0.011	0.010	0.010	36.30 – 44.95
6	0.918	0.917	0.917	0.915	36.18 – 49.59
	84.243	84.234	84.217	84.189	

5.4 Isotopomers - ^{3}HeH$^+$ and ^{3}HeD$^+$

In previous tritium β-decay experiments the source has had a significant contamination of HT molecules. In references [106, 117], an elaborate final state distribution of ^{3}HeH$^+$ was calculated. This distribution has been recalculated here for HT in states $J_i = 0$ and 1. However in the future KATRIN experiment the main contamination is expected to come from DT molecules. Therefore the probability of ^{3}HeD$^+$ has been calculated for DT in initial states $J_i = 0$ and 1. The distributions of ^{3}HeD$^+$have not been calculated previously.

The ground state electronic potentials for ^{3}HeD$^+$, DT, ^{3}HeH$^+$ and HT were obtained in the same way as for ^{3}HeT$^+$ and T_2. The same Born-Oppenheimer potentials were used, and the mass dependent adiabatic corrections were scaled accordingly (using m_D = 3670.482 and m_H = 1836.152). These potentials are given in columns 4 - 7 of table 5.1. For the electronically excited states of ^{3}HeD$^+$ and ^{3}HeH$^+$ the same potentials used for ^{3}HeT$^+$ were employed as no mass dependent corrections had been applied to them. Effective reduced masses were used for the ground electronic state potentials of ^{3}HeD$^+$ and ^{3}HeH$^+$, dissociation reduced masses for the electronically excited states and nuclear reduced masses for DT and HT. The same electronic overlaps, $S_n(R)$, were used as for T_2.

As for the rotational excitation of the T_2 molecules, the energies of the probability distribution must be shifted in order to make the endpoint energies the same. For DT (HT) molecules in the $J_i = 0$ state, there are three energy shifts that need to be taken into account.

1. **The difference in the ground rovibrational state energies of ^{3}HeT$^+$ and ^{3}HeD$^+$ (^{3}HeH$^+$)** The ground state energies of ^{3}HeD$^+$ and ^{3}HeH$^+$ are higher in energy than that of ^{3}HeT$^+$. This leaves less energy available for the β electron and so reduces the endpoint energy. Therefore this energy must be **added** to the distribution energies.

2. **The difference in the ground rovibrational state energies of T_2 and DT (HT)** The ground state energies of DT and HT lie higher than that of T_2, therefore providing extra energy for the β electron. This increases the endpoint energy and so this energy difference must be **subtracted** from the distribution energies.

3. **The difference in the (centre of mass motion) recoil energy of the ^{3}HeT$^+$**

and ^{3}HeD$^+$ (^{3}HeH$^+$) molecules $E_{\rm rec}^{^3{\rm HeH}^+} > E_{\rm rec}^{^3{\rm HeD}^+} > E_{\rm rec}^{^3{\rm HeT}^+}$, therefore the endpoint energies decrease and so these differences must be **added** to the distribution energies.

For rotationally excited DT (HT) the rotational excitation energy must also be taken into account as for T_2. All energy shifts were performed before energy binning was performed.

The final state distributions were obtained for the first six electronic states of ^{3}HeD$^+$ and ^{3}HeH$^+$ using the same method as for ^{3}HeT$^+$.

For the electronic ground state of ^{3}HeD$^+$ (^{3}HeH$^+$), a total of 243 (151) bound states and 34 (22) predissociative resonances were found by the LEVEL program. The probability/probability density distributions were binned as before using 0.01 eV bins. The final state distributions of the electronic ground states of ^{3}HeD$^+$ and ^{3}HeH$^+$ due to the β-decay of DT and HT in initial rovibrational states $J_i = 0$ and 1 are shown in figure 5.7. For comparison, the Gaussian distributions are shown in figure 5.8.

Figure 5.9 shows the final state probability density distribution for the first five excited electronic states of ^{3}HeT$^+$, ^{3}HeD$^+$ and ^{3}HeH$^+$ for initial J_i=0.

As will be shown in chapter 5, an uncertainty in the percentage of DT molecules has a significant effect on the reliability of the neutrino mass obtained.

5.5 Sum rules

To check the accuracy of our calculations two sum rules satisfied by P_{nvJ} and $P_{nJ}(E)$, discussed in chapter 2, have been used. The LEVEL and BCONT codes were modified to also calculate these sum rules. Our probability distributions were summed over J and n and compared. For all J, our errors in P_{nJ} were found to be $< 2 \times 10^{-5}\%$ for the electronic ground state ($n = 1$), and $< 1 \times 10^{-4}\%$ for the electronically excited states ($n = 2$ - 6). The error in P_n was found to be $< 1 \times 10^{-4}\%$ for $n = 1$, and $< 7 \times 10^{-4}\%$ for $n > 1$.

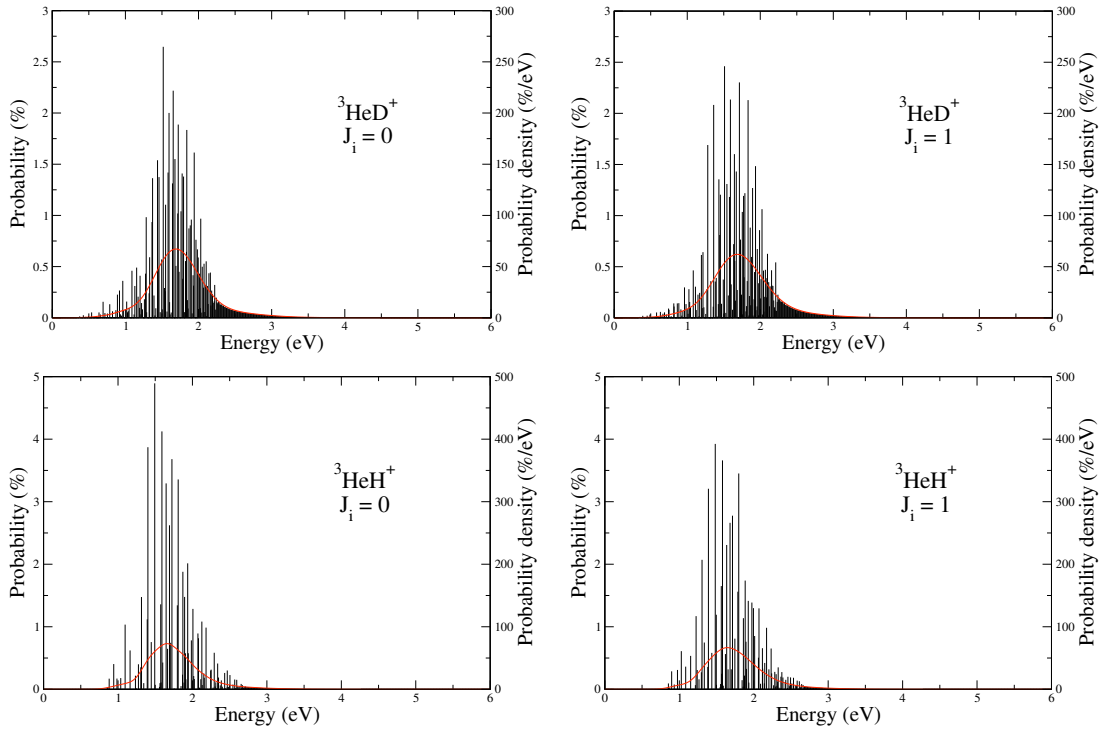

Figure 5.7: The final state probability distributions of the electronic ground states of ^{3}HeD$^+$ and ^{3}HeH$^+$ for the β-decay of DT and HT molecules in initial rovibrational states $J_i = 0$ and 1. The black lines, which correspond with the left-hand y-axis, is the binned (0.01 eV bins) final state probability distribution. The red curve, which corresponds with the right-hand y-axis, is the Gaussian convolution of the binned results in terms of probability density.

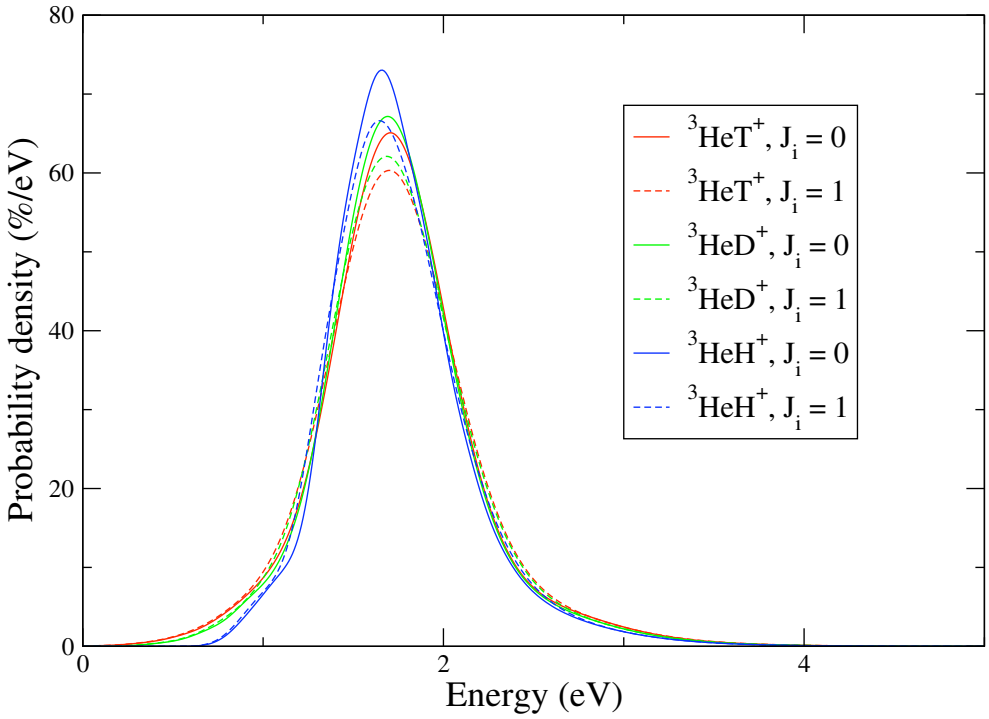

Figure 5.8: The Gaussian distributions for the electronic ground states of ^{3}HeT$^+$, ^{3}HeD$^+$ and ^{3}HeH$^+$ for the β-decay of T_2, DT and HT molecules in initial rovibrational states $J_i = 0$ and 1.

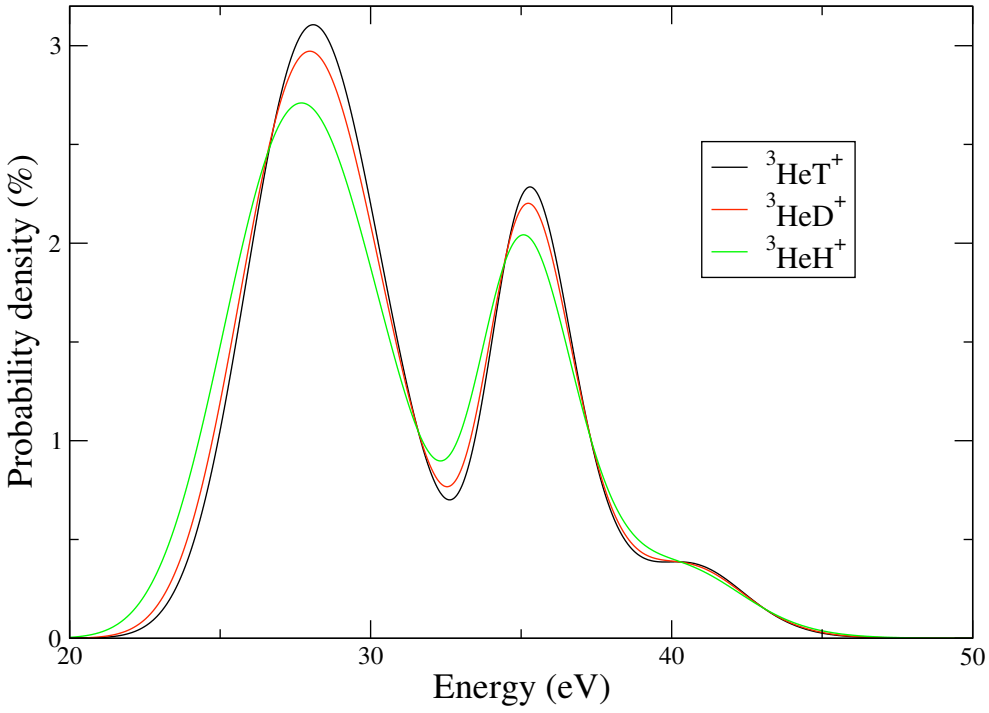

Figure 5.9: The final state probability density distribution for the first five excited electronic states of ^{3}HeT$^+$, ^{3}HeD$^+$ and ^{3}HeH$^+$ for initial J_i=0

Chapter 6

The error budget

In the previous chapter the calculation of the final state distribution of the six lowest lying electronic states of $^3HeT^+$ resulting from the β-decay of T_2, to accommodate the increased sensitivity and requirements of the future neutrino mass experiment, KATRIN, was discussed. Due to impurities in the KATRIN source calculations of the final state distributions of $^3HeD^+$ and $^3HeH^+$ were also performed. The effect of rotational excitation of the parent molecule was also investigated, by explicitly calculating separate final state distributions for the daughter molecule following the β-decay of T_2 in rotational states $J_i = 0$, 1, 2 and 3, and DT/HT in states $J_i = 0$ and 1. Using this data an overall final state distribution for a given source can be obtained by summing the separate calculated final state distributions weighted by the percentage of molecules in that state.

In this chapter, estimates of the error in the value of the neutrino mass deduced from fitting theoretical curves, due to uncertainties in the source temperature, ortho:para ratio of T_2 and the percentage of DT molecules in the source are discussed.

6.1 Determination of the neutrino rest mass and the integral β-decay spectrum

The recorded spectrum obtained by the KATRIN experiment is an *integral* β-decay spectrum. The spectrometer used in the KATRIN experimental set-up acts as an integrating high-energy filter (see chapter 1 for a description of how the spectrometer works). The mass of the neutrino is obtained by fitting the experimental spectra to theoretical spectra.

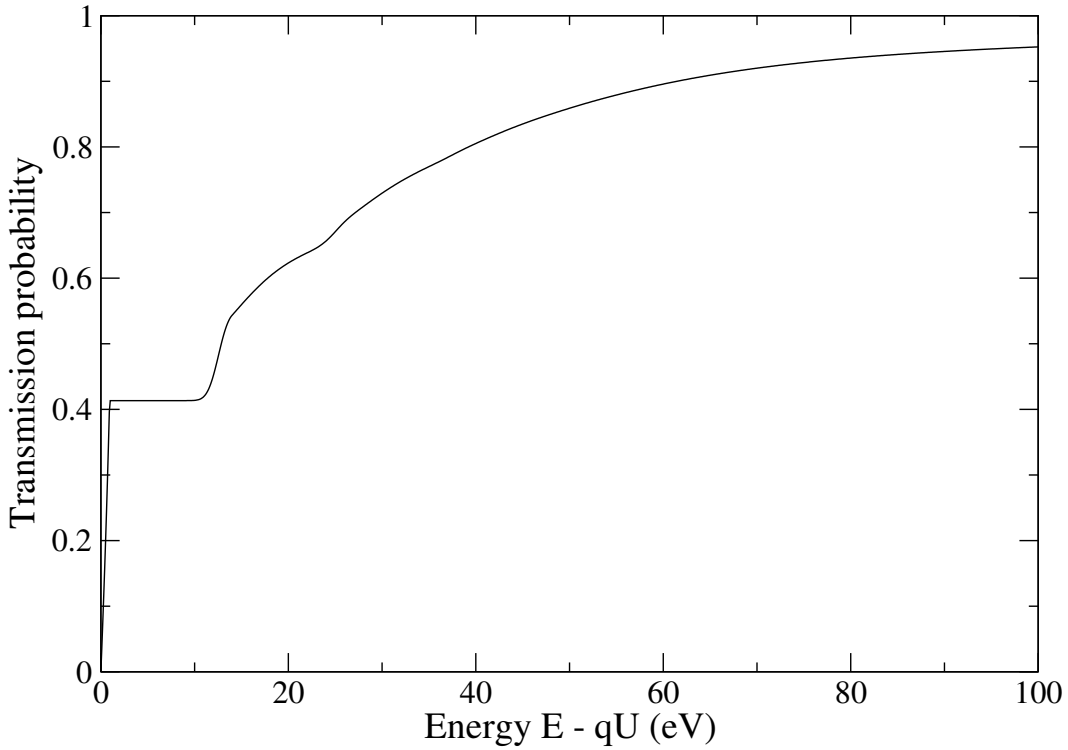

Figure 6.1: Response function of the KATRIN spectrometer for isotropically emitted electrons with fixed energy E as a function of the retarding energy qU.

The theoretical integral β-decay spectrum is given by [98]:

$$N(qU) = N_{\mathrm{tot}} t_U \int_0^{W_0} I(E_e) f_{\mathrm{res}}(E_e, qU)\, dE_e, \tag{6.1}$$

where U is the retarding potential, N_{tot} is the total number of tritium nuclei in the source, t_U is the measuring time at retarding potential U and $I(E_e)$ is the intensity of β electrons with kinetic energy E_e given by equation (2.3). f_{res} is the response function of the KATRIN spectrometer for isotropically emitted electrons [98] and is shown in figure 6.1. q is the charge.

The experiments are not free from systematic and statistical errors, therefore these must also be accounted for in the theoretical spectra as fit parameters. For a complete investigation of the uncertainty effects discussed in this chapter, one would ideally include the effect of all these parameters. However, to obtain an estimate of the error in the neutrino mass caused by uncertainty in the source temperature, ortho:para ratio and isotope contamination, fits have been performed with idealised conditions (no systematic or statistical errors) using only the fit parameters expected from a theoretical point of view.

6.2 Rotational temperature effect - thermal source

The source in the KATRIN experiment is expected to be at a temperature of around 30 K [104]. If the source is thermal, the relative populations of rotational states of the T_2 molecules are dependent on the temperature of the source and are given by a Boltzmann distribution:

$$P_J(T) = \frac{g_s g_J e^{-E_J/kT}}{Q_T}, \tag{6.2}$$

where $P_J(T)$ is the probability that the molecule will be in rotational state J at temperature T, $g_s = (2s+1)$ is the nuclear spin degeneracy factor, $g_J = (2J+1)$ is a rotational degeneracy factor, E_J is the energy of the state with rotational quantum number J with respect to E_0, and k is Boltzmann's constant. Q_T is the rotational partition function for T_2 at low temperature T and is given by:

$$Q(T) = \sum_J g_s g_J e^{-E_J/kT}, \tag{6.3}$$

where we have ignored other terms as they are for high T.

At a temperature of 30 K, the amount of T_2 molecules in states $J_i = 0$, 1, 2 and 3 are 42.856%, 56.458%, 0.676% and 0.01% respectively. The overall final state distribution at a given temperature is obtained by summing the final state distributions for each different initial state J_i, weighted by the percentage of T_2 molecules in that state.

An uncertainty in the temperature of the source could result in an inaccurate overall final state distribution being used in the calculation of the theoretical spectrum, and hence an error in the neutrino mass deduced from fitting the theoretical and experimental spectra.

To determine how accurately the temperature of the source must be known, the effect of uncertainties in the source temperature on the value of the neutrino mass deduced from fitting, have been investigated.

A range of temperatures from 0 to 50 K in steps of 5 K were considered. The distribution of T_2 molecules in each J_i state for each of these temperatures is shown in figure 6.2. For comparison, in figure 6.3, the overall final state distributions of the ground state of $^3HeT^+$ for different source temperatures are shown. The distributions of the excited states from 20 - 30 eV do not vary significantly so are not shown. For these calculations a pure tritium source has been assumed.

The temperature $T = 30$ K was taken as our reference temperature. Using the final state distribution at this temperature, a reference integral β spectrum was produced us-

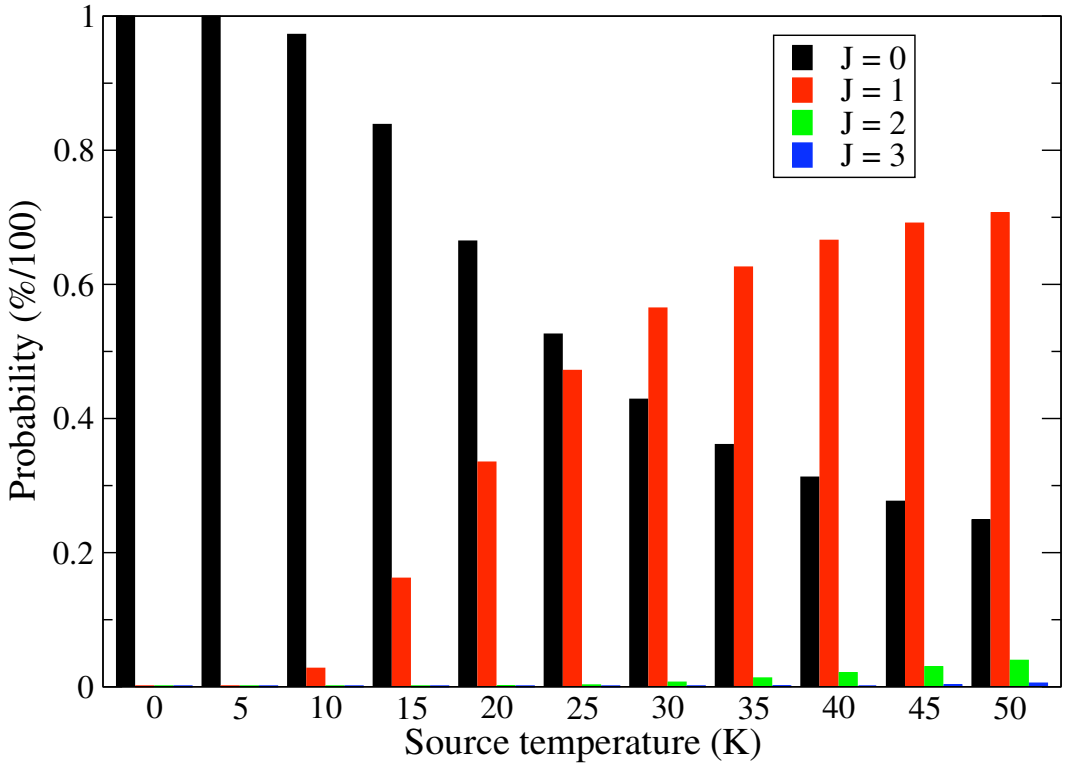

Figure 6.2: Distribution of T_2 molecules in each J state as a function of temperature

ing equation (6.1) and chosen values for the fit parameters A, W_0 and $m^2_{\overline{\nu}_e}$. The endpoint energy, W_0, was fixed at a value of 18.575 keV, and the normalisation constant omitted. Separate calculations were performed for three different values of the neutrino mass, 0.0 eV/c^2, 0.2 eV/c^2 and 0.5 eV/c^2. The theoretical integral β spectra for the other temperatures were fitted to the reference spectra with $m^2_{\overline{\nu}_e}$ as the only free parameter, by using the corresponding final state distributions. A χ^2 fitting was performed using subroutines MRQMIN, MRQCOF, COVSRT and GAUSSJ from Numerical Recipes [171].

For the fitting an energy window with a lower limit of 30 eV below the endpoint was chosen, as this will be the energy interval analysed in the KATRIN experiment. The last 2 eV below the endpoint was not included in the fitting, as it will also be excluded from the fit in the KATRIN experiment as the spectrum here is dominated by the background noise. A statistical distribution for the error in the intensity of β electrons, $\sigma = \sqrt{I}$, was assumed. The mass errors, defined as the absolute difference in $m^2_{\overline{\nu}_e}$, are shown in figure 6.4. These absolute differences in $m^2_{\overline{\nu}_e}$ are very similar for all three values of the neutrino mass squared tested. For a 0.2 eV/c^2 neutrino mass this translates to a $\pm$ 0.25% error in the value of $m_{\overline{\nu}_e}$, as a result of an uncertainty in the source temperature of $\pm$ 5 K.

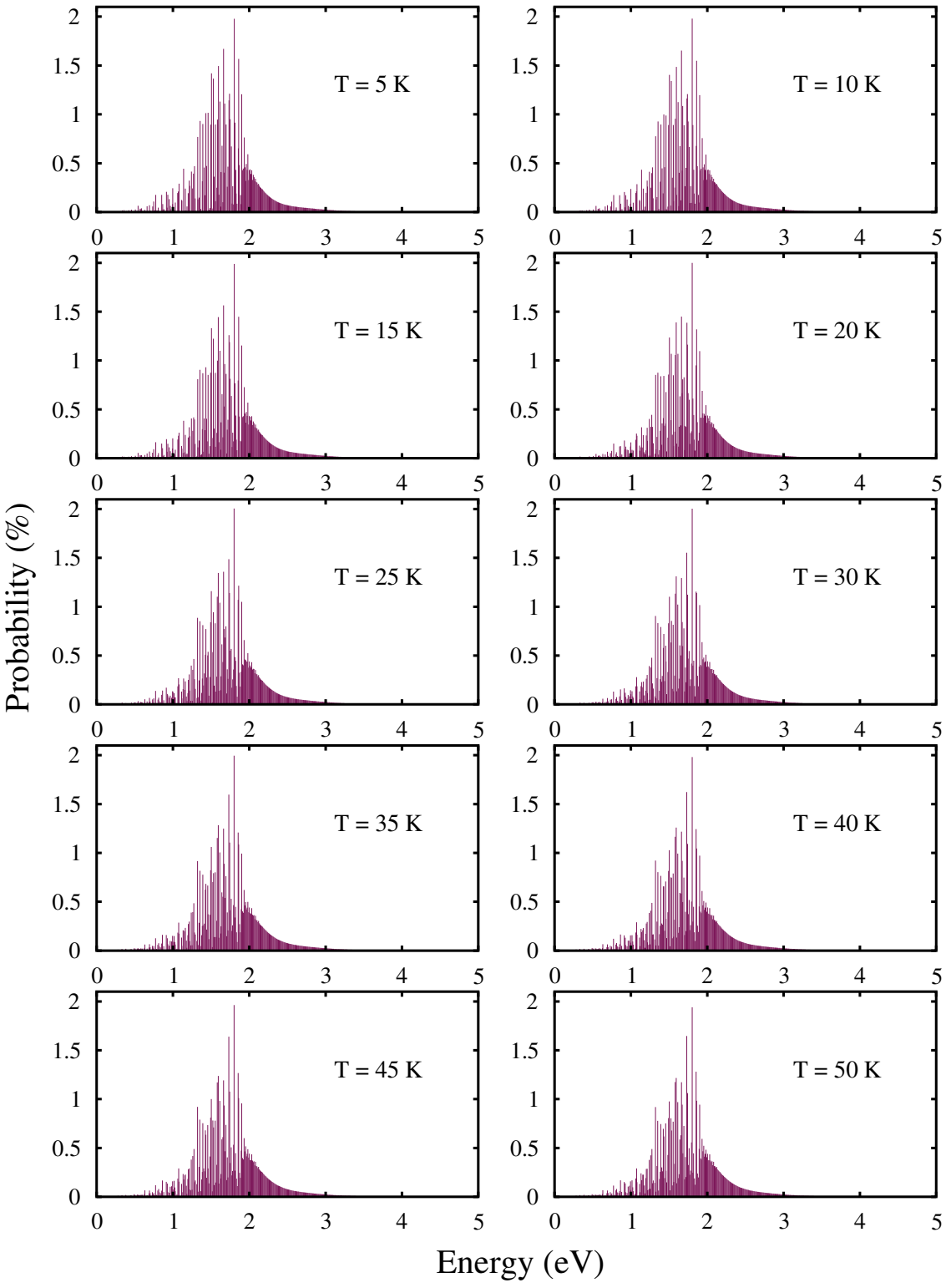

Figure 6.3: Overall final state distributions for a pure T_2 source at different temperatures between 5 - 50 K

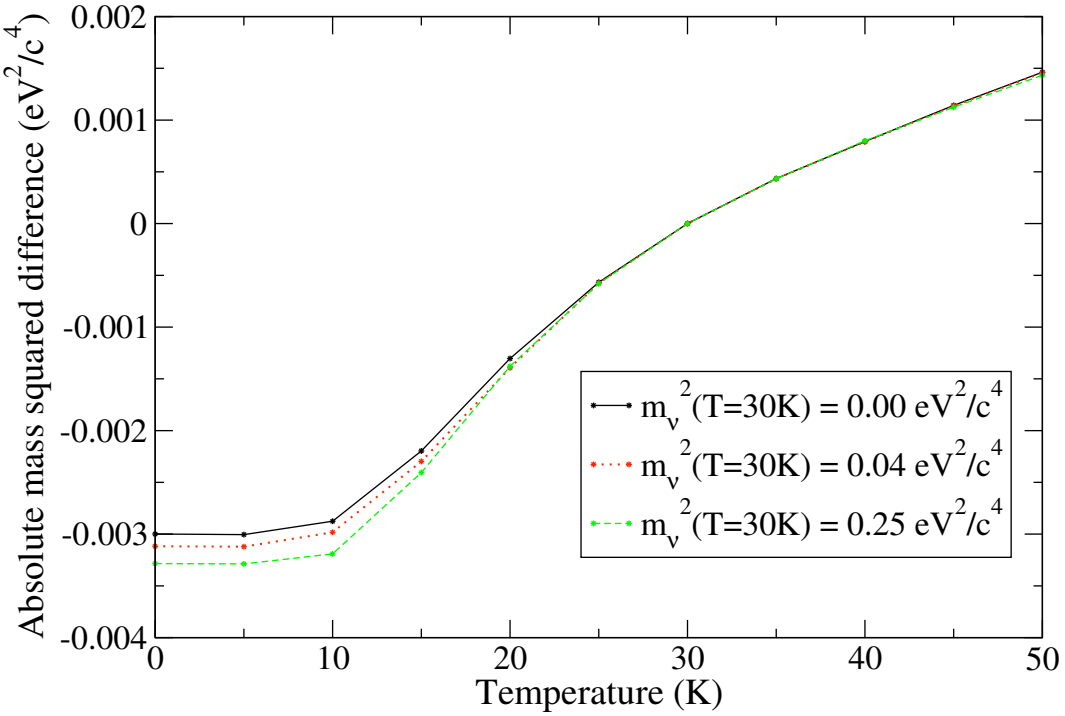

Figure 6.4: Error in the neutrino mass squared deduced from fitting, due to uncertainties in the source temperature (from fitting of β spectra with $W_0 = 18.575$ keV and 100% T_2).

6.3 Ortho:para ratio - non thermal source

In the previous section a thermal source was considered. However if the source is not completely thermalised then the ratio of ortho-T_2 to para-T_2 in the source must be considered.

For homonuclear molecules with non-zero nuclear spin, the selection rule prohibiting interconversion between the symmetric and anti-symmetric states (i.e. transitions between even J states and odd J states are not allowed), although not rigorous, still holds sufficiently strictly that it may take months or years before a molecule goes spontaneously from an even numbered rotational level to an odd numbered level. Therefore if the source is initially at a higher (lower) temperature than 30 K and is then cooled (heated) to 30 K, it may take a long time before the source becomes thermal. In this case the T_2 molecules may be regarded as a mixture of two separate species: para-T_2 (even J) and ortho-T_2 (odd J), and separate partition functions used for each species:

$$Q_p(T) = \sum_{J_{\text{even}}} g_J e^{-E_J/kT}, \tag{6.4a}$$

$$Q_o(T) = \sum_{J_{\text{odd}}} g_J e^{-E_J/kT}, \tag{6.4b}$$

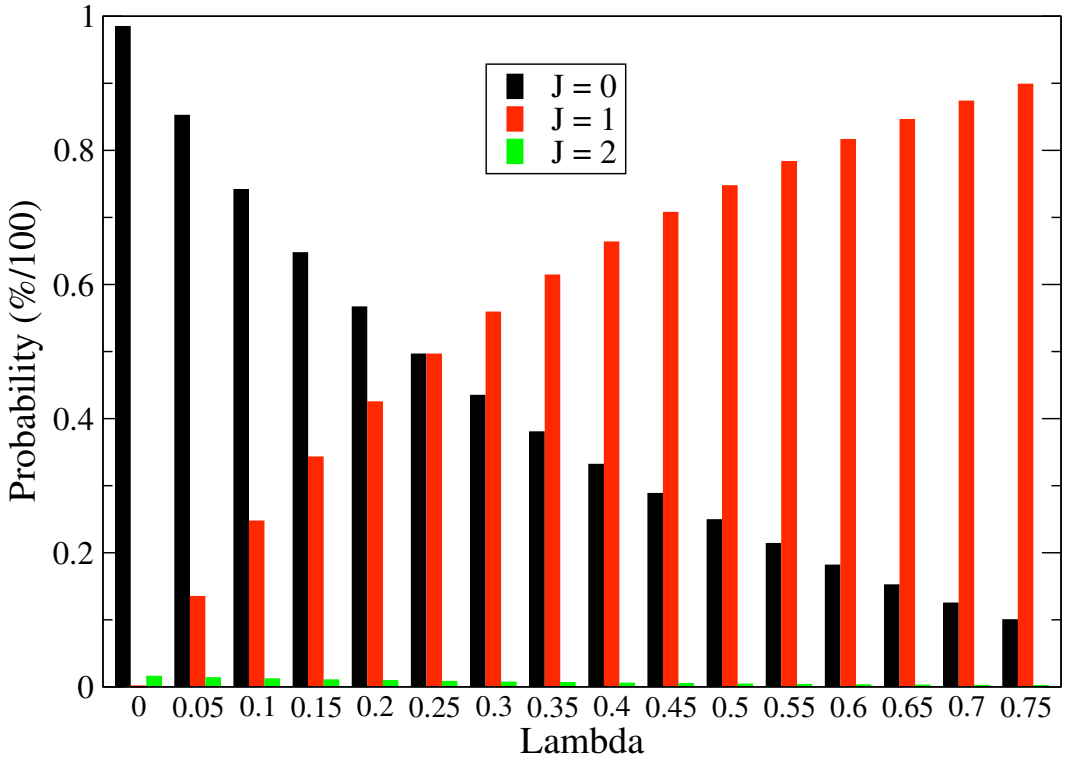

Figure 6.5: Distribution of T_2 molecules in each J state as a function of the ortho:para ratio, λ

where $Q_p(T)$ and $Q_o(T)$ are the partition functions for the para and ortho T_2 at temperature T.

The total partition function is then given by:

$$Q_T = (1-\lambda)Q_p + (\lambda)Q_o \tag{6.5}$$

where λ (which includes the spin degeneracy) defines the ortho:para ratio. For thermalised T_2 at $T = 0$ K, λ is 0 and at high temperatures λ is 3/4. The relative populations are then:

$$P(J_{\text{even}}) = \frac{(1-\lambda)g_J e^{-E_J/kT}}{Q_T}, \tag{6.6a}$$

$$P(J_{\text{odd}}) = \frac{\lambda g_J e^{-E_J/kT}}{Q_T}. \tag{6.6b}$$

Estimates of the error in the deduced neutrino mass due to uncertainties in the ortho:para ratio of the source have been obtained. A range of values of λ varying between 0 and 3/4 in steps of 0.05 were considered. Figure 6.5 shows the distribution of T_2 molecules in each J state for each of value of λ. Again, a pure tritium source has been assumed.

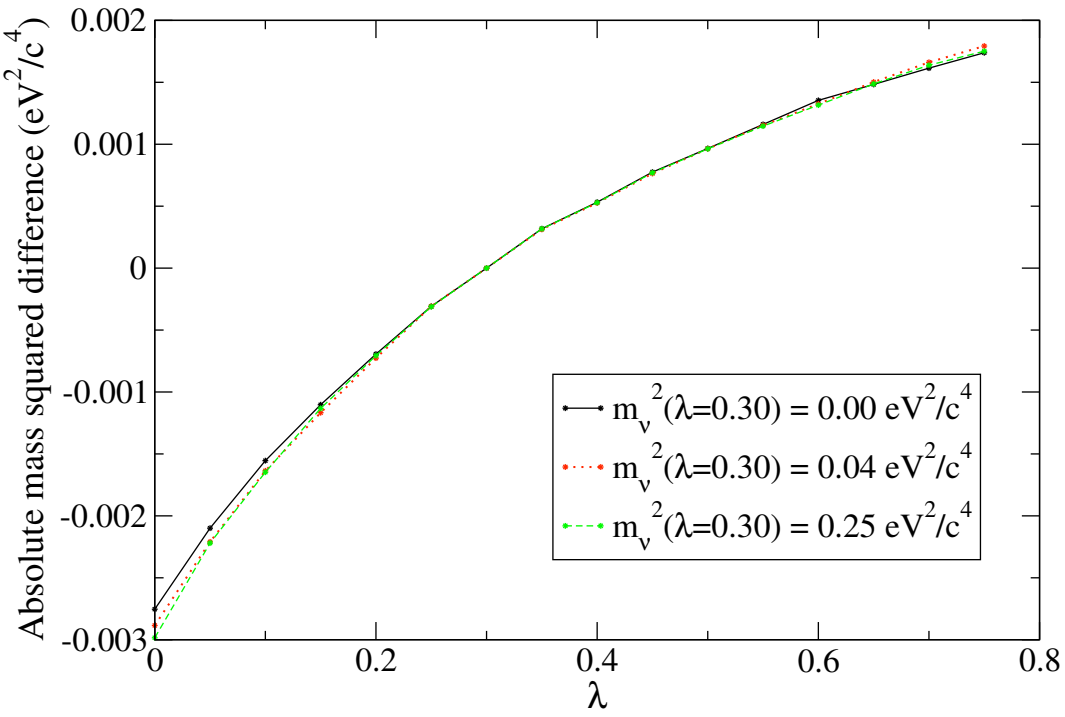

Figure 6.6: Error in the neutrino mass squared deduced from fitting, due to uncertainties in the ortho:para ratio (from fitting of β spectra with $W_0 = 18.575$ keV and 100% T_2).

Using the same fitting procedure described in the previous section, theoretical integral β spectra for different values of λ were fitted to a reference spectrum for $\lambda = 0.3$ (which corresponds to a temperature $T = 29.6$ K). The results are shown in figure 6.6. The error of the neutrino mass squared is similar to the error caused by temperature uncertainty.

6.4 Isotope effects

Even though the isotopic purity of tritium atoms in the source of the KATRIN experiment is expected to be at least 95%, this means that the amount of DT molecules may be anything between 0 and 10%. To see how accurately this percentage needs to be known, the error in the neutrino mass deduced as a result of uncertainties in the amount of DT in the source between 0 and 20% has been investigated. Figure 6.7 shows how the final state distribution changes with the amount of DT contamination in the source. It has been assumed that the source is thermal and at a temperature of 30 K.

Theoretical integral β spectra for different DT:T_2 ratios were fitted to a reference spectrum (10% DT) using the same fit procedure as before. The results of these fits are

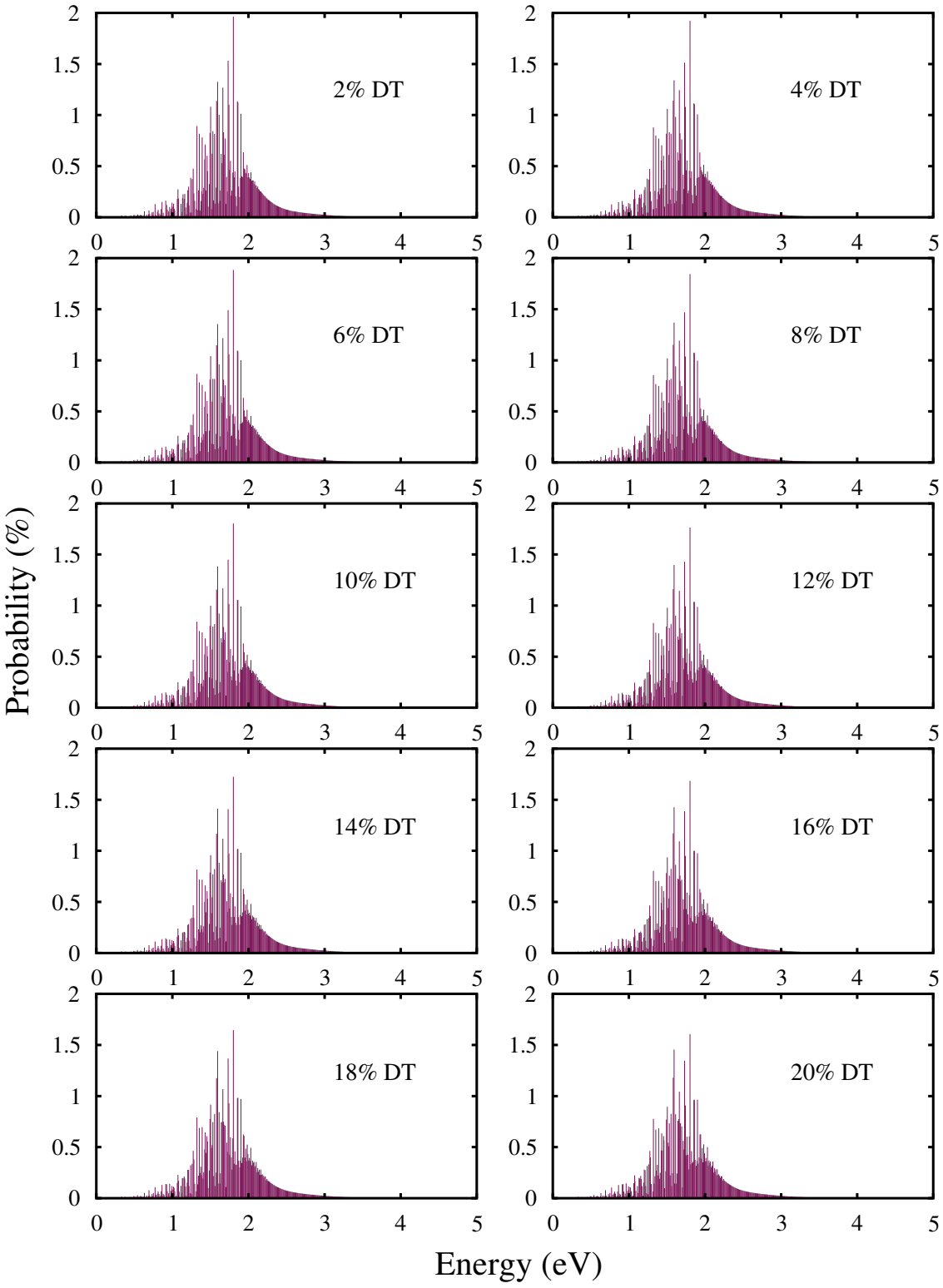

Figure 6.7: Overall final state distribution for a source at temperature $T = 30$ K for different DT:T_2 ratios

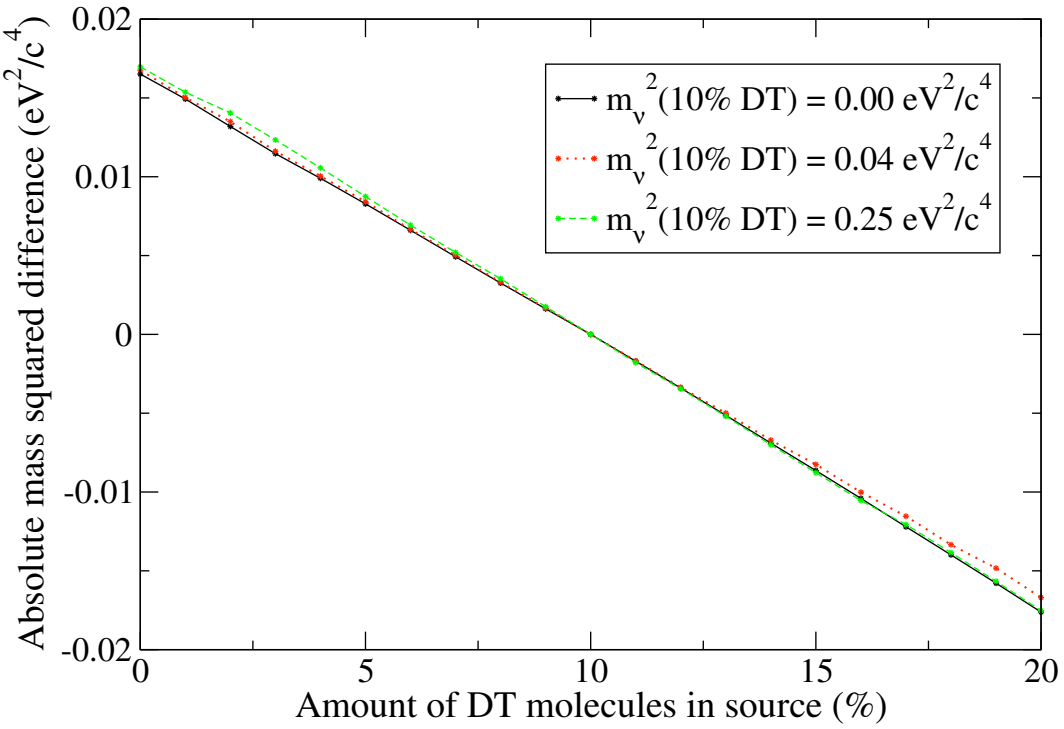

Figure 6.8: Error in the neutrino mass squared deduced from fitting, due to uncertainties in the amount of DT molecules in the source (from fitting of β spectra with W_0 = 18.575 keV and T = 30 K).

shown in figure 6.8. For a neutrino mass of 0.2 eV/c^2, a 10% change in the amount of DT molecules in the source, gives an error in the deduced neutrino mass of $\approx$ 18%. This is a significant difference and therefore the isotope contamination needs to be measured more accurately than the current estimate.

6.5 Summary

In the KATRIN experiment, the main systematic error of the windowless gaseous tritium source is associated with the column density of the tritium molecules, which must be known to a precision of 0.1% [98]. This means that to avoid tritium density changes in the source, the temperature must be stabilised to a precision of about 1% [105]. Therefore an uncertainty in the temperature of this amount should have a negligible affect on the deduced value of the neutrino mass. The KATRIN experiment will use thermalised T_2 which will be rapidly cooled, so λ values in the range $0.3 < \lambda < 0.75$ are to be expected. In section 6.3 it was shown that the error on the deduced neutrino mass due to uncertainty in the ortho:para ratio is also small. However, it should be noted that the

stability of the ortho and para T_2 ratio also depends completely on experimental conditions. The long life-time stabilisation is valid for isolated molecules, however molecular collisions with the walls (and possibly external fields) may very well change these numbers. It is therefore recommended that the ortho:para ratio be measured directly when running the experiment rather than obtained from theoretical considerations. Of the three uncertainties considered, it was found that uncertainties in the amount of isotopic contamination could give a significant error in the deduced neutrino mass. It is therefore essential that the gas composition be quantitatively monitored in line and as close to real time as possible. To do this, laser Raman spectroscopy will be used [172].

Chapter 7

The final state probability distribution for the electronic continuum of $^3HeT^+$

So far the final state distribution (FSD) of the electronically bound states of $^3HeT^+$ has been considered, however from about 40 eV below the endpoint of the β spectrum the contribution from the electronic continuum begins to have an effect. Although the KATRIN experiment aims to deduce the mass of the neutrino by analysing the last 30 eV of the β spectrum, other parameters such as the background noise will be investigated by analysing a larger energy interval. The electronic continuum of $^3HeT^+$ consists of the background singly excited molecular continuum together with contributions from Feshbach resonances (Feshbach resonances have been discussed in chapter 3). It has been shown that these resonances track strongly repulsive states of $^3HeT^{2+}$ and therefore have a very strong dependence on the internuclear separation [173]. This means that for an accurate calculation of the FSD of the electronic continuum, the nuclear motion effects must be considered as each resonance will effect a wider range of energies than its (generally) narrow width suggests [173].

In the calculation of the FSD to date, the part associated with the electronic continuum is the least accurately determined. Early works [108, 149, 174, 175] were limited by the number of resonances obtained and did not take into account their variation as a function of the internuclear separation, R. The R dependence of the final state distribution was later considered explicitly by Saenz and Froelich [151] for a few low lying resonances. Also, as discussed in chapter 4, the previous FSD's had some missing probability. In [106], this missing probability (0.17%) was found to belong to the electronic continuum part. These investigations have been discussed in more detail in chapter 4.

In this chapter the calculation of the final state distribution of the electronic continuum, using a different method to the previous works mentioned above, is described. In this work, the R-matrix method has been used to perform a geometry dependant calculation of the $^1\Sigma^+$ total symmetry resonance states of $^3HeT^+$ (as this is the relevant symmetry for T_2 β-decay [113]). The positions and widths of resonances converging to the first eight excited states of $^3HeT^{2+}$ have been obtained. By performing a similar R-matrix (inner region only) calculation for T_2, the wavefunction for the electronic ground state of T_2 was obtained, and hence overlaps integrals between 9 resonance states and the ground state of T_2 were calculated. Probability density distributions for each resonance were then obtained using the modified BCONT code discussed in chapters 3 and 5. A discrete probability distribution for the background continuum has also been determined for $R = 1.4$ a_0.

7.1 R-matrix calculation of the resonance states of $^3HeT^+$

Resonance states of an atom/molecule can manifest themselves in collisions of an electron with the corresponding ion. Hence calculations on the resonance states of $^3HeT^+$ can be performed by considering the collision between an electron and $^3HeT^{2+}$:

$$e^- + {}^3HeT^{2+} \rightarrow {}^3HeT^{+**} \rightarrow e^- + {}^3HeT^{2+}. \tag{7.1}$$

Tennyson presented results for resonant states of $^3HeT^+$ converging to the first three excited states of $^3HeT^{2+}$ as a function of internuclear separation [173], using the UK molecular R-matrix programs [135]. In the work presented below, the same method and programs as in [173] have been used to perform an improved calculation of the continuum states. Calculations have been performed for 21 internuclear separations in the range R = 1.0 - 2.0 a_0, in steps of 0.05 a_0.

7.1.1 Target calculation

The quality of the calculation depends heavily on the quality of the target and hence on the basis set used to represent it. The quality of a given basis set can be tested by comparing the target state energies obtained using that basis, as a function of the internuclear separation, with 'exact' energies. However problems can arise as a basis set that works well at one particular geometry may be poor at others.

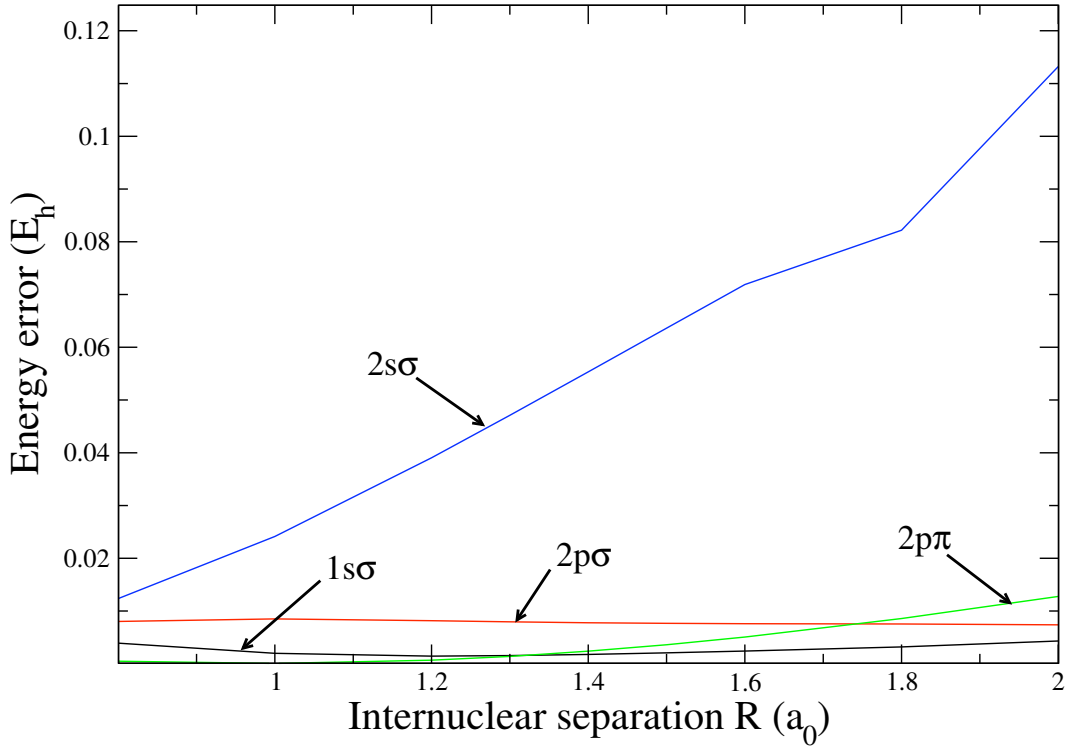

Figure 7.1: Error in the target state energies from [173] when compared to the exact energies computed using the code by Power [176], as a function of internuclear separation. E_h represents the Hartree unit of energy

In this calculation a basis set of Slater-type orbitals (STO's) was used. The criteria determining the choice of the STO's are that the basis be small enough to be manageable but flexible enough to be able to represent the target sufficiently at all the internuclear separations used. In this work the basis set used by Tennyson [173] was taken as a starting point. Tennyson used 3 s, 2 p and 1 d Slater-type orbitals on each atom, where the exponents of each orbital were optimised for the four lowest target states at the equilibrium geometry $R = 1.4\ a_0$ by comparison with exact energies computed using the code by Power [176]. Figure 7.1 shows the energy errors of the target states from [173] when compared to the exact energies. Units of E_h, which represents the Hartree unit of energy, are used. As can be seen from the plot, the 1sσ, 2pσ and 2pπ states are in reasonably good agreement with the exact energies. The errors are considerably worse for the 2sσ state. (It must be noted that in the calculation of the exact energies, the 2pσ state is the first excited state and the 2sσ state is the third excited state, whereas in [173] these assignments are reversed. Here the assignments of the exact energies are used).

The basis set of Tennyson was adjusted in order to meet the following criteria:

- to improve the energies of the 2sσ target state,
- and to include higher energy target states with reasonable accuracy.

For each atom, one compact orbital (large ζ exponent) and one diffuse orbital (small ζ exponent) were added to the basis set. Unfortunately, extending the basis set caused linear dependency problems between the states. To combat this the ζ exponents were adjusted one at a time until this problem could be eliminated but at the same time trying to retain as much as possible reasonable energies for the target states. However, by adjusting a given exponent to improve the situation at a certain internuclear separation sometimes worsened it at other separations. Therefore, the exponents were adjusted by considering their effect at three geometries, $R = 1.0$, 1.4 and 2.0 a_0, until a reasonable compromise could be reached. To remove this linear dependency entirely the extra diffuse hydrogen orbital added to the set had to be dropped.

The final basis set used in this work is given in table 7.1. The target energy levels calculated using this basis set, as a function of internuclear separation, are given in table 7.2. Figure 7.2 shows the energy errors of the target states obtained using the new basis set when compared to the exact energies. The target states obtained are in good agreement with the exact energies. All the states, except the 3pσ state, have energy errors that are < 0.02 E_h, The error of the 3pσ state is < 0.04 E_h.

7.1.2 Scattering calculation

To represent the continuum, numerical functions were obtained by solving for a Coulomb potential $V = -2/r$ (in a.u.) inside the R-matrix sphere using an $l \leq 7$ partial wave expansion. A total of 162 orbitals consisting of 64 σ, 54 π and 44 δ orbitals were obtained. Using Lagrange orthogonalisation [134], 2 σ and 1 π continuum orbitals were removed from the basis in order to alleviate linear dependence problems. The remaining continuum orbitals were then Schmidt orthogonalised to the entire set of target functions.

The general form for the target plus electron wavefunction in the inner region is given by equation (3.38). Using an R-matrix sphere of radius 10 a_0, scattering calculations were performed including all nine of the target states given in table 7.2. As the target molecule $^3HeT^{2+}$ has just the one electron, it was possible to include all the symmetry allowed L^2 configurations (configurations with 2 electrons in any target orbital) to account for correlation and polarisation effects, without the risk of over-correlation of the system.

Table 7.1: Slater-type basis set for $^3HeT^{2+}$.

T				He			
n	l	m	ζ	n	l	m	ζ
1	0	0	3.5	1	0	0	7.0
1	0	0	1.74122	1	0	0	4.05813
2	0	0	0.94122	2	0	0	3.12675
				3	0	0	1.520
2	1	0	1.29241	2	1	0	1.4109
3	1	0	1.93496	3	1	0	6.36
3	2	0	1.2	3	2	0	1.25
2	1	1	1.5	2	1	1	2.4
3	1	1	0.8	3	1	1	1.6
3	2	1	1.0	3	2	1	1.25
3	2	2	1.75	3	2	2	1.25

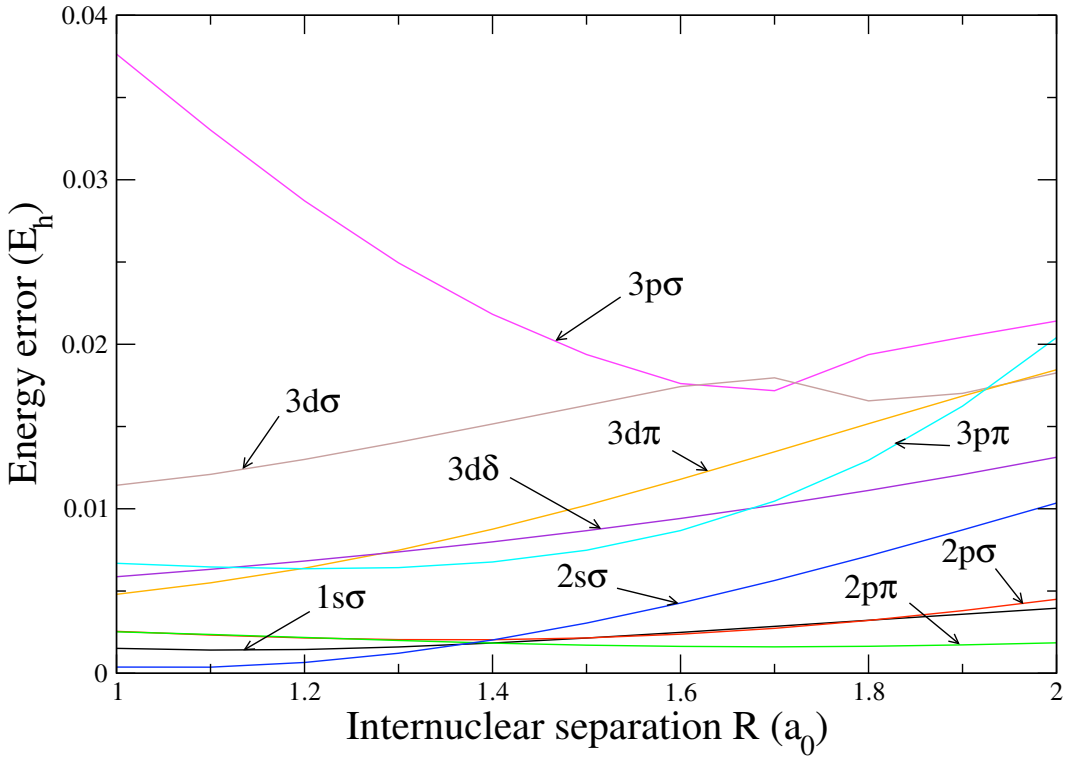

Figure 7.2: Error in the target state energies obtained in this work when compared to the exact energies computed using the code by Power [176], as a function of internuclear separation.

Table 7.2: Computed energy levels of $^3HeT^{2+}$, in E_h, as a function of the internuclear separation R, in a_0.

R	$1s\sigma$	$2p\sigma$	$2p\pi$	$2s\sigma$	$3p\sigma$	$3d\sigma$	$3d\pi$	$3d\delta$	$3p\pi$
1.00	−1.031838	0.664206	0.974206	1.092261	1.487324	1.497228	1.499393	1.517294	1.535361
1.05	−1.082963	0.558405	0.885805	1.005321	1.388263	1.400653	1.404026	1.423331	1.442084
1.10	−1.128108	0.462461	0.806054	0.926800	1.298218	1.312706	1.317360	1.338070	1.357489
1.15	−1.168239	0.375292	0.733811	0.855582	1.216100	1.232233	1.238272	1.260379	1.280452
1.20	−1.204142	0.295979	0.668127	0.790737	1.140985	1.158272	1.165823	1.189317	1.210038
1.25	−1.236461	0.223729	0.608204	0.731485	1.072089	1.090018	1.099224	1.124091	1.145463
1.30	−1.265725	0.157856	0.553366	0.677169	1.008737	1.026788	1.037810	1.064033	1.086066
1.35	−1.292375	0.097756	0.503039	0.627226	0.950351	0.967999	0.981010	1.008570	1.031287
1.40	−1.316773	0.042895	0.456729	0.581178	0.896428	0.913156	0.928335	0.957214	0.980648
1.45	−1.339224	−0.007202	0.414011	0.538610	0.846533	0.861828	0.879365	0.909543	0.933739
1.50	−1.359981	−0.052960	0.374518	0.499165	0.800284	0.813646	0.833731	0.865191	0.890206
1.55	−1.379257	−0.094762	0.337928	0.462529	0.757346	0.768291	0.791114	0.823839	0.849744
1.60	−1.397231	−0.132953	0.303962	0.428431	0.717421	0.725489	0.751232	0.785208	0.812088
1.65	−1.414053	−0.167846	0.272371	0.396631	0.680219	0.685026	0.713836	0.749053	0.777007
1.70	−1.429852	−0.199726	0.242939	0.366916	0.645170	0.647029	0.678706	0.715157	0.744299
1.75	−1.444736	−0.228849	0.215472	0.339099	0.609647	0.613733	0.645645	0.683330	0.713784
1.80	−1.458796	−0.255452	0.189799	0.313015	0.574915	0.583526	0.614479	0.653399	0.685307
1.85	−1.472114	−0.279750	0.165766	0.288515	0.541686	0.555388	0.585049	0.625214	0.658726
1.90	−1.484756	−0.301938	0.143236	0.265466	0.509885	0.529117	0.557216	0.598637	0.633917
1.95	−1.496781	−0.322196	0.122087	0.243750	0.479409	0.504571	0.530850	0.573547	0.610768
2.00	−1.508241	−0.340687	0.102205	0.223260	0.450158	0.481628	0.505838	0.549834	0.589175

In the outer region the R-matrices were propagated to 50 a_0 and the K-matrices obtained.

7.1.3 Resonances

A Rydberg series of resonance states converges to each electronic state of $^3HeT^{2+}$. In each series there is one member for each (n, l) combination with $n > l$. There are therefore an infinite number of increasingly narrow resonances in each series. The $^3HeT^{2+}$ states are often referred to as 'parent' states and the resonances as 'daughter' states.

At each internuclear separation, R, resonances converging to the eight excited target states of HeT^{2+} were detected and their positions and widths determined by fitting the associated eigenphase sum to a Breit-Wigner profile using the RESON program [147]. For each resonance, the fit was performed for 20 energy points. The quality of a fit can be defined by the goodness factor gf, which analyses the sum of the residues:

$$gf = -log_{10} \left| \sum_{i=1}^{20} \eta_{\text{fit}}(E_i) - \eta_{\text{calc}}(E_i) \right|, \tag{7.2}$$

where η is the eigenphase sum. Fits with $gf \geq 4$ give reliable results and those with $gf \leq 0$ give unreliable results. For intermediate values of gf the positions are reliable but the widths are often too large [173]. Hence gf values give us some idea of the error in the calculated positions and widths which result from the fact that the resonances are not calculated directly, but through a fit procedure. The accuracy of the resonance parameters are of course also dependant on the accuracy of the target representation. Improvements in the target representation should give lower energies and narrower widths for the resonances.

Resonance curves which describe the (energy) position of a resonance as a function of R, have been obtained by correlating the resonances detected at different geometries using quantum defect analysis (For detailed information on quantum defect theory see [177]). The quantum defect can be used to parameterise a Rydberg series of states below a threshold. This has proved to be the most reliable method of interpolating resonance parameters over a grid of geometries [178].

The complex quantum defect μ_{nl} is given by:

$$\mu_{nl} = \alpha_{nl} + i\beta_{nl}. \tag{7.3}$$

From the position determined by the fit, the RESON program calculates the effective

quantum number n^* of the resonance using the relation:

$$E_{\text{target}} - E_{\text{res}} = \frac{R_\infty Z^2}{(n^*)^2}, \tag{7.4}$$

where $E_{\text{res}}(R)$ and $E_{\text{target}}(R)$ are the energies at R of the resonance and the relevant 'parent' target state threshold respectively, R_∞ is the Rydberg constant and Z is the residual charge. The effective quantum number n^* is related to the real part of the complex quantum defect, α_{nl}, by:

$$n^* = n - \alpha_{nl}. \tag{7.5}$$

α_{nl} (and hence n^*) varies gently and smoothly as a function of internuclear separation. Resonances were therefore matched at different geometries by matching their effective quantum numbers. α_{nl} has a very weak dependence on n but depends strongly on l. In general, α_{nl} decreases rapidly as l increases. It is therefore generally easier to match n^* for the low-l states than for the high-l states because at high-l the quantum defects are close to zero. Within a series of resonances converging to a particular target state, it is also possible to identify separate series of resonances with increasing n but the same l as the quantum defects will be the same for these resonances and so the effective quantum numbers will differ by a whole number.

Table 7.3 gives the positions, widths, goodness factors and effective quantum numbers for resonances detected converging to the first three excited states of $^3HeT^{2+}$. The assignments of the resonance states comes from the quantum defect analysis, but they should not be regarded as definitive. The resonance curves and $^3HeT^{2+}$ target states are also shown graphically in figure 7.3.

As can be seen from the figure, there are a number of resonances crossing the thresholds belonging to lower target states. The RESON program, however, calculates the effective quantum number of these resonances, relative to the nearest threshold. These 'intruder' resonances can normally be identified easily if the shape of the target state curve to which they actually belong varies significantly from the lower threshold curve, as the effective quantum numbers calculated by RESON will not vary smoothly as a function of R. For these resonances, the effective quantum numbers given in table 7.3 have been recalculated relative to the correct parent target state.

The $n = 3$ electronic states of $^3HeT^{2+}$ lie very close together in energy (see table 7.2). The resonances detected above the $2s\sigma$ and below the $3p\sigma$ state, are not all related to the series converging to $3p\sigma$, but include contributions from resonances converging to the

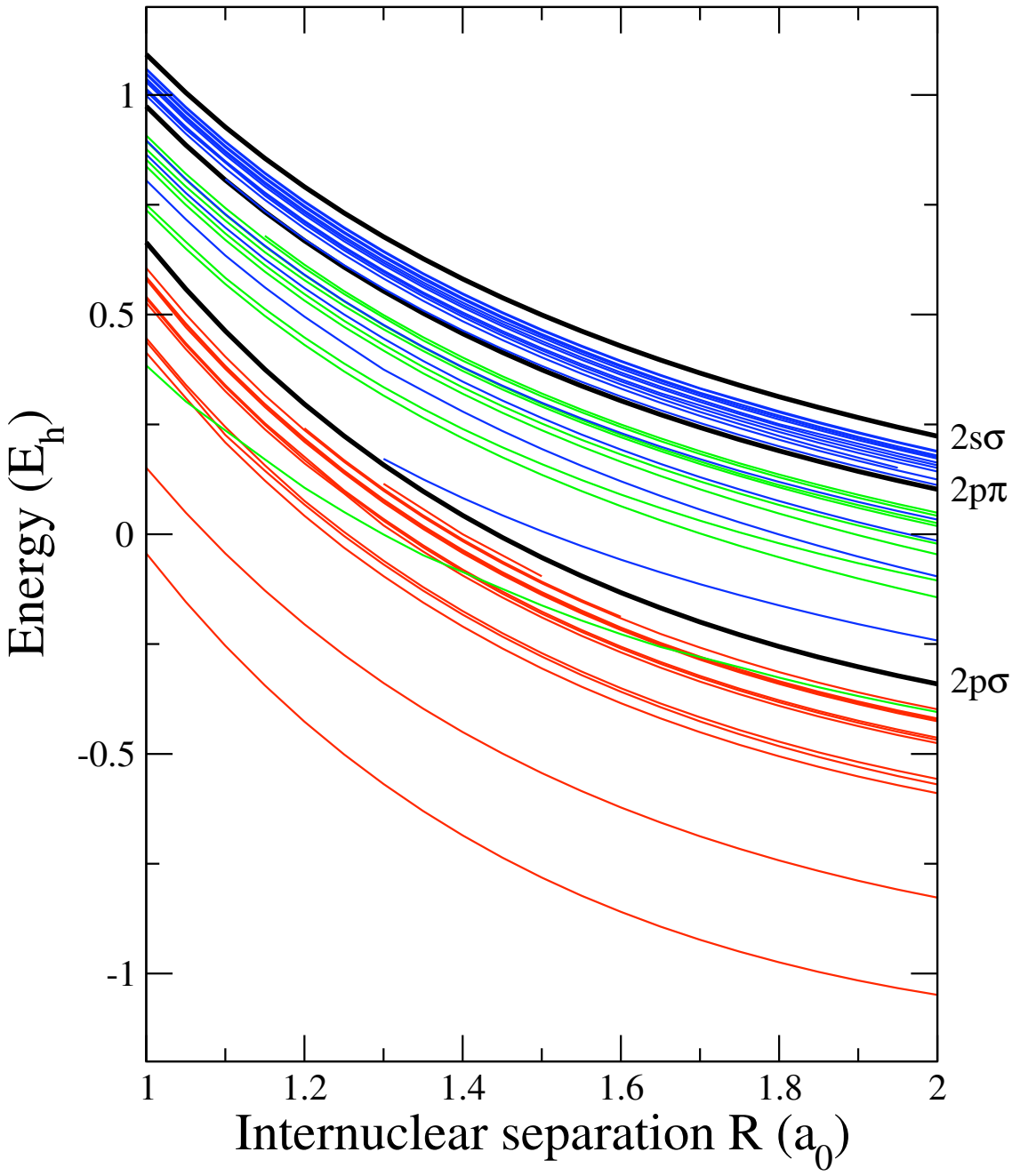

Figure 7.3: $^3HeT^+$ resonance curves and $^3HeT^{2+}$ target potentials as a function of internuclear separation R. Resonances converging to the 2pσ, 2pπ and 2s target states are drawn in red, green and blue respectively.

Table 7.3: Positions E_{res}, and widths Γ, for $^1\Sigma^+$ resonance states of $^3HeT^+$, as a function of internuclear separation R. Also given are assignments, effective quantum numbers n^*, and goodness factors gf

R (a_0)	E_{res} (E_h)	Γ (E_h)	n^*	gf	E_{res} (E_h)	Γ (E_h)	n^*	gf
		$2p\sigma^2$				$2p\sigma 3s$		
1.00	−0.04349	0.02607	1.68109	9	0.15136	0.01704	1.97479	8
1.05	−0.15385	0.02644	1.67571	7	0.04910	0.01756	1.98165	7
1.10	−0.25379	0.02655	1.67100	6	−0.04366	0.01793	1.98787	7
1.15	−0.34401	0.02656	1.66747	6	−0.12817	0.01830	1.99312	7
1.20	−0.42647	0.02645	1.66384	6	−0.20490	0.01819	1.99825	7
1.25	−0.50101	0.02629	1.66121	6	−0.27483	0.01802	2.00290	8
1.30	−0.56864	0.02600	1.65920	7	−0.33863	0.01780	2.00706	8
1.35	−0.62997	0.02555	1.65779	9	−0.39692	0.01753	2.01074	7
1.40	−0.68557	0.02493	1.65696	8	−0.45022	0.01722	2.01392	7
1.45	−0.73590	0.02412	1.65669	7	−0.49898	0.01685	2.01665	7
1.50	−0.78142	0.02316	1.65696	7	−0.54361	0.01641	2.01897	7
1.55	−0.82253	0.02209	1.65774	8	−0.58446	0.01593	2.02093	7
1.60	−0.85964	0.02092	1.65899	8	−0.62186	0.01540	2.02255	8
1.65	−0.89307	0.01969	1.66065	9	−0.65611	0.01486	2.02390	8
1.70	−0.92317	0.01843	1.66270	9	−0.68747	0.01430	2.02498	9
1.75	−0.95022	0.01718	1.66508	8	−0.71618	0.01375	2.02584	10
1.80	−0.97450	0.01594	1.66777	8	−0.74246	0.01320	2.02650	10
1.85	−0.99625	0.01475	1.67073	8	−0.76653	0.01268	2.02698	9
1.90	−1.01572	0.01358	1.67392	8	−0.78856	0.01217	2.02730	9
1.95	−1.03309	0.01247	1.67730	8	−0.80873	0.01169	2.02749	8
2.00	−1.04857	0.01140	1.68087	8	−0.82719	0.01122	2.02756	8
		$2p\sigma 3p\sigma$				$2p\sigma 3d\sigma$		
1.00	0.41355	0.00398	2.82471	6	0.43863	0.00148	2.97759	6
1.05	0.31031	0.00439	2.83927	4	0.33268	0.00201	2.97665	5
1.10	0.20880	0.00535	2.80795	5	0.22598	0.00580	2.90817	6
1.15	0.12208	0.00477	2.81044	6	0.14466	0.00415	2.94477	5
1.20	0.04196	0.00461	2.80597	6	0.06744	0.00314	2.95823	4
1.25	−0.03051	0.00441	2.80474	6	−0.00390	0.00268	2.96414	5
1.30	−0.09547	0.00429	2.80982	6	−0.06872	0.00255	2.97106	5
1.35	−0.15536	0.00410	2.81096	7	−0.12831	0.00227	2.97441	5
1.40	−0.21003	0.00390	2.81205	7	−0.18285	0.00203	2.97652	5
1.45	−0.25985	0.00369	2.81357	7	−0.23276	0.00182	2.97771	5
1.50	−0.30529	0.00347	2.81533	7	−0.27846	0.00168	2.97813	5
1.55	−0.34675	0.00324	2.81724	7	−0.32031	0.00157	2.97782	5
1.60	−0.38458	0.00301	2.81928	7	−0.35863	0.00151	2.97693	5
1.65	−0.41909	0.00277	2.82145	7	−0.39372	0.00149	2.97562	5
1.70	−0.45057	0.00254	2.82365	7	−0.42587	0.00149	2.97387	6
1.75	−0.47933	0.00231	2.82572	8	−0.45533	0.00152	2.97167	6
1.80	−0.50555	0.00208	2.82785	8	−0.48230	0.00155	2.96925	6
1.85	−0.52949	0.00188	2.82989	8	−0.50701	0.00161	2.96657	6
1.90	−0.55134	0.00167	2.83180	8	−0.52964	0.00166	2.96371	6
1.95	−0.57130	0.00148	2.83353	8	−0.55035	0.00171	2.96071	6
2.00	−0.58954	0.00130	2.83495	8	−0.56933	0.00176	2.95756	6
		$2p\sigma 4s$				$2p\sigma 4p\sigma$		
1.00	0.44646	0.00208	3.03065	5	0.52709	0.00155	3.81917	6
1.05	0.34013	0.00199	3.02698	5	0.42136	0.00167	3.82021	6
1.10	0.24420	0.00394	3.02709	2	0.32548	0.00167	3.82104	6
1.15	0.15705	0.00237	3.02720	7	0.23883	0.00162	3.82833	6
1.20	0.07601	0.00296	3.01535	5	0.16140	0.00118	3.85495	6
1.25	0.00544	0.00326	3.02691	5	0.09314	0.00097	3.91343	6
1.30	−0.06025	0.00346	3.02814	4	0.02023	0.00138	3.81211	9
1.35	−0.12029	0.00370	3.02861	4	−0.03917	0.00129	3.82186	6
1.40	−0.17504	0.00390	3.02937	4	−0.09383	0.00109	3.82459	4
1.45	−0.22502	0.00407	3.03016	4	−0.14378	0.00119	3.82669	5
1.50	−0.27065	0.00414	3.03107	4	−0.18935	0.00111	3.82937	6
1.55	−0.31231	0.00416	3.03205	4	−0.23093	0.00103	3.83243	6
1.60	−0.35037	0.00412	3.03299	4	−0.26894	0.00094	3.83505	6
1.65	−0.38511	0.00405	3.03405	4	−0.30366	0.00087	3.83742	7
1.70	−0.41684	0.00393	3.03510	5	−0.33538	0.00079	3.83976	7
1.75	−0.44582	0.00382	3.03606	5	−0.36428	0.00071	3.84292	7
1.80	−0.47228	0.00367	3.03707	5	−0.39073	0.00064	3.84507	7
1.85	−0.49645	0.00353	3.03797	5	−0.41488	0.00057	3.84722	7
1.90	−0.51850	0.00337	3.03894	5	−0.43694	0.00050	3.84899	7
1.95	−0.53863	0.00322	3.03984	6	−0.45709	0.00044	3.85053	7
2.00	−0.55699	0.00307	3.04076	6	−0.47549	0.00038	3.85187	6

Table 7.3 – Continued from previous page

R (a_0)	E_{res} (E_h)	Γ (E_h)	n^*	gf	E_{res} (E_h)	Γ (E_h)	n^*	gf
		2pσ4dσ				2pσ5s		
1.00	0.53645	0.00090	3.95664	5	0.54077	0.00083	4.02531	5
1.05	0.43068	0.00095	3.95707	5	0.43506	0.00078	4.02683	5
1.10	0.33537	0.00090	3.96698	5	0.33920	0.00089	4.02813	5
1.15	0.24873	0.00090	3.97518	5	0.25255	0.00094	4.03662	5
1.20					0.17604	0.00101	4.08347	6
1.25					0.09998	0.00087	4.02017	5
1.30					0.03483	0.00144	4.03202	4
1.35					−0.02522	0.00168	4.03284	2
1.40					−0.08045	0.00148	4.02671	2
1.45					−0.13034	0.00158	4.03013	5
1.50	−0.18091	0.00192	3.95357	4	−0.17601	0.00167	4.03157	4
1.55	−0.22208	0.00138	3.96342	4	−0.21774	0.00170	4.03275	4
1.60	−0.26000	0.00113	3.96760	4	−0.25588	0.00171	4.03356	4
1.65	−0.29480	0.00101	3.96906	4	−0.29070	0.00169	4.03475	4
1.70	−0.32667	0.00096	3.96920	4	−0.32251	0.00166	4.03598	4
1.75	−0.35583	0.00093	3.96863	4	−0.35157	0.00161	4.03704	4
1.80	−0.38252	0.00095	3.96734	3	−0.37810	0.00156	4.03823	5
1.85	−0.40692	0.00091	3.96579	4	−0.40232	0.00149	4.03941	5
1.90	−0.42923	0.00094	3.96386	3	−0.42444	0.00143	4.04058	5
1.95	−0.44962	0.00093	3.96182	4	−0.44463	0.00137	4.04173	5
2.00	−0.46823	0.00096	3.95991	3	−0.46305	0.00131	4.04284	5
		2pσ5pσ				2pσ5dσ		
1.00	0.57987	0.00112	4.86980	5	0.58277	0.00046	4.95567	6
1.05	0.47089	0.00052	4.78056	7	0.47703	0.00068	4.95744	1
1.10	0.37626	0.00074	4.81678	6	0.38141	0.00049	4.96760	3
1.15	0.28942	0.00077	4.82597	6	0.29452	0.00044	4.97609	1
1.20	0.21043	0.00073	4.83521	6				
1.25	0.13894	0.00077	4.85681	6				
1.30	0.07191	0.00068	4.82389	7				
1.35	0.01203	0.00066	4.83007	7				
1.40	−0.04278	0.00064	4.83166	7				
1.45	−0.09277	0.00062	4.83465	7				
1.50	−0.13842	0.00061	4.83770	6				
1.55	−0.18010	0.00061	4.84108	7				
1.60	−0.21816	0.00068	4.84486	8				
1.65	−0.25289	0.00095	4.84957	5				
1.70	−0.28558	0.00154	4.82645	3				
1.75	−0.31436	0.00043	4.83620	4	−0.31172	0.00240	4.91249	3
1.80	−0.34077	0.00028	4.84165	4	−0.33763	0.00166	4.93331	3
1.85	−0.36496	0.00024	4.84473	5	−0.36164	0.00127	4.94199	4
1.90	−0.38708	0.00021	4.84654	6	−0.38369	0.00114	4.94625	3
1.95	−0.40731	0.00020	4.84755	6	−0.40388	0.00097	4.94818	3
2.00	−0.42579	0.00019	4.84780	6	−0.42234	0.00089	4.94912	3
		2pσ6s				2pσ6pσ		
1.00	0.58604	0.00040	5.05836	6	0.60586	0.00058	5.85475	5
1.05					0.50029	0.00068	5.86639	3
1.10	0.38317	0.00050	5.02218	4				
1.15	0.29634	0.00053	5.03294	4	0.31612	0.00038	5.81352	6
1.20	0.21768	0.00062	5.05395	5	0.23706	0.00041	5.82647	6
1.25	0.14487	0.00066	5.03610	4	0.16502	0.00043	5.83682	6
1.30	0.07885	0.00071	5.03123	4	0.09897	0.00038	5.82781	6
1.35	0.01876	0.00077	5.03158	3	0.03896	0.00037	5.83237	6
1.40	−0.03606	0.00082	5.03307	3	−0.01585	0.00035	5.83472	6
1.45	−0.08612	0.00081	5.03426	3	−0.06589	0.00034	5.83765	6
1.50	−0.13183	0.00081	5.03580	3	−0.11159	0.00033	5.84065	6
1.55	−0.17353	0.00070	5.03903	2	−0.15333	0.00031	5.84380	6
1.60	−0.21234	0.00055	5.01937	2	−0.19145	0.00030	5.84705	5
1.65	−0.24705	0.00078	5.02512	3	−0.22628	0.00030	5.85041	5
1.70	−0.27880	0.00090	5.02919	4	−0.25809	0.00030	5.85401	5
1.75	−0.30783	0.00090	5.03204	4	−0.28713	0.00031	5.85813	6
1.80	−0.33436	0.00087	5.03437	4	−0.31365	0.00032	5.86247	6
1.85	−0.35860	0.00083	5.03623	4	−0.33785	0.00035	5.86733	5
1.90	−0.38074	0.00079	5.03789	4	−0.35993	0.00040	5.87273	5
1.95	−0.40095	0.00076	5.03935	4	−0.38007	0.00045	5.87868	5
2.00	−0.41940	0.00073	5.04073	5	−0.39844	0.00050	5.88487	4

Table 7.3 – Continued from previous page

R (a_0)	E_{res} (E_h)	Γ (E_h)	n^*	gf	E_{res} (E_h)	Γ (E_h)	n^*	gf
		2pσ7s				2pσ7pσ		
1.00								
1.05								
1.10								
1.15								
1.20	0.24115	0.00038	6.03979	4				
1.25								
1.30	0.10286	0.00040	6.03054	3	0.11496	0.00023	6.82842	5
1.35	0.04277	0.00044	6.03101	3				
1.40	−0.01207	0.00047	6.03219	3	0.00009	0.00022	6.83565	5
1.45								
1.50	−0.10788	0.00046	6.03465	3	−0.09569	0.00020	6.84180	5
1.55								
1.60	−0.18782	0.00044	6.03773	3				
1.65								
1.70								
1.75								
1.80								
1.85								
1.90								
1.95								
2.00								
		$2p\pi^2$				2pπ3pπ		
1.00	0.38429	0.00060	1.84128	6	0.73813	0.00521	2.91066	4
1.05	0.30243	0.00924	1.85157	2	0.64998	0.00451	2.91222	3
1.10					0.56953	0.00519	2.90791	4
1.15	0.17054	0.00522	1.88433	5	0.49687	0.00505	2.90535	5
1.20	0.10598	0.00062	1.88621	5	0.43098	0.00506	2.90405	5
1.25	0.05085	0.00593	1.89430	4	0.37070	0.00503	2.90187	5
1.30	−0.00057	0.00616	1.90014	6	0.31560	0.00507	2.90029	5
1.35	−0.04778	0.00631	1.90551	3	0.26495	0.00510	2.89829	6
1.40					0.21829	0.00513	2.89619	6
1.45	−0.12408	0.00314	1.92791	4	0.17521	0.00518	2.89399	6
1.50	−0.16200	0.00436	1.93074	5	0.13533	0.00524	2.89164	6
1.55	−0.19610	0.00472	1.93523	8	0.09827	0.00528	2.88883	6
1.60	−0.22754	0.00470	1.93983	5	0.06387	0.00534	2.88617	6
1.65	−0.25662	0.00499	1.94442	2	0.03176	0.00539	2.88310	6
1.70					0.00178	0.00545	2.87978	6
1.75	−0.30275	0.00268	1.96452	4	−0.02629	0.00551	2.87621	6
1.80	−0.32651	0.00334	1.96816	5	−0.05263	0.00557	2.87225	7
1.85	−0.34828	0.00356	1.97249	6	−0.07746	0.00562	2.86752	7
1.90	−0.36846	0.00356	1.97701	6	−0.10078	0.00568	2.86288	7
1.95	−0.38723	0.00345	1.98162	5	−0.12279	0.00576	2.85786	7
2.00	−0.40472	0.00328	1.98629	4	−0.14361	0.00584	2.85238	7
		2pπ3dπ				2pπ4pπ		
1.00	0.75034	0.00418	2.98898	4	0.83755	0.00293	3.82566	3
1.05	0.66585	0.00284	3.01542	5	0.74960	0.00280	3.83196	3
1.10	0.58351	0.00385	2.99783	5	0.67000	0.00243	3.83402	4
1.15	0.51277	0.00358	3.00798	5	0.59763	0.00222	3.83228	5
1.20	0.44790	0.00353	3.01358	6	0.53197	0.00209	3.83256	5
1.25	0.38890	0.00349	3.01987	6	0.47211	0.00202	3.83349	6
1.30	0.33472	0.00307	3.02443	6	0.41785	0.00174	3.84171	6
1.35	0.28524	0.00329	3.03032	6	0.36621	0.00191	3.82326	6
1.40	0.23982	0.00326	3.03649	6	0.31970	0.00189	3.82039	6
1.45	0.19810	0.00322	3.04354	7	0.27662	0.00187	3.81534	6
1.50	0.15959	0.00318	3.05050	7	0.23666	0.00187	3.80885	6
1.55	0.12362	0.00313	3.05488	7	0.19949	0.00188	3.80090	7
1.60	0.09023	0.00306	3.05898	7	0.16488	0.00189	3.79215	7
1.65	0.05957	0.00303	3.06570	2	0.13255	0.00192	3.78203	7
1.70	0.03100	0.00300	3.07189	8	0.10228	0.00195	3.77077	7
1.75	0.00409	0.00295	3.07595	9	0.07385	0.00198	3.75790	7
1.80	−0.02070	0.00294	3.08239	7	0.04711	0.00201	3.74388	7
1.85	−0.04422	0.00294	3.08617	7	0.02188	0.00203	3.72826	8
1.90	−0.06589	0.00295	3.09249	6	−0.00195	0.00205	3.71154	8
1.95	−0.08624	0.00297	3.09845	5	−0.02452	0.00205	3.69356	8
2.00	−0.10537	0.00301	3.10407	5	−0.04593	0.00203	3.67441	8

Table 7.3 – Continued from previous page

R (a_0)	E_{res} (E_h)	Γ (E_h)	n^*	gf	E_{res} (E_h)	Γ (E_h)	n^*	gf
		2pπ4dπ				2pπ5pπ		
1.00	0.85269	0.00051	4.05699	7	0.87646	0.00167	4.52346	6
1.05	0.76439	0.00053	4.05862	8	0.79137	0.00208	4.60204	7
1.10	0.68471	0.00054	4.05973	8	0.71399	0.00225	4.66090	7
1.15	0.61224	0.00055	4.05596	9	0.64206	0.00138	4.66877	8
1.20	0.54646	0.00057	4.05434	8	0.57834	0.00135	4.71953	7
1.25	0.48594	0.00062	4.04458	7	0.51999	0.00125	4.76162	6
1.30	0.43131	0.00072	4.04798	6	0.46665	0.00120	4.80247	6
1.35	0.38057	0.00064	4.04106	7	0.41732	0.00113	4.83041	6
1.40	0.33434	0.00072	4.04240	7	0.37182	0.00105	4.85346	5
1.45	0.29152	0.00075	4.04074	7	0.32977	0.00101	4.87245	6
1.50	0.25191	0.00078	4.03879	7	0.29075	0.00097	4.88624	6
1.55	0.21514	0.00081	4.03590	6	0.25439	0.00096	4.89310	5
1.60	0.18155	0.00082	4.04202	6	0.22066	0.00096	4.90004	5
1.65	0.14974	0.00084	4.03851	7	0.18922	0.00096	4.90440	5
1.70	0.12045	0.00086	4.04080	7	0.15989	0.00096	4.90728	5
1.75	0.09261	0.00087	4.03460	8	0.13249	0.00098	4.90942	5
1.80	0.06669	0.00089	4.03054	8	0.10681	0.00100	4.90902	5
1.85	0.04272	0.00086	4.03161	5	0.08259	0.00102	4.90355	5
1.90	0.01995	0.00087	4.02768	6	0.05999	0.00104	4.90156	5
1.95	−0.00137	0.00086	4.02485	6	0.03875	0.00107	4.89894	5
2.00	−0.02154	0.00085	4.02019	6	0.01873	0.00109	4.89493	5
		2pπ5dπ				2pπ6pπ		
1.00	0.89499	0.00052	5.02465	4	0.90794	0.00122	5.49392	9
1.05	0.80685	0.00046	5.03289	4	0.82063	0.00129	5.53961	8
1.10	0.72730	0.00043	5.03925	4	0.74241	0.00135	5.60568	7
1.15	0.65532	0.00047	5.04783	3	0.67106	0.00092	5.64550	7
1.20	0.58978	0.00045	5.05231	3	0.60585	0.00092	5.66697	7
1.25	0.53007	0.00049	5.05937	2	0.54676	0.00084	5.70504	7
1.30	0.47534	0.00044	5.06280	3	0.49329	0.00076	5.77001	6
1.35	0.42505	0.00040	5.06411	4	0.44120	0.00096	5.68703	7
1.40	0.37880	0.00038	5.06592	4	0.39509	0.00095	5.69608	7
1.45	0.33618	0.00038	5.06906	4	0.35306	0.00093	5.72830	6
1.50	0.29679	0.00037	5.07255	4	0.31390	0.00094	5.74407	7
1.55	0.26036	0.00040	5.07779	4	0.27769	0.00090	5.76188	7
1.60	0.22636	0.00037	5.07679	4	0.24376	0.00094	5.76392	7
1.65	0.19481	0.00036	5.07816	4				
1.70	0.16557	0.00036	5.08435	5				
1.75	0.13774	0.00033	5.07239	4	0.15542	0.00101	5.77117	6
1.80	0.11203	0.00031	5.07132	5	0.12974	0.00102	5.77063	6
1.85	0.08880	0.00040	5.09754	6	0.10583	0.00100	5.77673	6
1.90	0.06630	0.00037	5.09859	6	0.08323	0.00101	5.77342	6
1.95	0.04517	0.00035	5.09918	6	0.06199	0.00103	5.76870	6
2.00	0.02525	0.00032	5.09789	6	0.04197	0.00104	5.76230	7
		2pπ6dπ						
1.00								
1.05								
1.10								
1.15	0.67911	0.00018	6.04692	3				
1.20	0.61342	0.00018	6.04639	3				
1.25	0.55355	0.00022	6.04913	2				
1.30	0.49882	0.00028	6.05522	3				
1.35	0.44844	0.00031	6.05236	3				
1.40	0.40225	0.00037	6.05904	3				
1.45	0.35969	0.00040	6.06761	4				
1.50	0.32034	0.00040	6.07604	4				
1.55	0.28384	0.00042	6.08091	4				
1.60	0.24985	0.00046	6.07932	1				
1.65								
1.70								
1.75	0.16155	0.00039	6.09017	5				
1.80								
1.85	0.11216	0.00042	6.10814	5				
1.90	0.08975	0.00040	6.11469	5				
1.95								
2.00	0.04889	0.00035	6.12455	6				

Table 7.3 – Continued from previous page

R (a_0)	E_{res} (E_h)	Γ (E_h)	n^*	gf	E_{res} (E_h)	Γ (E_h)	n^*	gf
		2s3s				2s3pσ		
1.00					0.80540	0.00403	2.64046	7
1.05					0.71695	0.00375	2.63354	8
1.10					0.63461	0.00363	2.61627	4
1.15					0.56199	0.00336	2.61001	8
1.20					0.49541	0.00321	2.60234	9
1.25					0.43434	0.00303	2.59436	10
1.30	0.17174	0.00617	1.98923	8	0.37503	0.00357	2.57283	4
1.35	0.12523	0.00603	1.99602	8	0.32678	0.00281	2.58007	10
1.40	0.08252	0.00590	2.00269	8	0.27923	0.00270	2.57365	9
1.45	0.04320	0.00576	2.00924	9	0.23516	0.00261	2.56727	9
1.50	0.00692	0.00562	2.01569	9	0.19423	0.00254	2.56101	9
1.55	−0.02665	0.00550	2.02200	9	0.15613	0.00247	2.55488	8
1.60	−0.05777	0.00539	2.02818	9	0.12066	0.00243	2.54918	8
1.65	−0.08667	0.00528	2.03426	9	0.08741	0.00241	2.54320	8
1.70	−0.11357	0.00519	2.04021	9	0.05625	0.00239	2.53728	8
1.75	−0.13864	0.00511	2.04607	9	0.02699	0.00240	2.53140	7
1.80	−0.16205	0.00504	2.05182	9	−0.00054	0.00241	2.52556	7
1.85	−0.18394	0.00497	2.05748	9	−0.02654	0.00243	2.51954	7
1.90	−0.20445	0.00491	2.06303	9	−0.05101	0.00247	2.51388	6
1.95	−0.22368	0.00487	2.06851	9	−0.07412	0.00251	2.50836	6
2.00	−0.24175	0.00483	2.07388	9	−0.09596	0.00255	2.50305	5
		2s3dσ				2s4s		
1.00	0.86441	0.00450	2.96271	6	0.89683	0.00051	3.19903	4
1.05	0.77700	0.00430	2.95966	6	0.80847	0.00051	3.18747	4
1.10	0.69796	0.00395	2.95630	6	0.72876	0.00047	3.17789	4
1.15	0.62595	0.00338	2.95120	8	0.65661	0.00047	3.17044	4
1.20	0.56028	0.00317	2.94591	8	0.59099	0.00047	3.16428	4
1.25	0.50032	0.00297	2.94140	8	0.53126	0.00048	3.16050	3
1.30	0.44556	0.00276	2.93858	7	0.47661	0.00046	3.15787	4
1.35	0.39453	0.00259	2.93171	7	0.42651	0.00055	3.15663	4
1.40	0.34753	0.00239	2.92573	7	0.38051	0.00059	3.15701	4
1.45	0.30449	0.00223	2.92278	7	0.33826	0.00069	3.15951	4
1.50	0.26450	0.00209	2.91938	7	0.29936	0.00077	3.16382	5
1.55	0.22721	0.00197	2.91532	7	0.26371	0.00083	3.17165	5
1.60	0.19250	0.00184	2.91154	7	0.23047	0.00087	3.17852	6
1.65	0.16022	0.00172	2.90858	7	0.19962	0.00090	3.18618	6
1.70	0.13004	0.00160	2.90573	7				
1.75	0.10193	0.00150	2.90393	7	0.14406	0.00090	3.20224	7
1.80	0.07547	0.00140	2.90163	7	0.11902	0.00090	3.21085	7
1.85	0.05074	0.00131	2.90023	6	0.09562	0.00088	3.21999	8
1.90	0.02742	0.00124	2.89858	6	0.07359	0.00087	3.22853	9
1.95	0.00552	0.00118	2.89746	6	0.05286	0.00086	3.23686	9
2.00	−0.01507	0.00114	2.89685	6	0.03337	0.00085	3.24537	8
		2s5s				2s5pσ		
1.00					0.99852	0.00223	4.61914	4
1.05					0.91158	0.00298	4.61914	4
1.10	0.80825	0.00152	4.10733	5	0.83272	0.00316	4.61079	4
1.15	0.73561	0.00082	4.08288	5	0.76110	0.00323	4.60085	4
1.20	0.67148	0.00080	4.09520	6	0.69591	0.00314	4.59259	4
1.25	0.61251	0.00075	4.10008	6	0.63637	0.00312	4.58555	5
1.30	0.55885	0.00078	4.11134	6	0.58187	0.00312	4.58105	5
1.35	0.50926	0.00070	4.11745	7	0.53125	0.00284	4.56499	5
1.40	0.46389	0.00067	4.12948	7	0.48493	0.00266	4.55858	5
1.45	0.42194	0.00065	4.14028	7	0.44220	0.00262	4.55462	5
1.50	0.38308	0.00064	4.15083	7	0.40254	0.00256	4.54953	5
1.55	0.34703	0.00065	4.16132	7	0.36568	0.00248	4.54436	5
1.60	0.31349	0.00065	4.17127	8	0.33136	0.00235	4.53921	5
1.65	0.28225	0.00064	4.18149	8	0.29934	0.00229	4.53398	5
1.70	0.25308	0.00062	4.19162	8	0.26940	0.00220	4.52885	5
1.75	0.22577	0.00063	4.20086	8	0.24136	0.00216	4.52346	5
1.80	0.20019	0.00063	4.21032	10	0.21504	0.00214	4.51801	4
1.85	0.17617	0.00065	4.21929	8	0.19029	0.00217	4.51242	4
1.90	0.15357	0.00069	4.22768	7	0.16714	0.00258	4.51010	3
1.95	0.13223	0.00081	4.23488	6	0.14521	0.00194	4.50524	4
2.00	0.11204	0.00121	4.24049	5	0.12437	0.00187	4.49710	5

Table 7.3 – Continued from previous page

R (a_0)	E_{res} (E_h)	Γ (E_h)	n^*	gf	E_{res} (E_h)	Γ (E_h)	n^*	gf
		2s5dσ				2s5fσ		
1.00	1.00823	0.00296	4.87859	3	1.01215	0.00049	4.99668	3
1.05	0.92133	0.00343	4.87986	2	0.92517	0.00042	4.99536	3
1.10					0.84668	0.00041	4.99632	3
1.15	0.77071	0.00291	4.85440	3	0.77550	0.00044	4.99740	5
1.20	0.70561	0.00274	4.84710	3	0.71060	0.00044	4.99572	5
1.25	0.64614	0.00279	4.84100	3	0.65131	0.00042	4.99461	3
1.30	0.59152	0.00267	4.83220	3	0.59701	0.00044	4.99509	4
1.35	0.54126	0.00252	4.82344	3	0.54693	0.00045	4.99080	3
1.40	0.49487	0.00219	4.81386	4	0.50043	0.00049	4.97670	3
1.45	0.45200	0.00226	4.80545	4	0.45817	0.00041	4.98634	4
1.50	0.41221	0.00226	4.79583	4	0.41878	0.00041	4.98811	4
1.55	0.37518	0.00224	4.78500	4	0.38224	0.00044	4.99102	5
1.60	0.34071	0.00224	4.77495	4	0.34814	0.00044	4.99095	5
1.65	0.30853	0.00234	4.76451	3	0.31633	0.00044	4.99054	7
1.70	0.27850	0.00248	4.75602	3	0.28660	0.00046	4.99015	5
1.75	0.25074	0.00283	4.75765	3	0.25876	0.00047	4.98936	4
1.80	0.22344	0.00177	4.72520	3	0.23268	0.00052	4.98946	4
1.85	0.19811	0.00222	4.70351	3	0.20821	0.00051	4.99042	4
1.90	0.17426	0.00275	4.68291	4	0.18516	0.00047	4.99033	4
1.95	0.15134	0.00381	4.65228	4	0.16343	0.00045	4.99019	5
2.00					0.14293	0.00044	4.98976	6
		2s6s				2s6pσ		
1.00	1.01392	0.00038	5.05262	3	1.02904	0.00171	5.62465	4
1.05	0.92756	0.00032	5.07135	4	0.94178	0.00169	5.61016	5
1.10	0.84936	0.00035	5.08180	5	0.86296	0.00177	5.59711	4
1.15	0.77783	0.00031	5.07169	5	0.79150	0.00183	5.58663	5
1.20	0.71337	0.00031	5.08446	5	0.72647	0.00179	5.57870	4
1.25	0.65428	0.00029	5.08979	5	0.66703	0.00178	5.57026	5
1.30	0.60028	0.00029	5.10015	5	0.61256	0.00175	5.56361	4
1.35	0.55041	0.00030	5.10270	5	0.56242	0.00174	5.55511	4
1.40	0.50482	0.00028	5.11801	6	0.51627	0.00161	5.55101	4
1.45	0.46253	0.00029	5.12732	6	0.47356	0.00158	5.54498	4
1.50	0.42333	0.00033	5.13553	6	0.43397	0.00154	5.53870	4
1.55	0.38690	0.00040	5.14240	7	0.39718	0.00183	5.53220	3
1.60	0.35288	0.00060	5.14511	7	0.36313	0.00155	5.53436	6
1.65	0.32096	0.00125	5.14096	4	0.33114	0.00142	5.52609	6
1.70					0.30126	0.00135	5.51908	5
1.75	0.26587	0.00090	5.22599	5	0.27327	0.00132	5.51189	5
1.80	0.23983	0.00059	5.22744	6	0.24698	0.00140	5.50320	4
1.85	0.21547	0.00046	5.23281	7	0.22224	0.00190	5.49335	3
1.90	0.19261	0.00040	5.23949	6	0.19976	0.00179	5.51715	3
1.95	0.17108	0.00045	5.24614	5	0.17767	0.00115	5.50153	5
2.00	0.15089	0.00053	5.25711	4	0.15685	0.00097	5.48764	6
		2s6dσ				2s7s		
1.00	1.03417	0.00163	5.86761	3	1.03739	0.00020	6.03748	3
1.05	0.94712	0.00182	5.86187	2	0.95079	0.00016	6.05617	3
1.10	0.86843	0.00153	5.85350	3	0.87248	0.00017	6.06771	4
1.15	0.79705	0.00151	5.84529	3	0.80118	0.00017	6.06325	4
1.20	0.73205	0.00150	5.83755	3	0.73655	0.00017	6.07538	4
1.25	0.67263	0.00152	5.82916	3	0.67740	0.00017	6.08106	5
1.30	0.61811	0.00146	5.81943	3	0.62324	0.00018	6.08997	5
1.35	0.56795	0.00178	5.80880	2	0.57316	0.00021	6.08220	4
1.40	0.52173	0.00145	5.80026	3	0.52737	0.00030	6.09640	5
1.45					0.48468	0.00067	6.08963	5
1.50	0.43969	0.00103	5.79913	3				
1.55	0.40258	0.00100	5.77578	5	0.41029	0.00064	6.18775	5
1.60	0.36814	0.00103	5.75972	5	0.37619	0.00040	6.18733	6
1.65	0.33599	0.00106	5.74289	5	0.34447	0.00031	6.19239	6
1.70	0.30587	0.00113	5.72366	6	0.31488	0.00027	6.19969	7
1.75	0.27751	0.00131	5.69854	6	0.28719	0.00024	6.20711	7
1.80	0.25062	0.00178	5.66180	5	0.26124	0.00023	6.21535	5
1.85					0.23687	0.00028	6.22300	4
1.90					0.21403	0.00032	6.23592	5
1.95	0.18385	0.00190	5.77838	4	0.19247	0.00027	6.24516	6
2.00	0.16291	0.00172	5.75675	4	0.17213	0.00026	6.25431	5

Table 7.3 – Continued from previous page

R (a_0)	E_{res} (E_h)	Γ (E_h)	n^*	gf	E_{res} (E_h)	Γ (E_h)	n^*	gf
		2s7pσ				2s7dσ		
1.00	1.04659	0.00109	6.61739	4	1.04979	0.00115	6.86230	2
1.05	0.95946	0.00112	6.60361	4	0.96276	0.00096	6.85531	3
1.10	0.88076	0.00116	6.59121	4	0.88416	0.00092	6.84839	3
1.15	0.80939	0.00120	6.57996	4	0.81283	0.00116	6.84007	2
1.20	0.74445	0.00118	6.57334	4	0.74788	0.00089	6.83129	3
1.25	0.68506	0.00118	6.56375	4	0.68850	0.00092	6.82101	3
1.30	0.63067	0.00114	6.55841	4	0.63404	0.00097	6.80948	2
1.35	0.58031	0.00125	6.52915	4	0.58453	0.00073	6.84424	4
1.40	0.53446	0.00125	6.54274	3	0.53798	0.00076	6.80403	6
1.45	0.49184	0.00112	6.53902	4	0.49521	0.00069	6.78811	4
1.50	0.45231	0.00107	6.53352	5	0.45557	0.00067	6.77328	4
1.55	0.41558	0.00102	6.52681	5	0.41872	0.00063	6.75678	5
1.60	0.38138	0.00096	6.51998	4	0.38439	0.00065	6.73864	4
1.65	0.34946	0.00095	6.51169	4	0.35227	0.00071	6.71440	4
1.70	0.31959	0.00096	6.50081	4	0.32208	0.00090	6.67921	5
1.75	0.29153	0.00116	6.48419	3				
1.80	0.26625	0.00128	6.53942	3	0.27000	0.00128	6.81860	4
1.85	0.24134	0.00090	6.51109	5	0.24509	0.00112	6.78687	4
1.90	0.21799	0.00082	6.49071	6	0.22176	0.00104	6.76473	4
1.95	0.19610	0.00139	6.47857	6	0.19985	0.00097	6.74966	5
2.00	0.17573	0.00110	6.48658	6	0.17921	0.00090	6.73787	6
		2s8s				2s8pσ		
1.00	1.05178	0.00012	7.02867	2	1.05775	0.00077	7.61298	4
1.05	0.96502	0.00011	7.04486	2	0.97069	0.00079	7.59910	4
1.10	0.88664	0.00011	7.05689	3	0.89206	0.00081	7.58766	4
1.15	0.81541	0.00012	7.05589	3	0.82074	0.00083	7.57630	4
1.20	0.75058	0.00037	7.05715	0	0.75584	0.00082	7.57063	4
1.25	0.69148	0.00013	7.07090	4	0.69650	0.00082	7.56044	4
1.30	0.63721	0.00019	7.07513	4	0.64216	0.00085	7.55792	3
1.35	0.58684	0.00037	7.03695	2				
1.40	0.54242	0.00090	7.18324	4	0.54598	0.00086	7.53795	4
1.45	0.49965	0.00040	7.16453	4	0.50336	0.00078	7.53270	4
1.50	0.46020	0.00026	7.16427	5	0.46385	0.00075	7.52591	4
1.55	0.42362	0.00021	7.16919	5	0.42714	0.00072	7.51787	4
1.60	0.38960	0.00018	7.17665	6	0.39296	0.00068	7.50846	4
1.65	0.35789	0.00016	7.18520	6	0.36102	0.00072	7.49440	3
1.70	0.32827	0.00016	7.19412	6	0.33106	0.00097	7.46881	3
1.75	0.30054	0.00015	7.20177	3	0.30393	0.00082	7.54114	4
1.80	0.27455	0.00023	7.21060	4	0.27756	0.00065	7.51112	5
1.85	0.25019	0.00020	7.22432	4				
1.90	0.22725	0.00018	7.23385	4	0.22988	0.00093	7.49664	5
1.95	0.20563	0.00017	7.24321	6	0.20807	0.00071	7.48709	4
2.00	0.18523	0.00017	7.25230	7	0.18745	0.00061	7.47338	5
		2s8dσ						
1.00	1.05988	0.00068	7.85942	2				
1.05	0.97287	0.00090	7.85005	2				
1.10	0.89431	0.00071	7.84639	2				
1.15	0.82302	0.00062	7.83705	2				
1.20	0.75810	0.00064	7.82786	2				
1.25	0.69889	0.00146	7.83261	1				
1.30	0.64458	0.00044	7.83443	4				
1.35	0.59414	0.00075	7.77533	2				
1.40	0.54821	0.00054	7.78846	4				
1.45								
1.50	0.46596	0.00043	7.76088	4				
1.55	0.42916	0.00041	7.74164	4				
1.60	0.39484	0.00045	7.71660	4				
1.65	0.36270	0.00059	7.67757	3				
1.70	0.33240	0.00088	7.61192	4				
1.75								
1.80	0.28002	0.00071	7.78517	3				
1.85								
1.90	0.23215	0.00059	7.74812	6				
1.95	0.21033	0.00057	7.73548	5				
2.00	0.18974	0.00055	7.72467	6				

other $n = 3$ states. These resonances lie very close together and make the interpolation of the resonances as a function of R very difficult. Also as the $n = 3$ target states have similar shaped curves it is also difficult to determine which are the 'intruder' resonances. Therefore resonance curves for the resonances detected between the 2sσ and 3pσ states have not been determined. The resonances detected above 3pσ have negative goodness factors implying that the fit is poor, hence these resonances were ignored.

In principle there are an infinite number of resonances associated with each target state for each n and each l. There is in fact a double infinity, as for each l there is an infinite number of n, and there are an infinite number of l. However in practise the number of resonances determined is limited by the choice of partial waves, which in this calculation is states with $l \leq 7$. Hence we can assume that states with $l > 7$ have quantum defects very close to zero.

7.2 Final state distribution results

For the final state probability distribution of the electronic continuum the contribution from resonances and the background continuum have been calculated separately. Transitions involving the β-decay of T_2 molecules in the ground rovibrational level of the $n = 1$ electronic state have been considered.

7.2.1 Probability distribution of the resonances

In chapter 2, the following equation (given by Jeziorski *et al.* [112]) was stated for the probability distribution involving transitions to the nuclear motion continuum of the electronically bound states of $^3HeT^+$:

$$P_{nJ}(E) = (2J+1)\left|\int_0^\infty S_n(R) j_J(KR) f_{nJ}^{^3HeT^+}(R|E) f_{100}^{T_2}(R)\, dR\right|^2, \qquad (7.6)$$

where $P_{nJ}(E)$ is the probability per unit energy that the $^3HeT^+$ molecule dissociates via the nth electronic state and that the dissociation products are in a state with energy E and angular momentum J, $j_J(KR)$ is the spherical Bessel function, $f_{100}^{T_2}(R)$ is the radial vibrational wave function of the $n = 1$, $v = 0$, $J = 0$ state of T_2 and $f_{nJ}^{^3HeT^+}(R|E)$ is the energy normalised radial function of the continuous spectrum. $S_n(R)$ is the overlap integral providing the R-dependent probability amplitude of transition to the n^{th} electronic

state of the daughter system given by:

$$S_n(R) = \int \psi_n^{^3\mathrm{HeT}^{+}\,*}(r_1, r_2; R)\psi_1^{\mathrm{T}_2}(r_1, r_2; R)\, dr_1\, dr_2. \tag{7.7}$$

where $\psi_n^c(r_1, r_2; R)$ are the clamped-nuclei electronic wavefunctions for the initial ($c = \mathrm{T}_2$) and final ($c = {}^3\mathrm{HeT}^+$) state.

Equation (7.6) can also be used to calculate the probability density distribution of the resonance states if they are considered as quasibound states embedded in the continuum and are decoupled from the background continuum. The label n in equations (7.6) and (7.7) now refers to the combined configuration of the 2 electrons. By using this equation, the R dependence of the resonance is taken into account explicitly. However, before $P_{nJ}(E)$ for a particular resonance can be calculated, the overlap $S_n(R)$ must be determined. The electronic wavefunctions for the resonance states can be extracted from the R-matrix calculation discussed in the previous section whilst the wavefunction for T_2 can be obtained by performing an e - T_2^+ scattering calculation.

As discussed in chapter 3, the full energy-dependant scattering wavefunction Ψ_E in the inner region, is a linear combination of the energy-independent eigenfunctions, ψ_k, describing the target molecule plus scattering electron system within the R-matrix sphere:

$$\Psi_E = \sum_k A_{Ek}\psi_k, \tag{7.8}$$

where the coefficients A_{Ek} are found by matching with the computed outer region functions at the boundary using the R-matrix. ψ_k are represented by the close coupling expansion given by equation (3.38) and have associated energies, E_k, called 'R-matrix poles', which are calculated by the SCATCI module. In the outer region, the total wavefunction Ψ_E is given by equation (3.39).

In order to determine $S_n(R)$ several assumptions have been made. The first key assumption is that the wavefunction describing the ground electronic state of T_2, with energy $E_1^{\mathrm{T}_2}$, is entirely localised inside the R-matrix sphere. Therefore in equation (7.8) the coefficient A_{Ek} at $\mathrm{E} \simeq \mathrm{E}_1^{\mathrm{T}_2}$ becomes the Dirac delta function, $\delta(E - E_1^{\mathrm{T}_2})$, and so the wavefunction for the T_2 ground state is given by the eigenfunction $\psi_1^{\mathrm{T}_2}$ which has an associated R-matrix pole $\mathrm{E}_k \simeq \mathrm{E}_1^{\mathrm{T}_2}$. This is a valid assumption for the short range ground electronic state of T_2 which is the only state considered in this work. By making this assumption we can therefore ignore the total wavefunction describing the ${}^3\mathrm{HeT}^+$ system in the outer region as the overlap of this wavefunction with the T_2 wavefunction will be zero.

The next assumption made is that the wavefunction describing the resonance is also totally localised inside the R-matrix box. This is a reasonable assumption for the low lying resonances but becomes worse for higher lying resonances. The coefficient A_{Ek} at $E \simeq E_{res}$ becomes the Dirac delta function, and so the wavefunction for the resonance is given by the eigenfunction $\psi_k^{^3HeT^+}$ with an associated R-matrix pole $E_k \simeq E_{res}$.

The eigenfunction describing the resonance state n is given by (c.f. equation (3.38)):

$$\psi_n^{^3HeT^+}(r_1, r_2; R) = \sum_l c_l(R)\phi_l^{CSF}(r_1, r_2), \tag{7.9}$$

where ϕ_l^{CSF} are configuration state functions normalised over the inner region, which include the contribution from both the 'target+continuum' functions and L^2 functions. Similarly, the eigenfunction describing the T_2 ground state is given by:

$$\psi_1^{T_2}(r_1, r_2; R) = \sum_m d_m(R)\varphi_m^{CSF}(r_1, r_2), \tag{7.10}$$

and the overlap integral is then:

$$S_n(R) = \int \sum_l c_l^*(R)\phi_l^{CSF*}(r_1, r_2) \sum_m d_m(R)\varphi_m^{CSF}(r_1, r_2)\, dr_1\, dr_2. \tag{7.11}$$

If $\psi_n^{^3HeT^+}$ and $\psi_1^{T_2}$ are expanded in the same basis, i.e. ϕ_l^{CSF} and φ_m^{CSF} are identical, then $S_n(R)$ reduces to:

$$\begin{aligned} S_n(R) &= \sum_l c_l^*(R) \sum_m d_m(R) \int \phi_l^{CSF*}(r_1, r_2)\varphi_m^{CSF}(r_1, r_2)\, dr_1\, dr_2 \\ &= \delta_{lm} \sum_l c_l^*(R) d_l(R). \end{aligned} \tag{7.12}$$

which is a straightforward vector multiplication.

To obtain $\psi_1^{T_2}$ in the same basis as $\psi_n^{^3HeT^+}$ an (inner region only) R-matrix calculation for e - T_2^+ scattering was performed using the same target molecular orbitals and continuum orbitals as in the e - $^3HeT^{2+}$ calculation discussed above, for the same geometries. At each R, the first (i.e. lowest energy) R-matrix pole corresponds to the ground state of T_2. The eigenfunction associated to that pole was therefore selected to represent the state at that R. The R-matrix poles obtained for the T_2 ground state in this calculation are given in table 7.4. The poles were compared to the T_2 potential from [163], which has been used in this work for the calculation of the final state distribution (see chapter 5). This potential and the differences between it and the poles are also given in the table. The poles are in good agreement with the energies, with differences

Table 7.4: Energies of the T_2 ground state, in E_h, as a function of the internuclear separation R, in a_0, obtained in the R-matrix calculation. Also given are the T_2 potential from [163] (column 2) and the difference between these energies (column 3)

R	R-matrix	[163]	Difference
1.00	−1.121904077	−1.124350006	0.002445929
1.05	−1.136284136		
1.10	−1.147507149	−1.149874337	0.002367188
1.15	−1.156087015		
1.20	−1.162466567	−1.164758239	0.002291672
1.25	−1.166992423		
1.30	−1.169962863	−1.172175518	0.002212655
1.35	−1.171621233	−1.173794540	0.002173307
1.40	−1.172174258	−1.174308820	0.002134562
1.45	−1.171796390	−1.173892312	0.002095922
1.50	−1.170632358	−1.172692313	0.002059955
1.55	−1.168819496		
1.60	−1.166448621	−1.168424160	0.001975539
1.65	−1.163614991		
1.70	−1.160400060	−1.162302522	0.001902462
1.75	−1.156870805		
1.80	−1.153085747	−1.154915030	0.001829283
1.85	−1.149094483		
1.90	−1.144941649		
1.95	−1.140664067		
2.00	−1.136295566	−1.137982819	0.001687253

less than 0.0025 E_h, which proves the validity of the assumption made on the entire localisation of the T_2 ground state wavefunction inside the R-matrix sphere.

Obtaining the eigenfunctions for the resonance states was a little more complicated. There are a large number of poles that lie in the energy region corresponding to the electronic continuum of $^3HeT^+$, whose associated eigenfunctions $\psi_k^{^3HeT^+}$ describe the resonance states and the background continuum in a discrete form. To identify which eigenfunction represents a particular resonance two methods were used simultaneously. Firstly, as the poles lie close together, the resonances were matched to poles by their effective quantum number rather than matching by energy. n^* were obtained for all of the poles, relative to the nearest $^3HeT^{2+}$ target threshold, and so were consistent with the n^* obtained in RESON for the resonances. Although this proved to be easier than matching by energy, there were cases where there was a couple of poles with very similar n^*. Even though the entire localisation of the resonance inside the R-matrix sphere is a reasonable assumption for lower lying resonances, it is not exact, hence the resonance energy will not match a pole exactly but be very close. This means that the pole with the closest energy may not necessarily be the one describing the resonance.

The second method used was to analyse the overlaps of all the eigenfunctions with the ground state T_2 eigenfunction $\psi_1^{T_2}$. For every eigenfunction ψ_k in the set, the overlap $S_n(R)$ was obtained by using equation (7.12) for every geometry. The coefficients c_l and d_l are calculated in the SCATCI module. It is expected the eigenfunctions describing the resonance states will have larger overlaps than those describing the background continuum. This was found to be true for most of the poles. Using both these methods simultaneously, the poles/eigenfunctions and overlap integrals as a function of R for nine resonance states were determined.

For some of the cases where the pole describing the resonance state lay very close to another pole there was some mixing of the overlaps, resulting in a slightly too small or too large value for the overlap of the resonance at that R. To treat this the overlap was smoothed out against those at the neighbouring geometries. The (smoothed) overlaps $S_n(R)$ for the nine resonance states are given in table 7.5. At some geometries it was not possible to determine the correct pole with sufficient certainty and no overlap was determined. For some of the higher lying resonances which lie very close together, it was not possible to identify the corresponding eigenfunction because of the overlap mixing as mentioned above. For even higher resonances the transition probability to these states

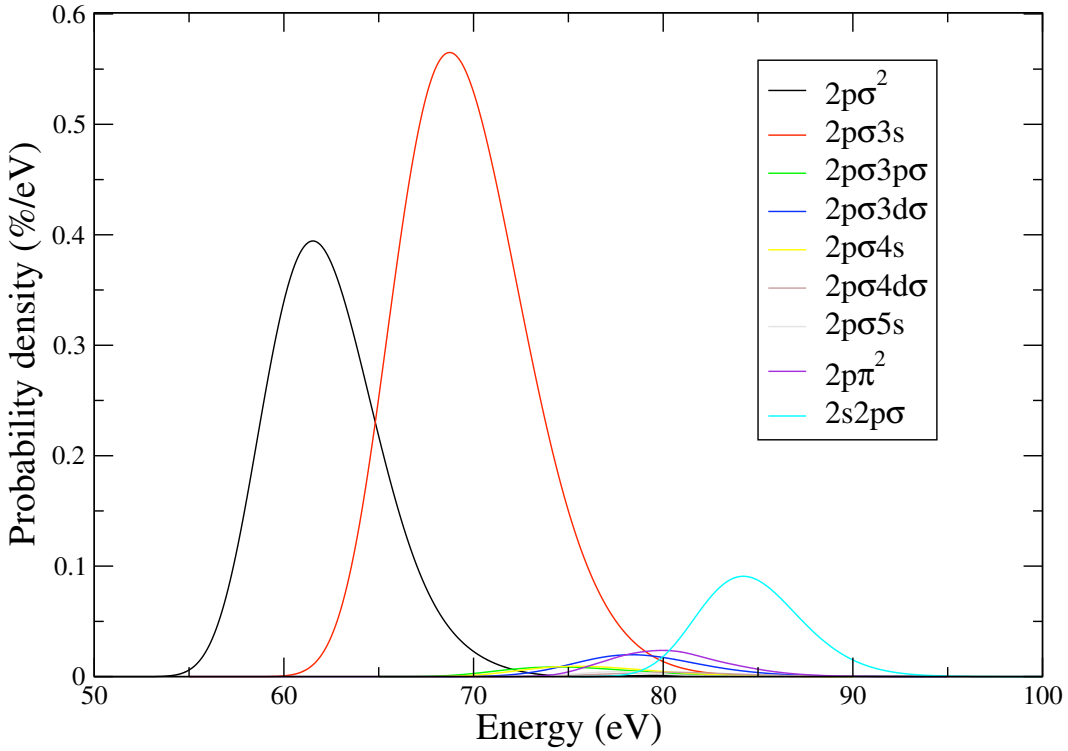

Figure 7.4: Final state probability density distribution for nine resonance states of $^3HeT^+$ resulting from the β-decay of a T_2 molecule in the ground rovibrational state of the $n = 1$ electronic state.

is very small and so the overlap integral for the resonances is of the same order as the overlap for the background continuum.

The probability density distribution of each resonance was obtained by using the modified BCONT code to calculate the radial functions $f_{100}^{T_2}(R)$ and $f_{nJ}^{^3HeT^+}(R|E)$ and hence the probability density $P_{nJ}(E)$, as described in chapters 3 and 5, for the β-decay of a T_2 molecule in the ground rovibrational state of the $n = 1$ electronic state. The probability density distributions of the nine resonance states of $^3HeT^+$ are shown in figure 7.4. The total probabilities associated with each resonance are given in table 7.6 together with the probabilities obtained by Froelich *et al.* [149] for the first five resonances. As can be seen from the figure and table, there is a significant contribution from the $2p\pi^2$ and $2s2p\sigma$ which were not present in the calculation of reference [149].

Table 7.5: Overlap integrals $S_n(R)$ between nine resonance states of $^3HeT^+$ with the electronic ground state of T_2.

R	$2p\sigma^2$	$2p\sigma 3s$	$2p\sigma 3p\sigma$	$2p\sigma 3d\sigma$	$2p\sigma 4s$	$2p\sigma 4d\sigma$	$2p\sigma 5s$	$2p\pi^2$	$2s2p\sigma$
1.00			0.02716						
1.05			0.02630		0.02116				
1.10			0.02600		0.02231				
1.15			0.02576		0.02369				
1.20	0.09774	0.19751	0.02568	0.05381	0.02352			0.05095	
1.25	0.11281	0.20146	0.02446	0.05189	0.02324	0.02190	0.01019	0.04886	
1.30	0.12016	0.20504	0.02386	0.04959	0.02331	0.02027	0.00971	0.04437	0.08073
1.35	0.14483	0.20841	0.02437	0.04659	0.02494	0.01910	0.00947	0.04272	0.08037
1.40	0.16025	0.21128	0.02487	0.04291	0.02597	0.01928	0.00940	0.03945	0.07922
1.45	0.17765	0.21657	0.02666	0.03785	0.02747	0.01983		0.03956	0.07820
1.50	0.19183	0.22252	0.02849	0.03249	0.02942	0.01408	0.02234	0.03947	0.07776
1.55	0.20221	0.23058	0.03020	0.02756	0.03143	0.01560	0.02265	0.03926	0.07619
1.60	0.21506	0.24088	0.03382		0.03432	0.01600	0.02220	0.04156	0.07441
1.65	0.22535	0.24830				0.01550	0.02148	0.04080	0.07058
1.70	0.23346	0.25536				0.01620	0.01880	0.03902	0.06963
1.75	0.23484	0.25701				0.01532	0.01919	0.03909	0.06669
1.80	0.23447	0.26122				0.01453	0.01976	0.03886	0.06312
1.85	0.23556	0.26574				0.01205	0.02174	0.04214	0.06091
1.90	0.23520	0.26992				0.01218	0.02196	0.03644	0.05455
1.95	0.23696	0.27406				0.01121	0.02266	0.04203	0.05360
2.00	0.23751	0.27909				0.01200	0.02466	0.03306	0.04617

Table 7.6: Total probabilities, in %, of nine resonance states of $^3HeT^+$. For comparison, the probabilites obtained for the first five resonances in ref. [149] are also given.

Resonance	This work	[149]
$2p\sigma^2$	2.91	2.9
$2p\sigma 3s$	4.74	4.8
$2p\sigma 3p\sigma$	0.08	0.02
$2p\sigma 3d\sigma$	0.16	0.2
$2p\sigma 4s$	0.08	0.3
$2p\sigma 4d\sigma$	0.03	
$2p\sigma 5s$	0.03	
$2p\pi^2$	0.17	
$2s2p\sigma$	0.61	

7.2.2 Probability distribution of the background continuum

The total transition probability P_n from the T_2 ground state to all rovibrational and scattering states associated with the n^{th} electronic state of $^3HeT^+$ is given by [118]:

$$P_n = \int_0^\infty S_n(R) f_{100}^{T_2}(R)\, dR \tag{7.13}$$

The use of this equation to check the internal consistency and accuracy of the calculated probabilities to the first six lowest electronic states of $^3HeT^+$ has been discussed in chapter 5.

If $S_n(R)$ is a slowly varying function of R then:

$$\begin{aligned} P_n &\simeq S_n^2(R_e) \int_0^\infty [f_{100}^{T_2}(R)]^2\, dR \\ &= S_n^2(R_e) \end{aligned} \tag{7.14}$$

where R_e is the equilibrium geometry of the T_2 molecule ($R_e = 1.4\ a_0$). Hence if nuclear motion is not taken into account, the probability to a given state n is simply given by the overlap integral squared.

If the eigenfunctions $\psi_k^{^3HeT^+}$ representing the nine resonance states are removed from the complete set, as well as those representing the bound states, the remaining eigenfunctions can be used as a discrete representation of the background continuum and the remaining infinite number of resonances. Equation (7.14) can then be used

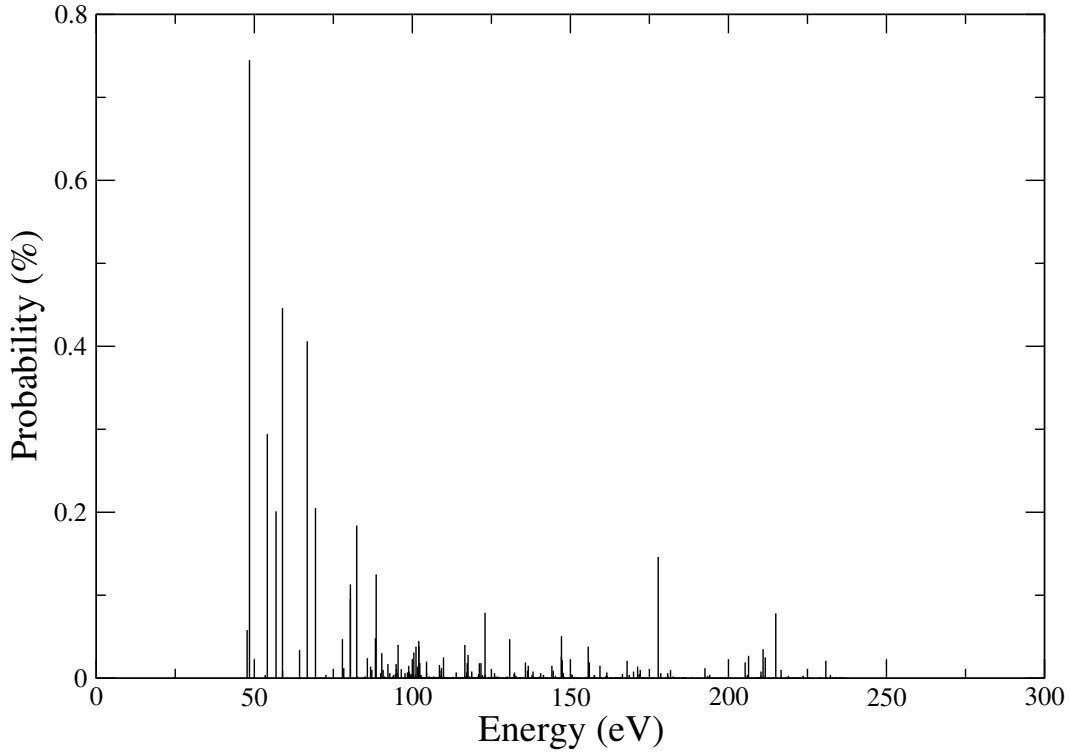

Figure 7.5: Discrete final state probability distribution of the background continuum and remaining resonances. See text for details

to obtain the (discrete) probability distribution of the background continuum and the remaining resonances. These results are shown in figure 7.5.

To obtain a continuous final state spectrum of the background continuum, a Gaussian was run through the discrete distribution with an energy resolution of 4 eV. The final state probability density distribution of the background continuum and remaining resonances is shown in figure 7.6 together with the distribution of the nine resonance states of $^3HeT^+$ that were considered separately.

The total probability associated with the electronic continuum obtained in this work up to 240 eV is 13.66%. Above 240 eV the total probability from the background continuum and remaining resonances is 0.58%.

A comparison of the (binned) final state probability distribution of the electronic continuum obtained in this work with the most recent distribution obtained by Saenz, Jonsell and Froelich [106] is shown and discussed in chapter 9.

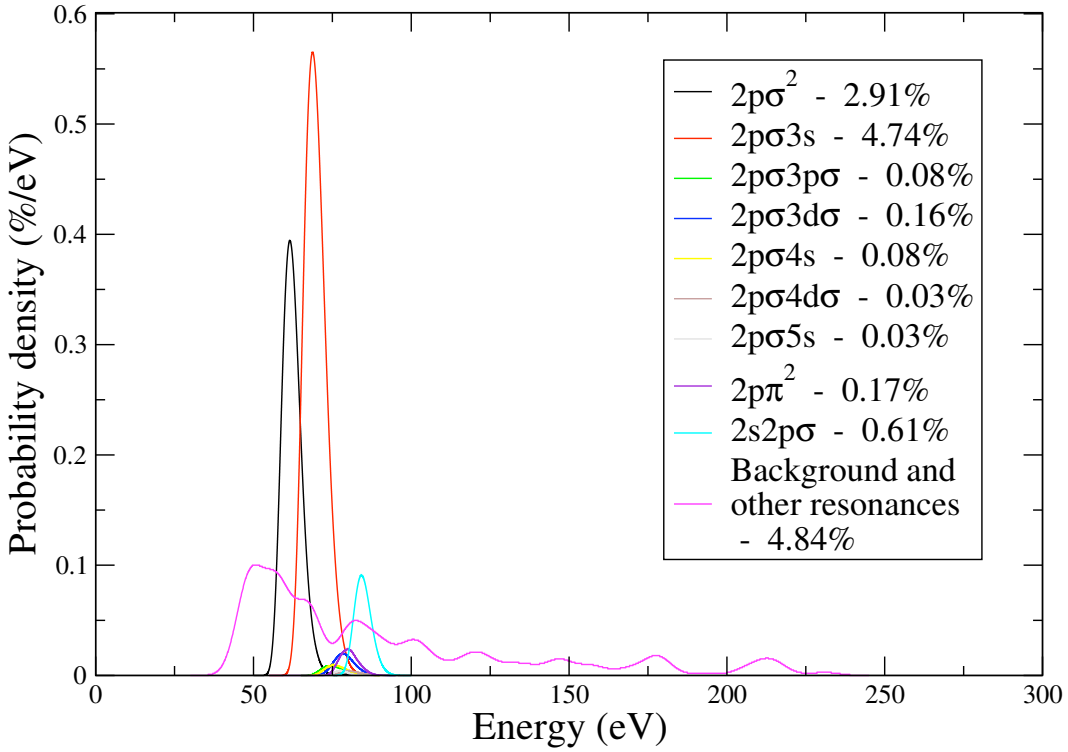

Figure 7.6: Final state probability density distribution for the electronic continuum of $^3HeT^+$ resulting from the β-decay of a T_2 molecule in the ground rovibrational state of the $n = 1$ electronic state.

Chapter 8

Endpoint considerations of other tritium species

In chapter 5 the final state distributions of the first six electronic states of $^3HeD^+$ and $^3HeH^+$ resulting from the β-decay of the T_2 isotopomers, HT and DT, were calculated. With the main contamination of the T_2 source expected to be from DT molecules, estimates of the error in the value of the neutrino mass deduced from fitting theoretical curves, due to uncertainties in the percentage of DT molecules in the source were obtained and discussed in chapter 6. This isotope contamination, which comes from the fact that the isotopic purity of tritium is around 95%, will be monitored using laser Raman spectroscopy [172].

However, source contamination from other tritium containing species could also occur in the WGTS. These other species – T^-, T, T^+, T_2^+, T_3^+ and T_5^+ – can arise from the interaction of the β electrons with the source molecules, and from the β-decay itself. The β-decay of these species, which will have slightly different endpoint energies due to the different ground state energies of the parent and daughter atom/molecule, will contribute to the overall β spectrum. In this chapter, estimates of the endpoint energies of the different species relative to the endpoint energy of T_2 are obtained, to see if they will have any contribution in the small energy region (about 30 eV) close to the endpoint which will be analysed by the KATRIN experiment.

The tritium species discussed above can be created by the processes listed below. These processes have been obtained from the KATRIN Design Report [98]. For more information the reader is referred to the KATRIN Design Report and the references therein.

The scattering of the energetic β electrons by the source molecules can result in the formation of T_2^+, T^+ and T through:

$$e^- + T_2 \rightarrow T_2^+ + 2e^-, \tag{8.1}$$

$$e^- + T_2 \rightarrow T + T^+ + 2e^-. \tag{8.2}$$

Subsequent collisions of the T_2^+ ions and source molecules produce T_3^+:

$$T_2^+ + T_2 \rightarrow T_3^+ + T. \tag{8.3}$$

T_5^+ ions can be created by further (three-body) collisions of the T_3^+ ions with the neutral gas molecules:

$$T_3^+ + 2T_2 \rightarrow T_5^+ + T_2. \tag{8.4}$$

The T^- ions can be formed from the dissociative attachment of T_2:

$$e^- + T_2 \rightarrow T^- + T^+. \tag{8.5}$$

T^+ is also formed from the break up of the daughter molecule created in the primary β-decay:

$$T_2 \rightarrow e^- + {}^3HeT^+ \rightarrow e^- + T^+ + {}^3He. \tag{8.6}$$

The equations for the β-decay of these species are:

$$T^+ \rightarrow {}^3He^{++} + e^- + \bar{\nu}_e, \tag{8.7}$$

$$T \rightarrow {}^3He^+ + e^- + \bar{\nu}_e, \tag{8.8}$$

$$T^- \rightarrow {}^3He + e^- + \bar{\nu}_e, \tag{8.9}$$

$$T_2^+ \rightarrow {}^3HeT^{++} + e^- + \bar{\nu}_e, \tag{8.10}$$

$$T_3^+ \rightarrow {}^3HeT_2^{++} + e^- + \bar{\nu}_e, \tag{8.11}$$

$$T_5^+ \rightarrow {}^3HeT_4^{++} + e^- + \bar{\nu}_e. \tag{8.12}$$

To obtain the endpoint energies of these species relative to the endpoint of T_2, the ground state energies of the parent atoms/molecules need to be determined on the same energy scale, and similarly for the daughter atoms/molecules. Here, the energies of the bare nuclei, T^+ and ${}^3He^{++}$ have been set as the energy zeros. For the ground states of the T_2 and ${}^3HeT^+$ molecules, results obtained from the LEVEL code discussed in chapter 5 have been used. On this energy scale, the energies of the (v=0, J=0) rovibrational levels of T_2 and ${}^3HeT^+$ are -31.8 and -80.9 eV respectively.

For the atomic species the energies are trivial. The ionisation energies for atomic hydrogen and helium and the electron affinity of hydrogen, which are well known, can be found in many books or online databases. The ground state energy of the hydrogen atom is simply given by the negative of the ionisation energy, i.e. -13.6 eV. The electron affinity of the hydrogen atom is approximately 0.75 eV, therefore the energy of T^- is -14.35 eV. The first and second ionisation energies for the helium atom are 24.6 and 54.4 eV, hence the ground state energies of $^3He^+$ and ^3He are -54.4 eV and -79.0 eV respectively.

The solution of the exact wavefunctions and energy values of the ground electronic state of the hydrogen molecular ion have been studied by many authors, e.g [179–184]. The equilibrium internuclear separation is found to be approximately $R = 2.0\ a_0$ [183] and the electronic energy at this R is -2.20525 Rydbergs (-1.102625 E_h) [184]. To obtain the potential energy, the nuclear repulsion energy, $E = \frac{Z_A Z_B e^2}{R} = \frac{1}{2}\ E_h$, must be added to the electronic energy. Converting to electronvolts, the potential energy is -16.4 eV. This value corresponds to the potential minimum, hence for the the ground rovibrational state, the zero point energy (ZPE) must be taken into account. The ZPE of T_2^+ was obtained from 'Constants of Diatomic Molecules' by Huber and Herzberg [185] and is approximately 0.08 eV, thus giving the energy of the (v=0, J=0) state to be -16.32 eV. For the electronic ground state of $^3HeT^{++}$, the potential energy at $R = 2.0\ a_0$, -41.15 eV, was computed using the code by Power [176] as in chapter 7.

The equilibrium geometry of T_3^+ is an equilateral triangle, however when the zero point energy effect is taken into account the range of geometries corresponding to the ground rovibrational state will deviate from the equilibrium structure. As the ground state potential curve of $^3HeT_2^{++}$ is repulsive, by considering vertical transitions, any small changes in the geometry of T_3^+ could result in large energy changes of $^3HeT_2^{++}$. A 1-dimensional image of this situation is shown in figure 8.1, although in reality the potentials of T_3^+ and $^3HeT_2^{++}$ are of course 3-dimensional. Therefore, by taking into account this ZPE effect, the β-decay endpoint will lie within a range of energies and will be dependant on the geometry of the molecule. The limits of the energy range will correspond to the geometry limits of the T_3^+ rovibrational ground state and the endpoints for intermediate geometries will fall within the range.

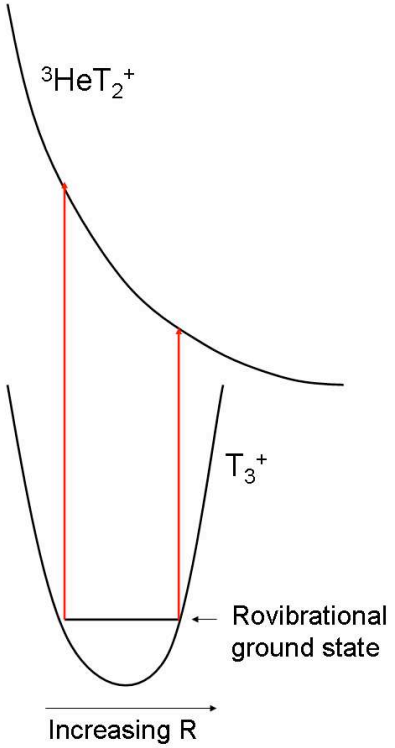

Figure 8.1: ZPE effect on the repulsive curve of $^3HeT_2^{++}$. See text for details.

To determine the geometry limits, the wavefunction and energy for the ground state of T_3^+ was calculated using the DVR3D program suite [186]. The DVR3D program suite calculates wavefunctions, energy levels, and dipole transition moments, for rotating and vibrating triatomic molecules. To describe the geometry of T_3^+, Jacobi coordinates were used, see figure 8.2. The Jacobi coordinate system uses two lengths and an angle (r_1, r_2, θ). r_1 represents the distance between the two atoms, T^1 and T^3, the 'diatom', and r_2 represents the distance from the centre of mass of the diatom to the third atom T^2. θ is the angle between r_1 and r_2.

The wavefunction of the rovibrational ground state obtained from the DVR3D program is shown in figure 8.3 as a function of r_1 and r_2, for $\theta = 90°$. The energy of the state relative to the potential minimum is 0.011795 E_h. In figure 8.4 the contours at 8%, 16%, 32%, and 64% of the wavefunction maximum are shown together with the contour of the potential energy curve at the energy of the rovibrational ground state. The geometry limits were taken from the black contour (8% of the wavefunction maximum), therefore allowing for some tunneling effects. The limits chosen were ($r_1 = 1.69\ a_0$, $r_2 = 1.92\ a_0$) and ($r_1 = 1.78\ a_0$, $r_2 = 1.05\ a_0$).

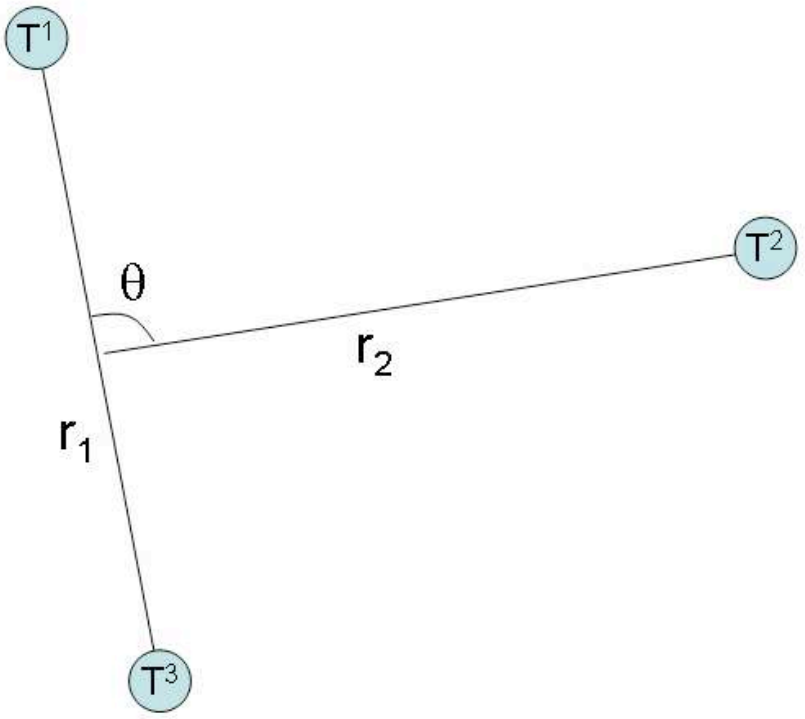

Figure 8.2: Jacobi coordinate system for T_3^+

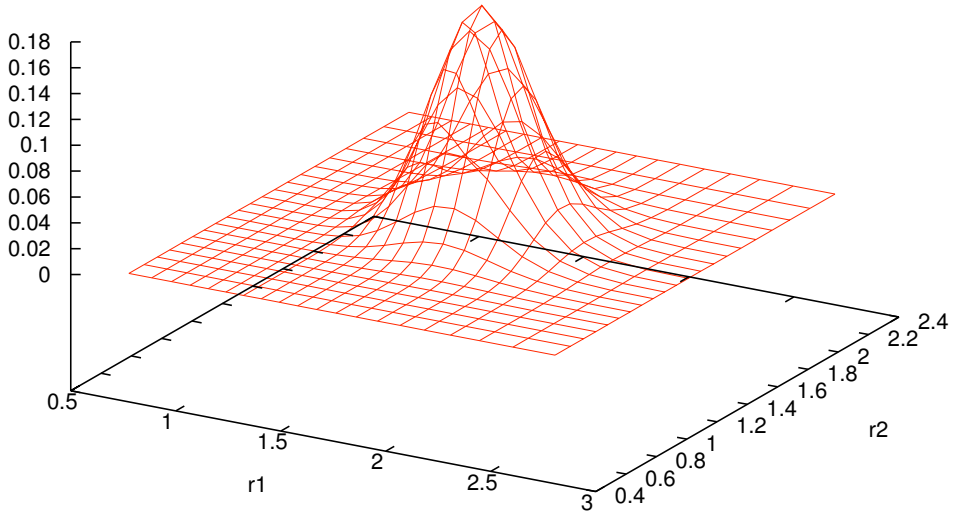

Figure 8.3: Wavefunction of the rovibrational ground state of T_3^+ calculated using the DVR3D program suite for $\theta = 90°$.

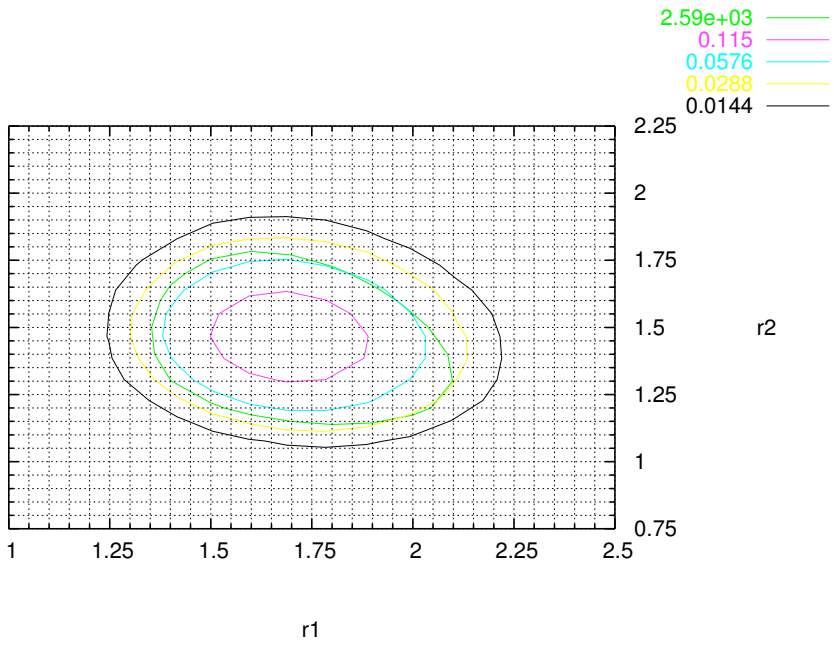

Figure 8.4: Contours of the wavefunction of the rovibrational ground state of T_3^+ drawn at 8% (black), 16% (yellow), 32% (blue) and 64% (pink) of the wavefunction maximum. Also shown is the contour of the potential energy curve at the energy of the rovibrational ground state (green).

The energy of the rovibrational ground state of T_3^+ calculated by the DVR3D program is given relative to the potential minimum, hence it is the ZPE of T_3^+. Therefore to obtain the absolute energy of the state, the energy of the potential minimum must be known. To determine this we used the MOLPRO package. MOLPRO is a package for ab initio molecular electronic structure calculations. It performs highly accurate computations with extensive treatment of the electron correlation problem through multiconfiguration reference CI, coupled cluster and associated methods. The potential energy was calculated for the equilibrium geometry of H_3^+, which is an equilateral triangle where the distance between any two of the atoms is 1.65 a_0. The energy given by MOLPRO for a CISD (closed-shell configuration interaction) calculation is -1.34359 E_h. Including the ZPE, the energy of the T_3^+ ground state is therefore -36.24 eV (-1.3318 E_h).

The potential energies of $^3HeT_2^{++}$ at the two geometry limits obtained earlier, were also calculated using MOLPRO. However, the potential energy of $^3HeT_2^{++}$ will differ depending on the which T nucleus is replaced with a ^{3}He nucleus. From symmetry

considerations, replacing either T^1 or T^3 with ^3He (see figure 8.2), will result in the same potential energy of $^3HeT_2^{++}$. However if it is T^2 which decays then the energy will be different. Therefore for each geometry both the decay of T^1 and T^2 was considered. Considering first the geometry ($r_1 = 1.69\ a_0$, $r_2 = 1.92\ a_0$), by replacing the T^1 nucleus with a ^3He nucleus, the potential energy obtained is -69.60 eV. Replacing the T^2 nucleus with a ^3He nucleus gives -67.39 eV. For the second geometry, ($r_1 = 1.78\ a_0$, $r_2 = 1.05\ a_0$), replacing the T^1 nucleus gives a potential energy of -65.45 eV, and replacing the T^2 nucleus gives -67.39 eV. Therefore the energy limits are -69.60 eV and -65.45 eV. To account for zero point energy in the repulsive curve of $^3HeT_2^{++}$, the ZPE of the dissociation products was considered. The electronic ground state of $^3HeT_2^{++}$ will dissociate to $^3HeT^+ + T^+$. The ZPE of $^3HeT^+$, which is obtained from the difference in the rovibrational ground state energy, -80.9 eV (see above), and the potential energy at the equilibrium distance $R = 1.46\ a_0$, -81.04 eV (see table 5.1), is 0.14 eV. This energy was added to the energy limits, giving final energy limits of -69.46 eV and -65.31 eV.

Several studies have been performed on the potential energy surface of H_5^+ [187–189]. The structure of the H_5^+ cluster is described by a tightly bound H_3^+ ion and an H_2 molecule. The structure that is found to give the lowest energy is of $C_{2\nu}$ symmetry [188], and is shown in figure 8.5. The energy of the stationary point on the potential for this geometry is -2.530509 E_h [188]. The ZPE for H_5^+, taken from reference [189], is 0.89 eV (7210 cm^{-1}). For an estimate of the ZPE for T_5^+, the ZPE of H_5^+ was scaled by the ratio of the ZPE's of T_3^+ and H_3^+. Using the ZPE of T_3^+ given above and the ZPE of H_3^+ from reference [190], 0.54 eV, this gives a value for the ZPE of T_5^+ of 0.53 eV. Hence the ground state energy of T_5^+ is estimated to be -68.33 eV.

For the potential energy of $^3HeT_4^{++}$, the same structure as shown in figure 8.5 was used. Considering that any of the five T atoms can undergo β-decay, and taking into account the symmetry of the molecule there are three possible structures of $^3HeT_4^{++}$ that will give different energies. The potential energies were calculated using MOLPRO. The three distinct energies obtained are -102.93, -104.96 and -109.30 eV. An estimate of the ZPE for $^3HeT_4^{++}$ was obtained in the same way as for $^3HeT_2^{++}$, by considering the the ZPE of the dissociation products. Assuming that $^3HeT_4^{++}$ dissociates to $^3HeT^+ + T_3^+$, the ZPE of $^3HeT_4^{++}$ is estimated to be 0.46 eV, using the values of the ZPE's of $^3HeT^+$ and T_3^+ given above. Hence the final energies are -102.47, -104.50 and -108.84

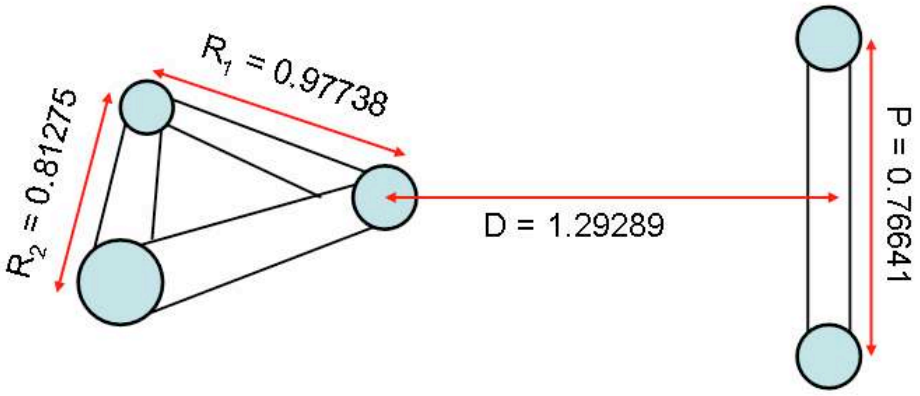

Figure 8.5: Global minimum structure for H_5^+

Table 8.1: Endpoint energies, in eV, for the β-decays of the other tritium species, relative to the endpoint for T_2 β-decay, represented by E_0

Decay Process	Endpoint energy (eV)
$T^+ \rightarrow {}^3He^{++} + e^- + \bar{\nu}_e$	$E_0 - 49.1$
$T \rightarrow {}^3He^+ + e^- + \bar{\nu}_e$	$E_0 - 8.3$
$T^- \rightarrow {}^3He + e^- + \bar{\nu}_e$	$E_0 + 15.55$
$T_2^+ \rightarrow {}^3HeT^{++} + e^- + \bar{\nu}_e$	$E_0 - 24.27$
$T_3^+ \rightarrow {}^3HeT_2^{++} + e^- + \bar{\nu}_e$	$(E_0 - 20.03) - (E_0 - 15.64)$
$T_5^+ \rightarrow {}^3HeT_4^{++} + e^- + \bar{\nu}_e$	$E_0 - 14.96$
	$E_0 - 12.93$
	$E_0 - 8.59$

eV.

The ground state energies of the tritium species discussed above are shown in figure 8.6. The arrows correspond to the β-decay between the parent and daughter molecule.

By taking the endpoint energy for T_2 β-decay as E_0, the endpoint energies for the β-decays of the other tritium species have been obtained and are given in table 8.1.

In table 8.2 the endpoint energies obtained in this work are compared to the values given in the KATRIN Design Report [98]. In reference [98] the endpoints are given relative to the atomic mass difference $\Delta M({}^3\mathrm{He}, \mathrm{T})$, hence for comparison the results obtained in this work have been shifted accordingly. Most of the results are in exact, or very good, agreement. However there appears to be a large difference, about 8 eV, for

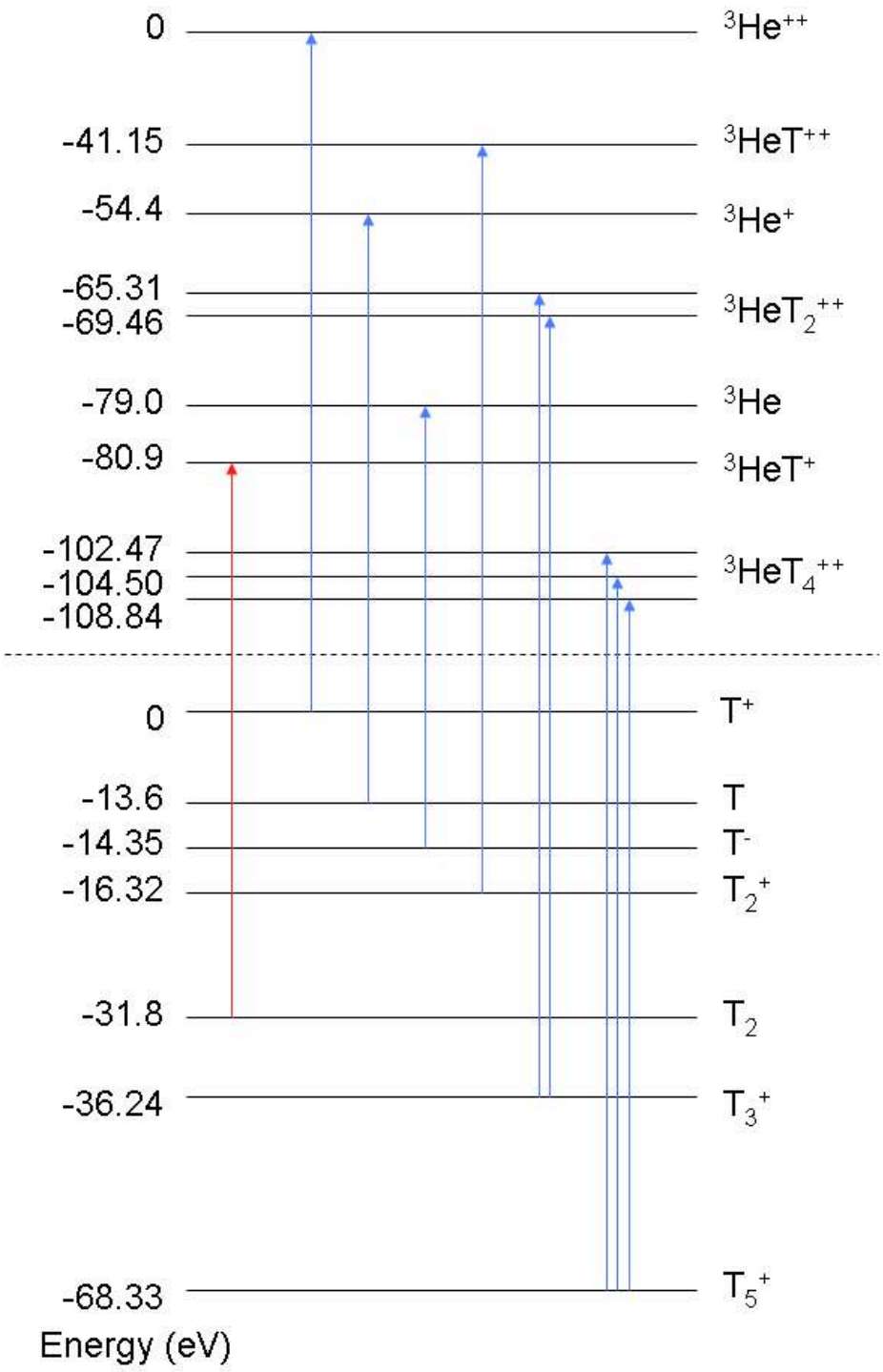

Figure 8.6: Ground state energies of the tritium species. See text for details.

Table 8.2: Endpoint energies, in eV, for the β-decays of the other tritium species with respect to the mass difference $\Delta M(^3\mathrm{He}, \mathrm{T})$

Decay Process	From [98]	This work
$\mathrm{T}^+ \rightarrow {}^3\mathrm{He}^{++} + e^- + \bar{\nu}_e$	-65.4	-65.4
$\mathrm{T} \rightarrow {}^3\mathrm{He}^+ + e^- + \bar{\nu}_e$	-24.6	-24.6
$\mathrm{T}^- \rightarrow {}^3\mathrm{He} + e^- + \bar{\nu}_e$	-0.75	-0.75
$\mathrm{T}_2 \rightarrow {}^3\mathrm{HeT}^+ + e^- + \bar{\nu}_e$	-16.5	-16.3
$\mathrm{T}_2^+ \rightarrow {}^3\mathrm{HeT}^{++} + e^- + \bar{\nu}_e$	-48.9	-40.57
$\mathrm{T}_3^+ \rightarrow {}^3\mathrm{HeT}_2^{++} + e^- + \bar{\nu}_e$	-35.1	(-31.94) - (-36.09)
$\mathrm{T}_5^+ \rightarrow {}^3\mathrm{HeT}_4^{++} + e^- + \bar{\nu}_e$		-31.26
		-29.23
		-24.89

the endpoint of T_2^+. No values are given in [98] for T_5^+.

As can be seen from tables 8.1 and 8.2 the β-decay of T^- is the only species to have a higher endpoint energy than the decay of T_2, and apart from T^+, all the other species have endpoints that lie within 30 eV below the endpoint of T_2, the energy interval to be analysed by the KATRIN experiment. Therefore the β-decay of all the species, bar T^+, may affect the β spectrum if there are high enough concentrations of them.

In the KATRIN Design Report [98] it is stated that due to the cubic rise of the count rate of the integral spectrum, the β-decay of all the species, except for T and T^- can be neglected. In reference [98] results of simulations of the unaccounted contributions of T and T^- in the WGTS which lead to a systematic shift of m_ν^2 of $\Delta m_\nu^2 = 0.01$ eV^2/c^4, as a function of the analysing interval below the endpoint, are shown. They find that an unaccounted concentration of T^- of a few 10^{-6} relative to T_2 would limit the sensitivity of KATRIN. For T this concentration is about two orders of magnitude larger. An estimate of the anticipated relative concentration of T^- to T_2 within the WGTS has been deduced as being $\leq 2 \times 10^{-8}$, which is two orders of magnitude smaller than the concentration found to limit the sensitivity [98].

Chapter 9

Conclusions

Neutrinos form part of the fundamental group of leptons in the Standard Model of particle physics. According to the Standard model neutrinos have zero mass. However the question of a possible finite neutrino mass, and its fundamental implications, is one of the most investigated and controversial topics in particle physics and cosmology today. Experimental investigations of neutrino oscillations have been and continue to be performed using atmospheric, solar, reactor and accelerator neutrinos. Although neutrino oscillations do not depend on the absolute masses of the neutrinos, but on the differences of the masses, their existence has provided compelling evidence for non-zero neutrino masses.

There are three main methods/experiments that are sensitive to the absolute mass of the neutrino and have been used to obtain upper limits for the mass. Neutrinoless double beta decay provides a very sensitive means of obtaining an absolute value of a neutrino mass. A number of experiments have studied/are currently studying this process using different $\beta\beta$ unstable nuclei. Cosmological data has also been used to give information on the sum of the neutrino masses using data from several sources including studies of the cosmic microwave background, large scale structures and Lyman-α forests. However the experiments that provide the most direct measurements of the neutrino mass are based on the study of the β-decay of tritium. The idea of these experiments is to detect the energies of the electrons created in the decay and to deduce the mass of the electron anti-neutrino by analysing the shape of the continuous electron energy spectrum close to the endpoint.

In the 60 year history of tritium β-decay experiments, the experiments have become more sophisticated and the upper limit for the neutrino mass decreased significantly. As

the sensitivity improved it was recognised that knowledge of the final state probability distribution is crucial in the analysis of the spectrum. However, a disturbing trend in the data which became apparent was that the analysis of the β spectra returned unphysical negative values for the neutrino mass squared. One of the possible errors for this that was suggested was an inaccuracy in the theoretical final state distribution. The two most recent experiments, Mainz and Troitsk, which ran from the early 1990's to 2001, initially reported negative values for the neutrino mass squared, however both experiments eliminated this problem by reducing the systematic uncertainties in the case of the Mainz experiment, and accounting for the bump in the spectrum due to excess count rate in the case of the Troitsk experiment. The upper limits for the neutrino mass obtained by these experiments are $m_\nu < 2.3$ eV/c^2 (Mainz) and $m_\nu < 2.05$ eV/c^2 (Troitsk). Having reached their sensitivity limits, a new experiment with the ability to measure the electron neutrino mass in the sub eV region was proposed. The KATRIN experiment, which is currently under construction, is a next generation tritium β-decay experiment with a sensitivity in the neutrino mass of $m_\nu < 0.2$ eV/c^2. As the accuracy of the neutrino mass determined is limited by the the accuracy of the final state distribution (FSD), a very accurate knowledge of the FSD is required.

In the 1980's an elaborate FSD for the β-decay of T_2 was constructed [113] to aid the interpretation of the neutrino mass experiment at the Lawrence Livermore National Laboratory. In the 1990's a reinvestigation of the FSD was performed [106], which was initiated by the negative neutrino mass squared problem. The main aim of the new investigation was to validate the underlying approximations used in the previous work, including the sudden approximation and Born-Oppenheimer approximation, and to meet the sensitivity requirements of the Mainz and Troitsk experiments.

In this work a reinvestigation of the FSD has been performed to satisfy the higher resolution requirements and increased sensitivity of the KATRIN experiment. The KATRIN experiment aims to obtain a value for the neutrino mass by analysing the β spectrum in an energy interval with a lower limit of 30 eV below the endpoint energy. In this energy region only the effect from the lowest lying electronic states of the daughter molecule need to be considered for the FSD. However as other parameters, such as the background noise, will be investigated by KATRIN by analysing a much larger energy interval, the FSD resulting from the high lying electronic states and electronic continuum of the daughter molecule must also be known.

A recalculation of the final state distribution of the first six electronic states of $^3HeT^+$ resulting from the β-decay of T_2 in the ground rovibrational state has been performed. Energies and radial wavefunctions for the bound rovibrational states of $^3HeT^+$, as well as for the ground state of T_2 were determined using the LEVEL code by Le Roy, and providing as input the electronic potentials for the daughter and parent molecules. For the nuclear motion continuum, the energies and radial wavefunctions of the continuum states of $^3HeT^+$ were determined at chosen energy steps using the BCONT code by Le Roy. Using these radial wavefunctions as well as the electronic overlap, the probabilities of decay to each of the bound states and probability density distribution of the nuclear motion continuum has been determined. Two different methods were used to account for the predissociative resonance (quasibound) states, depending on their position and shape. For isolated resonances with narrow widths, the discrete result determined by the LEVEL program was used. For non-isolated resonances with larger widths, the probability density profile of the resonance was determined using the BCONT program.

As the gaseous tritium source in the KATRIN experiment will be at a temperature of about 30 K, there will be thermal excitation of the T_2 molecules. At this temperature, the T_2 molecules will be mainly distributed in the first four rotational states of the electronic and vibrational ground state. In fact there will be more molecules in the $J_i = 1$ state than $J_i = 0$. Previous calculations of the final state distribution mainly focused on $J_i = 0$, with the distribution for the β-decay from $J_i = 1$ only calculated for the ground electronic state of $^3HeT^+$. In this work separate final state distributions for the ground state and first five electronically excited states of $^3HeT^+$ resulting from the β-decay of T_2 in rotational states $J_i = 0$, 1, 2 and 3 have been calculated.

The isotopic purity of tritium atoms in the KATRIN experiment is about 95%, therefore there can be up to 5% contamination from deuterium and hydrogen atoms and hence up to 10% of isotopomers HT and DT in the source, with the main contamination expected to come from DT molecules. Therefore the final state distributions of the first six electronic states of $^3HeD^+$ and $^3HeH^+$ resulting from the β-decay of DT an HT in rotational states $J_i = 0$ and 1, have been calculated. This is the first time the final state distribution for $^3HeD^+$ has been calculated.

The accuracy of the final state distributions of the low lying electronic states calculated in this work were checked by using two useful sum rules.

Using the final state distributions calculated here, the overall distribution for a source

at a given temperature and with a known amount of isotopic contamination can be determined. However any uncertainty in the temperature or amount of contamination, can lead to an inaccurate distribution being used. In this work, estimates of the error in the value of the neutrino mass deduced from fitting theoretical curves, due to uncertainties in the temperature for a thermal source, ortho:para ratio of T_2 for a non thermal source at 30 K and percentage of DT molecules in the source have been obtained, in order to see how accurately these parameters need to be known. As the source temperature will be stabilised to a precision of 1% in the KATRIN experiment, uncertainties in the temperature of this scale will have negligible effect on the deduced neutrino mass. Uncertainties in the ortho:para ratio give errors of the same order as the temperature uncertainties, however as the stability of the ortho:para ratio depends on the experimental conditions the errors may change therefore it is recommended that the ortho:para ratio be measured directly when running the experiment. The largest errors come from the DT contamination of the source. It is found that for a neutrino mass of 0.2 eV/c^2, a 10% change in the amount of DT molecules in the source gives an error on the deduced neutrino mass of about 18%. Laser Raman spectroscopy will be used to provide a real-time quantitative analysis of the composition of the gas mixture.

In previous calculations of the final state distribution, the part associated with the electronic continuum of $^3HeT^+$ is the least accurately determined. The missing probability in the most recent FSD [106] was associated to this part of the spectrum. Therefore in this work, the probability distribution of the electronic continuum has been calculated using a different method to previous works. The R-matrix method has been used to perform a geometry dependant treatment of the resonance states of $^3HeT^+$ by considering electron collisions with a $^3HeT^{2+}$ target. Positions and widths of resonances converging to the first eight excited states of $^3HeT^{2+}$ have been detected for 21 internuclear separations in the range R = 1.0 - 2.0 a_0 in steps of 0.05 a_0. Resonance curves were obtained by correlating the resonances detected at different geometries using quantum defect analysis. The electronic wavefunction of the resonance states were extracted from the R-matrix calculation. By considering electron collisions with T_2^+, the electronic wavefunction for the ground state of T_2 was obtained and the overlap integrals between 9 resonance states and T_2 determined. Using the BCONT program, the probability density distribution for each resonance was obtained. A discrete probability distribution of the background continuum and remaining infinite number of resonances has also been

determined for $R = 1.4\ a_0$.

The entire FSD was discretized by dividing the spectrum into small energy bins of 0.01 eV. This approach is the best for the analysis by the KATRIN experiment.

In figures 9.1 and 9.2 the FSD obtained in this work is compared to the most recent FSD given by Saenz, Jonsell and Froelich [106]. The final state distribution given in [106] is for the β-decay of T_2 in the $J_i = 0$ state, and is presented as a discretized distribution with energy bins varying in size from 0.1 eV for the ground state of $^3HeT^+$ to 1.0 eV for the excited electronic states and electronic continuum up to 90 eV, to 2.0 eV for the remaining spectrum up to 240 eV. To compare the FSD obtained in this work with that of reference [106] the energy binning has been performed on the same scale.

In figure 9.1 the FSD obtained in this work for a source temperature of 30 K is compared to the FSD given in [106] where thermal excitation of T_2 is not included, i.e T = 0 K. The FSD from this work (red lines) has been offset from the FSD of reference [106] (black lines) by 0.02 eV for clarity. As can be seen from the figure there is some differences in the two distributions, suggesting that the correct FSD corresponding to the source temperature should be used in the analysis of the β spectrum. Only the FSD of the ground electronic state is shown as the FSD of the excited states do not differ significantly.

In figure 9.2 the two FSD's are compared for the electronically excited states and electronic continuum of $^3HeT^+$ up to 240 eV. In this figure the FSD obtained in this work (red points) does not account for thermal excitation, i.e. only $J_i = 0$ is considered. For clarity, the drop-lines are not shown and the points of the probability have been joined together. As the same method was used in this work as in [106] for the calculation of the FSD of the first six electronic states of $^3HeT^+$, the two FSD's in this region (< 40 eV) are in excellent agreement. In the figure the FSD of the ground state is not shown, but the excellent agreement in the excited states ($20 - 40$ eV) can be seen from the exact overlap of the two distributions.

In the region 40 - 55 eV there is some probability missing from the FSD obtained in this work. This probability corresponds to the high-lying electronic or Rydberg series of states. As the integrated probability of these states is very small, and as a sufficiently accurate probability distribution of these states has been calculated by Jonsell *et al* [117], it has not been recalculated in this work. From the R-matrix calculation discussed in

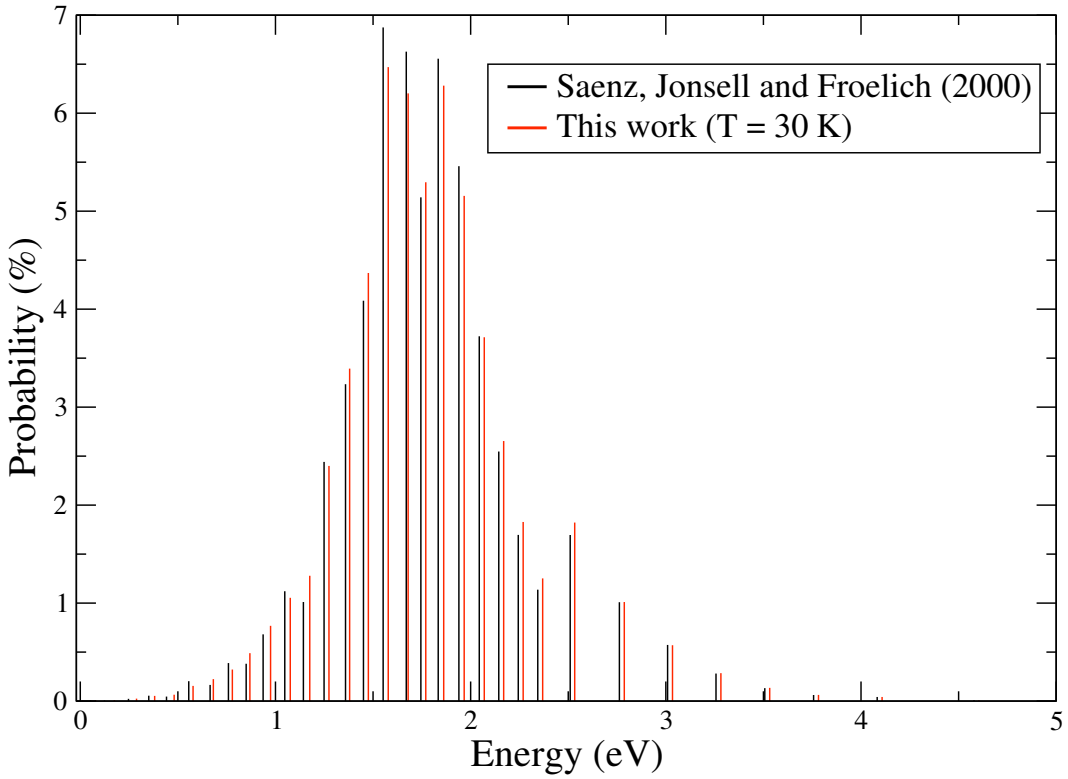

Figure 9.1: Comparison of the final state distribution of the electronic ground state of $^3HeT^+$ obtained in this work for a source temperature of 30 K with the FSD given in [106] for a source temperature of 0 K.

chapter 7, a total probability of the contribution from the Rydberg states of 1.46% is determined. This value agrees very well with the value obtained by Jonsell *et al* [117] of 1.4%.

For the probability distribution of the electronic continuum the complex scaling method was used in the previous work [149] and the R-matrix method used here. The two distributions obtained using different methods are in good agreement. In the FSD from this work there appears to be slightly less probability attributed to region where the probability of the resonance states including nuclear motion has been determined explicitly, but slightly more probability attributed to the higher energy region of the continuum.

In the previous calculation the probability in the energy region above 240 eV was represented by an atomic tail, with a total probability of about 0.13%. From the R-matrix calculation performed in this work, a total probability above 240 eV of 0.58 % is obtained.

By summing all the probabilities of the FSD, the total unnormalised probability of

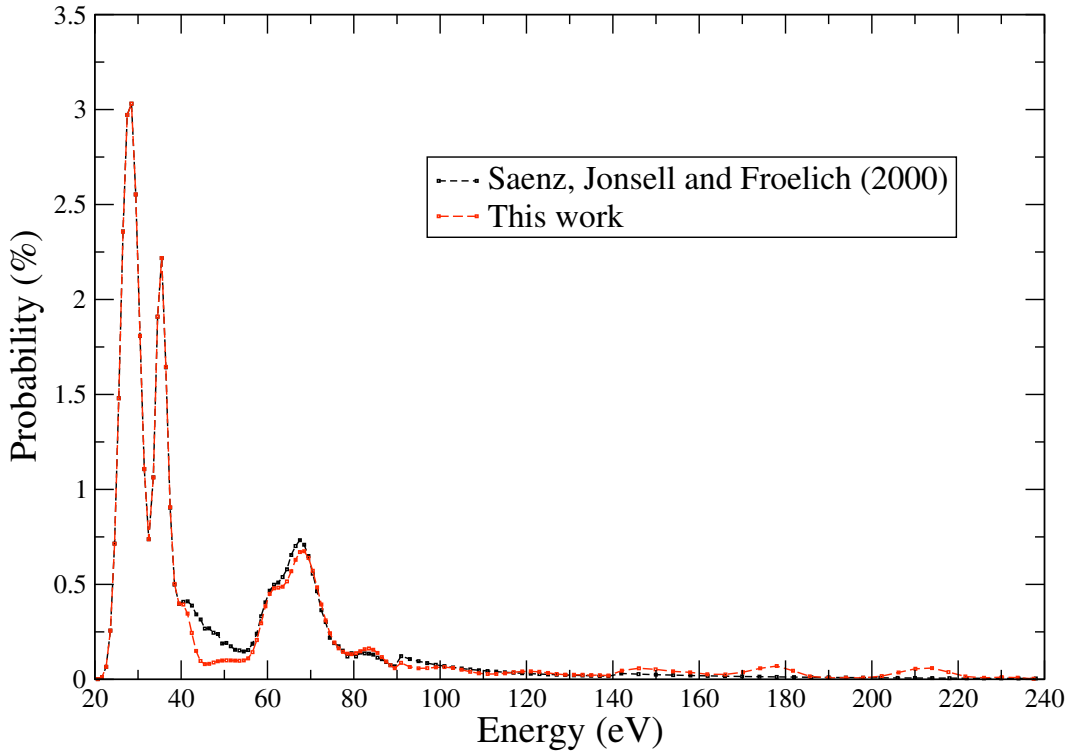

Figure 9.2: Comparison of the final state distribution of the electronically excited states and electronic continuum of $^3HeT^+$ up to 240 eV obtained in this work with the FSD given in [106]. Exact agreement is found between the two calculations at energies below 40 eV.

the FSD given in [106] adds up to 99.83%. By summing all the contributions obtained in this work, including the total contribution from the Rydberg states and the probability above 240 eV obtained from the R-matrix calculation instead of the atomic tail, the total probability in this work adds up to 99.94%. Therefore some of the missing probability has been recovered in this new calculation of the final state distribution.

In conclusion, our final state distribution with addition of the contribution due to Rydberg states evaluated previously by Jonsell *et al* [117] gives an accurate and consistent treatment of the molecular decay channels over a wide range of energies. It will allow not only the accurate fitting of the decays in the region up to 30 eV below the endpoint, but also tests to be performed over a much wider range of energies from the end point. We believe that this study resolves the molecular physics issues with decays that will be measured in the KATRIN experiment and these are now determined well enough not to cause systematic errors within the sensitivity of the proposed experiment.

Appendix A

Publications

Molecular effects in investigations of tritium molecule beta decay endpoint experiments.

N. Doss, J. Tennyson, A. Saenz and S. Jonsell.

Phys. Rev. C 73, 025502 (2006)

Molecular effects in neutrino mass measurements.

N. Doss, J. Tennyson, A. Saenz and S. Jonsell.

Book of Invited Lectures of XXIV ICPEAC, World Scientific Publishing (2006)

Calculated spectra for HeH^+ and its effect on the opacity of cool metal-poor stars

E. A. Engel, N. Doss, G. J. Harris and J. Tennyson

Mon. Not. R. Astr. Soc. 357, 471 (2005)

Bibliography

[1] http://www2.slac.stanford.edu/VVC/theroy/fundamental.html.

[2] E. Fermi. Versuch einer Theorie der beta-Strahlen. *Z. Phys*, 88:161, 1934.

[3] C. L. Cowan et al. Detection of the free neutrino - a confirmation. *Science*, 124:103–104, 1956.

[4] G. Danby et al. Observation of high-energy neutrino reactions and the existence of two kinds of neutrinos. *Phys. Rev. Lett.*, 9:36–44, 1962.

[5] K. Kodama et al. Observation of tau neutrino interactions. *Phys. Lett. B*, 504:218–224, 2001.

[6] B. Kayser. Neutrino mass, mixing and flavour change, in the review by S. Eidelman et al. *Phys. Lett. B*, 592:1, 2004.

[7] G. L. Fogli et al. Global analysis of three-flavour neutrino masses and mixings. *Prog. Part. Nucl. Phys*, 57:742–795, 2006.

[8] M. C. Gonzalez-Garcia and M. Maltoni. Phenomenology with massive neutrinos. *arXiv:0704.1800v1 [hep-ph]*, 2007.

[9] Y. Fukuda et al. Evidence for oscillation of atmospheric neutrinos. *Phys. Rev. Lett.*, 81:1562–1567, 1998.

[10] M. Sanchez et al. Measurement of the L/E distributions of atmospheric ν in Soudan 2 and their interpretation as neutrino oscillations. *Phys. Rev. D*, 68:113004, 2003.

[11] M Ambrosio et al. Matter effects in upward-going muons and sterile neutrino oscillations. *Phys. Lett. B*, 517:59–66, 2001.

[12] J. N. Bahcall, A. M. Serenelli, and S. Basu. New solar opacities, abundances, helioseismology and neutrino fluxes. *Astrophys. J.*, 621:L85–L88, 2005.

[13] R. Davis, D. S. Harmer, and K. C. Hoffman. Search for neutrinos from the sun. *Phys. Rev. Lett.*, 20:1205–1209, 1968.

[14] B. T. Cleveland et al. Measurement of the solar electron neutrino flux with the Homestake chlorine detector. *Astrophys. J.*, 496:505–526, 1998.

[15] J. N. Abdurashitov et al. Solar neutrino flux measurements by the Soviet-American Gallium Experiment (SAGE) for half the 22-year solar cycle. *J. Exp. Theo. Phys.*, 95:181–193, 2002.

[16] W. Hampel et al. GALLEX solar neutrino observations: results for GALLEX IV. *Phys. Lett. B*, 447:127–133, 1999.

[17] M. Altmann et al. Complete results for five years of GNO solar neutrino observations. *Phys. Lett. B*, 616:174–190, 2005.

[18] Q. R. Ahmad et al. Measurement of the rate of $\nu_e + d \rightarrow p + p + e^-$ interactions produced by ^{8}B solar neutrinos at the Sudbury Neutrino Observatory. *Phys. Rev. Lett.*, 87:071301, 2001.

[19] Q. R. Ahmad et al. Direct evidence for neutrino flavor transformation from neutral-current interactions in the Sudbury Neutrino Observatory. *Phys. Rev. Lett.*, 89:011301, 2002.

[20] Q. R. Ahmad et al. Measurement of day and night neutrino energy spectra at SNO and constraints on neutrino mixing parameters. *Phys. Rev. Lett.*, 89:011302, 2002.

[21] I. Apollonio et al. Limits on neutrino oscillations from the CHOOZ experiment. *Phys. Lett. B*, 466:415–430, 1999.

[22] F. Boehm et al. Final results from the Palo Verde neutrino oscillation experiment. *Phys. Rev. D*, 64:112001, 2001.

[23] K. Eguchi et al. Final results from KamLAND: Evidence for reactor antineutrino disappearance. *Phys. Rev. Lett.*, 90:021802, 2003.

[24] F. Ardellier et al. Double Chooz: A search for the neutrino mixing angle θ_{13}. *hep-ex/0606025*, 2006.

[25] M. H. Ahn et al. Measurement of neutrino oscillation by the K2K experiment. *Phys. Rev. D*, 74:072003, 2006.

[26] S. Yamamoto et al. Improved search for ν_μ to ν_e oscillation in a long-baseline accelerator experiment. *Phys. Rev. Lett.*, 96:181801, 2006.

[27] D. G. Michael et al. Observation of muon neutrino disappearance with the MINOS detectors in the NuMI neutrino beam. *Phys. Rev. Lett.*, 97:191801, 2006.

[28] Y. Hayato et al. Letter of intent: Neutrino oscillation experiment at JHF. http://neutrino.kek.jp/jhfnu/loi/loi_JHFcor.pdf.

[29] I. Ambats et al. NOνA proposal to build a 30 kiloton off-axis detector to study neutrino oscillations in the Fermilab NuMI beamline. *hep-ex/0503053*, 2005.

[30] G. L. Fogli et al. Observables sensitive to absolute neutrino masses. A reappraisal after WMAP 3-year and first MINOS results. *Phys. Rev. D*, 75:053001, 2007.

[31] A. Aguilar et al. Evidence for neutrino oscillations from the observation of $\bar{\nu}_e$ appearance in a $\bar{\nu}_\mu$ beam. *Phys. Rev. D*, 64:112007, 2001.

[32] B. Armbruster et al. Upper limits for neutrino oscillations $\bar{\nu}_\mu \rightarrow \bar{\nu}_e$ from muon decay at rest. *Phys. Rev. D*, 65:112001, 2002.

[33] A. O. Bazarko et al. MiniBooNE: Status of the Booster Neutrino Experiment. *Nucl. Phys. B (Proc. Suppl.)*, 91:210–215, 2001.

[34] http://nemo.in2p3.fr/physics/dbd.php.

[35] S. R. Elliott and J. Engel. Double-beta decay. *J. Phys. G*, 30:R183–R215, 2004.

[36] P. Vogel. Neutrinoless double beta decay. *arXiv:hep-ph/0611243v1*, 2006.

[37] H. V. Klapdor-Kleingrothaus et al. Latest results from the Heidelberg-Moscow double beta decay experiment. *Eur. Phys. J. A*, 12:147–154, 2001.

[38] H. V. Klapdor-Kleingrothaus et al. Evidence for neutrinoless double beta decay. *Mod. Phys. Lett. A*, 16:2409–2420, 2001.

[39] H. V. Klapdor-Kleingrothaus et al. Search for neutrinoless double beta decay with enriched ^{76}Ge in Gran Sasso 1990-2003. *Phys. Lett. B*, 586:198–212, 2004.

[40] C. E. Aalseth et al. Comment on 'Evidence for neutrinoless double beta decay'. *Mod. Phys. Lett. A*, 17:1475–1478, 2002.

[41] F. Feruglio, A. Strumia, and F. Vissani. Neutrino oscillations and signals in beta and $0\nu 2$beta experiments. *Nucl. Phys. B*, 637:345–377, 2002.

[42] C. E. Aalseth et al. IGEX ^{76}Ge neutrinoless double beta decay experiment: Prospects for next generation experiments. *Phys. Rev. D*, 65:092007, 2002.

[43] R. Arnold et al. First results of the search for neutrinoless double-beta decay with the NEMO3 detector. *Phys. Rev. Lett.*, 95:182302, 2005.

[44] C. Arnaboldi et al. New limit on the neutrinoless beta beta decay of ^{130}Te. *Phys. Rev. Lett.*, 95:142501, 2005.

[45] D. N. Spergel et al. Wilkinson Microwave Anisotropy Probe (WMAP) three year results: Implications for cosmology. *astro-ph/0603449*, 2006.

[46] L. Page et al. Wilkinson Microwave Anisotropy Probe (WMAP) observations: Polarization analysis. *astro-ph/0603450*, 2006.

[47] G. Hinshaw et al. Wilkinson Microwave Anisotropy Probe (WMAP) observations: Temperature analysis. *astro-ph/0603451*, 2006.

[48] M. Tegmark et al. The three-dimensional power spectrum of galaxies from the Sloan Digital Sky Survey. *Astrophys. J.*, 606:702–740, 2004.

[49] D. J. Eisenstein et al. Detection of the baryon acoustic peak in the large-scale correlation function of SDSS luminous red galaxies. *Astrophys. J.*, 633:560–574, 2005.

[50] W. J. Percival et al. The 2dF Galaxy Redshift Survey: the power spectrum and the matter content of the Universe. *Mon. Not. R. Astr. Soc*, 327:1297–1306, 2001.

[51] S. Cole et al. The 2dF Galaxy Redshift Survey: power-spectrum analysis of the final data set and cosmological implications. *Mon. Not. R. Astr. Soc*, 362:505–534, 2005.

[52] S. Hannestad. Primordial neutrinos. *Ann. Rev. Nucl. Part Sci.*, 56:137–161, 2006.

[53] J. Lesgourgues and S. Pastor. Massive neutrinos and cosmology. *Phys. Rep.*, 429:307–379, 2006.

[54] U. Seljak, A. Slosar, and P. McDonald. Cosmological parameters from combining the Lyman-α forest with CMB, galaxy clustering and SN constraints. *J. Cosmol. Astropart. Phys.*, 10:014, 2006.

[55] A. Goobar et al. The neutrino mass bound from WMAP 3 year data, the baryon acoustic peak, the SNLS supernovae and the Lyman-α forest. *J. Cosmol. Astropart. Phys.*, 6:019, 2006.

[56] R. Barate et al. An upper limit on the τ neutrino mass from three- and five-prong tau decays. *Eur. Phys. J. C*, 2:395–406, 1998.

[57] K. Assamagan. Upper limit of the muon-neutrino mass and charged-pion mass from momentum analysis of a surface muon beam. *Phys. Rev. D*, 53:6065–6077, 1996.

[58] R. G. H. Robertson and D. A. Knapp. Direct measurements of neutrino mass. *Ann. Rev. Nucl. Part Sci.*, 38:185–215, 1988.

[59] E. Holzschuh. Measurement of the neutrino mass from tritium β-decay. *Rep. Prog. Phys.*, 55:1035–1091, 1992.

[60] KATRIN homepage: http://www-ik.fzk.de/ katrin/index.html.

[61] S. C. Curran, J. Angus, and A. L. Cockroft. Beta-spectrum of tritium. *Nature*, 162:302–303, 1948.

[62] S. C. Curran, J. Angus, and A. L. Cockroft. Investigation of soft radiations II. The beta spectrum of tritium. *Philosophical Magazine*, 40:53–60, 1949.

[63] S. C. Curran, J. Angus, and A. L. Cockroft. The beta spectrum of tritium. *Phys. Rev.*, 76:853–854, 1949.

[64] G. C. Hanna and B. Pontecorvo. The β-spectrum of H^3. *Phys. Rev.*, 75:983–984, 1949.

[65] L. M. Langer and R. J. D. Moffat. The beta spectrum of tritium and the mass of the neutrino. *Phys. Rev.*, 88:689–694, 1952.

[66] D. R. Hamilton, W. P. Alford, and L. Gross. Upper limits on the neutrino mass from the tritium beta spectrum. *Phys. Rev.*, 92:1521–1525, 1953.

[67] R. C. Salgo and H. H. Staub. Re-determination of beta-energy of tritium and its relation to neutrino rest mass and Gamow-Teller matrix element. *Nucl. Phys. A*, 138:417–428, 1969.

[68] R. Daris and C. St. Pierre. Beta decay of tritium. *Nucl. Phys. A*, 138:545–555, 1969.

[69] K. E. Bergkvist. High luminosity, high resolution study of endpoint behaviour of tritium beta-spectrum (I) - Basic experimental procedure and analysis with regard to neutrino mass and neutrino degeneracy. *Nucl. Phys. B*, 39:317–370, 1972.

[70] K. E. Bergkvist. High luminosity, high resolution study of endpoint behaviour of tritium beta-spectrum (II) - Endpoint energy of spectrum - Comparison of experimental axial -vector matrix element with predictions based on PCAC. *Nucl. Phys. B*, 39:371–406, 1972.

[71] E. F. Tret'yakov et al. Measurements of tritium beta-spectrum in order to improve upper limit for rest mass of anti-neutrino. *Izvestiya Akademii Nauk SSSR Seriya Fizicheskaya*, 40:2025–2035, 1976.

[72] V. A. Lubimov et al. Estimate of the ν_e mass from the beta-spectrum of tritium in the valine molecule. *Phys. Lett. B*, 94:266–268, 1980.

[73] J. J. Simpson. Re-evaluation of an experiment claiming a non-zero neutrino mass. *Phys. Rev. D*, 30:1110–1111, 1984.

[74] K. E. Bergkvist. A questioning of a claim of evidence of finite neutrino mass. *Phys. Lett. B*, 154:224–230, 1985.

[75] K. E. Bergkvist. A further comment on the ITEP neutrino mass experiments. *Phys. Lett. B*, 159:408–410, 1985.

[76] S. Boris et al. The neutrino mass from the tritium beta-spectrum in valine. *Phys. Lett. B*, 159:217–222, 1985.

[77] S. Boris et al. Neutrino mass from the beta-spectrum in the decay of tritium. *Phys. Rev. Lett.*, 58:2019–2022, 1987.

[78] M. Fritschi et al. An upper limit for the mass of the ν_e from tritium beta-decay. *Phys. Lett. B*, 173:485–489, 1986.

[79] E. Holzschuh, M. Fritschi, and W. Kundig. Measurement of the electron neutrino mass from tritium beta-decay. *Phys. Lett. B*, 287:381–388, 1986.

[80] H. Kawakami et al. An upper limit for the mass of the electron anti-neutrino from the INS experiment. *Phys. Lett. B*, 187:198–204, 1987.

[81] H. Kawakami et al. Neutrino mass and endpoint energy of ^{3}H beta-decay. *Journal of the Physical Society of Japan*, 57:2873–2876, 1988.

[82] H. Kawakami et al. New upper bound on the electron anti-neutrino mass. *Phys. Lett. B*, 256:105–111, 1991.

[83] J. F. Wilkerson et al. Limit on $\bar{\nu}_e$ mass from free molecular tritium beta-decay. *Phys. Rev. Lett.*, 58:2023–2026, 1987.

[84] R. G. H. Robertson et al. Limit on ν_e^- mass from observation of the β decay of molecular tritium. *Phys. Rev. Lett.*, 67:957–960, 1991.

[85] W. Stoefflㅣ and D. J. Duncan. Anomalous structure in the beta decay of gaseous molecular tritium. *Phys. Rev. Lett.*, 75:3237–3240, 1995.

[86] C. Weinheimer et al. Improved limit on the electron-antineutrino rest mass from tritium β-decay. *Phys. Lett. B*, 300:210–216, 1993.

[87] H. Barth et al. Status and perspectives of the Mainz neutrino mass experiment. *Prog. Part. Nucl. Phys*, 40:353–376, 1998.

[88] A. I. Belesev et al. Results of the Troitsk experiment on the search for the electron antineutrino rest mass in tritium β-decay. *Phys. Lett. B*, 350:263–272, 1995.

[89] V. M. Lobashev et al. Direct search for the mass of neutrino and anomaly in the tritium beta-spectrum. *Phys. Lett. B*, 460:227–235, 1999.

[90] C. Weinheimer et al. High precision measurement of the tritium β-decay spectrum near its endpoint and upper limit on the neutrino mass. *Phys. Lett. B*, 460:219–226, 1999.

[91] V. M. Lobashev et al. Direct search for the neutrino mass in the beta-decay of tritium: Status of the Troitsk ν-mass experiment. *Phys. At. Nucl.*, 63:1037–1043, 2000.

[92] J. Bonn et al. Results from the Mainz neutrino mass experiment. *Prog. Part. Nucl. Phys*, 48:133–139, 2002.

[93] S. Jonsell and H. J. Monkhorst. Effect from changes in the final state spectrum on the neutrino mass determination from T_2 beta decay experiments. *Phys. Rev. Lett.*, 76:4476–4479, 1996.

[94] G. Beamson, H. Q. Porter, and D. W. Turner. The collimating and magnifying properties of a superconducting field photoelectron spectrometer. *J. Phys. E*, 13:64–66, 1980.

[95] V. M. Lobashev et al. Numerical simulation of a low-energy electron electrostatic integral spectrometer with adiabatic magnetic collimation. *Nucl. Inst. Meth. A*, 238:496–499, 1985.

[96] V. M. Lobashev and P. E. Spivak. A method for measuring the electron antineutrino rest mass. *Nucl. Inst. Meth. A*, 240:305–310, 1985.

[97] A. Picard et al. A solenoid retarding spectrometer with high resolution and transmission for keV electrons. *Nucl. Inst. Meth. B*, 63:345–358, 1992.

[98] J. Angrik et al. KATRIN Design Report 2005. *FZKA scientific report 7090*, 2005.

[99] L. Fleischmann et al. On dewetting dynamics of solid films of hydrogen isotopes and its influence on tritium beta spectroscopy. *Eur. Phys. J. B*, 16:521–529, 2000.

[100] V. N. Aseev et al. Energy loss of 18 keV electrons in gaseous T_2 and quench condensed D_2 films. *Eur. Phys. J. D*, 10:39–52, 2000.

[101] Mainz homepage: http://www.physik.uni-mainz.de/exakt/neutrino/index.html.

[102] C. Kraus et al. Final results from phase II of the Mainz neutrino mass search in tritium beta decay. *Eur. Phys. J. C*, 40:447–468, 2005.

[103] V. M. Lobashev. The search for the neutrino mass by direct method in the tritium beta-decay and perspectives of study it in the project KATRIN. *Nucl. Phys. A*, 719:153–160, 2003.

[104] A. Osipowicz et al. Letter of Intent - KATRIN: A next generation tritium beta decay experiment with sub-eV sensitivity for the electron neutrino mass. *FZKA scientific report 6691, hep-ex/0109033*, 2001.

[105] T. Thümmler et al. Addendum to the Letter of Intent. *FZKA scientific report 6752*, 2002.

[106] A. Saenz, S. Jonsell, and P. Froelich. Improved molecular final-state distribution of HeT^+ for the β-decay process of T_2. *Phys. Rev. Lett.*, 84:242–245, 2000.

[107] M. Cantwell. Molecular excitation in beta decay. *Phys. Rev.*, 101:1747–1756, 1956.

[108] K. Szalewicz, O. Fackler, B. Jeziorski, W. Kołos, and H. J. Monkhorst. Molecular effects in tritium β decay. III: Electronic resonances of the HeT^+ ion and dependence of neutrino mass on the accuracy of the theoretical model. *Phys. Rev. A*, 35:965–979, 1987.

[109] A. Saenz and P. Froelich. Effect of final-state interactions in allowed β decays. I: General formalism. *Phys. Rev. C*, 56:2132–2161, 1997.

[110] R. D. Williams and S. E. Koonin. Atomic final-state interactions in tritium decay. *Phys. Rev. C*, 27:1815–1817, 1983.

[111] W. Kołos, B. Jeziorski, K. Szalewicz, and H. J. Monkhorst. Molecular effects in tritium β decay: Transitions to the discrete electronic states of the HeT^+ molecule. *Phys. Rev. A*, 31:551–555, 1985.

[112] B. Jeziorski, W. Kołos, K. Szalewicz, O. Fackler, and H. J. Monkhorst. Molecular effects in tritium β decay. II: Rotation-vibration excitation, dissociation, and predissociation in the decay of the T_2 and TH molecules. *Phys. Rev. A*, 32:2573–2583, 1985.

[113] O. Fackler, B. Jeziorski, W. Kołos, H. J. Monkhorst, and K. Szalewicz. Accurate theoretical β-decay energy spectrum of the tritium molecule and its neutrino mass dependence. *Phys. Rev. Lett.*, 55:1388–1391, 1985.

[114] E. Merzbacher. *Quantum Mechanics*. John Wiley and Sons, 1998.

[115] A. R. Edmonds. *Angular Momentum in Quantum Mechanics*. Princeton University Press, 1996.

[116] D. M. Brink and G. R. Satchler. *Angular Momentum*. Oxford University Press, 1979.

[117] S. Jonsell, A. Saenz, and P. Froelich. Neutrino-mass determination from tritium β decay: Corrections to and prospects of experimental verification of the final-state spectrum. *Phys. Rev. C*, 60:034601, 1999.

[118] L. Wolniewicz. Variational treatment of the HeH^+ ion and the β-decay in HT. *J. Chem. Phys.*, 43:1087–1091, 1965.

[119] M. Born and J. P. Oppenheimer. Zur quantentheorie der molekeln. *Ann. Phys.*, 84:457, 1927.

[120] R. J. Le Roy. LEVEL 6.0 - A computer program for solving the radial Schrödinger equation for bound and quasibound levels, and various expectation values and matrix elements. *University of Waterloo Chemical Physics Research Report CP-555R*, 1996.

[121] R. J. Le Roy. Bound continuum intensities - A computer program for calculating absorption coefficients, emission intensities or (golden rule) predissociation rates. *Comput. Phys. Commun.*, 52:383–395, 1989.

[122] J. W. Cooley. An improved eigenvalue corrector formula for solving the Schrödinger equation for central fields. *Math. Computations*, 15:363–374, 1961.

[123] J. Cashion. Testing of diatomic potential-energy functions by numerical methods. *J. Chem. Phys.*, 39:1872–1877, 1963.

[124] R. N. Zare and J. K. Cashion. The IBM Share Program D2 NU SCHR 1072 for solution of the Schrödinger Radial Equation, by J. W. Cooley: Necessary and useful modifications for its use on an IBM 7090. *University of California Lawrence Radiation Laboratory Report UCRL-10881*, 1963.

[125] R. N. Zare. Programs for calculating relative intensities in the vibrational structure of electronic band systems. *University of California Lawrence Radiation Laboratory Report UCRL-10925*, 1963.

[126] R. N. Zare. Calculation of intensity distribution in the vibrational structure of electronic transitions: The $B^3\Pi_{0^+u} - X^1\Sigma_{0^+g}$ resonance series of molecular iodine. *J. Chem. Phys.*, 40:1934–1944, 1964.

[127] K. Smith. *The Calculation of Atomic Collision Processes, Chapter 4.* Wiley-Interscience, New York, 1971.

[128] P. O. Löwdin. An elementary iteration-variation procedure for solving the schrödinger equation. *Technical Note No. 11, Quantum Chemistry Group, Uppsala University, Uppsala, Sweden*, 1958.

[129] R. J. Le Roy and R. B. Bernstein. Shape resonances and rotationally predissociating levels: the atomic collision time-delay functions and quasibound level properties of $H_2(X^1\Sigma_g^+)$. *J. Chem. Phys.*, 54:5114–5126, 1971.

[130] R. J. Le Roy and W. K. Liu. Energies and widths of quasibound levels (orbiting resonances) for spherical potentials. *J. Chem. Phys.*, 69:3622–3631, 1978.

[131] P. G. Burke and K. A. Berrington. *Atomic and molecular processes: an R-matrix approach*. Institute of Physics Publishing, 1993.

[132] J. C. Slater. *Quantum Theory of Atomic Structure*. McGraw-Hill, 1960.

[133] B. H. Bransden and C. J. Joachain. *Physics of Atoms and Molecules*. Longman Scientific and Technical, 1983.

[134] J. Tennyson, P. G. Burke, and K. A. Berrington. The generation of continuum orbitals for molecular R-matrix calculations using Lagrange orthogonalisation. *Comput. Phys. Commun.*, 47:207–212, 1987.

[135] C. J. Gillan, J. Tennyson, and P. G. Burke. *Computational methods for electron molecule collisions ed W. M. Huo and F. A. Gianturco*. Plenum Press, New York 233 Spring street, New York, NY 10013, USA, 1995.

[136] K. L. Baluja, P. G. Burke, and L. A. Morgan. R-matrix propagation program for solving coupled second-order differential equations. *Comput. Phys. Commun.*, 27:299–307, 1982.

[137] L. A. Morgan. A generalized R-matrix propagation program for solving coupled second-order differential equations. *Comput. Phys. Commun.*, 31:419–422, 1984.

[138] M. Gailitis. New forms of asymptotic expansions for wavefunctions of charged-particle scattering. *J. Phys. B*, 9:843–854, 1976.

[139] C. J. Noble and R. K. Nesbet. CFASYM, a program for the calculation of the asymptotic solutions of the coupled equations of electron collision theory. *Comput. Phys. Commun.*, 33:399–411, 1984.

[140] H. Feshbach. Unified theory of nuclear reactions. *Ann. Phys. (N.Y.)*, 5:357–390, 1958.

[141] H. Feshbach. A unified theory of nuclear reactions II. *Ann. Phys. (N.Y.)*, 19:287–313, 1962.

[142] G. Breit and E. P. Wigner. Capture of slow neutrons. *Phys. Rev.*, 49:519–531, 1936.

[143] A. D. McLean. in W. A. Lester, ed., 'Potential Energy Surfaces in Chemistry' San Jose. *IBM Research Laboratory*, page 87, 1971.

[144] C. J. Noble. The ALCHEMY Linear Molecule Integral Generator. *Daresbury Laboratory Technical Memorandum, page DL/SCI/TM33T*, 1982.

[145] J. Tennyson. Phase factors in electron-molecule collsion calculations. *Comput. Phys. Commun.*, 100:26–30, 1997.

[146] J. Tennyson. A new algorithm for Hamiltonian matrix construction in electron-molecule collsion calculations. *J. Phys. B*, 29:1817–1828, 1996.

[147] J. Tennyson and C. J. Noble. RESON - A program for the detection and fitting of Breit-Wigner resonances. *Comput. Phys. Commun.*, 33:421–424, 1984.

[148] W. Kołos, B. Jeziorski, H. J. Monkhorst, and K. Szalewicz. Quantum chemical contribution to electron neutrino mass determination. *Int. J. Quantum Chem.*, S 19:421–441, 1986.

[149] P. Froelich, B. Jeziorski, W. Kołos, H. Monkhorst, A. Saenz, and K. Szalewicz. Probability distribution of excitations to the electronic continuum of HeT^+ following the β decay of the T_2 molecule. *Phys. Rev. Lett.*, 71:2871–2874, 1993.

[150] P. Froelich and A. Saenz. Calculation of the β-decay spectrum of the T_2 molecule beyond the sudden impulse approximation. *Phys. Rev. Lett.*, 77:4724–4727, 1996.

[151] A. Saenz and P. Froelich. Effect of final-state interactions in allowed β decays. II: Reliability of the β-decay spectrum for T_2. *Phys. Rev. C*, 56:2162–2184, 1997.

[152] S. Jonsell, A. Saenz, and P. Froelich. Non-adiabatic couplings between the final states of tritium beta decay. *Pol. J. Chem.*, 72:1323–1333, 1998.

[153] W. Kołos and J. M. Peek. New *ab initio* potential curve and quasibound states of HeH^+. *Chem. Phys.*, 12:381–386, 1976.

[154] W. Kołos and L. Wolniewicz. Improved potential energy curve and vibrational energies for the electronic ground state of the hydrogen molecule. *J. Mol. Spectrosc.*, 54:303–311, 1975.

[155] W. Kołos and L. Wolniewicz. Accurate adiabatic treatment of the ground state of the hydrogen molecule. *J. Chem. Phys.*, 41:3663–3673, 1964.

[156] W. Kołos. Long- and intermediate-range interaction in the three lowest sigma states of the HeH^+ ion. *Int. J. Quantum Chem.*, 10:217–224, 1976.

[157] D. M. Bishop and L. M. Cheung. A theoretical investigation of HeH^+. *J. Mol. Spectrosc.*, 75:462–473, 1979.

[158] W. Kołos, B. Jeziorski, J. Rychlewski, K. Szalewicz, H. J. Monkhorst, and O. Fackler. Molecular effects in tritium β decay. IV: Effect of crystal excitations on neutrino mass determination. *Phys. Rev. A*, 37:2297–2303, 1988.

[159] P. Froelich, A. FLores-Riveros, and W. Weyrich. Nonrelativistic Compton scattering in Furry's picture. II: Bethe surface by means of the complex-coordinate method. *J. Chem. Phys.*, 82:2305, 1985.

[160] W. Kołos and L. Wolniewicz. Potential-energy curves for the $X^1\Sigma_g^+$, $b^3\Sigma_u^+$, and $C^1\Pi_u$ states of the hydrogen molecule. *J. Chem. Phys.*, 43:2429–2441, 1965.

[161] W. Kołos, K. Szalewicz, and H. J. Monkhorst. New Born-Oppenheimer potential energy curve and vibrational energies for the electronic ground state of the hydrogen molecule. *J. Chem. Phys.*, 84:3278–3283, 1986.

[162] NIST Physical Reference Data: http://physics.nist.gov/PhysRefData/contents.html.

[163] L. Wolniewicz. Relativistic energies of the ground state of the hydrogen molecule. *J. Chem. Phys.*, 99:1851–1868, 1993.

[164] J. A. Coxon and P. G. Hajigeorgiou. Experimental Born-Oppenheimer potential for the $X^1\Sigma^+$ ground state of HeH^+: Comparison with the *ab* initio potential. *J. Mol. Spectrosc.*, 193:306–318, 1999.

[165] A. Carrington, R. A. Kennedy, T. P. Softley, P. G. Fournier, and E. G. Richard. Infrared bound to quasibound vibration-rotation spectrum of HeH^+ and its isotopes. *Chem. Phys.*, 81:251–261, 1983.

[166] M. W. Crofton, R. S. Altman, N. N. Haese, and T. Oka. Infrared-spectra of $^4HeH^+$, $^4HeD^+$, $^3HeH^+$, and $^3HeD^+$. *J. Chem. Phys.*, 91:5882–5886, 1989.

[167] F. Matsushima, T. Oka, and K. Takagi. Observation of the rotational spectra of $^4HeH^+$, $^4HeD^+$, $^3HeH^+$, and $^3HeD^+$. *Phys. Rev. Lett.*, 78:1664–1666, 1997.

[168] E. A. Engel, N. Doss, G. J. Harris, and J. Tennyson. Calculated spectra for HeH^+ and its effect on the opacity of cool metal-poor stars. *Mon. Not. R. Astr. Soc*, 357:471–477, 2005.

[169] D. K. Viers and G. M. Rosenblatt. Raman line positions in molecular hydrogen: H_2, HD, HT, D_2, DT and T_2. *J. Mol. Spectrosc.*, 121:401–419, 1987.

[170] M. Chuang and R. N. Zare. Rotation-vibration spectrum of HT: Line position measurements of the 1-0, 4-0, and 5-0 bands. *J. Mol. Spectrosc.*, 121:380–400, 1987.

[171] W. H. Press, B. P. Flannery, S. A. Teukolsky, and W. T. Vetterling. *Numerical Recipes in Fortran.* Cambridge University Press, 1992.

[172] Richard James Lewis. *Development of a Raman system for in-line monitoring of tritium at the Karlsruhe Tritium Neutrino (KATRIN) experiment.* PhD thesis, Swansea University, 2007.

[173] J. Tennyson. Continuum states of HeH^+. *J. Phys. B*, 31:L177–L185, 1998.

[174] R. L. Martin and J. S. Cohen. Excitation and ionisation accompanying the beta decay of T_2. *Phys. Lett. A*, 110:95–98, 1985.

[175] P. Froelich, K. Szalewicz, B. Jeziorski, W. Kołos, and H. J. Monkhorst. Electronic resonances of HeT^+ resulting from the β decay of the tritium molecule. *J. Phys. B*, 20:6173–6187, 1987.

[176] J. D. Power. Program No. 233. *Quantum Chem. Program Exchange*, 1973.

[177] M. J. Seaton. Quantum Defect Theory. *Rep. Prog. Phys.*, 46:167–257, 1983.

[178] J. Tennyson. Continuum and bound states of the e^--CH^+ system using the R-matrix method. *J. Phys. B*, 21:806–815, 1988.

[179] O. Burrau. . *K. Danske Vid. Selsk. Mat.-fys. Meddel.*, 7:14, 1927.

[180] E. A. Hylleraas. Über die Elektronenterme des Wasserstoffmolekuls. *Z. Phys*, 71:739, 1931.

[181] G. Jaffe. Zur Theorie des Wasserstoffmolekulions. *Z. Phys*, 87:535, 1934.

[182] I. Sandeman. . *Proc. Roy. Soc. Edinb.*, 55:72, 1935.

[183] V. A. Johnson. Correction for nuclear motion in H_2^+. *Phys. Rev.*, 60:373–377, 1941.

[184] D. R. Bates, K. Ledsham, and A. L. Stewart. Wave functions of the hydrogen molecular ion. *Phil. Trans. Roy. Soc. Lond.*, 246:215–240, 1953.

[185] K. P. Huber and G. Herzberg. *Constants of Diatomic Molecules*. Van Nostrand Reinhold, New York, 1979.

[186] J. Tennyson et al. DVR3D: a program suite for the calculation of rotation-vibration spectra of triatomic molecules. *Comput. Phys. Commun.*, 163:85–116, 2004.

[187] Y. Yamaguchi et al. The H_5^+ potential-energy hypersurface: Characterization of ten distinct energetically low lying stationary points. *J. Chem. Phys.*, 86:5072–5081, 1987.

[188] R. Prosmiti et al. Modeling the H_5^+ potential-energy surface: a first attempt. *Theor. Chem. Acc.*, 106:426–433, 2001.

[189] Z. Xie, B. J. Braams, and J. M. Bowman. *A*b initio global potential-energy surface for $H_5^+ \rightarrow H_3^+ + H_2$. *J. Chem. Phys.*, 122:224307, 2005.

[190] J. Ramanlal, O. L. Polyansky, and J. Tennyson. Zero point energy of H_3^+ and its deuterated isotopomers. *Astro. Astrophys.*, 406:383–384, 2003.